UNIVERSITY OF PADUA

Department of Pharmaceutical and Pharmacological Sciences

_____

PH.D. COURSE IN MOLECULAR SCIENCES

PHARMACEUTICAL SCIENCES CURRICULUM

XXXI CYCLE

MOLECULAR MECHANISMS IN
THE ALTERATION OF HEMOSTASIS

Coordinator: Ch.mo Prof. Leonard Jan PRINS

Supervisor: Ch.mo Prof. Vincenzo DE FILIPPIS

Ph.D. Student: Daniele PETERLE

Contents

Contents |

ABSTRACT

Hemostasis is a finely tuned physiological process that, through the concerted action of several blood cells and proteins, maintains the integrity of the vascular system. This stepwise process begins after a vessel wall injury and includes: an initial vasospasm, a platelet plug formation (primary hemostasis), an assembly and activation of the coagulation factors that results in fibrin deposition at the site of injury (secondary hemostasis), and a final dissolution of the fibrin clot that restores the blood vessel patency (fibrinolysis) (**Chapter 1**). Alterations affecting one or more of these delicate processes lead to a large number of pathological manifestations, commonly referred to as cardiovascular diseases (CVD). Nowadays, CVD are the major cause of mortality and morbidity worldwide. Despite the social and economic burden of CVD, the currently available pharmaceutical repertoire is relatively limited to a few classes of molecules (heparins, platelet antiaggregants, vitamin-K antagonists, direct thrombin inhibitors) which, however, display important side effects and need to be employed with careful dose adjustments. These difficulties stem primarily from: i) the intrinsically complex nature of the procoagulant and anticoagulant biochemical mechanisms leading to physiological hemostasis, which renders external intervention very risky and unpredictable; ii) the inadequate knowledge of the biochemical mechanisms linking blood coagulation to other vital physio-pathological processes.

The general aim of this Ph.D. project was to investigate some of the molecular mechanisms underlying hemostatic disorders. To address this relevant question, we proceeded by studying selected pathologies for which association with hemostatic complications has either been long-established (i.e., Antiphospholipid Syndrome (APS), infectious diseases) or has just been hypothesized (Parkinson's disease (PD), Transthyretin-related Amyloidosis (ATTR)), focusing our attention on the physio-pathological proteins involved in the onset of these disorders. In a first stage, our attention was focused on the study of novel interactions between α-thrombin (αT), the key enzyme of the coagulation cascade, with other plasma proteins (i.e., β_2-glycoprotein-I, α-synuclein). In a second stage, we investigated an alternative mechanism of activation of prothrombin, the precursor of αT, by a bacterial protease (subtilisin from *B. subtilis*). Finally, some selected proteases were tested against human transthyretin, whose proteolyzed form is a key factor in the onset of ATTR.

In its traditional pathway, blood coagulation culminates with the FXa-mediated conversion of prothrombin zymogen into active αT, through the formation of the prothrombinase complex on the platelet surface. Mature αT is a 36.7 kDa serine protease with a chymotrypsin-like fold. αT plays a pivotal role in blood coagulation, being able to exert both procoagulant (platelets aggregation, fibrin generation) and anticoagulant (protein C activation) functions. The equilibrium between such

different activities is regulated by the interaction of αT with other proteins through its active site and two positively charged regions, called exosites (exosite I and exosite II), which flank the catalytic cleft. In addition, αT is a multifunctional protease that, beyond blood coagulation, plays important roles also in other physiological processes such as inflammation, innate immune system, and nervous systems.

In **Chapter 2** we mapped the interaction between αT and β2-Glycoprotein I (β2GpI). β2GpI is a heavily glycosylated 45 kDa protein that resides in human plasma at a physiological concentration of 4 μM (0.25 mg/ml). Since the early 90's, β2GpI has been identified as the major autoantigen in the antiphospholipid syndrome (APS), a severe autoimmune disease clinically characterized by hemostatic alterations such as venous and arterial thrombosis, fetal loss and thrombocytopenia. Despite its involvement in the pathogenesis of APS, the physiological roles of β2GpI remain unclear and both pro- and anti-coagulant functions have been reported for this protein. In a recent work, we have shown that β2GpI selectively inhibits the procoagulant functions of human α-thrombin (i.e. prolongs fibrin clotting time, t_c, and inhibits α-thrombin-induced platelets aggregation) without affecting the unique anticoagulant activity of the protease (i.e. the proteolytic generation of the anticoagulant protein C). Here, combining molecular modeling with biochemical/biophysical techniques, we provided a coherent structural model of αT-β2GpI complex. The model has allowed us to understand at the molecular level our previous *in vitro* results. In particular, our findings suggested that β2GpI may function as an anticoagulant protein, acting as a scavenger of αT for the binding to GpIbα receptor, thus impairing platelets aggregation while enabling normal cleavage of fibrinogen and protein C.

Chapter 3 was dedicated to the role of bacterial proteases in inducing blood coagulation by direct proteolytic activation of prothrombin. This knowledge gap is particularly concerning, as bacterial infections are frequently complicated by severe coagulopathies, and, in about 35% of sepsis cases, by disseminated intravascular coagulopathies (DIC). Here, we show that addition of subtilisin (50 nM–2 μM), a serine protease secreted by the nonpathogenic bacterium *Bacillus subtilis*, to human plasma induces clotting by proteolytically converting prothrombin into active σPre2, a nicked Pre2 derivative with a single cleaved Ala470–Asn471 bond. Notably, we found that this non-canonical cleavage at Ala470–Asn471 is instrumental for the onset of catalytic activity in σPre2, which was however reduced of about 100-200 fold compared with natural αT. Of note, σPre2 could generate fibrin clots from fibrinogen, either in solution or in blood plasma, and could aggregate human platelets, either isolated or in whole blood. Our findings demonstrate that alternative cleavage of prothrombin by proteases, even by those secreted by non-virulent bacteria such as *B. subtilis*, can shift the delicate procoagulant-anticoagulant equilibrium toward thrombosis.

Abstract |

The study object presented in **Chapter 4** is the interplay between αT and α-synuclein (αSyn). αSyn is a small (14.6 kDa) presynaptic protein mainly synthesized in the brain and whose aggregation has been shown to trigger the onset of different neurodegenerative diseases, commonly referred to as synucleinopathies (i.e., Parkinson disease). As for β2GpI, the exact physiological role of αSyn is still elusive. Intriguingly, αSyn is also synthesized by platelets and was found to inhibit the Ca^{2+}-dependent release of procoagulant α-granules after αT stimulation. Moreover, clinical evidences clearly indicate that patients affected by neurodegenerative disorders have lower risks of ischemic attack. The collateral effects of αSyn in the pathogenesis and its localization on platelet surfaces prompted us to investigate a possible role of it in the hemostatic system. Here, we studied the effects of αSyn on fibrin generation and platelet activation. Furthermore, we mapped the interaction sites on αSyn and αT. Briefly, our results indicate that the negatively charged C-terminal tail of αSyn binds to the electropositive exosite-2 of thrombin, thus impairing αT-mediated platelet activation in whole blood. At variance, αSyn does not alter the rate of fibrin generation, resulting only in a minor change in the ensuing fibrin structure.

In **Chapter 5** we attempted to correlate the onset of systemic transthyretin amyloidosis to an altered activation of blood coagulation. Human transthyretin (hTTR) is an abundant homo-tetrameric plasma protein (0.2 mg/ml) involved in the transport of thyroxine and retinol through the binding to retinol binding protein. Beyond its physiological roles, hTTR is known as an amyloidogenic protein whose aggregation is responsible for several amyloid diseases, including senile systemic amyloidosis (SSA), familial amyloid polyneuropathy (FAP), and familial amyloid cardiomyopathy (FAC). From a mechanistic point of view, the proteolytic cleavage of hTTR represents an important step in fibril formation. In particular, after cleavage around position 50, hTTR C-terminal fragments have been found to aggregate far more efficiently than the full-length hTTR. Nowadays, the protease(s) responsible for this cleavage is yet to be identified although it is predicted to be a serine protease with a trypsin-like fold. Since all coagulation factors are trypsin-like serine proteases, we decided to probe them for the proteolytic cleavage of hTTR. In addition, we also probed some selected bacterial proteases, as well as some digestive apparatus and immune system proteases. hTTR was resistant to all proteases tested except to subtilisin from *B. subtilis*, which was able to cleave hTTR at pH 7.4, generating in high yields the amyloidogenic fragment hTTR(59-127). Since the hTTR(59-127) fragment was identified in amyloid deposits, these new insights might have relevant implications in hTTR-based amyloidosis.

INTRODUCTION

CHAPTER 1.1

Hemostasis: an overview

Hemostasis literally means "blood stop". It comes from the two Greek words *haeme*, meaning blood and *stasis*, meaning to stop. The ancients referred to it to describe the stoppage of blood once it left the warmth of the body (**1**).

Today, hemostasis is a finely regulated physiological process that maintains the integrity of the vascular system. It involves several cells and proteins that act in a concerted way in order to seal off local damage of the vascular system through the formation of a platelet plug and a fibrin clot. Usually, hemostasis is activated upon the release of procoagulant molecules by disrupted endothelial cells, which delimit the blood vessels. Once the clot is removed, blood flow is restored. This delicate system could be though as a pendulum governed by procoagulant and anticoagulant forces (**Figure 1**). In a first stage, when a blood vessel injury occurs, the pendulum becomes unbalanced in favor of procoagulant forces, allowing the clot formation. Then, once the blood vessel is repaired, the pendulum swings towards the anticoagulant forces, which promote the clot lysis and the restoration of vascular integrity. However, this process can become unbalanced, leading to dangerous, often fatal, hemorrhagic or thrombotic events.

Hemostasis is typically divided into three processes: primary hemostasis, secondary hemostasis and fibrinolysis, even though, *in vivo*, all these processes occur simultaneously with an upregulation over time of one in comparison to the others. Another key aspect is that hemostasis is confined to cell surfaces (in particular to platelets, fibroblasts and endothelial cells) and the entire process regulation is mediated by changes that occur at this level (**2**).
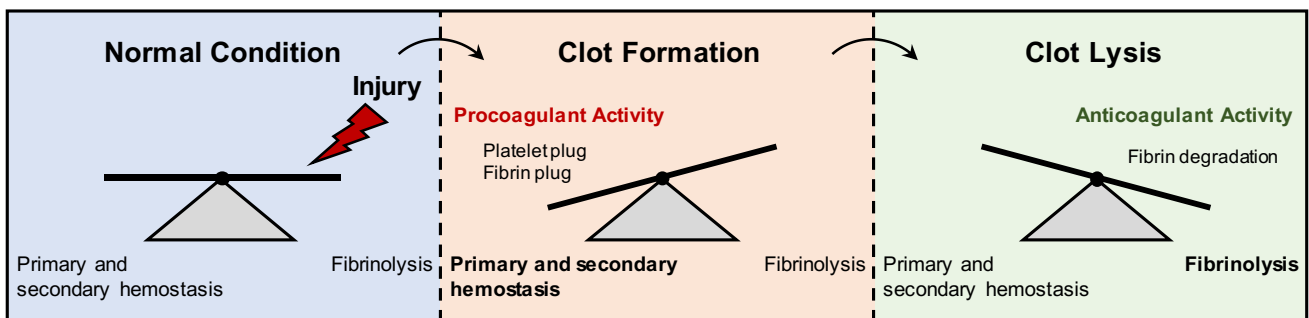

Figure 1. Hemostatic pendulum.

Primary hemostasis

Primary hemostasis consists in the formation of an initial platelet plug. The plug is particularly helpful in sealing small injuries in micro-vessels and mucosal tissues. The presence of platelets in the plug is also necessary for the correct formation of fibrin clot during secondary hemostasis. In fact, activated platelets expose negatively charged phospholipids on their surface (i.e., phosphatidylserine PS), which are a crucial binding site for the recognition and assemblage of coagulation factor complexes. In addition, platelets activate neutrophils, resulting in extrusion of the Neutrophil Extracellular Traps (NETs, networks of extracellular fibers, primarily composed of DNA), which are strong pro-coagulant mediators (**3,4**).

Primary hemostasis is subdivided into three steps: platelet adhesion, platelet activation and platelet plug formation.

Platelet adhesion

Platelet adhesion starts when the injured endothelium exposes the highly pro-coagulant subendothelial matrix (mainly composed of collagen, laminin and fibronectin). In this context, the endothelium acts as a physical barrier between the circulating platelets and the pro-coagulant substances of the extracellular space. Platelets bind the subendothelial matrix proteins through their receptors, such as Glycoprotein VI (GpVI), $\alpha_2\beta_1$ and GpIb-IX-V and other adhesion molecules constitutively expressed on their surface. In detail, GpVI and $\alpha_2\beta_1$ directly bind to collagen, whereas, GpIb-IX-V binds the matrix through the von Willebrand Factor (vWF). vWF is a very large multimeric protein (ranging in size from 260 to 20000 kDa) produced exclusively by endothelial cells and megakaryocytes and secreted both into the plasma and the subendothelial space (**5**). vWF acts as a sort of molecular "glue" between platelet receptors and the subendothelial matrix proteins. It has been demonstrated that this type of adhesion is especially important in vessels with high shear rates (**6**). In fact, under high-shear forces, vWF unfolds and exhibits new surfaces that capture platelets streaming off by the damage. Of note, mutations affecting both vWF or GpIb-IX-V result in hemorrhagic complications, such as von Willebrand disease (**7**) and Bernard-Soulier syndrome (**8**).

Platelet activation

Platelet adhesion to the subendothelial matrix, either directly or via vWF binding, leads to their activation, which includes an increase of intracellular Ca^{2+} concentration that triggers cell signalling. Activation causes a variety of changes in platelets.

Firstly, activated platelets lose their discoidal shape and assume an elongated form, also exposing characteristic protuberances called pseudopods.

After that, platelets degranulate and release preformed cytoplasmic granules into the extracellular environment (i.e., α-granules and dense bodies). Platelet α-granules are rich in vWF, coagulation factors, such as fibrinogen (FI), Factor V (FV) and Factor XIII (FXIII) and adhesion molecules, such as P selectine. All these proteins participate in primary (vWF and fibrinogen) or secondary (fibrinogen, FV and FXIII) hemostasis. On the other hand, dense granules (or δ-granules) contain ADP and serotonin, two other pro-coagulant molecules that promote the accumulation of Ca^{2+}, an important cofactor for further platelet activation.

Activated platelets also undergo a shift in their phospholipid metabolism pathway. Arachidonic acid is released from phosphatidylcholine after activation of phospholipase A_2 and is subsequently processed by different enzymes (COX-1, COX-2) into several compounds belonging to the eicosanoid family. Among these, the most important compound is thromboxane-A_2, a strong platelet activator.

Membrane flipping is another change that occurs during platelet activation. In normal conditions, the charged phospholipids are asymmetrically distributed in the phospholipid bilayer. In particular, phosphatidylserine (PS), a negatively charged phospholipid, is preferentially positioned on the inner membrane leaflet. Upon platelet activation, PS molecules are exposed to the outer side of the membrane. This is a crucial step since PS provides an optimal binding site for many coagulation factors, constituting a support on which they can assemble into complexes, thus accelerating fibrin clot formation (**9**). It is also reported that platelets spread out microvesicles rich in PS over their surface, extending the surface on which factors can assemble (**10**).

Platelets are further activated by a positive feedback mechanism. In fact, platelet degranulation induces the release of molecules, such as ADP and Thromboxane A2, which activates receptors positioned in the extracellular space of other non-active platelets, triggering an outside-in signalling that provokes their activation (**11**). In a similar way, coagulation factors localized on the platelets surface (α-thrombin) can also mimic this effect. The signalling is mediated by G protein-coupled receptors (GPCRs), such as $P2Y_{12}$ (the receptor for ADP), and PARs (Protease Activated Receptors), such as PAR-1 and PAR-4. Mature α-thrombin is the main activator of PAR-1 and PAR-4, cleaving these receptors at their extracellular amino terminus. Once cleaved, the newly generated N-terminal fragment activates the receptor by binding to a conserved pocket in the second extracellular loop (**12**). In this way, even if α-thrombin dissociates from PARs, the receptors remain activated.

Finally, platelets activate an inside-out signalling which induces a conformational rearrangement of the GpIIb/IIIa receptor, an integrin which is constitutively expressed in an inactive form by platelets. This conformational rearrangement enhances the receptor's affinity for fibrinogen

and ensures that platelets are able to aggregate and mediate the formation of the fibrin plug. Low levels of this receptor result in Glanzmann's thrombasthenia, a disorder in which the bleeding time is significantly prolonged (**13**).

Platelet aggregation

The last step in primary hemostasis is platelet aggregation. The main mediator is fibrinogen, which, upon binding to GpIIb/IIIa receptor, allows platelets to adhere to each other and to form a solid plug. The platelet plug is particularly important in blood microvessels in response to small, daily trauma. Nevertheless, in those cases in which the dimension of blood vessels is bigger, or the injury is more drastic, the platelet plug is not sufficient to stop the bleeding and a further stabilization is mandatory. This is accomplished by the fibrin clot, the final effector of secondary hemostasis.

Secondary hemostasis

Secondary hemostasis, or blood coagulation, refers to the sequence of events that result in the deposition of a fibrin network over the platelet plug. This process involves cells (such as fibroblasts, endothelial cells, leucocytes and platelets) and enzymatic or non-enzymatic (substrates and cofactors) proteins, called coagulation factors. These factors are identified by Roman numerals, on the base of the order in which they were historically isolated (**Table 1**). However, the first four factors, fibrinogen, prothrombin, tissue factor (TF) and calcium are usually not named with Roman numerals. Coagulation factors circulate in the bloodstream in an inactive form. The precursors of the proteolytic enzymes are called "zymogens". The active form of zymogens is conventionally indicated by inserting a small "a" after the protein's name.

With the exception of Factor III, IV and FVIII, the coagulation factors are produced in the liver, where they undergo a post-translational modification (vitamin K dependent γ-carboxylation of the glutamic acids residues) that enables them to bind calcium (promoting a conformational change) which is, in turn, required for the binding to PS (**14**). Non-carboxylated factors are inactive because they cannot bind to platelet surfaces and, therefore, neither can participate in the coagulation cascade. Of note, the anticoagulant drug warfarin acts at this level by inhibiting vitamin K-epoxide reductase, the enzyme which converts oxidized vitamin K back into its biologically active form. Another crucial constituent of secondary hemostasis are the membrane phospholipids, particularly PS (phosphatidylserine phospholipids). PSs on the surface of activated platelets act as an "aircraft carrier" on which the coagulation factors land and get in touch with each other. Binding to PS strongly enhances coagulation factor complexes activity (by 1000-fold) and protects them from inhibitors. Furthermore, platelets promote coagulation by creating a high local concentration of coagulation

factors and by producing short-chain polyphosphates which increase thrombin generation and fibrin deposition.

Table 1. Nomenclature and function of the coagulation factors [adapted from Palta et al., 2014]

Factor number	Factor name	Function	Plasma half-life (h)	MW (kDa)	Plasma conc. (mg/ml)
I	Fibrinogen	Clot formation	90	340	2.6
II	Prothrombin	Activation of I, V, VII, VIII, XI, XIII, protein C, platelets	65	72	0.1
III	TF	Co factor of VIIa	-	35	-
IV	Calcium	Facilitates coagulation factor binding to phospholipids	-	-	0.9
V	Proacclerin, labile factor	Co-factor of X-prothrombinase complex	15	330	7 µg/ml
VI	Unassigned				
VII	Stable factor, proconvertin	Activates factors IX, X	5	50	0.5 µg/ml
VIII	Antihaemophilic factor A	Co-factor of IX-tenase complex	10	300	0.1 µg/ml
IX	Antihaemophilic factor B	Activates X: Forms tenase complex with factor VIII	25	55	5 µg/ml
X	Stuart-Prower factor	Prothrombinase complex with factor V: Activates factor II	40	59	10 µg/ml
XI	Plasma thromboplastin antecedent	Activates factor IX	45	160	5 µg/ml
XII	Hageman factor	Activates factor XI, VII and prekallikrein	-	80	40 µg/ml
XIII	Fibrin-stabilising factor	Crosslinks fibrin	200	320	30 µg/ml
XIV	Prekallikerin (F Fletcher)	Serine protease zymogen	35	86	50 µg/ml
XV	HMWK (F Fitzgerald)	Co factor	150	110	70 µg/ml
XVI	vWf	Binds to FVIII, mediates platelet adhesion	12	260-20000	10 µg/ml
XVII	Antithrombin III	Inhibits IIa, Xa, and other proteases	72	58	150 µg/ml
XVIII	Heparin cofactor II	Inhibits IIa	60	65	90 µg/ml
XIX	Protein C	Inactivates Va and VIIIa	0.4	62	5 µg/ml
XX	Protein S	Cofactor for activated protein C	-	69	10 µg/ml

TF, tissue Factor; vWF, von Willebrand Factor; HMWK, High Molecular Wheight Kininogen

The coagulation cascade

Since the 1960s, the coagulation process has been fitted into a model that resembles a cascade (this is where the term coagulation cascade comes from) (**15,16**). This model foresees the existence of two distinct pathways (extrinsic and intrinsic) that converge onto a common pathway at the activation of FX, and in which each zymogen is activated by the upstream activated coagulation factor. (**Figure 2**).

According to this model, the extrinsic pathway starts with the exposure of tissue factor (TF) by the subendothelial tissue (**17**). After a vascular insult, the endothelium becomes interrupted allowing the contact between TF, circulating FVIIa and calcium, which in turn trigger FX activation (**18**).

On the other hand, the intrinsic pathway begins with FXII, HMW kininogen, prekallikrein and FXI. The interaction between these proteins results in the activation of FXIa, which in turn activates FIX. Subsequently, FIXa binds to FVIII and to a phospholipids surface (PS) to form the so-called *tenase complex,* which is responsible for the activation of FX (**14**).
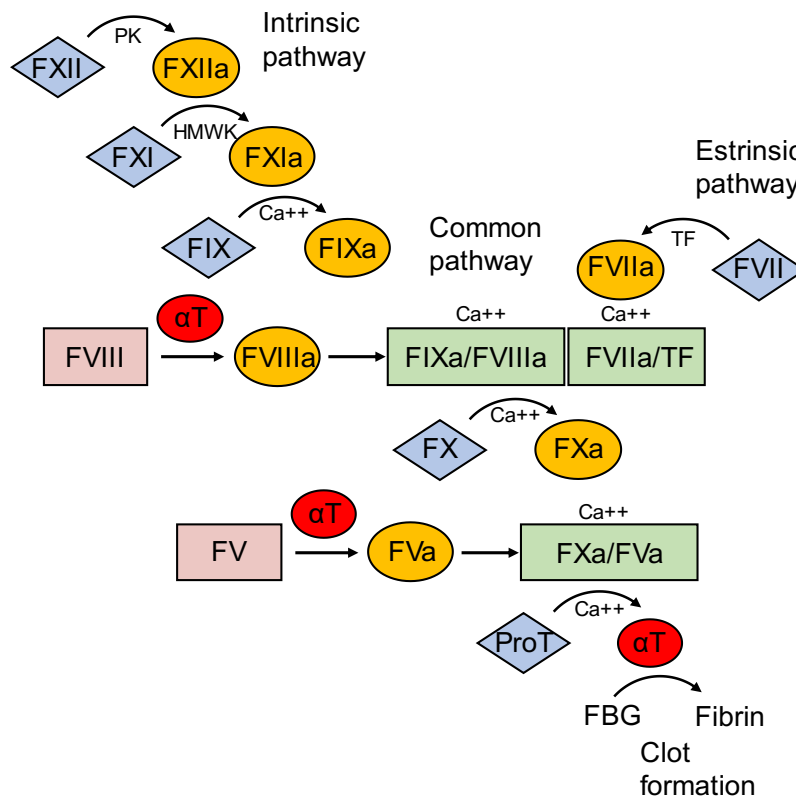
Figure 2. Earlier or *in vitro* concept of coagulation [adapted from Bunn and Aster, 2011]. The fibrin clot can be formed by activation of the intrinsic or the extrinsic pathway. In *in vitro* tests, the intrinsic pathway is triggered by surface contacts. Key: blue diamonds, zymogens; orange circles, cofactors and active enzymes; pink rectangles, pro-cofactors; green rectangles, biomolecular complexes; αT in small red circles, α-thrombin; ProT, prothrombin; HMWK, high molecular weight kininogen; PK, prekallikrein; TF, tissue factor; FBG, fibrinogen.

The common pathway starts with the activation of FX. FXa interacts with cofactor V (FV), and calcium on a phospholipid membrane, thereby establishing the *prothrombinase complex*, which converts prothrombin (FII) into α-thrombin (FIIa). Mature α-thrombin (from here on also called αT) activates FXIII and cleaves circulating fibrinogen forming an insoluble fibrin network.

The coagulation cascade model is particularly useful in understanding *in vitro* coagulation tests (thrombin time, TT; prothrombin time, PT; partial thromboplastin time, aPTT) but does not incorporate the crucial role of cell-based surfaces during *in vivo* coagulation (**19**). Indeed, the waterfall model does not take into account the intricate interplay between cells, negatively charged surfaces and coagulation factors. In addition, FXII has no role in the activation of physiologic coagulation and people lacking this factor, as well as prekallikrein and HMW kininogen, do not display any hemorrhagic tendencies (**20**). However, other physiological roles in fibrinolysis, angiogenesis and inflammation have been documented for FXII (**21**). For these reasons, nowadays the most widely accepted model is a time-dependent one in which coagulation is divided into four consecutive steps: initiation, amplification, propagation (of thrombin generation) and fibrin formation (**22**) (**Figure 3**).

Initiation

The initiation step of blood coagulation begins with the exposure of TF (extrinsic pathway) and results in the generation of a small amount of α-thrombin and FIXa. TF is present in an inactive (cryptic) conformation on the surface of fibroblasts, which are located in the perivascular district. In damaged vessels, TF is exposed to the bloodstream and binds to FVII, thus triggering its activation by proteolytic cleavage. The TF/FVIIa complex cleaves and activates traces of circulating FIX and FX. FXa associates with cofactor FVa to form the *prothrombinase complex* [FXa/FVa/PS/Ca^{2+}] on the surface of TF-expressing cells (**22**). On the other hand, FIXa further activates FX. Propagation of FXa towards more distant cells is avoided by the presence of protease inhibitors such as the Kunitz-type protease inhibitor, tissue factor pathway inhibitor (TFPI) and antithrombin III (AT) (**23,24**). However, FIXa is not targeted by TFPI and can more easily spread towards other cell surfaces. Of note, it has been reported by immunohistochemical evidences that TF exists, below the intact endothelium, in a pre-bound form with FVIIa (FXa is too large to enter the extravascular space), giving rise to the concept of "idling" or ongoing low-level activity, in which the complex is immediately ready to respond when blood vessels are injured. (**25**). Moreover, it seems that FVII preferentially interacts with phosphatidic acid rather than PS on membrane surfaces (**26**).

However, in this step the amount of generated α-thrombin is not sufficient to obtain a proper fibrin clot and could actually be extinguished by TF pathway inhibitor.

Amplification

At this stage, the events switch from fibroblasts to activated platelets that have adhered to the site of injury. The main player is α-thrombin, which activates cofactor FV (common pathway; this leads to amplification of prothrombinase activity), cofactor FVIII (intrinsic pathway; this enhances FXa generation), and FXI (intrinsic pathway). Factors FXI and FVII are crucial in the amplification process, and their absence leads to severe bleeding complications (haemophilia B and A, respectively). This positive feedback loop results in a massive production of α-thrombin which generate an amount of fibrin that overpowers the fibrinolytic system. Furthermore, it has been demonstrated that FXIa can also inactivate TFPI, thereby promoting the FXa generation via the extrinsic pathway (**27**). In conclusion, the sum of these events accelerates production of FXa and α-thrombin.
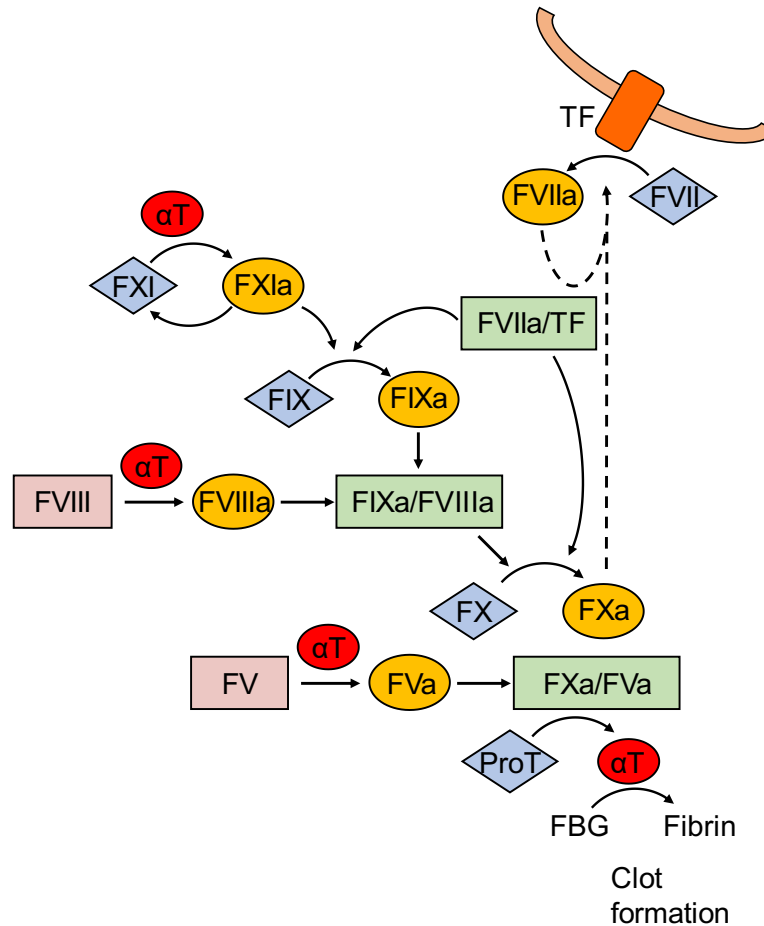
Figure 3. Current concept of coagulation [adapted from Bunn and Aster, 2011]. After a blood vessel injury, tissue factor (TF) is exposed and triggers the initiation of the coagulation cascade. TF binds to FVIIa, which catalyses the activation of FX and the activation of FIX. This dual role of the FVIIa/TF complex contributes to the *in vivo* amplification of blood coagulation. Key: blue diamonds, zymogens; orange circles, cofactors and active enzymes; pink rectangles, pro-cofactors; green rectangles, biomolecular complexes; αT in small red circles, α-thrombin; ProT, prothrombin; FBG, fibrinogen.

Propagation

The propagation phase consists in further production of α-thrombin in regions detached from the TF-expressing surfaces. This ensures the formation of a sufficiently large fibrin clot. The main surface on which this process takes place is, again, represented by platelet membranes. Nevertheless, mounting evidence suggests that other PS-bearing cells (such as leukocytes and endothelial cells) contribute to α-thrombin generation. In fact, while platelets are confined around the injured spot, α-thrombin is also produced in areas where platelets are absent or lower in number (**28**).

On PS-exposing cell membranes, the *tenase complex* [FIXa/FVIIIa/PS/Ca^{2+}] amplifies the activation of FX into FXa, and the subsequent assemblage of additional *prothrombinase complex* [FXa/FVa/PS/Ca^{2+}] (FV is mostly activated by α-thrombin during the amplification step) leads to an explosive burst of α-thrombin production. Of great importance, α-thrombin activates platelets and stimulates the exposure of PS and the release of cofactors (such as polyphosphates and FV), producing a high local concentration of prothrombotic substances right where they are needed.

Fibrin formation and stabilization

The last step in secondary hemostasis is accomplished by α-thrombin conversion of fibrinogen into a fibrin fibers, and proteolytical activation of FXIII, a transglutaminase which crosslinks and consolidates the fibrin clot. The huge amount of α-thrombin produced during the amplification and propagation steps is now sufficient to produce fibrin and to inhibit its dissolution (fibrinolysis). Fibrinogen (Fbg, Factor I) is a large plasma glycoprotein of 340 kDa. It is a dimer of heterotrimers (α$_2$ β$_2$ γ$_2$ chains) linked together by a complex set of disulfide bonds and organized in two lateral α-chain domains, two D domains and a central E domain (**Figure 4**) (**29**). The conversion of Fbg into a proper fibrin clot is a multi-step process. Initially, Fbg is cleaved by α-thrombin at the central E domain to form a soluble fibrin monomer. The cleavage causes the release of two peptides from the N-terminal end of the α and β chains, called fibrinopeptide A and B (FpA and FpB), respectively. They are also used as markers for α-thrombin generation. Hereafter, the fibrin monomer exposes a "knob" (primarily due to the release of FpA) in the E domain that non-covalently interacts with ever-present "holes" positioned in the D domains of neighbouring fibrin molecules. This assemblage generates a double-stranded, half-staggered protofibril that grows in length. Then, the loosely associated protofibrils undergo lateral aggregation and generate a thicker fibrin fiber. Finally, the fibrin clot is consolidated by α-thrombin-activated FXIII, a transglutaminase that forms forms covalent bonds either between γ-chains or between γ- and α-chains (**30**). Together with FXIIIa, α-thrombin also activates TAFI (Thrombin-Activatable Fibrinolytic Inhibitor) and thus, as the clot is developing, its breakdown is prevented by the inhibition of the fibrinolytic system.
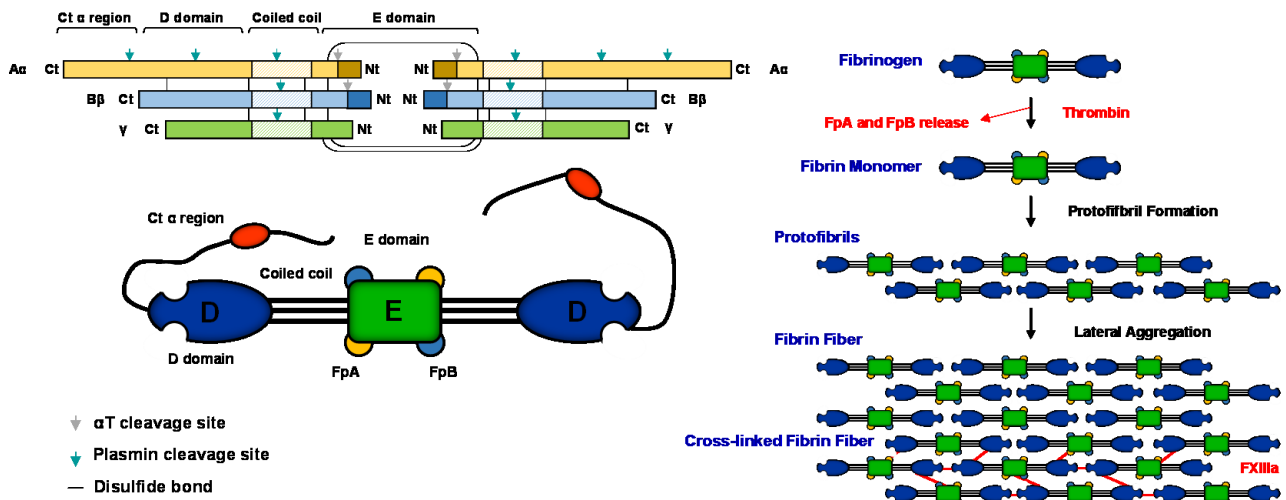
Figure 4. Schematic representations of Fbg structure and fibrin polymerization pathway.

Clot formation, stability and structure are influenced by different factors, including both concentration and "quality" of fibrinogen, as well as the conditions present during fibrin deposition (i.e polyphosphates, FXIIIa activity, extracellular DNA and α-thrombin concentration). Among these, the role of α-thrombin concentration is gaining more and more attention. In fact, a high concentration of α-thrombin results in thinner but, at the same time, denser fibrils, which are more resistant to fibrinolysis. Conversely, low concentrations of α-thrombin generate thicker fibrin fibers, more prone to be degraded (**31**). In addition, polyphosphates are antifibrinolytic substances that help to create a denser clot. Also, extracellular DNA, released form neutrophils, are procoagulant and antifibrinolytic molecules. In fact, thanks to their negative charges, DNA facilitates α-thrombin generation via contact activation and through the intrinsic pathway (**32,33**). In addition, DNA contributes to retain platelets in the injured area (acting like fibrinogen) and was found to inhibit plasmin (antifibrinolytic). Worth noting, in pathological conditions, such as bacterial sepsis or cancer, the release of DNA from neutrophils and other cells may be involved in the pathogenesis of DIC (Disseminated Intravascular Coagulation) (**34**).

Anticoagulant system

The entire coagulation process is controlled by a finely tuned inhibitory system, that prevents the propagation of the thrombus outside the injured spot (**35**). The main physiological anticoagulant mechanisms include:

- Antithrombin III or simply Antithrombin (AT). It is a serine protease that inhibits α-thrombin and other coagulation factors (i.e., IXa, Xa, XIa, XIIa). AT is activated by heparin sulphate that resides on the endothelial surface and inactivates the coagulation factors via complex formation. The 1:1 complex is then removed in a second stage by reticuloendothelial cells.

Other inhibitors of α-thrombin are heparin, α₂-macroglobulin and α₁-antitrypsin (**36**).

- Protein C (PC). PC is a serine protease activated by α-thrombin itself (forming APC) that acts by inhibiting FVa and FVIIIa. It also has potent profibrinolytic and anti-inflammatory activities. Endothelial protein C receptor helps in the activation of PC and Protein S, a vitamin K-dependent glycoprotein and cofactor of APC. Protein S alone can also inhibit the *prothrombinase complex* (**37**).

- Tissue factor plasminogen activator. It is an inhibitor of the extrinsic pathway which acts by inhibiting the TF-FVIIA complex (**38**).

- Protein Z (PZ) dependent protease inhibitor. It is another anticoagulant protein that inhibits FXa after formation of a complex with PZ and Ca^{2+}.

The fibrinolytic system

The fibrinolytic system is the third parallel system that is activated along with the activation of primary and secondary hemostasis (**Figure 5**). It limits the growth of the fibrin clot through an enzymatic dissolution of fibrin by plasmin, a trypsin-like serine protease. This process is necessary to repristinate the vessel patency. In normal conditions, the overall hemostatic balance is shifted towards fibrinolysis only when the clot is formed and the stimulus for clot formation is reduced.

This system could be schematically splitted into three steps: release of plasminogen activators, plasmin production and clot lysis.

Release of plasminogen activators

The first step starts when tPA (tissue Plasminogen Activator), the main plasminogen activator, is released by injured endothelial cells. Along with this mechanism, the release of tPA from endothelial cells is also stimulated by bradykinin, a potent vasoactive peptide, which also triggers the release of platelet inhibitors, such as prostacyclin and nitric oxide. Proteolysis of HMWK forms bradykinin after formation of the auto-activating complex (kallikrein-kinin system) formed by FXIIa (activated by proteins of the subendothelial matrix), prekallikrein and HMWK. Kallikrein (obtained from prekallikrein), FXIIa and uPA (urokinase Plasminogen Activator) are other three plasminogen activators, even though they are weaker than tPA.

Plasmin production

Plasminogen activators cleave plasminogen to form active plasmin. Both plasminogen and plasmin bind to fibrin through lysine residues (kringle regions) (**39**). In this way, fibrin acts both as a cofactor for plasminogen activation and as a final substrate for plasmin (**40**). In fact, the binding

allows a high effective concentration of plasminogen/plasmin, resulting in an amplification of plasmin production and fibrin lysis. Intriguingly, TAFI inhibits the activity of plasminogen/plasmin because it removes their lysine residues, thus lowering the plasminogen/plasmin concentration around the fibrin clot. In addition, since plasmin is a potent enzyme, the binding to fibrin ensures that it remains localized in the clot, preventing it from spreading and lysing other proteins.

Clot lysis

Plasmin-mediated degradation of fibrin is the last step in fibrinolysis. Fibrin proteolysis leads to the release of variably sized fibrin fragments. The smallest fragment is D-dimer, which is formed by two D domains of two adjacent fibrin monomers which had been previously linked together by FXIIIa. Plasmin also cleaves fibrinogen, from which fragments X, Y, E and D (FDPs, Fibrin Degradation Products) are obtained. FDPs and D-dimer are used as biomarkers of ongoing fibrinolysis. The rate at which plasmin cleaves fibrin depends on the structure of fibrin itself and on other environmental factors (i.e., polyphosphates). As mentioned previously, thinner fibrin fibers are more resistant to proteolysis compared to thicker ones (**29**).
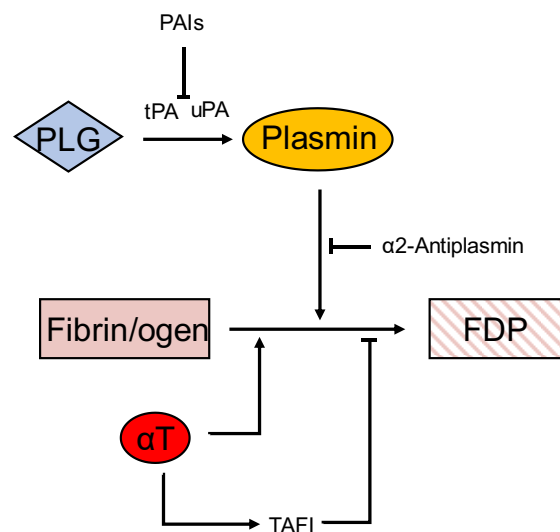
Figure 5. Regulation of the fibrinolytic system. Key: blue diamonds, zymogens; orange circles, active enzymes; pink rectangles, fibrin(ogen) and fibin(ogen) degradation products (FDP); αT in small red circle, α-thrombin; TAFI, Thrombin-Activatable Fibrinolytic Inhibitor; PAIs, plasminogen activators inhibitors.

Fibrinolytic inhibitors

As for blood coagulation, fibrinolysis must be carefully controlled. The main proteins that control this delicate process are:

- Plasmin inhibitors. α2-antiplasmin is a plasma glycoprotein belonging to the serpin family. It is the main plasmin inhibitor and inhibits plasmin activity in one of the fastest protein-protein

interaction known (**36**). After the interaction, the complex is targeted to degradation. α2-macroglobulin is the second plasmin inhibitor. It is a circulating protein synthesized in the liver. It inhibits plasmin, plasminogen activators and also α-thrombin.

- Plasminogen Activators Inhibitors (PAI). PAIs are glycoproteins of the serpin family. There are three PAIs, but the primary physiological inhibitor is PAI type 1 (PAI-1). PAI-1 prevents the initial fibrinolysis phase by blocking both tPA and uPA activity (**41**).

- Thrombin-activatable Fibrinolytic Inhibitor (TAFI). TAFI, also known as carboxypeptidase B, is a plasma proenzyme activated by α-thrombin. When α-thrombin is bound to thrombomodulin (TM) , TAFI activation is enhanced by 1000-fold (**42**). TAFI acts by removing lysine residues from fibrin/fibrinogen C-terminal regions (which are binding sites for both plasminogen and plasmin).

Thrombin Functions

Mature α-thrombin (αT) is the final protease generated by the coagulation cascade, resulting from activation of its precursor prothrombin (FII, ProT) by prothrombinase complex (FXa-FVa-Ca^{2+}-membrane phospholipids). Actually, αT is the key enzyme of the entire hemostatic process and is able to exert both procoagulant and anticoagulant functions. Procoagulant roles entail fibrin generation and platelets aggregation, while the anticoagulant action involves protein C activation (**43,44**) Moreover, αT promotes massive amplification of the coagulation cascade by proteolytically converting FV, FVIII and FXI to their active forms, eventually leading to its own generation, by a positive feedback mechanism (**45**) (**Figure 6**).
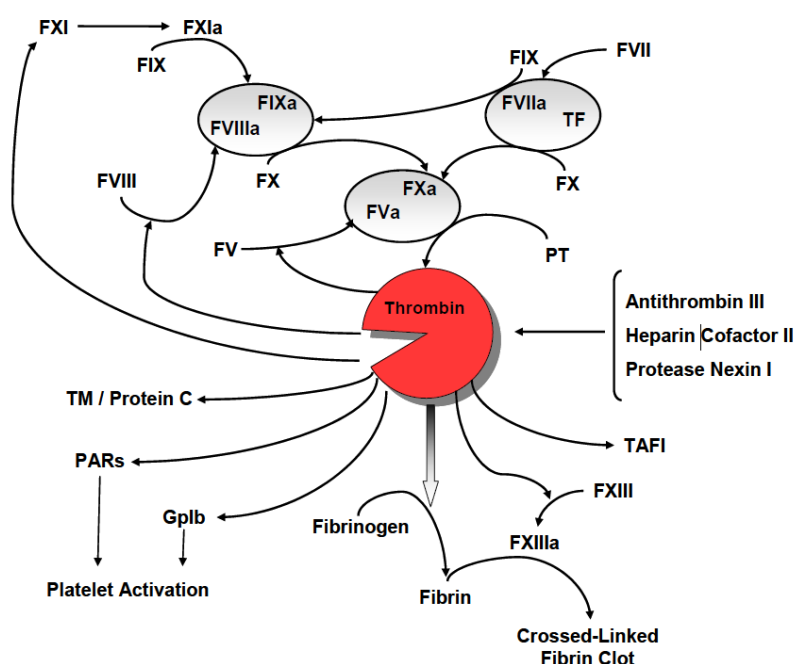
Figure 6. α-thrombin functions in hemostasis. Once released in the bloodstream, αT promotes the generation of a localized clot at the site of injury by platelet activation (through binding to GpIbα and cleavage of PARs) and fibrin generation, further stabilized by FXIIIa. Thrombin amplifies the coagulation cascade through the activation of FV, FVIII and FXI; on the other hand, it promotes its own down-regulation by protein C activation pathway. Antithrombin III, heparin cofactor II and protease nexin I are the main serine proteases inhibitors, acting in different body districts.

The primary procoagulant effect active αT, consists in the conversion of soluble fibrinogen (FI) into a insoluble fibrin network (FIa). Then, the fibrin network is further stabilized by αT-activated FXIIIa which establishes covalent cross-linking connections on adjacent fibrin molecules.

In addition, αT triggers platelets aggregation through the proteolysis of surface protease activated receptors (PARs), which are members of the G-protein-coupled-receptors superfamily (**46**).

PARs are cleaved by the protease within the extracellular N-terminal domain, generating a newly exposed N-terminus, which binds itself on the receptor body promoting signal transduction (**47**) (**Figure 7**). αT binds to platelets through the surface glycoprotein GpIbα, which acts as a cofactor in PAR-1 cleavage, but may also mediate platelet activation in a non-proteolytic manner (**48**).
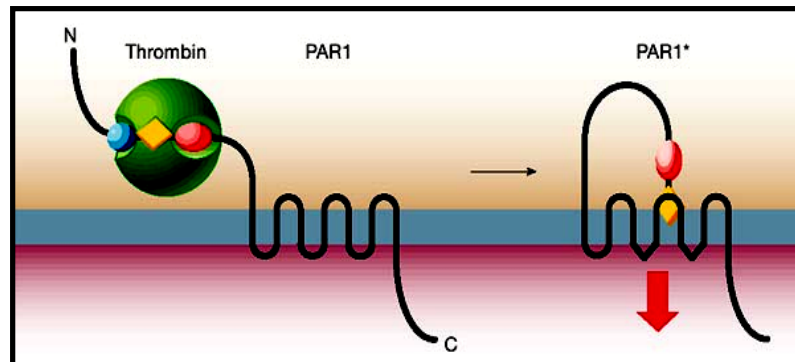

Figure 7. Platelet activation by thrombin-mediated PAR-1 cleavage. αT recognizes and cleaves PAR-1 N-terminal extracellular domain. The newly generated N-terminus acts itself as a ligand, bending on the receptor body.

By contrast, αT promotes its own down-regulation by activating the protein C (PC) pathway. The specificity constant of the enzyme towards the zymogen protein C is enhanced more than thousand-fold upon contact with thrombomodulin (TM), which is an integral membrane protein present on the vascular endothelial cells. A further increase of the reaction rate is provided by the presence of a specific endothelial cell protein C receptor (EPCR) (**49**). Activated protein C (aPC) cleaves and inactivates FVa and FVIIIa, two essential co-factors for the amplification of the coagulation cascade. The activation of PC in the microcirculation, associated with αT and TM interaction, constitutes the natural anticoagulant pathway that prevents the massive intravascular conversion of fibrinogen into an insoluble clot upon αT generation.

Besides coagulation, αT elicits its action on many cells other than platelets, mainly by activating surface PARs. For example, αT stimulates a variety of responses in endothelial cells, including expression of growth factors and secretion of cytokines and adhesion molecules. Human αT also promotes cytokine production by smooth muscle cells and stimulates the proliferation of both smooth muscle cells and fibroblasts.

Since αT is involved in a variety of biochemical pathways, an efficient regulation of its activity is essential to prevent an excessive or improper clot formation. Some members of the serine protease inhibitor (serpin superfamily), such as antithrombin (ATIII), heparin cofactor II (HCII) and protease nexin I (PNI), hinder αT catalytic activity. ATIII circulates in the blood at 2.3 μM. It is the main

inhibitor of intravascular coagulation and acts on several serine procoagulant proteases. In contrast, HCII is highly specific for αT and regulates its activity in extravascular tissues following vascular injury, whereas PNI seems to inhibit αT at or near the surface of a variety of cell types, especially in the brain (**50**). For all serpins, the rate of inhibition is greatly accelerated in the presence of glycosamminoglycans such as heparin, heparan sulphate, and dermatan sulphate (**51**). In addition to these endogenous αT inhibitors, several potent exogenous ones have been isolated from hematophagous organisms, including hirudin and haemadin from the leeches *Hirudo medicinalis*, *Hirudinaria manillensis* and *Haemadipsa sylvestris,* respectively.

αT has an extremely short half-life *in vivo*. However, in *ex vivo* conditions, some of its non-physiologic autolytic degradation products could be isolated. Upon prolonged storage in solution, human αT is first autolytically converted to β-thrombin (βT) by the cleavage at R75-Y76 and R77a-N78 bonds (chymotrypsinogen numbering - see **Appendix B**). An additional cleavage at the K149e-G150 bond in βT generates γ-thrombin (γT). Although the catalytic activities of α-, β-, and γ-thrombin are roughly similar with respect to the hydrolysis of small chromogenic substrates, βT and γT are significantly less active towards physiologic macromolecular substrates such as fibrinogen.

In conclusion, αT plays an absolutely pivotal role in the regulation of hemostasis and also exerts key functions in several other physio-pathological processes. This versatility towards such numerous physiological substrates relies on thrombin's unique structural features.

Thrombin Structure

Human αT is a serine protease belonging to the chymotrypsin family, with which it shares a 49% degree of similarity and a 35% degree of identity. Consequently, its sequence numbering follows the numeration of chymotrypsinogen (see **Appendix B**), (**52**).

Active αT is a globular protein composed by a light A chain (36 aa), covalently linked by a disulphide bridge to a heavy B chain (259 aa). The B chain, with three intra-chain disulfide bonds, carries the functional epitopes of the enzyme and contains the catalytic triad residues H57, D102, S195, which lie at the interface between two similar but asymmetrical six-stranded β-barrels (**Figure 8**).

The catalytic triad polarizes the side chain of the residue S195 for a nucleophilic attack on the carbonyl C atom in the substrate's scissile bond. The formation of a new covalent bond between this C and the side chain O of S195 leads to the formation of a tetrahedral intermediate in which the previous carbonyl oxygen is stabilized as an oxyanion by the enzyme's oxyanion hole, a region in which the oxyanion forms hydrogen bonds with the amide hydrogen atoms of S195 and G193. The protonated H57 reacts with the tetrahedral intermediate and frees the substrate's C-terminal fragment.

The N-terminal fragment is, then, released from S195 after nucleophilic attack by H_2O, thus restoring the enzyme's catalytic activity (**53**).
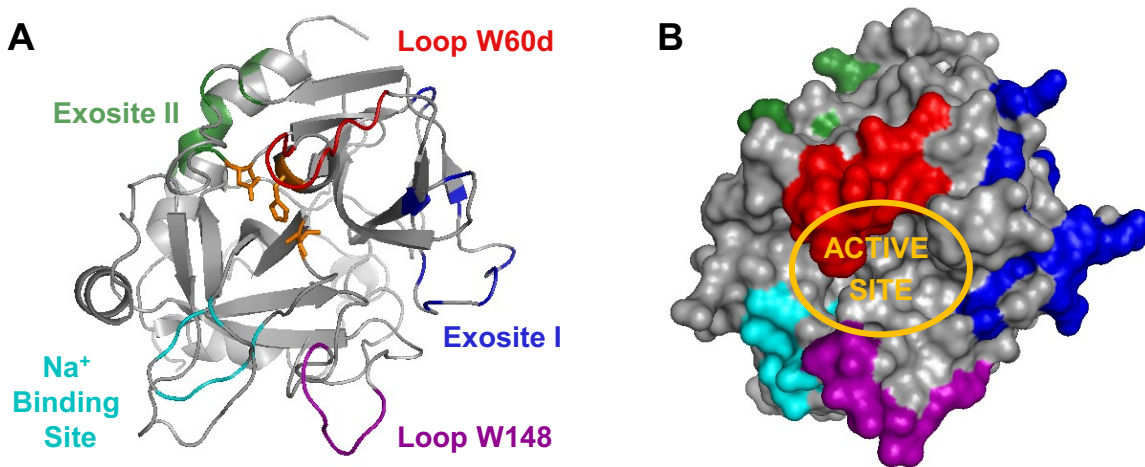

Figure 8. αT three-dimensional structure. αT (pdb: 1ppb-des PPACK) is shown in grey in the classical Bode orientation, either in cartoon (**A**) or surface (**B**) representations. Significant regions are displayed with different colours: W60d loop (Y60a-T60i) in red; W148 loop, or autolysis loop (W148-K149e) in violet; Na$^+$ binding site (D189, E217, D221, R221a, D222, K224, Y225) in cyan; exosite I (F34, K36, R67, K70, R73, R75, Y76, R77a, K81) in blue; exosite II (H91, R93, R101, R126, R165, R233, L234, K235, K236, K240) in green. In **panel A**, side chains of H57, D102 and S195 are highlighted in orange as sticks, while in **panel B** the active site is stressed by an orange circle. Both the exosites and the Na$^+$ binding site are located 15-20Å away from the catalytic cleft.

Active Site Cleft and Direct Substrate/Inhibitor Interactions

Numerous insertions relative to trypsin or chymotrypsin are present in the B chain of αT, shaped as loops connecting the β-strands. Particularly, the loop W60d in the upper side and the loop W148 in the bottom side define and constrain the access to the catalytic site, a narrow cleft with the residues H57, D102 and S195 in the centre. The nine residues of the W60d loop (Y60a-I60i) screens H57 and S195 from the solvent through the steric hindrance of the tryptophan bulky side chain. (**43**). Opposite to the W60d loop, the W148 loop, or autolysis loop, is a highly exposed and flexible region of seven residues (W148-K149e), crucial for fibrinogen recognition. It is still unclear whether the heterogeneous conformations observed for the W148 loop represent real responses to different ligands or if they are an artefact from crystal packing.

Human αT active site architecture is well characterized as well as its cleavage specificity. The trypsin-like specificity for basic residues at P1 (based on the nomenclature of Schetcher and Berger, 1967) (**Figure 9**) is due to the presence of D189, located in the S1 site at the bottom of the catalytic pocket. However, in contrast to trypsin pocket, αT's increased flexibility allows accommodation of more hydrophobic or even uncharged P1 groups, conferring strong preference for Arg over Lys

residues. A unique feature of αT is the presence of the acidic E192 residue, which bears a charged side chain not compensated by hydrogen bonds or ion pair interactions with neighbour residues. This uncompensated negative chain, encountered at the entrance of the catalytic pocket, discriminates against substrates carrying acidic groups near the scissile bond, like PC or PAR-1 (**54**). Based on the W215 indole moiety, a hydrophobic surface groove extends on top of the S1 pocket, which is partially delimited by the W60d loop. The S2 cavity and the aryl binding site/S4 groove form an apolar binding region, obtained by the conjunction of hydrophobic residues together with the pavement of the active site. The S4 groove hosts P4 side chain of all L-amino acid substrates, whereas the P3 side chain extends alongside E192, away from the active site. The S1′ site is particularly suited to accommodate small and polar P1′ residues since it is limited in size by the bulky side chain of K60f. The S2′ site, of medium size and mainly hydrophobic, prefers bulky apolar P2′ residues. Finally, the S3′ site is open and slightly acidic, resulting in a weak preference for basic P3′ side chains (**Table 2**).

On these bases, a P4 to P3′ consensus sequence of an optimal αT polypeptide substrate should contain a P4-Phe/Leu, any P3 residue, a P2-Pro/Val, a P1-Arg, a P1′-Ser/Gly, a P2′-Phe, and a P3′-Arg residue. Although most αT substrates follow the proposed scheme, fibrinogen A chain, FXIII, PC and HCII are important exceptions. Notably, the thrombin active site is assisted by two electropositive allosteric sites called exosites, which provide an additional favourable contact for its ligands. Virtually all the relevant physiological substrates/inhibitors exert their influence on αT by interacting with exosite I and/or exosite II.

Exosite I or ABE I

Exosite I is a prominent loop centred on K70, homologous to the Ca^{2+}-binding loop of the representative proteases trypsin and chymotrypsin (**55**). In these pancreatic proteases, Ca^{2+} stabilizes the structure and increases the resistance to proteolytic digestion. Otherwise, the need for Ca^{2+} is removed in αT by the insertion of K70, whose side chain mimics the bound Ca^{2+} and obliterates the cavity available for binding this cation. In fact, αT does not bind Ca^{2+} up to mM concentrations.

Exosite I (Anion Binding Exosite I, ABE I), located about 10-15Å away from the active site, is placed mainly on the R67 to I82 loop, and bordered by the 37-loop and by the segment K109-K110. In this domain, four charged residues (R67, K70, E77, E80) form a salt bridge cluster, which is buried well below the surface of the exosite, substantially contributing to the rigidity of the loop (**56**). Over this buried charged spot, several non-compensated cationic residues (R73, R75, R77a, K81) provide a strong electropositive field.
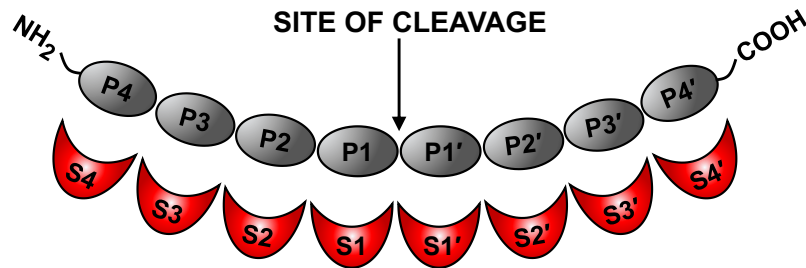
Figure 9. Schetcher-Berger nomenclature. Scheme of the interaction of a polypeptide substrate (in grey) with the active site of an enzyme (in red) before the proteolytic cleavage. Usually at least an eight-residue segment (P4-P4′) substrate interacts with the corresponding subsites (S4-S4′) of the enzyme. Enzyme specificity is mainly defined by the interaction between P1 and S1; generally, proteases cleave at the carboxy-terminal side of the scissile bond.

Table 2. Cleavage sequences of αT substrates around the scissile peptide bond.

	P4	P3	P2	P1	P1′	P2′	P3′	Cofactor and Exosite
Fibrinogen A	Gly	Gly	Val	Arg	Gly	Pro	Arg	1
Fibrinogen B	Phe	Ser	Ala	Arg	Gly	His	Arg	1
FV (709)	Leu	Gly	Ile	Arg	Ser	Phe	Arg	1 and 2
FV (1018)	Leu	Ser	Pro	Arg	Thr	Phe	His	1 and 2
FV (1545)	Trp	Tyr	Leu	Arg	Ser	Asn	Asn	1 and 2
FVIII (372)	Ile	Gln	Ile	Arg	Ser	Val	Ala	1 and 2
FVIII (740)	Ile	Glu	Pro	Arg	Ser	Phe	Ser	1 and 2
FVIII (1618)	Gln	Ser	Pro	Arg	Ser	Phe	Gln	1 and 2
FXIII	Gly	Val	Pro	Arg	Gly	Val	Asn	None
PAR-1	Leu	Asp	Pro	Arg	Ser	Phe	Leu	1
PAR-4	Pro	Ala	Pro	Arg	Gly	Tyr	Pro	None
FXI	Ile	Lys	Pro	Arg	Ile	Val	Gly	1
PC	Val	Asp	Pro	Arg	Ile	Val	Gly	TM (1)
TAFI	Val	Ser	Pro	Arg	Ala	Ser	Ala	TM (1)
ATIII	Ile	Ala	Gly	Arg	Ser	Leu	Asn	Heparin (2)
HCII	Phe	Met	Pro	Leu	Ser	Thr	Gln	1 and Heparin (2)

PAR, protease activated receptor; PC, protein C; TAFI, thrombin-activatable fibrinolysis inhibitor; ATIII, antithrombin; HC, heparin cofactor.

Exosite I is the recognition site for many macromolecular ligands, such as fibrin(ogen), TM, PAR-1, HCII, FV, FVIII, FXIII and the C-terminus of anticoagulant hirudin (**57-61**). Hypothetically, the positive electrostatic forces of exosite I could pre-orient the enzyme for a productive interaction

("electrostatic steering"). In addition, the recognition on this extended region communicates changes to the catalytic moiety of the enzyme, meaning these two sites are allosterically coupled. It has been reported that the binding of peptides derived from HCII (**62**), thrombin receptor I (**63**) or hirudin C-terminal domain (**64**) influences αT catalytic activity.

Exosite II or ABE II

Opposite to exosite I, the Anion Binding Exosite II (ABE II) or exosite II is a prominent C-terminal helix rich in positive charges. At this surface, a small hydrophobic L234-based groove is surrounded (in clockwise order) by the basic residues R93, R101, R165, R233, R126, K236, K235, K240, and H91, with most of their charged side chains not compensated by neighbouring residues. This assignment was confirmed with exosite II mutants by measuring αT inhibition by ATIII in the presence of heparin (**65**), and crystallographically by the complex between αT and an eight-unit heparin fragment, in which each unit is sandwiched between two serine protease molecules.

As a consequence, exosite II can interacts with poly-anionic ligands, such heparin and glycosaminoglycans. Moreover, exosite II is the region of recognition of platelet receptor GpIbα and of fibrinogen elongated γ'-chain (**66,67**).

Since this C-terminal helix packs tightly against the domain supporting D102, it is plausible that binding to exosite II could affect the position of this residue and allosterically influence the enzymatic activity of αT.

Na^+-binding Site and Allosteric Effect

Sodium plays an important role in the allosteric modulation of αT. The binding of this monovalent cation to αT converts the serine protease from a Na^+-free form, referred to as *slow*, to a Na^+-bound conformation, referred to as *fast*. At physiological ionic strength (150mM) the two forms are significantly populated in a 3:2 ratio respectively, since Na^+ affinity for αT (K_d) is 110mM at 37°C. The two forms display different activity toward the physiological substrates (see **Table 3**). In detail, the *fast* form exhibits procoagulant, pro-thrombotic and pro-signalling properties, cleaving PARs and fibrinogen more efficiently. Conversely, the *slow* form preferentially cleaves protein C, performing remarked anticoagulant properties (**68**).

The Na^+-binding site is centred in the 222-loop in a cavity behind the S1 specificity site. It is located at 15-20Å from the catalytic triad and at 5Å from D189. The ion is octahedrally coordinated by the carbonyl oxygens of R221a and K224, and by four buried water molecules. The interactions are further stabilized by ionic salt bridges with D221 and D222. Di Cera and co-workers identified residues D189, E217, D222, and Y225 clustering around the Na^+ site, being energetically linked and

responsible for transducing Na^+ binding into enhanced catalytic activity. In particular, Na^+ binding reorients the R221a carbonyl group to form the R187-D222 salt bridge, favourably reorienting D189, E192, S195 in the catalytic cleft. Moreover, the E146-R221a salt bridge freezes the 148-loop in a more rigid and open conformation (**43**).

Table 3 [from Di Cera et al., 2007]. Effect of Na^+ on the catalytic activity of αT towards some relevant physiological substrates.

	k_{cat}/K_m ($\mu M^{-1} \cdot s^{-1}$)		r
	Fast	**Slow**	
(D)FPR-pNA	88.9 ± 4	3.5 ± 0.5	26
Fibrinopeptide A release	35 ± 4	1.5 ± 0.1	23
Fibrinopeptide B release	17 ± 1	0.73 ± 0.03	23
PAR-1	54 ± 2	1.4 ± 0.1	39
Protein C	0.21 ± 0.001	0.32 ± 0.01	0.7

All measures were performed in buffer that stabilized either the fast (0.2M NaCl) or the slow (0.2M ChCl) form.

Larger structural changes observed in human S195A or E217K mutants seemed to be typical for the slow form of αT, and these crystal structures suggested an allosteric switch mechanism due to Na^+ interaction. In detail, Na^+ removal induces flipping of the C168-C182 disulphide bridge, and of F227, W215 and W60d aromatic side chains. These small but significant atomic movements result in the constriction of the active site cleft, limiting the access to the substrates.

Currently available data suggest that Na^+-bound αT form is more stable and characterized by a more accessible and rigid active site cleft, whereas the Na^+-free form displays a more closed, flexible substrate-binding region. Thus, the *fast* form of αT would be a better template for productive binding of the inherently-flexible cleavage segments of fibrinogen and PAR-1, such that the scissile peptide bonds are optimally presented to the S195 Oγ and to the oxyanion hole. Importantly, thrombin-substrate complexes go through short-lived transition states, both in the presence or absence of Na^+, making the structural characterization of these states extremely difficult. Finally, several naturally occurring mutations of the ProT gene, like ProT Frankfurt, Salakta, Greenville, Scranton, Copenhagen and Saint Denis, affect residues linked to Na^+ binding and are often associated with bleeding (**69**).

REFERENCES

1.   Thornton, P., and Douglas, J. (2010) Coagulation in pregnancy. *Best Pract Res Clin Obstet Gynaecol* **24**, 339-352

2.   Hoffman, M., and Monroe, D. M., 3rd. (2001) The action of high-dose factor VIIa (FVIIa) in a cell-based model of hemostasis. *Semin Hematol* **38**, 6-9

3.   Carestia, A., Kaufman, T., and Schattner, M. (2016) Platelets: New Bricks in the Building of Neutrophil Extracellular Traps. *Front Immunol* **7**, 271

4.   Liaw, P. C., Ito, T., Iba, T., Thachil, J., and Zeerleder, S. (2016) DAMP and DIC: The role of extracellular DNA and DNA-binding proteins in the pathogenesis of DIC. *Blood Rev* **30**, 257-261

5.   Furlan, M. (1996) Von Willebrand factor: molecular size and functional activity. *Ann Hematol* **72**, 341-348

6.   Springer, T. A. (2014) von Willebrand factor, Jedi knight of the bloodstream. *Blood* **124**, 1412-1425

7.   Xu, A. J., and Springer, T. A. (2013) Mechanisms by which von Willebrand disease mutations destabilize the A2 domain. *J Biol Chem* **288**, 6317-6324

8.   McEwan, P. A., Yang, W., Carr, K. H., Mo, X., Zheng, X., Li, R., and Emsley, J. (2011) Quaternary organization of GPIb-IX complex and insights into Bernard-Soulier syndrome revealed by the structures of GPIbbeta and a GPIbbeta/GPIX chimera. *Blood* **118**, 5292-5301

9.   Hemker, H. C., van Rijn, J. L., Rosing, J., van Dieijen, G., Bevers, E. M., and Zwaal, R. F. (1983) Platelet membrane involvement in blood coagulation. *Blood Cells* **9**, 303-317

10.   Brooks, M. B., Catalfamo, J. L., Brown, H. A., Ivanova, P., and Lovaglio, J. (2002) A hereditary bleeding disorder of dogs caused by a lack of platelet procoagulant activity. *Blood* **99**, 2434-2441

11.   Jin, J., Quinton, T. M., Zhang, J., Rittenhouse, S. E., and Kunapuli, S. P. (2002) Adenosine diphosphate (ADP)-induced thromboxane A(2) generation in human platelets requires coordinated signaling through integrin alpha(IIb)beta(3) and ADP receptors. *Blood* **99**, 193-198

12.   Ossovskaya, V. S., and Bunnett, N. W. (2004) Protease-activated receptors: contribution to physiology and disease. *Physiol Rev* **84**, 579-621

13.   Solh, T., Botsford, A., and Solh, M. (2015) Glanzmann's thrombasthenia: pathogenesis, diagnosis, and current and emerging treatment options. *J Blood Med* **6**, 219-227

14.   Palta, S., Saroa, R., and Palta, A. (2014) Overview of the coagulation system. *Indian J Anaesth* **58**, 515-523

15.   Macfarlane, R. G. (1965) A clotting scheme for 1964. *Thromb Diath Haemorrh Suppl* **17**, 45-52

16.   Davie, E. W., and Ratnoff, O. D. (1964) WATERFALL SEQUENCE FOR INTRINSIC BLOOD CLOTTING. *Science* **145**, 1310-1312

17. Lasne, D., Jude, B., and Susen, S. (2006) From normal to pathological hemostasis. *Can J Anaesth* **53**, S2-11

18. Owens, A. P., 3rd, and Mackman, N. (2010) Tissue factor and thrombosis: The clot starts here. *Thromb Haemost* **104**, 432-439

19. Bombeli, T., and Spahn, D. R. (2004) Updates in perioperative coagulation: physiology and management of thromboembolism and haemorrhage. *Br J Anaesth* **93**, 275-287

20. Schmaier, A. H. (2008) The elusive physiologic role of Factor XII. *J Clin Invest* **118**, 3006-3009

21. Woodruff, R. S., Sullenger, B., and Becker, R. C. (2011) The many faces of the contact pathway and their role in thrombosis. *J Thromb Thrombolysis* **32**, 9-20

22. Monroe, D. M., and Hoffman, M. (2006) What does it take to make the perfect clot? *Arterioscler Thromb Vasc Biol* **26**, 41-48

23. Broze, G. J., Jr., Warren, L. A., Novotny, W. F., Higuchi, D. A., Girard, J. J., and Miletich, J. P. (1988) The lipoprotein-associated coagulation inhibitor that inhibits the factor VII-tissue factor complex also inhibits factor Xa: insight into its possible mechanism of action. *Blood* **71**, 335-343

24. Jesty, J. (1978) The inhibition of activated bovine coagulation factors X and VII by antithrombin III. *Arch Biochem Biophys* **185**, 165-173

25. Hoffman, M., Colina, C. M., McDonald, A. G., Arepally, G. M., Pedersen, L., and Monroe, D. M. (2007) Tissue factor around dermal vessels has bound factor VII in the absence of injury. *J Thromb Haemost* **5**, 1403-1408

26. Tavoosi, N., Smith, S. A., Davis-Harrison, R. L., and Morrissey, J. H. (2013) Factor VII and protein C are phosphatidic acid-binding proteins. *Biochemistry* **52**, 5545-5552

27. Puy, C., Tucker, E. I., Matafonov, A., Cheng, Q., Zientek, K. D., Gailani, D., Gruber, A., and McCarty, O. J. (2015) Activated factor XI increases the procoagulant activity of the extrinsic pathway by inactivating tissue factor pathway inhibitor. *Blood* **125**, 1488-1496

28. Ivanciu, L., and Stalker, T. J. (2015) Spatiotemporal regulation of coagulation and platelet activation during the hemostatic response in vivo. *J Thromb Haemost* **13**, 1949-1959

29. Wolberg, A. S. (2007) Thrombin generation and fibrin clot structure. *Blood Rev* **21**, 131-142

30. Kollman, J. M., Pandi, L., Sawaya, M. R., Riley, M., and Doolittle, R. F. (2009) Crystal structure of human fibrinogen. *Biochemistry* **48**, 3877-3886

31. Wolberg, A. S. (2008) Polyphosphate: physiologic? Pathologic? Pharmacologic? *Blood* **112**, 2598-2599

32. Gould, T. J., Vu, T. T., Swystun, L. L., Dwivedi, D. J., Mai, S. H., Weitz, J. I., and Liaw, P. C. (2014) Neutrophil extracellular traps promote thrombin generation through platelet-dependent and platelet-independent mechanisms. *Arterioscler Thromb Vasc Biol* **34**, 1977-1984

33. Massberg, S., Grahl, L., von Bruehl, M. L., Manukyan, D., Pfeiler, S., Goosmann, C., Brinkmann, V., Lorenz, M., Bidzhekov, K., Khandagale, A. B., Konrad, I., Kennerknecht, E.,

Reges, K., Holdenrieder, S., Braun, S., Reinhardt, C., Spannagl, M., Preissner, K. T., and Engelmann, B. (2010) Reciprocal coupling of coagulation and innate immunity via neutrophil serine proteases. *Nat Med* **16**, 887-896

34. Demers, M., Krause, D. S., Schatzberg, D., Martinod, K., Voorhees, J. R., Fuchs, T. A., Scadden, D. T., and Wagner, D. D. (2012) Cancers predispose neutrophils to release extracellular DNA traps that contribute to cancer-associated thrombosis. *Proc Natl Acad Sci U S A* **109**, 13076-13081

35. Colvin, B. T. (2004) Physiology of haemostasis. *Vox Sang* **87 Suppl1**, 43-46

36. Ezihe-Ejiofor, J. A., and Hutchinson, N. (2013) Anticlotting mechanisms 1: physiology and pathology. *Continuing Education in Anaesthesia Critical Care & Pain* **13**, 87-92

37. Rigby, A. C., and Grant, M. A. (2004) Protein S: a conduit between anticoagulation and inflammation. *Crit Care Med* **32**, S336-341

38. Price, G. C., Thompson, S. A., and Kam, P. C. (2004) Tissue factor and tissue factor pathway inhibitor. *Anaesthesia* **59**, 483-492

39. Brzoska, T., Tanaka-Murakami, A., Suzuki, Y., Sano, H., Kanayama, N., and Urano, T. (2015) Endogenously generated plasmin at the vascular wall injury site amplifies lysine binding site-dependent plasminogen accumulation in microthrombi. *PLoS One* **10**, e0122196

40. Tollefsen, D. M. (2002) Heparin cofactor II deficiency. *Arch Pathol Lab Med* **126**, 1394-1400

41. Dellas, C., and Loskutoff, D. J. (2005) Historical analysis of PAI-1 from its discovery to its potential role in cell motility and disease. *Thromb Haemost* **93**, 631-640

42. Bajzar, L., Nesheim, M. E., and Tracy, P. B. (1996) The profibrinolytic effect of activated protein C in clots formed from plasma is TAFI-dependent. *Blood* **88**, 2093-2100

43. Di Cera, E., Dang, Q. D., and Ayala, Y. M. (1997) Molecular mechanisms of thrombin function. *Cell Mol Life Sci* **53**, 701-730

44. Coughlin, S. R. (2005) Protease-activated receptors in hemostasis, thrombosis and vascular biology. *J Thromb Haemost* **3**, 1800-1814

45. Davie, E. W., and Kulman, J. D. (2006) An overview of the structure and function of thrombin. *Semin Thromb Hemost* **32 Suppl 1**, 3-15

46. Vu, T. K., Hung, D. T., Wheaton, V. I., and Coughlin, S. R. (1991) Molecular cloning of a functional thrombin receptor reveals a novel proteolytic mechanism of receptor activation. *Cell* **64**, 1057-1068

47. De Cristofaro, R., and De Filippis, V. (2003) Interaction of the 268-282 region of glycoprotein Ibalpha with the heparin-binding site of thrombin inhibits the enzyme activation of factor VIII. *Biochem J* **373**, 593-601

48. De Candia, E., Hall, S. W., Rutella, S., Landolfi, R., Andrews, R. K., and De Cristofaro, R. (2001) Binding of thrombin to glycoprotein Ib accelerates the hydrolysis of Par-1 on intact platelets. *J Biol Chem* **276**, 4692-4698

49. Esmon, C. T. (1989) The roles of protein C and thrombomodulin in the regulation of blood coagulation. *J Biol Chem* **264**, 4743-4746

50.   Arcone, R., Chinali, A., Pozzi, N., Parafati, M., Maset, F., Pietropaolo, C., and De Filippis, V. (2009) Conformational and biochemical characterization of a biologically active rat recombinant Protease Nexin-1 expressed in E. coli. *Biochim Biophys Acta* **1794**, 602-614

51.   Johnson, D. J., Adams, T. E., Li, W., and Huntington, J. A. (2005) Crystal structure of wild-type human thrombin in the Na+-free state. *Biochem J* **392**, 21-28

52.   Bode, W., Mayr, I., Baumann, U., Huber, R., Stone, S. R., and Hofsteenge, J. (1989) The refined 1.9 A crystal structure of human alpha-thrombin: interaction with D-Phe-Pro-Arg chloromethylketone and significance of the Tyr-Pro-Pro-Trp insertion segment. *Embo j* **8**, 3467-3475

53.   Warshel, A., Naray-Szabo, G., Sussman, F., and Hwang, J. K. (1989) How do serine proteases really work? *Biochemistry* **28**, 3629-3637

54.   Guinto, E. R., Vindigni, A., Ayala, Y. M., Dang, Q. D., and Di Cera, E. (1995) Identification of residues linked to the slow-->fast transition of thrombin. *Proc Natl Acad Sci U S A* **92**, 11185-11189

55.   Bartunik, H. D., Summers, L. J., and Bartsch, H. H. (1989) Crystal structure of bovine beta-trypsin at 1.5 A resolution in a crystal form with low molecular packing density. Active site geometry, ion pairs and solvent structure. *J Mol Biol* **210**, 813-828

56.   Stubbs, M. T., Oschkinat, H., Mayr, I., Huber, R., Angliker, H., Stone, S. R., and Bode, W. (1992) The interaction of thrombin with fibrinogen. A structural basis for its specificity. *Eur J Biochem* **206**, 187-195

57.   Steen, M., and Dahlback, B. (2002) Thrombin-mediated proteolysis of factor V resulting in gradual B-domain release and exposure of the factor Xa-binding site. *J Biol Chem* **277**, 38424-38430

58.   Esmon, C. T., and Lollar, P. (1996) Involvement of thrombin anion-binding exosites 1 and 2 in the activation of factor V and factor VIII. *J Biol Chem* **271**, 13882-13887

59.   Sadasivan, C., and Yee, V. C. (2000) Interaction of the factor XIII activation peptide with alpha -thrombin. Crystal structure of its enzyme-substrate analog complex. *J Biol Chem* **275**, 36942-36948

60.   Hall, S. W., Nagashima, M., Zhao, L., Morser, J., and Leung, L. L. (1999) Thrombin interacts with thrombomodulin, protein C, and thrombin-activatable fibrinolysis inhibitor via specific and distinct domains. *J Biol Chem* **274**, 25510-25516

61.   Myles, T., Le Bonniec, B. F., Betz, A., and Stone, S. R. (2001) Electrostatic steering and ionic tethering in the formation of thrombin-hirudin complexes: the role of the thrombin anion-binding exosite-I. *Biochemistry* **40**, 4972-4979

62.   Hortin, G. L., and Trimpe, B. L. (1991) Allosteric changes in thrombin's activity produced by peptides corresponding to segments of natural inhibitors and substrates. *J Biol Chem* **266**, 6866-6871

63.   Liu, L. W., Rezaie, A. R., Carson, C. W., Esmon, N. L., and Esmon, C. T. (1994) Occupancy of anion binding exosite 2 on thrombin determines Ca2+ dependence of protein C activation. *J Biol Chem* **269**, 11807-11812

64.   Jackman, M. P., Parry, M. A., Hofsteenge, J., and Stone, S. R. (1992) Intrinsic fluorescence changes and rapid kinetics of the reaction of thrombin with hirudin. *J Biol Chem* **267**, 15375-15383

65.   Gan, Z. R., Li, Y., Chen, Z., Lewis, S. D., and Shafer, J. A. (1994) Identification of basic amino acid residues in thrombin essential for heparin-catalyzed inactivation by antithrombin III. *J Biol Chem* **269**, 1301-1305

66.   De Cristofaro, R., De Candia, E., Landolfi, R., Rutella, S., and Hall, S. W. (2001) Structural and functional mapping of the thrombin domain involved in the binding to the platelet glycoprotein Ib. *Biochemistry* **40**, 13268-13273

67.   Lancellotti, S., Rutella, S., De Filippis, V., Pozzi, N., Rocca, B., and De Cristofaro, R. (2008) Fibrinogen-elongated gamma chain inhibits thrombin-induced platelet response, hindering the interaction with different receptors. *J Biol Chem* **283**, 30193-30204

68.   De Filippis, V., De Dea, E., Lucatello, F., and Frasson, R. (2005) Effect of Na+ binding on the conformation, stability and molecular recognition properties of thrombin. *Biochem J* **390**, 485-492

69.   Di Cera, E. (2004) Thrombin: a paradigm for enzymes allosterically activated by monovalent cations. *C R Biol* **327**, 1065-1076

CHAPTER 1.2

Alterations of hemostasis

Hemostasis is an extremely complex and finely regulated biological process, whose final goal is limiting the bleeding after a vascular injury. Alterations affecting this delicate process lead to many different pathological manifestations, commonly referred to as cardiovascular diseases (CVD). In this Ph.D. project we explored some of the molecular mechanisms underlying these hemostatic disorders, starting from unrelated pathologies at the interface between thrombosis and amyloidosis, namely antiphospholipid syndrome (APS), Parkinson's disease (PD), and transthyretin systemic amyloidosis (ATTR). In all these cases, we focused our attention on the proteins involved in the onset and progression of the diseases, i.e. β2-glycoprotein-I, α-synuclein and transthyretin, respectively.

In detail, we explored the interaction between αT, the key enzyme of the coagulation cascade, and β2-glycoprotein-I, a plasma protein identified as the major autoantigen in the antiphospholipid syndrome, an autoimmune disease characterized by thrombotic manifestations. In analogy, we mapped out the novel interaction between αT and α-synuclein, a presynaptic protein implicated in Parkinson's disease. Intriguingly, α-synuclein, beyond being localized at the presynaptic terminals of the central nervous system, is also expressed on platelets, the major cellular target of αT. In a late stage, we focused our attention on the effect of bacterial proteases on blood coagulation. In particular, we dissected an alternative mechanism of activation of prothrombin, the precursor of αT, by the bacterial protease subtilisin, secreted from the gut commensal *B. Subtilis*. Finally, we tested a set of proteases of different origin (coagulative, fibrinolytic, bacterial, digestive) against human transthyretin, since it is known that the C-terminally truncated forms of transthyretin are crucial in the onset and progression of systemic amyloidosis.

This chapter will introduce the case studies extended in the results chapters, with a brief description of the pathological context and the main proteins involved in it.

The Antiphospholipid Syndrome

The antiphospholipid syndrome (APS) is a severe autoimmune disease characterized by arterial and venous thrombotic events, thrombocytopenia and pregnancy morbidity, originally associated with the presence of antiphospholipid antibodies (aPLAb) (**1**). Over the years, it has been assessed that the so-called "aPLAb" are actually a heterogeneous group of autoantibodies that recognize a number of phospholipid-binding proteins, phospholipid molecules, and phospholipid-protein complexes including β2GpI, prothrombin, protein C, protein S, kininogens, thrombomodulin, or annexin V (**2**). Since the 90s, β2-glycoprotein I (β2GpI) was recognised as the major auto-antigen target for the "aPLAb" group. In addition, it was observed that the affinity of aPLAb for β2GpI was significant only when β2GpI was pre-bound on anionic phospholipid membranes. To complicate the picture, several different subpopulations of antibodies targeting β2GpI have been identified (**3**). Despite this evidence, the exact mechanism of thrombus formation induced by these antibodies is still unknown. It is believed that aPLAb in patients with APS activate different cell types involved in the regulation of hemostatic balance (**4**). According to this theory, circulating β2GpI recognises anionic cellular surfaces and changes its conformational state from circular-closed to elongated-open (J-shape). The latter, provokes the exposure of the cryptic epitopes placed in Domain I of β2GpI that are thus recognized by the antibodies (**5**).

Unlike the free protein, the [β2GpI/antibody] complex binds membrane phospholipids more strongly and it also displays affinity for various protein receptors, such as Toll-like receptor (TLR) 2, TLR4, TLR8, annexin A2, GpIbα and, finally, for LRP8, a member of the LDL-receptor family (**6**). All these receptors are exposed on the surface of platelets, monocytes and endothelial cells, and play pleiotropic roles in the cell activation processes promoting pro-inflammatory and prothrombotic signalling. (**Figure 1**). As a confirmation of their crucial role, it has been observed that the absence, either functional or absolute, of these receptors leads to a decrease of thrombi formation in APS affected mice (**3**).

The APS diagnosis relies on both clinical and laboratory diagnostic criteria that have been officially established in 2004 during a meeting in Sydney (they are also called Sapporo or Sydney criteria) (**7**). The clinical criteria are based on the occurrence of arterial, venous or small vessels thrombosis, or on complications attributable to placental insufficiency, such as loss of the fetus or premature birth. On the other hand, according to the laboratory criteria, APS diagnosis can only be confirmed if aPLAb are detected by least two tests performed more than 12 weeks apart (**1**). The aPLAb may be detected both through *in vitro* Lupus Anticoagulant test (LA), cardiolipin assay (aCL) or β2GpI ELISA assay. (**2**). It is important to underline that, although these three tests are the most

accredited for APS recognition, the diagnostic criteria are constantly evolving as new aPLAbs directed against other physiological targets are being discovered (**7**).
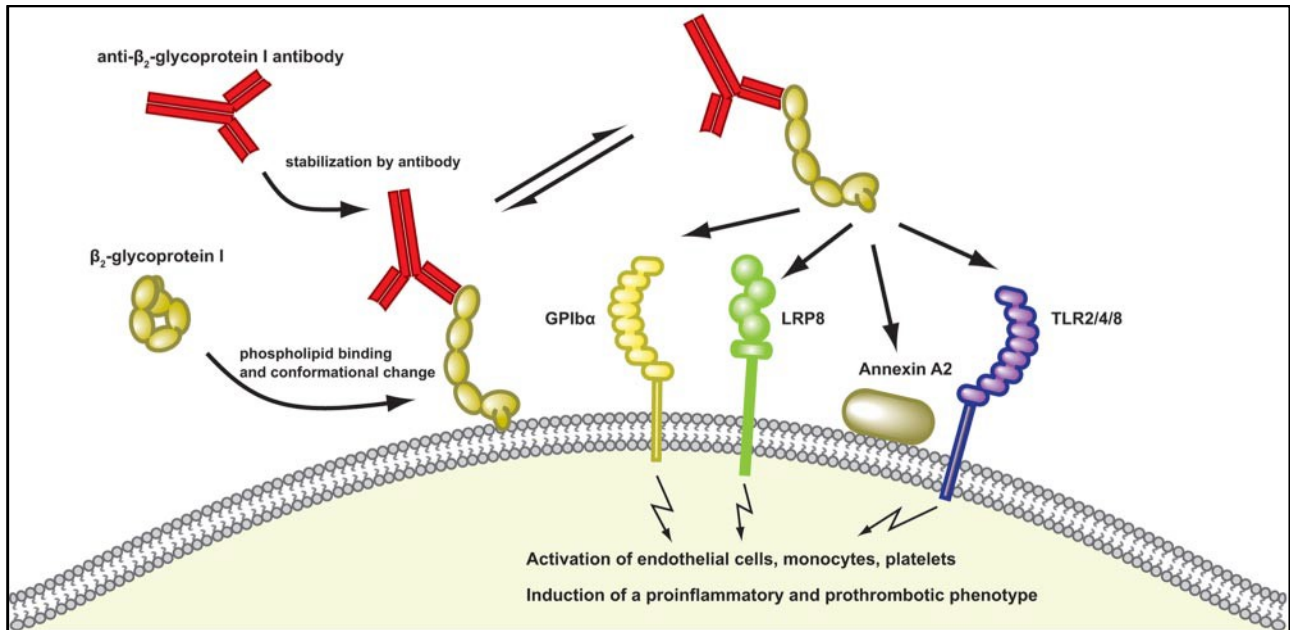

Figure 1. [from de Groot and Urbanus, 2012] Sequence of events that lead to cellular activation by [β2GpI/antibody] complex. In normal conditions, β2GpI circulates in the bloodstream and is not recognized by pathologic anti-β2GpI antibodies. When negatively charged phospholipids become exposed on cell membranes, β2GpI binds to them and undergoes a conformational change. This change causes exposure of the cryptic epitopes of domain I, which become available for recognition by the pathologic antibodies. Anti-β2GpI antibody binds to β2GpI and locks it in the open conformation, which is able to interact with several surface receptors, such as GpIbα, LRP8, annexin A2, and several members of the TLR family (TLR2, -4, and -8).

The risk of thrombotic manifestations is directly proportional to the number of positivity tests for the aPLAb. Thus, positivity for a single aPLAb entails a lower risk compared to a double or triple positivity (**8**). In addition, the risk is also related to the type of positivity: there are no documented cases of arterial or venous thrombosis in patients displaying only aCL positivity whereas patients with LA are very exposed to thrombotic complications (**9**).

There are still several controversies regarding the treatment of APS, especially in non-venous thrombotic manifestations (**7**) and different therapeutic approaches with both anticoagulant and non-anticoagulant drugs have been defined according to the patient's type of positivity.

β2-Glycoprotein I

β2-Glycoprotein I (β2GpI) is a heavily glycosylated 45 kDa protein that circulates in the bloodstream at high concentration (0.2 mg/ml, 4 μM). It is mainly synthesized in the liver and was described for the first time in 1961 (**10**). Initially, β2GpI did not receive much attention since it could

boast of not known biological or pathological function but, since the 1990s, when β2GpI was identified as the most important antigen in APS, the interest in this protein increased significantly.

From a structural standpoint, β2GpI consists of 326 amino acids organized in five contiguous domains (Domain I-V) arranged like "beads on a string" with a high content of β-sandwich secondary structure (**11**). Due to the sequence homology, β2GpI belongs to the Complement Control Protein (CCP) superfamily. The first four domains, also called "Sushi Domains", consist of about 60 amino acids with two disulphide bridges each (**12**). The fifth domain, unlike the other ones, has an extra disulfide bridge and an extension of 19 amino acids in its C-terminal portion, for a total of 82 amino acids in length. Another distinguishing characteristic of this domain is the presence of a lysine-rich sequence (^{282}KNKEKK^{287}) and a hydrophobic loop (^{314}AFWKTDA^{320}), thanks to which β2GpI can bind to membrane phospholipids (**13**) (**Figure 2**). Both hydrophobic and electrostatic interactions are necessary for effective binding to membrane phospholipids. Besides, the electrostatic contribution was found to be more critical, and the only interaction involved in the binding to other molecular species (such as heparin) (**14**).

The oligosaccharides linked to β2GpI are highly heterogeneous in structure and make up about 20% of the total protein mass. The glycan chains are linked to the asparagine residues (Asn143, Asn164, Asn174, and Asn234) located in the third and fourth domain.
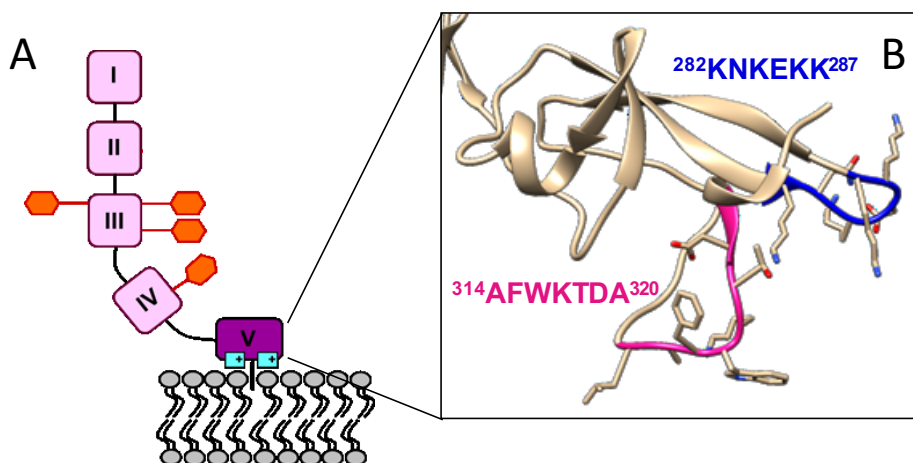

Figure 2. Schematic representation of β2GpI structure and its interaction with phospholipid membranes. (**A**) The five domains are indicated using Roman numerals and the four glycosylation sites in domain III and IV (i.e. Asn143, Asn164, Asn174, Asn243) by orange hexagons. (**B**) Zoom on the fifth domain (1C1Z.pdb). The lysine rich sequence is highlighted in blue (^{282}KNKEKK^{287}), whereas the hydrophobic loop is displayed in pink (^{314}AFWKTDA^{320}).

The investigation of the antigenic determinants confirms that, as mentioned before, antibodies bind to β2GpI only when this protein is bound to phospholipids and not when it is free in solution (**15**). This phenomenon has been attributed to the enormous conformational variability of β2GpI. In any case, the antigenic determinants are located in Domain I and can only be recognized after the

protein assumes an elongated shape. It is, in fact, believed that β2GpI exists in two conformations, a close, or circular one, and an open, or elongated (J-shape) conformation and that circulating β2GpI normally assumes a closed conformation in which Domain I interacts with Domain V and is, thus, hidden. The mechanism leading to Domain I exposure is still unknown but there are many proposed theories.

One of these theories alleges that, in a pathological state, Domain V, recognises the negatively-charged phospholipids thanks to its hydrophobic loop and positively-charged region, thus triggering a conformational change that exposes Domain I to the surrounding environment and renders its epitopes susceptible to antibody recognition (**16**). The best-known epitope spans the sequence between Arg39 and Arg43, but a second one has also been identified in the region near the Lys19 (**17,18**). As a confirmation, recent studies have demonstrated that mice injected with Domain I alone develop an autoimmune response and simultaneous lupus anticoagulant activity. Conversely, mice injected with a β2GpI mutant lacking Domain I did not produce antibodies (**3**).

With regards to β2GpI conformation, many questions remain open, as different techniques have led to the identification of different structures. In fact, crystallographic structures (such as 1C1Z.pdb) show β2GpI not in a circular form but in a J-shape in which Domain V is at right angles to the other domains (**11**) (**Figure 3A**). On the other hand, the Small Angle X-ray Scattering (SAXS) technique has suggested that in solution β2GpI may instead assume an S (shape) conformation, with an inflection point between Domains II and III (**19**). In this case, the epitopes are thought to be masked by the polysaccharide chains. (**Figure 3B**). Finally, electron microscopy (EM) studies have shown the previously described circular conformation (**5**) in which the epitopes are hidden by the interaction between Domain I and Domain V (**Figure 3C**). Of note, the exposure of the cryptic epitopes is sufficient for the development of antibodies and any factor that can trigger the shift from the open to the closed conformation is sufficient to induce antibody formation. The interaction of β2GpI with exogenous anionic surfaces, such as lipopolysaccharides (LPS), causes a conformational change of the protein from closed to open form which leads to an autoimmune response (**20**). Furthermore, denaturation and aggregation of β2GpI due to oxidative stress cause T cell proliferation and dendritic cell maturation (**21,22**). Finally, the Val247Leu polymorphism could cause an instability of the circular conformation, since it is associated with the presence of antibodies (**23,24**).
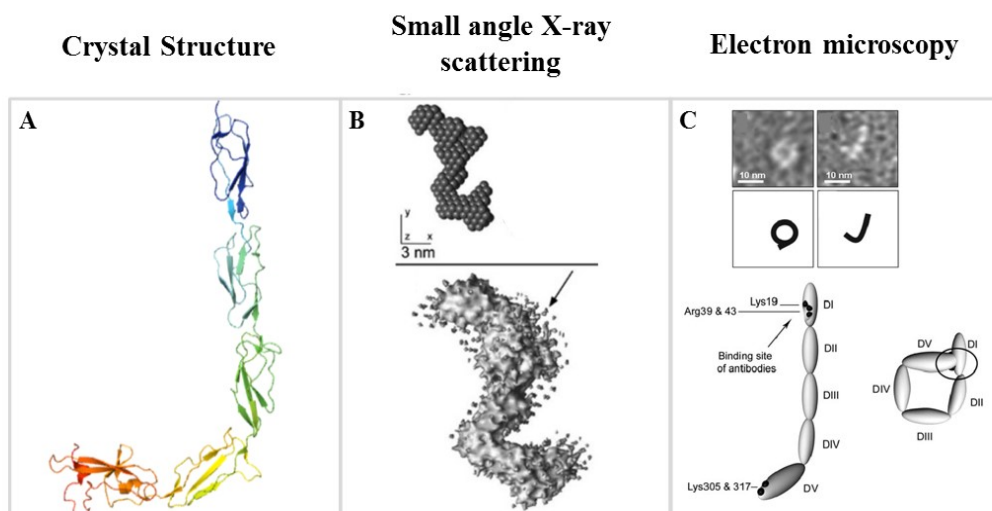
Figure 3. Different conformations of β2GpI. Panel **A** shows the crystallographic J-shape structure (1C1Z.pdb), panel **B** shows the S-shaped structure detected by SAXS technique, in **C** the closed-circular structure observable by electron microscopy. Noteworthy, only in the J-shape form the epitopes are exposed and available for autoantibody recognition.

β2-Glycoprotein I in the coagulation cascade

β2GpI is an abundant plasma protein (0.2 mg/ml) highly conserved in mammals (**25**). Among the plasma proteins involved in coagulation, this concentration is second only to fibrinogen (**26**). Due to its abundance, as well as its high degree of conservation among many species, it is easy to deduce that this protein has specific functions although, to date, these remain elusive. Nevertheless, numerous evidence suggests that β2GpI is implicated in several steps of the coagulation cascade and has both anticoagulant and procoagulant functions. Hereafter, a brief collection of the most important known correlations and interactions is reported.

β2GpI can be proteolyzed by plasmin at the peptide bond Lys317-Thr318 in Domain V. This proteolytic cleavage was found to activate a negative feedback mechanism that results in the inhibition of plasmin generation by tissue plasminogen activator (tPA) (**27**). This mechanism has been shown to be of physiological relevance, as plasmin-cleaved β2GpI has been detected in subjects who have had episodes of ischemic strokes or lacunar infarct. Intriguingly, patients who have experienced stroke or thrombotic disorders have relatively low levels of intact β2GpI whereas higher β2GpI blood concentrations seem to be related to a reduced risk of thrombotic manifestations (**26**). In addition, after cleavage by plasmin, β2GpI seems to change its physio-pathological functions, also gaining an antimicrobial activity. In particular, the C-terminal positive region binds to negatively-charged bacterial molecules (such as LPS, H protein, M1 protein).

It has been reported that β2GpI is able to prevent the inactivation of FVa by activated protein C (anticoagulant function) (**28**), but also to inhibit the activation of FXII and FX (procoagulant function). Intriguingly, these effects are absent in the presence of aPLAb (**29,30**).

β2GpI binds to FXI and inhibits its activation by either α-thrombin or FXIIa. Site-directed mutagenesis studies indicate that the positively charged portion of the Domain V is particularly important for this interaction. In fact, plasmin-cleaved β2GpI binds to FXI but loses the ability to inhibit its activation (**31**).

Another β2GpI anticoagulant function concerns the interaction with vWF. β2GpI is able to bind the A1 domain of the vWF, thus preventing platelet adhesion and agglutination, which are crucial steps in platelet plug formation (**32**).

Finally, it has also been discovered that β2GpI is an α-thrombin (αT) binder. In 2007 Krilis and co-workers (**33**) observed that β2GpI interacts with αT through its exosites. This purely qualitative result exploited in our laboratory in order to quantify and contextualize it in a physiological scenario. Our preliminary SPR analysis demonstrated that the interaction does not affect the active site and that β2GpI binds to αT at both exosites with an overall affinity of 50 nM (**34**).

In this context, structural information on the β2GpI-αT complex would much help to better understand the role of β2GpI in hemostasis. Here we combined biochemical/biophysical and molecular modelling techniques for mapping the binding sites in αT-β2GpI complex and provide a coherent structural model which could help to rationalize at the molecular level the effect of β2GpI on αT functions (**Chapter 2**).

Infection, inflammation and thrombosis

It is well-established that severe bacterial infections, leading to stimulation of the innate immune system with subsequent inflammatory responses, are frequently associated with hemostatic alterations, ranging from asymptomatic conditions to severe disseminated intravascular coagulation (DIC). In this scenario, it is known that inflammation triggers blood coagulation through tissue-mediated α-thrombin production (**35**), downregulation of physiological anticoagulant mechanisms and inhibition of fibrinolysis (**36**). During inflammation, platelets increase in number and become more thrombogenic. This is mainly due to the presence of pro-inflammatory IL-6 (**37**). In addition, it has been reported that inflammatory cytokines promote PARs and TF expression by endothelial cells (**38**) and alter the size of pro-adhesive von Willebrand Factor polymers (**39**). In detail, an unbalancing between the release of ultra-large vWF multimers (by endothelial cells) and degradation (by ADAMTS13) is able to trigger platelet adhesion and aggregation. Vice-versa, activation of the coagulation system may importantly affect inflammatory responses through direct and indirect

mechanisms. In particular, coagulation factors such as fibrin(ogen) (**40**) or TF-FVIIa complex (**41**) as well as active platelets can trigger inflammation (**42**). As a matter of facts, active platelets release P-selectine, a leukocyte chemoattractant molecule which recruits monocytes on the plug surface. In turn, activated monocytes release microparticles carrying TF on their surface, leading to the activation of coagulation (**43**).

The deep connection between bacterial infections and thrombotic manifestations, however, is not surprising. Actually, blood coagulation has evolved as a host defence system against infection, since injured blood vessels may represent a dangerous hot-spot for microorganisms attack and spreading. In this context, local fibrin clot formation facilitates the action of the innate immune system, trapping the invading pathogen and promoting its encounter with phagocytic cells (**44,45**). Not surprisingly, from an evolutionary point of view, the coagulation and the immune system seem to have the same root. Some species with highly conserved genomes, such as anthropoids (crustaceans and insects), produce hemolymph to trap pathogens, kill them and, at the same time, repair the wound, thus mimicking the role of both innate immunity and hemostasis of mammals. There are, however, some microorganisms that exploit coagulation to escape detection by the immune system (**45**). For example, some *S. aureus* proteins such as staphylocoagulase and vWF binding protein are prothrombin activators that stimulate fibrin production and mediate cell coating with a multi-layered fibrin film which protects the bacteria from immune cells.

In general, infectious diseases are all associated with a remarkably increased thrombotic risk (**46,47**). For instance, about 35% of the cases of bacterial sepsis are complicated by Disseminated Intravascular Coagulation (DIC), leading to multiple organ failure and final death (**46,48**). Despite this evidence, the molecular bases linking infectious and inflammatory diseases to severe thrombotic complications are largely unknown. In addition, sepsis-induced coagulopathies are only partially reverted in the case of successful antibiotic therapy and pathogen eradication. It is thought that bacterial lipopolysaccharides (LPS) interacting with Toll-like receptors on monocytes induce expression of TF, thus activating the "extrinsic" pathway of thrombin generation (**45,49**). However, LPS are present only on Gram-negative bacteria, but not on the surface of Gram-positive bacteria and infections from the latter group of pathogens are also dramatically complicated by DIC (**50**). These observations suggest that, in addition to LPS, other factors should be considered. Here, we hypothesize that extracellular proteases secreted by bacteria may play a role in the onset of procoagulant manifestations. Thus, in this part of the project (**Chapter 3**) we aimed to test whether bacterial proteases could bypass the whole coagulation cascade and directly activate ProT.

Subtilisin Carlsberg

Subtilisin Carlsberg is the first serine protease isolated form a bacterial source and consists of a single peptide chain of 274 amino acids (**51**). The catalytic triad Ser221, His64, Asp32 resides in a negatively-charged cleft and manifests a very broad substrate specificity, with preferences for large aromatic or aliphatic amino acids in the P1 and in P4 sites of the substrate (**52,53**). The tertiary structure is globular with a typical heart-shape and it is stabilized by two Ca^{2+} ions. The Ca^{2+} sites have different affinity: one strong, with a binding constant of $10^8 M$, and one weak, with a binding constant of $10^2 M$. The subtilisins are an extensive class of extracellular alkaline bacterial proteases that, according to their amino acid sequence, can be classified in two subfamilies or groups. Group A includes subtilisin Carlsberg and the enzyme from *B. pumilis*, whereas Group B comprises subtilisins Novo, BPN', and Amylosaccariticus (**51**).

Subtilisin is secreted by *B. subtilis*, an obligate aerobe, gram-positive bacterium living in the soil and in the gastrointestinal tract of humans and ruminants. *B. Subtilis* is often used as a probiotic and lacks any obvious pathogenicity (**54**) even though it could become virulent in immunodeficient subjects (**55**).

Here, we investigate the role that extracellular bacterial proteases, in particular subtilisin Carlsberg, may have in the onset of thrombotic manifestations. We hypothesized that extracellular proteases could bypass the entire coagulation cascade and directly activate prothrombin into active thrombin. In support of this hypothesis, few studies reported that human prothrombin is activated by extracellular microbial proteinases, such as staphylocoagulase from *S. Aureus* (**56**), gingipain from *Porphyromonas gingivalis* (**57**), a serine protease from *Aeromonas sobria* (**58**) and a metalloprotease from *Aeromonas hydrophila* (**59**).

Parkinson's Disease

Amyloidosis is a group of disorders characterized by deposition of protein material in the extracellular space of different tissues. Aggregation occurs when a protein, usually of small dimensions (10-15 kDa), acquires an alternative and relatively stable "misfolded state", which spontaneously undergoes self-association into oligomers and, subsequently, into polymers (**60**). These protein aggregates are called 'amyloids' and at least 23 amyloidogenic proteins have been described to date.

In amyloid disease, there are three possible mechanisms that potentially lead to formation of a pathogenic, misfolded protein (**61**). i) the protein may have intrinsic propensity to assume a misfolded state that becomes evident with aging (i.e. wild-type transthyretin in patients with senile systemic amyloidosis) or at critical serum concentration (i.e. serum amyloid A protein). ii) Peculiar

point mutations along the aminoacidic sequence may perturb native folding, as occurs in hereditary transthyretin amyloidosis (**62**). iii) Finally, misfolding may be induced by a proteolytic remodelling of the precursor protein (**63**). Of note, these mechanisms could act independently or in association with one another.

Beyond the intrinsic protein characteristics described above, there are other factors that could trigger amyloid formation. For example, the interaction of the protein with the extracellular matrix seems to play a crucial role during amyloid formation and may even lead to deposition of amyloid fibrils in particular body districts (**63**). Moreover, chronic inflammatory conditions (such as rheumatoid arthritis, inflamed bowel disease, infectious diseases, ulcerative colitis, lupus and Crohn's disease) are associated with high levels of inflammatory proteins have been found to facilitate protein misfolding and aggregation (**64**).

Parkinson's disease (PD) is the most common age-related motoric disorder and the second neurodegenerative pathology worldwide after Alzheimer's disease (AD). The prevalence of PD spans from 100 to 200 per 100,000 people in unselected population, with an average annual incidence of 15 per 100,000 (**65-67**), remarkably lower in Asia and Africa with respect to North America, Europe and Australia (**68**). The insurgence of PD reaches a peak at age 65 to 70 years (~ 1% incidence, late-onset variant), while before age of 50 years (early-onset variant) PD is rare (**69-71**). Albeit still elusive, the insurgence of both sporadic (~ 90% of cases) and autosomal PD arises from a combination of genetic, age-related and environmental risks factors leading to the progressive degeneration of dopaminergic neurons in the *substantia nigra* (**66**). Deficiency of dopamine results in resting tremor, rigidity and bradykinesia, which are regarded as the three cardinal signs of PD since 1817, when James Parkinson first described the pathology. As the disease proceeds, additional heterogeneous motor and non-motor manifestations appear, like psychiatric symptoms and cognitive impairment (**66,72**).

α-Synuclein (αSyn)

The neuropathological hallmark of PD is the presence of intracytoplasmic inclusions of α-Synuclein (αSyn), an abundant presynaptic protein belonging to the family of Naturally Unfolded Proteins (NUPs) (**73**). Although its physiological function is still matter of debate (**74,75**), αSyn cerebral aggregates are highly pathogenic, and spread from the *substantia nigra* through the brain along with the progression of the disease (**65,76**). Actually, PD is the most common synucleinopathy, displaying at least five morphologically distinct αSyn inclusions: Lewy Bodies (LBs), Lewy neurites (LNs), glial inclusions, neuronal inclusions and axonal spheroids (**77**).
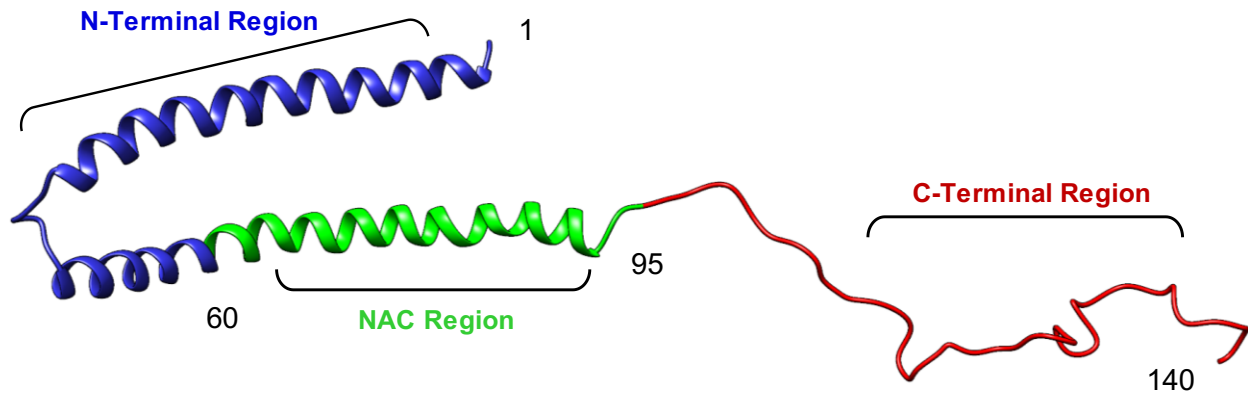
Figure 4. Three-dimensional representation of human αSyn (1XQ8.pdb). Human αSyn (140 aa, 14.5 kDa) in micelle-bound conformation is represented in its colour coded architecture domains. The N-terminal region (1-60) is coloured in blue, the NAC region (61-95) in green and the C-terminal region (96-140) in red. In this crystallographic model αSyn folds in two antiparallel α-helixes (V3-V37, K45-T92), which are connected by a stretched linker. The C-terminal region remains destructured even after binding to micelles.

The linear sequence of human αSyn (140 aa, 14.5 kDa) can be structurally divided in three regions: the N-terminal domain (NT), a central portion and the C-terminal domain (CT) (**77**). NT (1-60) is an amphipathic region composed of imperfect repetitions of the 11-aa string (X**KTKEGV**XXXX, consensus motif stressed in bold), which is responsible for αSyn interaction to negatively charged membranes (**78**). In its micelle-bound structure (1XQ8.pdb) (**Figure 4**), NT transiently organizes in two antiparallel α-helices, connected by a stretched linker (**79**). The central portion (61-95), named NAC (non-amyloid β-component) after its first detection in AD amyloid senile plaques (**80**) is the most hydrophobic region of the protein, and plays a crucial role on αSyn fibrillation. Shifting its conformation from a random coil to a β-sheet, αSyn molecules can associate at this level, forming oligomers that deposit in insoluble fibres (**70,81**). On the other hand, the CT (96-140) domain, rich in prolines and negative charges, remains always de-structured and scavenges the aggregation process by electrostatic repulsions (**82**).

Due to the protein susceptibility to aggregate, mutations in the αSyn encoding gene (*SNCA*) may lead to the development of autosomal PD both in elderly and young population. Triplications of the entire αSyn genetic *locus* lead to an early-onset aggressive form of PD, combined with dementia and psychiatric features (**83,84**). The juvenile variant of PD may be also induced by some missense mutations in the NT domain: A30P (**85**), E46K (**86**), H50Q (**87**), G51D (**88**), A53E (**89**) and A53T (**90**). On the other hand, duplication of *SNCA* gene is concerned with variable familial PD cases, from late-onset sporadic to early-onset PD forms indistinguishable from the triplication carriers (**91**).

α-Synuclein effects on coagulation

Beyond central nervous system, this protein is also expressed in the heart, skeletal muscles, pancreas and placenta (**92**). Surprisingly, αSyn can also be detected in the blood, and several efforts have been performed to address αSyn as a peripheral biomarker of PD, unfortunately without clear-cut evidences (**93-95**), since PD patients may present higher, lower or similar levels of plasma αSyn, compared to the healthy controls (**96**). In general, αSyn plasmatic concentration is variable, spanning from ~3 ng/ml to ~35 ng/ml, and increasing in those subjects with repetitions of the genetic *locus* (**96,97**). More than 99% of blood αSyn is localized in the red blood cells (RBCs), while the remaining is subdivided between plasma (0.1%), platelets (0.2%), and mononuclear cells (0.05%) (**98**).

While the massive level of αSyn in the erythrocytes can be simply addressed to their abundance, platelets are actually the main hosts of αSyn, yielding the highest protein rate in the bloodstream (264±36 ng αSyn *per* mg of total protein content, compared to 131±23 ng/mg in the RBCs) (**97**). In platelets, αSyn is largely diffused and loosely associated to the plasma membrane, the endoplasmic reticulum and the membranes of the secretory α-granules (**99**). The finding of αSyn in platelets is fascinating and still puzzling: while Hashimoto suggested an involvement in megakaryocytes differentiation (**99**), Park and colleagues demonstrated that exogenous-added full-length αSyn can penetrate the platelets and inhibit Ca^{2+}-dependent release of α-granules, after stimulation by α-thrombin (αT), the key enzyme of the coagulation cascade (**100**).

Platelets are able to respond even to the minimal αT concentration produced during the initial step of blood coagulation and are stimulated through proteolysis of PAR1 and PAR4 receptors (**101**). Once activated by αT, platelets expose phosphatidylserine on their outer surface by a flip-flop mechanism, providing the scaffold on which FXa, cofactor FVa and Ca^{2+} are recruited in the prothrombinase complex (**102,103**). Finally, during the propagation phase, prothrombin is converted to mature αT in a large-scale burst, thus allowing αT-mediated fibrin generation.

Even if still controversial, several clinical works report that patients suffering from PD undergo a minor incidence of strokes, ischemic attacks and myocardial diseases (**104-107**). This intriguing protective effect of PD towards vascular disorders was addressed either to abnormalities in platelets (**108-110**) or to impaired agglutination (**111**). The over-expression of αSyn in PD patients and its co-localization with αT on platelets surface in the amplification stage of αT generation, prompted us to investigate the interaction between these apparently disjointed proteins, and the possible implications of αSyn in the regulation of blood coagulation (**Chapter 4**).

Transthyretin Amyloidosis (ATTR)

Transthyretin amyloidosis (ATTR) is a systemic disorder caused by deposition of human transthyretin (hTTR) fibrils in various tissues. Among the systemic amyloidosis, ATTR is the third common form, after AL (immunoglobulin light chain) and AA (apo-serum amyloid A). There are two types of ATTR amyloidosis: a senile, or non-hereditary form, which is caused by wild-type hTTR and usually affects the elderly (age onset > 60 years), and a hereditary or familial form, which is due to single amino acid substitutions. To date, over 120 different hTTR mutations have been discovered and most of them are able to trigger amyloid disorders (**112**) (**Figure 5**).

Various biochemical and histological studies in cells and tissues suggest that, together with the type of mutation, the tendency towards aggregation and fibril formation are also largely influenced by proteolytic cleavage of TTR's C-terminal region (**113**). In particular, a cleavage leading to the formation of C-terminal hTTR fragments that start around position 50 generates fragments which have been found to aggregate far more readily than full length hTTR (**114**).

Nowadays, the protease(s) responsible for this cleavage is yet to be identified, although it is thought to be a serine protease with a trypsin-like fold. Seeing how all coagulation factors are trypsin-like serine proteases, we decided to test their ability to cleave hTTR. We also tested some selected bacterial proteases, as well as some proteases of the digestive apparatus and of the immune system (**Chapter 5**).

The main clinical manifestations of ATTR are polyneuropathy and cardiomyopathy. The neuropathic symptoms consist in a progressive sensory, motor and autonomic neuropathy that, during the first stages of the disease, is usually due to impaired function of small, unmyelinated nerve fibers which mediate temperature and pain sensation and autonomic nerve functions. As the disease progresses, larger, myelinated fibers become involved, affecting reflexes and position sensations. Eventually, a few years after the appearance of the first symptoms, motor neuropathy renders deambulation and performance of fine movement increasingly more difficult (**115**). Sensory and motor neuropathies are often accompanied by autonomic neuropathy, whose clinical manifestations are orthostatic hypotension, gastrointestinal disorders, nausea, vomiting, urinary incontinence. Central Nervous System (CNS) ATTR causes cerebral hemorrage and stroke-like, but the brain is a very rare site of ATTR onset (**115**). Cardiomyopathy is the other predominant feature of ATTR and is sometimes the initial manifestation of the disease (**116**). Here, the hTTR amyloid aggregates infiltrate the myocardium, leading to progressive myocardial stiffening that, in the end, leads to heart failure.
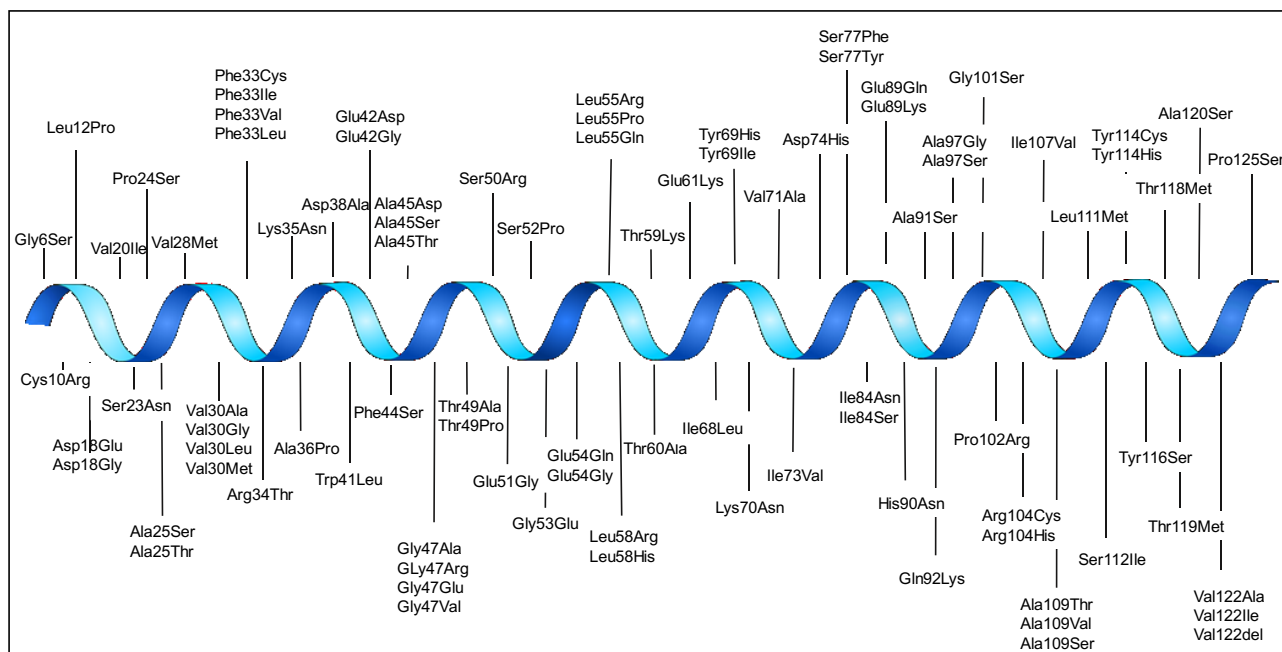
Figure 5. Single point mutations of hTTR. Schematic representation of the known hTTR single point mutations. Not all mutations are amyloidogenic. Indeed, the Thr119Met variant has a higher stability than wild-type hTTR and seems to have a protective role if present in heterozygosity with the amyloidogenic variant Val30Met (**117**).

Human Transthyretin (hTTR)

Human transthyretin (hTTR) is a 55 kDa homo-tetrameric protein abundantly present in plasma (0.2 mg/ml) and in cerebrospinal fluid (0.02 mg/ml). Each monomer consists of 127 amino acids and forms 8 β-strands, named from A to H, which are arranged as a β-sandwich of two four-stranded β-sheets and one small α-helix located between β-strands E and F (**Figure 6A and B**) (**118-120**). The monomers interact with each other through hydrogen bonds between adjacent antiparallel strands H-H' and F-F' to form dimers (**121**). The two dimers form the final tetramer mainly through hydrophobic interactions between the amino acid residues of the A-B and G-H loops. The resulting quaternary structure is globular, with a size of 70x55x50 Å (**Figure 6C**). At the interface of the dimers there is a channel (T4 channel), able to bind small lipophilic molecules, which, in detail, is formed by three elements. The first is a hydrophilic center moulded by the hydroxyl groups of Ser112, Ser115, Ser117, Thr119. The second element is represented by a hydrophobic patch generated by the methyl groups of Leu17, Thr106, Ala 108, Leu110, and Val121. The third element consists of a group of charged residues, Lys15, Glu54, and His56 (**120**).
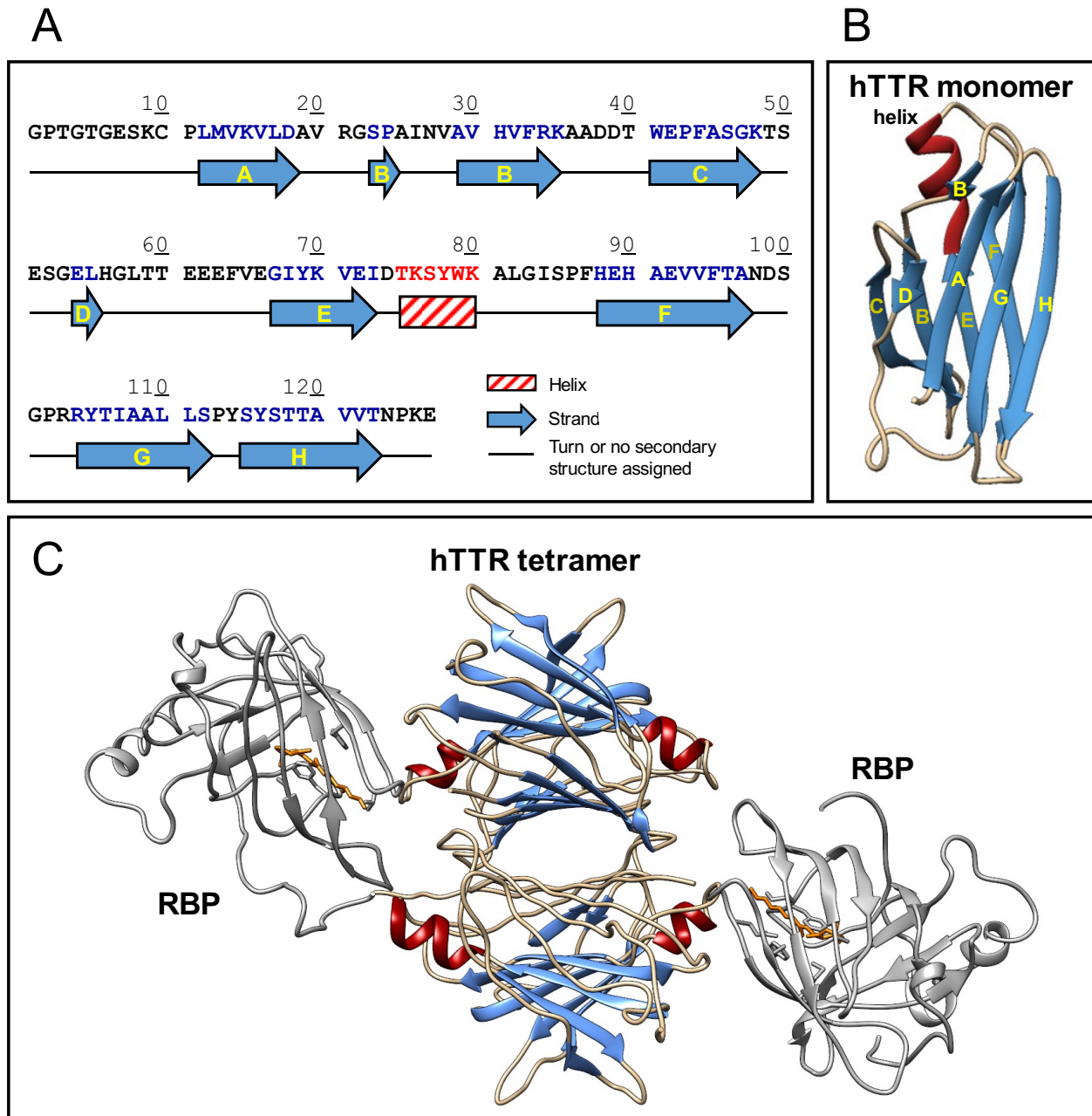
A

```
        10          20          30          40          50
GPTGTGESKC PLMVKVLDAV RGSPAINVAV HVFRKAADDT WEPFASGKTS
                  A          B      B            C

        60          70          80          90         100
ESGELHGLTT EEEFVEGIYK VEIDTKSYWK ALGISPFHEH AEVVFTANDS
           D              E       (Helix)          F

       110         120
GPRRYTIAAL LSPYSYSTTA VVTNPKE
         G              H
```

Helix
Strand
Turn or no secondary structure assigned

B

hTTR monomer

C

hTTR tetramer

RBP

RBP

Figure 6. human Tranthyretin (hTTR) structure. (**A**) Amino acid sequence of hTTR (1-127). The β-sheet forming amino acids are indicated in blue and the secondary structure of native TTR where they belong is depicted below the amino acid sequence. (**B**) hTTR monomer (1DVQ.pdb). The 8 β-strands are coloured in blue and named from A to H in yellow capital letters. (**C**) hTTR in its physiological tetrameric form (1QAB.pdb) bound to two RBPs (dark grey). Retinol molecules are shown in orange.

The hTTR gene is located on chromosome 18 and consists of 7 kb, with 4 exons of about 200 base pairs and 3 introns. Exon 1 contains the coding sequence of the first 3 amino acids of the mature protein whereas the other ones encode for the 4-47 (exon 2), 48-92 (exon 3) and 93-127 (exon 4) sequences (**122**). As previously mentioned, there are more than 120 known single point mutations, each having a different effect on the stability of the hTTR tetrameric structure (**Figure 5**). In addition

to genetic mutations, TTR is subjected to post-translational modifications of Cys10, whose thiol is variously oxidized to obtain different species (i.e. Cysteine sulfenic, sulfinic, sulfonic acid, S-Cys, S-Glutathione) (**123**).

hTTR is mainly produced in the liver and in the choroid plexus of the brain (**124**). Other secondary production sites are the retinal pigment epithelium and the Langerhans islands of the pancreas (**125,126**).

The hTTR physiological roles are the transport of the thyroid hormones T3 and T4 and the retinol, through the binding to the Retinol Binding Protein (RBP) (**Figure 6C**). hTTR is, however, only the third thyroxine carrier after thyroxine-binding globulin (TBG) and albumin (**127**), and less than 1% of plasma hTTR molecules are normally involved in transport. Each hTTR tetramer has two identical binding sites for T3 and T4 but, due to a negative cooperativity, only one can be occupied in physiological conditions (**128**). Binding to two RBPs is, instead, possible, but the low plasma concentration of these transporters only allow for formation of 1:1 molar complexes (**129**). Moreover, only ~30% of TTR is bound to RBP (**130**).

As previously described, hTTR is also a known amyloidogenic protein, whose aggregation is responsible for several amyloid diseases, including senile systemic amyloidosis (SSA), familial amyloid polyneuropathy (FAP), and familial amyloid cardiomyopathy (FAC) (**131**).

REFERENCES

1. Miyakis, S., Lockshin, M. D., Atsumi, T., Branch, D. W., Brey, R. L., Cervera, R., Derksen, R. H., PG, D. E. G., Koike, T., Meroni, P. L., Reber, G., Shoenfeld, Y., Tincani, A., Vlachoyiannopoulos, P. G., and Krilis, S. A. (2006) International consensus statement on an update of the classification criteria for definite antiphospholipid syndrome (APS). *J Thromb Haemost* **4**, 295-306

2. Kandiah, D. A., Sali, A., Sheng, Y., Victoria, E. J., Marquis, D. M., Coutts, S. M., and Krilis, S. A. (1998) Current insights into the "antiphospholipid" syndrome: clinical, immunological, and molecular aspects. *Adv Immunol* **70**, 507-563

3. de Groot, P. G., and Urbanus, R. T. (2012) The significance of autoantibodies against beta2-glycoprotein I. *Blood* **120**, 266-274

4. Tripodi, A., de Groot, P. G., and Pengo, V. (2011) Antiphospholipid syndrome: laboratory detection, mechanisms of action and treatment. *J Intern Med* **270**, 110-122

5. Agar, C., van Os, G. M., Morgelin, M., Sprenger, R. R., Marquart, J. A., Urbanus, R. T., Derksen, R. H., Meijers, J. C., and de Groot, P. G. (2010) Beta2-glycoprotein I can exist in 2 conformations: implications for our understanding of the antiphospholipid syndrome. *Blood* **116**, 1336-1343

6. de Groot, P. G., and Urbanus, R. T. (2012) The future of antiphospholipid antibody testing. *Semin Thromb Hemost* **38**, 412-420

7. Lim, W. (2013) Antiphospholipid syndrome. *Hematology Am Soc Hematol Educ Program* **2013**, 675-680

8. Pengo, V., Banzato, A., Bison, E., Denas, G., Padayattil Jose, S., and Ruffatti, A. (2010) Antiphospholipid syndrome: critical analysis of the diagnostic path. *Lupus* **19**, 428-431

9. Galli, M. (2003) Antiphospholipid syndrome: association between laboratory tests and clinical practice. *Pathophysiol Haemost Thromb* **33**, 249-255

10. Schultze, H. E. (1961) [Glycoproteins of human plasma]. *Bull Schweiz Akad Med Wiss* **17**, 77-91

11. Bouma, B., de Groot, P. G., van den Elsen, J. M., Ravelli, R. B., Schouten, A., Simmelink, M. J., Derksen, R. H., Kroon, J., and Gros, P. (1999) Adhesion mechanism of human beta(2)-glycoprotein I to phospholipids based on its crystal structure. *Embo J* **18**, 5166-5174

12. Steinkasserer, A., Estaller, C., Weiss, E. H., Sim, R. B., and Day, A. J. (1991) Complete nucleotide and deduced amino acid sequence of human beta 2-glycoprotein I. *Biochem J* **277 (Pt 2)**, 387-391

13. Sheng, Y., Sali, A., Herzog, H., Lahnstein, J., and Krilis, S. A. (1996) Site-directed mutagenesis of recombinant human beta 2-glycoprotein I identifies a cluster of lysine residues that are critical for phospholipid binding and anti-cardiolipin antibody activity. *J Immunol* **157**, 3744-3751

14. Guerin, J., Sheng, Y., Reddel, S., Iverson, G. M., Chapman, M. G., and Krilis, S. A. (2002) Heparin inhibits the binding of beta 2-glycoprotein I to phospholipids and promotes the

plasmin-mediated inactivation of this blood protein. Elucidation of the consequences of the two biological events in patients with the anti-phospholipid syndrome. *J Biol Chem* **277**, 2644-2649

15. Biasiolo, A., Rampazzo, P., Brocco, T., Barbero, F., Rosato, A., and Pengo, V. (1999) [Anti-beta2 glycoprotein I-beta2 glycoprotein I] immune complexes in patients with antiphospholipid syndrome and other autoimmune diseases. *Lupus* **8**, 121-126

16. de Laat, B., Wu, X. X., van Lummel, M., Derksen, R. H., de Groot, P. G., and Rand, J. H. (2007) Correlation between antiphospholipid antibodies that recognize domain I of beta2-glycoprotein I and a reduction in the anticoagulant activity of annexin A5. *Blood* **109**, 1490-1494

17. Iverson, G. M., Victoria, E. J., and Marquis, D. M. (1998) Anti-beta2 glycoprotein I (beta2GPI) autoantibodies recognize an epitope on the first domain of beta2GPI. *Proc Natl Acad Sci U S A* **95**, 15542-15546

18. Hunt, J. E., and Krilis, S. A. (1993) Antiphospholipid antibodies, beta 2-glycoprotein I and thrombosis. *Lupus* **2**, 285-287

19. Hammel, M., Kriechbaum, M., Gries, A., Kostner, G. M., Laggner, P., and Prassl, R. (2002) Solution structure of human and bovine beta(2)-glycoprotein I revealed by small-angle X-ray scattering. *J Mol Biol* **321**, 85-97

20. Levine, J. S., Subang, R., Nasr, S. H., Fournier, S., Lajoie, G., Wither, J., and Rauch, J. (2006) Immunization with an apoptotic cell-binding protein recapitulates the nephritis and sequential autoantibody emergence of systemic lupus erythematosus. *J Immunol* **177**, 6504-6516

21. Buttari, B., Profumo, E., Mattei, V., Siracusano, A., Ortona, E., Margutti, P., Salvati, B., Sorice, M., and Rigano, R. (2005) Oxidized beta2-glycoprotein I induces human dendritic cell maturation and promotes a T helper type 1 response. *Blood* **106**, 3880-3887

22. Morgan, P. E., Sturgess, A. D., and Davies, M. J. (2005) Increased levels of serum protein oxidation and correlation with disease activity in systemic lupus erythematosus. *Arthritis Rheum* **52**, 2069-2079

23. Camilleri, R. S., Mackie, I. J., Humphries, S. E., Machin, S. J., and Cohen, H. (2003) Lack of association of beta2-glycoprotein I polymorphisms Val247Leu and Trp316Ser with antiphospholipid antibodies in patients with thrombosis and pregnancy complications. *Br J Haematol* **120**, 1066-1072

24. Yasuda, S., Bohgaki, M., Atsumi, T., and Koike, T. (2005) Pathogenesis of antiphospholipid antibodies: impairment of fibrinolysis and monocyte activation via the p38 mitogen-activated protein kinase pathway. *Immunobiology* **210**, 775-780

25. Sheng, Y., Krilis, S. A., and Sali, A. (1997) Site-directed mutagenesis of recombinant human beta 2-glycoprotein I. Effect of phospholipid binding and anticardiolipin antibody activity. *Ann N Y Acad Sci* **815**, 331-333

26. Miyakis, S., Giannakopoulos, B., and Krilis, S. A. (2004) Beta 2 glycoprotein I--function in health and disease. *Thromb Res* **114**, 335-346

27.   Yasuda, S., Atsumi, T., Ieko, M., and Koike, T. (2004) Beta2-glycoprotein I, anti-beta2-glycoprotein I, and fibrinolysis. *Thromb Res* **114**, 461-465

28.   Ieko, M., Sawada, K. I., Koike, T., Notoya, A., Mukai, M., Kohno, M., Wada, N., Itoh, T., and Yoshioka, N. (1999) The putative mechanism of thrombosis in antiphospholipid syndrome: impairment of the protein C and the fibrinolytic systems by monoclonal anticardiolipin antibodies. *Semin Thromb Hemost* **25**, 503-507

29.   Schousboe, I., and Rasmussen, M. S. (1995) Synchronized inhibition of the phospholipid mediated autoactivation of factor XII in plasma by beta 2-glycoprotein I and anti-beta 2-glycoprotein I. *Thromb Haemost* **73**, 798-804

30.   Shi, W., Chong, B. H., Hogg, P. J., and Chesterman, C. N. (1993) Anticardiolipin antibodies block the inhibition by beta 2-glycoprotein I of the factor Xa generating activity of platelets. *Thromb Haemost* **70**, 342-345

31.   Shi, T., Giannakopoulos, B., Iverson, G. M., Cockerill, K. A., Linnik, M. D., and Krilis, S. A. (2005) Domain V of beta2-glycoprotein I binds factor XI/XIa and is cleaved at Lys317-Thr318. *J Biol Chem* **280**, 907-912

32.   Hulstein, J. J., Lenting, P. J., de Laat, B., Derksen, R. H., Fijnheer, R., and de Groot, P. G. (2007) beta2-Glycoprotein I inhibits von Willebrand factor dependent platelet adhesion and aggregation. *Blood* **110**, 1483-1491

33.   Rahgozar, S., Yang, Q., Giannakopoulos, B., Yan, X., Miyakis, S., and Krilis, S. A. (2007) Beta2-glycoprotein I binds thrombin via exosite I and exosite II: anti-beta2-glycoprotein I antibodies potentiate the inhibitory effect of beta2-glycoprotein I on thrombin-mediated factor XIa generation. *Arthritis Rheum* **56**, 605-613

34.   Pozzi, N., Acquasaliente, L., Frasson, R., Cristiani, A., Moro, S., Banzato, A., Pengo, V., Scaglione, G. L., Arcovito, A., De Cristofaro, R., and De Filippis, V. (2013) beta2 -Glycoprotein I binds to thrombin and selectively inhibits the enzyme procoagulant functions. *J Thromb Haemost* **11**, 1093-1102

35.   Wolbink, G. J., Bossink, A. W., Groeneveld, A. B., de Groot, M. C., Thijs, L. G., and Hack, C. E. (1998) Complement activation in patients with sepsis is in part mediated by C-reactive protein. *J Infect Dis* **177**, 81-87

36.   Esmon, C. T. (2005) The interactions between inflammation and coagulation. *Br J Haematol* **131**, 417-430

37.   Nystedt, S., Ramakrishnan, V., and Sundelin, J. (1996) The proteinase-activated receptor 2 is induced by inflammatory mediators in human endothelial cells. Comparison with the thrombin receptor. *J Biol Chem* **271**, 14910-14915

38.   Devaraj, S., Xu, D. Y., and Jialal, I. (2003) C-reactive protein increases plasminogen activator inhibitor-1 expression and activity in human aortic endothelial cells: implications for the metabolic syndrome and atherothrombosis. *Circulation* **107**, 398-404

39.   Bernardo, A., Ball, C., Nolasco, L., Moake, J. F., and Dong, J. F. (2004) Effects of inflammatory cytokines on the release and cleavage of the endothelial cell-derived ultralarge von Willebrand factor multimers under flow. *Blood* **104**, 100-106

40. Loike, J. D., el Khoury, J., Cao, L., Richards, C. P., Rascoff, H., Mandeville, J. T., Maxfield, F. R., and Silverstein, S. C. (1995) Fibrin regulates neutrophil migration in response to interleukin 8, leukotriene B4, tumor necrosis factor, and formyl-methionyl-leucyl-phenylalanine. *J Exp Med* **181**, 1763-1772

41. Cunningham, M. A., Romas, P., Hutchinson, P., Holdsworth, S. R., and Tipping, P. G. (1999) Tissue factor and factor VIIa receptor/ligand interactions induce proinflammatory effects in macrophages. *Blood* **94**, 3413-3420

42. Henn, V., Slupsky, J. R., Grafe, M., Anagnostopoulos, I., Forster, R., Muller-Berghaus, G., and Kroczek, R. A. (1998) CD40 ligand on activated platelets triggers an inflammatory reaction of endothelial cells. *Nature* **391**, 591-594

43. Day, S. M., Reeve, J. L., Pedersen, B., Farris, D. M., Myers, D. D., Im, M., Wakefield, T. W., Mackman, N., and Fay, W. P. (2005) Macrovascular thrombosis is driven by tissue factor derived primarily from the blood vessel wall. *Blood* **105**, 192-198

44. Dushay, M. S. (2009) Insect hemolymph clotting. *Cell Mol Life Sci* **66**, 2643-2650

45. Engelmann, B., and Massberg, S. (2013) Thrombosis as an intravascular effector of innate immunity. *Nat Rev Immunol* **13**, 34-45

46. Levi, M., and van der Poll, T. (2017) Coagulation and sepsis. *Thromb Res* **149**, 38-44

47. Novacek, G., Weltermann, A., Sobala, A., Tilg, H., Petritsch, W., Reinisch, W., Mayer, A., Haas, T., Kaser, A., Feichtenschlager, T., Fuchssteiner, H., Knoflach, P., Vogelsang, H., Miehsler, W., Platzer, R., Tillinger, W., Jaritz, B., Schmid, A., Blaha, B., Dejaco, C., and Eichinger, S. (2010) Inflammatory bowel disease is a risk factor for recurrent venous thromboembolism. *Gastroenterology* **139**, 779-787, 787.e771

48. Levi, M., and Ten Cate, H. (1999) Disseminated intravascular coagulation. *N Engl J Med* **341**, 586-592

49. Opal, S. M., and Esmon, C. T. (2003) Bench-to-bedside review: functional relationships between coagulation and the innate immune response and their respective roles in the pathogenesis of sepsis. *Crit Care* **7**, 23-38

50. Angus, D. C., and van der Poll, T. (2013) Severe sepsis and septic shock. *N Engl J Med* **369**, 2063

51. Smith, E. L., DeLange, R. J., Evans, W. H., Landon, M., and Markland, F. S. (1968) Subtilisin Carlsberg. V. The complete sequence; comparison with subtilisin BPN'; evolutionary relationships. *J Biol Chem* **243**, 2184-2191

52. Gron, H., and Breddam, K. (1992) Interdependency of the binding subsites in subtilisin. *Biochemistry* **31**, 8967-8971

53. Wells, J. A., and Estell, D. A. (1988) Subtilisin—an enzyme designed to be engineered. *Trends in biochemical sciences* **13**, 291-297

54. de Boer, A. S., and Diderichsen, B. (1991) On the safety of Bacillus subtilis and B. amyloliquefaciens: a review. *Appl Microbiol Biotechnol* **36**, 1-4

55. Oggioni, M. R., Pozzi, G., Valensin, P. E., Galieni, P., and Bigazzi, C. (1998) Recurrent septicemia in an immunocompromised patient due to probiotic strains of Bacillus subtilis. *J Clin Microbiol* **36**, 325-326

56. Friedrich, R., Panizzi, P., Fuentes-Prior, P., Richter, K., Verhamme, I., Anderson, P. J., Kawabata, S., Huber, R., Bode, W., and Bock, P. E. (2003) Staphylocoagulase is a prototype for the mechanism of cofactor-induced zymogen activation. *Nature* **425**, 535-539

57. Imamura, T., Banbula, A., Pereira, P. J., Travis, J., and Potempa, J. (2001) Activation of human prothrombin by arginine-specific cysteine proteinases (Gingipains R) from porphyromonas gingivalis. *J Biol Chem* **276**, 18984-18991

58. Nitta, H., Kobayashi, H., Irie, A., Baba, H., Okamoto, K., and Imamura, T. (2007) Activation of prothrombin by ASP, a serine protease released from Aeromonas sobria. *FEBS Lett* **581**, 5935-5939

59. Keller, T., Seitz, R., Dodt, J., and Konig, H. (2004) A secreted metallo protease from Aeromonas hydrophila exhibits prothrombin activator activity. *Blood Coagul Fibrinolysis* **15**, 169-178

60. Schultz, C. P. (2000) Illuminating folding intermediates. *Nat Struct Biol* **7**, 7-10

61. Hazenberg, B. P. (2013) Amyloidosis: a clinical overview. *Rheumatic Disease Clinics* **39**, 323-345

62. Buxbaum, J. N., and Tagoe, C. E. (2000) The genetics of the amyloidoses. *Annu Rev Med* **51**, 543-569

63. Merlini, G., and Bellotti, V. (2003) Molecular mechanisms of amyloidosis. *N Engl J Med* **349**, 583-596

64. Blank, N., and Schonland, S. O. (2013) [Chronic inflammation and AA amyloidosis]. *Dtsch Med Wochenschr* **138**, 1835-1838

65. Tysnes, O. B., and Storstein, A. (2017) Epidemiology of Parkinson's disease. *J Neural Transm (Vienna)* **124**, 901-905

66. de Lau, L. M., and Breteler, M. M. (2006) Epidemiology of Parkinson's disease. *Lancet Neurol* **5**, 525-535

67. von Campenhausen, S., Bornschein, B., Wick, R., Botzel, K., Sampaio, C., Poewe, W., Oertel, W., Siebert, U., Berger, K., and Dodel, R. (2005) Prevalence and incidence of Parkinson's disease in Europe. *Eur Neuropsychopharmacol* **15**, 473-490

68. Pringsheim, T., Fiest, K., and Jette, N. (2014) The international incidence and prevalence of neurologic conditions: how common are they? *Neurology* **83**, 1661-1664

69. de Rijk, M. C., Launer, L. J., Berger, K., Breteler, M. M., Dartigues, J. F., Baldereschi, M., Fratiglioni, L., Lobo, A., Martinez-Lage, J., Trenkwalder, C., and Hofman, A. (2000) Prevalence of Parkinson's disease in Europe: A collaborative study of population-based cohorts. Neurologic Diseases in the Elderly Research Group. *Neurology* **54**, S21-23

70.   Bisaglia, M., Tessari, I., Pinato, L., Bellanda, M., Giraudo, S., Fasano, M., Bergantino, E., Bubacco, L., and Mammi, S. (2005) A topological model of the interaction between alpha-synuclein and sodium dodecyl sulfate micelles. *Biochemistry* **44**, 329-339

71.   van der Walt, J. M., Nicodemus, K. K., Martin, E. R., Scott, W. K., Nance, M. A., Watts, R. L., Hubble, J. P., Haines, J. L., Koller, W. C., Lyons, K., Pahwa, R., Stern, M. B., Colcher, A., Hiner, B. C., Jankovic, J., Ondo, W. G., Allen, F. H., Jr., Goetz, C. G., Small, G. W., Mastaglia, F., Stajich, J. M., McLaurin, A. C., Middleton, L. T., Scott, B. L., Schmechel, D. E., Pericak-Vance, M. A., and Vance, J. M. (2003) Mitochondrial polymorphisms significantly reduce the risk of Parkinson disease. *Am J Hum Genet* **72**, 804-811

72.   Kalia, L. V., and Lang, A. E. (2015) Parkinson's disease. *Lancet* **386**, 896-912

73.   Bisaglia, M., Tessari, I., Mammi, S., and Bubacco, L. (2009) Interaction between alpha-synuclein and metal ions, still looking for a role in the pathogenesis of Parkinson's disease. *Neuromolecular Med* **11**, 239-251

74.   Clayton, D. F., and George, J. M. (1998) The synucleins: a family of proteins involved in synaptic function, plasticity, neurodegeneration and disease. *Trends Neurosci* **21**, 249-254

75.   Lavedan, C., Buchholtz, S., Auburger, G., Albin, R. L., Athanassiadou, A., Blancato, J., Burguera, J. A., Ferrell, R. E., Kostic, V., Leroy, E., Leube, B., Mota-Vieira, L., Papapetropoulos, T., Pericak-Vance, M. A., Pinkus, J., Scott, W. K., Ulm, G., Vasconcelos, J., Vilchez, J. J., Nussbaum, R. L., and Polymeropoulos, M. H. (1998) Absence of mutation in the beta- and gamma-synuclein genes in familial autosomal dominant Parkinson's disease. *DNA Res* **5**, 401-402

76.   Braak, H., and Del Tredici, K. (2017) Neuropathological Staging of Brain Pathology in Sporadic Parkinson's disease: Separating the Wheat from the Chaff. *J Parkinsons Dis* **7**, S71-s85

77.   Uversky, V. N. (2007) Neuropathology, biochemistry, and biophysics of alpha-synuclein aggregation. *J Neurochem* **103**, 17-37

78.   Davidson, W. S., Jonas, A., Clayton, D. F., and George, J. M. (1998) Stabilization of alpha-synuclein secondary structure upon binding to synthetic membranes. *J Biol Chem* **273**, 9443-9449

79.   Ulmer, T. S., and Bax, A. (2005) Comparison of structure and dynamics of micelle-bound human alpha-synuclein and Parkinson disease variants. *J Biol Chem* **280**, 43179-43187

80.   Iwai, A., Masliah, E., Yoshimoto, M., Ge, N., Flanagan, L., de Silva, H. A., Kittel, A., and Saitoh, T. (1995) The precursor protein of non-A beta component of Alzheimer's disease amyloid is a presynaptic protein of the central nervous system. *Neuron* **14**, 467-475

81.   Lucking, C. B., and Brice, A. (2000) Alpha-synuclein and Parkinson's disease. *Cell Mol Life Sci* **57**, 1894-1908

82.   Dedmon, M. M., Lindorff-Larsen, K., Christodoulou, J., Vendruscolo, M., and Dobson, C. M. (2005) Mapping long-range interactions in alpha-synuclein using spin-label NMR and ensemble molecular dynamics simulations. *J Am Chem Soc* **127**, 476-477

83. Singleton, A. B., Farrer, M., Johnson, J., Singleton, A., Hague, S., Kachergus, J., Hulihan, M., Peuralinna, T., Dutra, A., Nussbaum, R., Lincoln, S., Crawley, A., Hanson, M., Maraganore, D., Adler, C., Cookson, M. R., Muenter, M., Baptista, M., Miller, D., Blancato, J., Hardy, J., and Gwinn-Hardy, K. (2003) alpha-Synuclein locus triplication causes Parkinson's disease. *Science* **302**, 841

84. Olgiati, S., Thomas, A., Quadri, M., Breedveld, G. J., Graafland, J., Eussen, H., Douben, H., de Klein, A., Onofrj, M., and Bonifati, V. (2015) Early-onset parkinsonism caused by alpha-synuclein gene triplication: Clinical and genetic findings in a novel family. *Parkinsonism Relat Disord* **21**, 981-986

85. Kruger, R., Kuhn, W., Muller, T., Woitalla, D., Graeber, M., Kosel, S., Przuntek, H., Epplen, J. T., Schols, L., and Riess, O. (1998) Ala30Pro mutation in the gene encoding alpha-synuclein in Parkinson's disease. *Nat Genet* **18**, 106-108

86. Zarranz, J. J., Alegre, J., Gomez-Esteban, J. C., Lezcano, E., Ros, R., Ampuero, I., Vidal, L., Hoenicka, J., Rodriguez, O., Atares, B., Llorens, V., Gomez Tortosa, E., del Ser, T., Munoz, D. G., and de Yebenes, J. G. (2004) The new mutation, E46K, of alpha-synuclein causes Parkinson and Lewy body dementia. *Ann Neurol* **55**, 164-173

87. Appel-Cresswell, S., Vilarino-Guell, C., Encarnacion, M., Sherman, H., Yu, I., Shah, B., Weir, D., Thompson, C., Szu-Tu, C., Trinh, J., Aasly, J. O., Rajput, A., Rajput, A. H., Jon Stoessl, A., and Farrer, M. J. (2013) Alpha-synuclein p.H50Q, a novel pathogenic mutation for Parkinson's disease. *Mov Disord* **28**, 811-813

88. Kiely, A. P., Asi, Y. T., Kara, E., Limousin, P., Ling, H., Lewis, P., Proukakis, C., Quinn, N., Lees, A. J., Hardy, J., Revesz, T., Houlden, H., and Holton, J. L. (2013) alpha-Synucleinopathy associated with G51D SNCA mutation: a link between Parkinson's disease and multiple system atrophy? *Acta Neuropathol* **125**, 753-769

89. Pasanen, P., Myllykangas, L., Siitonen, M., Raunio, A., Kaakkola, S., Lyytinen, J., Tienari, P. J., Poyhonen, M., and Paetau, A. (2014) Novel alpha-synuclein mutation A53E associated with atypical multiple system atrophy and Parkinson's disease-type pathology. *Neurobiol Aging* **35**, 2180.e2181-2185

90. Polymeropoulos, M. H., Lavedan, C., Leroy, E., Ide, S. E., Dehejia, A., Dutra, A., Pike, B., Root, H., Rubenstein, J., Boyer, R., Stenroos, E. S., Chandrasekharappa, S., Athanassiadou, A., Papapetropoulos, T., Johnson, W. G., Lazzarini, A. M., Duvoisin, R. C., Di Iorio, G., Golbe, L. I., and Nussbaum, R. L. (1997) Mutation in the alpha-synuclein gene identified in families with Parkinson's disease. *Science* **276**, 2045-2047

91. Kara, E., Kiely, A. P., Proukakis, C., Giffin, N., Love, S., Hehir, J., Rantell, K., Pandraud, A., Hernandez, D. G., Nacheva, E., Pittman, A. M., Nalls, M. A., Singleton, A. B., Revesz, T., Bhatia, K. P., Quinn, N., Hardy, J., Holton, J. L., and Houlden, H. (2014) A 6.4 Mb duplication of the alpha-synuclein locus causing frontotemporal dementia and Parkinsonism: phenotype-genotype correlations. *JAMA Neurol* **71**, 1162-1171

92. Ueda, K., Fukushima, H., Masliah, E., Xia, Y., Iwai, A., Yoshimoto, M., Otero, D. A., Kondo, J., Ihara, Y., and Saitoh, T. (1993) Molecular cloning of cDNA encoding an unrecognized component of amyloid in Alzheimer disease. *Proc Natl Acad Sci U S A* **90**, 11282-11286

93.   Tinsley, R. B., Kotschet, K., Modesto, D., Ng, H., Wang, Y., Nagley, P., Shaw, G., and Horne, M. K. (2010) Sensitive and specific detection of alpha-synuclein in human plasma. *J Neurosci Res* **88**, 2693-2700

94.   Foulds, P. G., Diggle, P., Mitchell, J. D., Parker, A., Hasegawa, M., Masuda-Suzukake, M., Mann, D. M., and Allsop, D. (2013) A longitudinal study on alpha-synuclein in blood plasma as a biomarker for Parkinson's disease. *Sci Rep* **3**, 2540

95.   El-Agnaf, O. M., Salem, S. A., Paleologou, K. E., Curran, M. D., Gibson, M. J., Court, J. A., Schlossmacher, M. G., and Allsop, D. (2006) Detection of oligomeric forms of alpha-synuclein protein in human plasma as a potential biomarker for Parkinson's disease. *Faseb j* **20**, 419-425

96.   Malec-Litwinowicz, M., Plewka, A., Plewka, D., Bogunia, E., Morek, M., Szczudlik, A., Szubiga, M., and Rudzinska-Bar, M. (2018) The relation between plasma alpha-synuclein level and clinical symptoms or signs of Parkinson's disease. *Neurol Neurochir Pol* **52**, 243-251

97.   Barbour, R., Kling, K., Anderson, J. P., Banducci, K., Cole, T., Diep, L., Fox, M., Goldstein, J. M., Soriano, F., Seubert, P., and Chilcote, T. J. (2008) Red blood cells are the major source of alpha-synuclein in blood. *Neurodegener Dis* **5**, 55-59

98.   Shimura, H., Hattori, N., Kubo, S., Mizuno, Y., Asakawa, S., Minoshima, S., Shimizu, N., Iwai, K., Chiba, T., Tanaka, K., and Suzuki, T. (2000) Familial Parkinson disease gene product, parkin, is a ubiquitin-protein ligase. *Nat Genet* **25**, 302-305

99.   Hashimoto, M., Yoshimoto, M., Sisk, A., Hsu, L. J., Sundsmo, M., Kittel, A., Saitoh, T., Miller, A., and Masliah, E. (1997) NACP, a synaptic protein involved in Alzheimer's disease, is differentially regulated during megakaryocyte differentiation. *Biochem Biophys Res Commun* **237**, 611-616

100.   Park, S. M., Jung, H. Y., Kim, H. O., Rhim, H., Paik, S. R., Chung, K. C., Park, J. H., and Kim, J. (2002) Evidence that alpha-synuclein functions as a negative regulator of Ca(++)-dependent alpha-granule release from human platelets. *Blood* **100**, 2506-2514

101.   De Cristofaro, R., and De Filippis, V. (2003) Interaction of the 268-282 region of glycoprotein Ibalpha with the heparin-binding site of thrombin inhibits the enzyme activation of factor VIII. *Biochem J* **373**, 593-601

102.   Rosing, J., Tans, G., Govers-Riemslag, J. W., Zwaal, R. F., and Hemker, H. C. (1980) The role of phospholipids and factor Va in the prothrombinase complex. *J Biol Chem* **255**, 274-283

103.   Nesheim, M. E., Taswell, J. B., and Mann, K. G. (1979) The contribution of bovine Factor V and Factor Va to the activity of prothrombinase. *J Biol Chem* **254**, 10952-10962

104.   Scigliano, G., Musicco, M., Soliveri, P., Piccolo, I., Ronchetti, G., and Girotti, F. (2006) Reduced risk factors for vascular disorders in Parkinson disease patients: a case-control study. *Stroke* **37**, 1184-1188

105. Korten, A., Lodder, J., Vreeling, F., Boreas, A., van Raak, L., and Kessels, F. (2001) Stroke and idiopathic Parkinson's disease: does a shortage of dopamine offer protection against stroke? *Mov Disord* **16**, 119-123

106. Levine, R. L., Jones, J. C., and Bee, N. (1992) Stroke and Parkinson's disease. *Stroke* **23**, 839-842

107. Struck, L. K., Rodnitzky, R. L., and Dobson, J. K. (1990) Circadian fluctuations of contrast sensitivity in Parkinson's disease. *Neurology* **40**, 467-470

108. Rabey, J. M., Vered, Y., Shabtai, H., Graff, E., Harsat, A., and Korczyn, A. D. (1993) Broad bean (Vicia faba) consumption and Parkinson's disease. *Adv Neurol* **60**, 681-684

109. Bonuccelli, U., Piccini, P., Del Dotto, P., Pacifici, G. M., Corsini, G. U., and Muratorio, A. (1990) Platelet monoamine oxidase B activity in parkinsonian patients. *J Neurol Neurosurg Psychiatry* **53**, 854-855

110. Barbeau, A., Campanella, G., Butterworth, R. F., and Yamada, K. (1975) Uptake and efflux of 14-C-dopamine in platelets: evidence for a generalized defect in Parkinson's disease. *Neurology* **25**, 1-9

111. Sharma, P., Nag, D., Atam, V., Seth, P. K., and Khanna, V. K. (1991) Platelet aggregation in patients with Parkinson's disease. *Stroke* **22**, 1607-1608

112. Ihse, E., Rapezzi, C., Merlini, G., Benson, M. D., Ando, Y., Suhr, O. B., Ikeda, S., Lavatelli, F., Obici, L., Quarta, C. C., Leone, O., Jono, H., Ueda, M., Lorenzini, M., Liepnieks, J., Ohshima, T., Tasaki, M., Yamashita, T., and Westermark, P. (2013) Amyloid fibrils containing fragmented ATTR may be the standard fibril composition in ATTR amyloidosis. *Amyloid* **20**, 142-150

113. Saad, M., Lu, C., Koya, C., and Basak, A. (2016) Proteolytic truncation of human transthyretin linked to amyloidosis is mediated by a trypsin like enzyme: In vitro demonstration using model peptides. *Biochemical Compounds* **4**, 5

114. Westermark, P., Sletten, K., Johansson, B., and Cornwell, G. G., 3rd. (1990) Fibril in senile systemic amyloidosis is derived from normal transthyretin. *Proc Natl Acad Sci U S A* **87**, 2843-2845

115. Coelho, T., Merlini, G., Bulawa, C. E., Fleming, J. A., Judge, D. P., Kelly, J. W., Maurer, M. S., Plante-Bordeneuve, V., Labaudiniere, R., Mundayat, R., Riley, S., Lombardo, I., and Huertas, P. (2016) Mechanism of Action and Clinical Application of Tafamidis in Hereditary Transthyretin Amyloidosis. *Neurol Ther* **5**, 1-25

116. Connors, L. H., Lim, A., Prokaeva, T., Roskens, V. A., and Costello, C. E. (2003) Tabulation of human transthyretin (TTR) variants, 2003. *Amyloid* **10**, 160-184

117. Longo Alves, I., Hays, M. T., and Saraiva, M. J. (1997) Comparative stability and clearance of [Met30]transthyretin and [Met119]transthyretin. *Eur J Biochem* **249**, 662-668

118. Foss, T. R., Wiseman, R. L., and Kelly, J. W. (2005) The pathway by which the tetrameric protein transthyretin dissociates. *Biochemistry* **44**, 15525-15533

119.   Blake, C. C., Swan, I. D., Rerat, C., Berthou, J., Laurent, A., and Rerat, B. (1971) An x-ray study of the subunit structure of prealbumin. *J Mol Biol* **61**, 217-224

120.   Hamilton, J. A., and Benson, M. D. (2001) Transthyretin: a review from a structural perspective. *Cell Mol Life Sci* **58**, 1491-1521

121.   Azevedo, E. P., Ledo, J. H., Barbosa, G., Sobrinho, M., Diniz, L., Fonseca, A. C., Gomes, F., Romao, L., Lima, F. R., Palhano, F. L., Ferreira, S. T., and Foguel, D. (2013) Activated microglia mediate synapse loss and short-term memory deficits in a mouse model of transthyretin-related oculoleptomeningeal amyloidosis. *Cell Death Dis* **4**, e789

122.   Sasaki, H., Yoshioka, N., Takagi, Y., and Sakaki, Y. (1985) Structure of the chromosomal gene for human serum prealbumin. *Gene* **37**, 191-197

123.   Poulsen, K., Bahl, J. M., Tanassi, J. T., Simonsen, A. H., and Heegaard, N. H. (2012) Characterization and stability of transthyretin isoforms in cerebrospinal fluid examined by immunoprecipitation and high-resolution mass spectrometry of intact protein. *Methods* **56**, 284-292

124.   Stabilini, R., Vergani, C., Agostoni, A., and Agostoni, R. P. (1968) Influence of age and sex on prealbumin levels. *Clin Chim Acta* **20**, 358-359

125.   Martone, R. L., Herbert, J., Dwork, A., and Schon, E. A. (1988) Transthyretin is synthesized in the mammalian eye. *Biochem Biophys Res Commun* **151**, 905-912

126.   Cras-Meneur, C., Inoue, H., Zhou, Y., Ohsugi, M., Bernal-Mizrachi, E., Pape, D., Clifton, S. W., and Permutt, M. A. (2004) An expression profile of human pancreatic islet mRNAs by Serial Analysis of Gene Expression (SAGE). *Diabetologia* **47**, 284-299

127.   Larsson, M., Pettersson, T., and Carlstrom, A. (1985) Thyroid hormone binding in serum of 15 vertebrate species: isolation of thyroxine-binding globulin and prealbumin analogs. *Gen Comp Endocrinol* **58**, 360-375

128.   Ferguson, R. N., Edelhoch, H., Saroff, H. A., Robbins, J., and Cahnmann, H. J. (1975) Negative cooperativity in the binding of thyroxine to human serum prealbumin. Preparation of tritium-labeled 8-anilino-1-naphthalenesulfonic acid. *Biochemistry* **14**, 282-289

129.   Monaco, H. L. (2000) The transthyretin-retinol-binding protein complex. *Biochim Biophys Acta* **1482**, 65-72

130.   Filteau, S. M., Willumsen, J. F., Sullivan, K., Simmank, K., and Gamble, M. (2000) Use of the retinol-binding protein: transthyretin ratio for assessment of vitamin A status during the acute-phase response. *Br J Nutr* **83**, 513-520

131.   Faria, T. Q., Almeida, Z. L., Cruz, P. F., Jesus, C. S., Castanheira, P., and Brito, R. M. (2015) A look into amyloid formation by transthyretin: aggregation pathway and a novel kinetic model. *Phys Chem Chem Phys* **17**, 7255-7263

RESULTS

CHAPTER 2.1

Molecular Mapping of α-Thrombin(αT)/β2-Glycoprotein I(β2GpI) Interaction Reveals How β2GpI Affects αT Functions

Laura Acquasaliente[1], **Daniele Peterle**[1], Simone Tescari[1], Nicola Pozzi[2], Vittorio Pengo[3] and Vincenzo De Filippis[1]

[1]*Department of Pharmaceutical and Pharmacological Sciences, University of Padova, Via F. Marzolo 5, Padova, 35131, Italy*
[2]*Doisy Research Centre, Saint Louis University, St. Louis, Missouri, United States*
[3]*Department of Cardiac, Thoracic and Vascular Sciences, University of Padova, Padova, 35131, Italy*

INTRODUCTION

β2-Glycoprotein I (β2GpI) is a heavily glycosylated plasma protein (45kDa) which is synthesized in the liver (**1**) and represents the major autoantigen in the antiphospholipid syndrome (APS) (**2**), a severe thrombotic autoimmune disease characterized by arterial and venous thrombosis and recurrent fetal loss (**3**). Among the proteins of the coagulation system, the plasma concentration of β2GpI (3-7μM) is second only that of fibrinogen (7μM) and β2GpI sequence is highly conserved through the animal kingdom, from reptiles to mammals (**1**). Intriguingly, whereas the involvement of β2GpI in the pathogenesis of APS is widely accepted, the physiological role of this protein is yet to be firmly established and both pro- and anti-coagulant properties have been reported for this protein (**4**). From the structural standpoint, β2GpI is composed of five domains (D-I to D-V), arranged like beads on a string, and displays wide conformational heterogeneity (**5**). In particular, two independent X-ray diffraction analyses of β2GpI in the crystal state report an elongated J-shaped structure (**6,7**), whereas small-angle X-ray scattering in solution indicates that β2GpI predominantly assumes a S-shaped conformation (**8**). Furthermore, electron microscopy data have recently shown that β2GpI can explore either a closed/circular and an open/extended conformation (**9**). Interestingly, β2GpI exploits the highly electropositive D-V for binding to negative membrane phospholipids, heparin and cellular receptors (**1,4**).

Thrombin (αT) is a plasma serine protease with a chymotrypsin-like fold well positioned at the interface between coagulation, inflammation and cell differentiation (**10,11**). In haemostasis, αT plays either procoagulant and anticoagulant functions (**12**) and the equilibrium between these

opposite activities is regulated by interactions with other proteins (**12,13**). αT procoagulant functions mainly entail conversion of fibrinogen into fibrin and activation of platelets *via* proteolysis of type-1 protease activated receptor (PAR1), whereas the anticoagulant functions of αT are essentially related to its ability to proteolytically activate the anticoagulant protein C in the presence of thrombomodulin (TM) (**10,12**). αT functions are also regulated by sodium ion that binds to a specific site on the protease and enhances its hydrolytic efficiency mainly towards procoagulant substrates (**11,14,15**). Thrombin accomplishes most of its activities through the hydrolytic active site and two positively charged exosites (exosite-I and exosite-II) which are located at opposite sides from the catalytic cleft (**16**). Exosite-I binds physiological substrates like fibrinogen and PAR1, cofactors like TM, and non-physiological ligands/inhibitors like hirudin, hirugen and HD1 aptamer (**11,13,17**). Exosite-II is more electropositive than exosite-I and interacts with negatively charged ligands/inhibitors like heparin and heparan sulfate, the prothrombin (ProT) F2 fragment, the fibrinogen elongated γ-chain, and the platelet receptor glycoprotein Ibα (GpIbα) (**11,13,17**). In particular, GpIbα is responsible for the localization of αT on the platelets surface and orients αT for efficient PAR1 cleavage (**18**).

Very recently, we have shown that β2GpI selectively inhibits the procoagulant functions of αT, by moderately prolonging fibrin clotting time in plasma coagulation assays and by inhibiting αT-induced platelets aggregation in different experimental settings, i.e. whole blood, gel-filtered platelets, and PAR1 cleavage on platelet membranes (**19**). Notably, β2GpI did not alter the ability of αT to proteolytically convert the protein C zymogen (PC) into the active protease (aPC), in the presence or in the absence of TM. Hence, we concluded that β2GpI may function as a physiological anticoagulant by inhibiting the procoagulant properties of αT, i.e. fibrin generation and platelets activation), without affecting its unique anticoagulant activity, i.e. aPC generation (**19**).

In this context, structural information on the β2GpI-αT complex would much help to better understand the role of β2GpI in haemostasis. Unfortunately, despite our efforts during the last few years, we have failed in obtaining crystals of enough good quality for X-ray diffraction studies, likely because of the intrinsic conformational heterogeneity of β2GpI (**6-9**). Hence, in the absence of direct structural information, here we combined biochemical/biophysical and molecular modelling techniques for mapping the binding sites in αT-β2GpI complex and provide a coherent structural model which could help to rationalize at the molecular level the effect of β2GpI on αT functions.

EXPERIMENTALS

Reagents

Human plasma α-thrombin (αT) (EC-3.4.21.5) and prothrombin (ProT) were purchased from Haematologic Technologies (Essex Junction, VT, USA), while HD1 aptamer was from Primm (Milan, Italy). Hirugen and N^α-fluoresceinated hirugen ([F]-hirugen), GpIbα(268-282) peptide, β2GpI(219-232) peptide and its sequence randomized analogue R-β2GpI(219-232), and PAR1(38-60) were synthesised by the solid phase strategy on a PS3 automated synthesizer (Protein Technologies, AZ, USA) using the fluorenylmethyloxycarbonyl-chemistry (**20**), and thoroughly characterized by RP-HPLC and high-resolution mass spectrometry. Randomization of β2GpI(219-232) sequence was performed using the Mimotopes software (The Peptide Company, Victoria, Australia). Salts, solvents and reagents were of analytical grade and purchased from Sigma (St Louis, MO, USA) or Merck (Germany).

Purification and characterization of β2GpI from human plasma

Plasma samples from blood donors and non-smokers healthy subjects, with different blood groups (A^+ and 0^+), were obtained from the institutional blood bank of the University Hospital of Padua. All subjects gave their informed consent to the present study. Purification of β2GpI from human plasma was carried out following essentially the perchloric acid precipitation method, as recently modified (**19,21**). This procedure allowed us to obtain highly pure (**>98%**) preparations of β2GpI, where the major glycosylated component has a molecular mass of **45058.5±1.0a.m.u.** (**Fig. S1, Suppl. Data**).

Spectroscopic methods

Protein/peptide concentration was determined spectrophotometrically by measuring the absorbance at 280nm on a Jasco (Tokyo, Japan) V-630 double-beam spectrophotometer, using proper absorptivity values (**Suppl. Data**). All spectroscopic measurements were carried out at 25°C in 20mM HEPES, pH 7.4, 0.15M NaCl (HBS), containing additives as explicitly reported.

Dynamic light scattering (DLS)

DLS measurements were performed on a Zetasizer-Nano-S instrument (Malvern Instruments, UK). Each measurement consisted of a single run (15s). Scattering data were analyzed with the Nano-6.20 software and expressed as percentage intensity size distribution, from which the value hydrodynamic diameter (D_H) and percent polydisperisity (%Pd) were extracted. Notably, D_H is the diameter of the hard sphere that diffuses at the same speed as the molecule being measured, while

%Pd is a parameter describing the width of the particle size distribution of a protein in a given sample (**Suppl. Data**). The intensity data were then corrected for the relative abundance of each species, estimated from the volume size distribution analysis (**22**).

Fluorescence

Fluorescence binding measurements were carried out at 25°C in HBS, containing 0.1% PEG-8000, on a Jasco FP-6500 spectrofluorimeter. Aliquots of β2GpI were added to an αT solution and samples were excited at 280 or 295nm. After subtraction for the corresponding blank spectra of β2GpI, the data points were interpolated with **eq. 1** (**Suppl. Data**) to obtain the dissociation constant, K_d, of the complex. In fluorescence competition measurements, aliquots of αT S195A mutant stock solution were incrementally added to a solution of [F]-hirugen. Samples were then excited at 492nm and the decrease of fluorescence intensity of [F]-hirugen was recorded at 516nm as a function of αT concentration. The data points were interpolated with **eq. 1** (**Suppl. Data**), as described (**23**).

Surface plasmon resonance (SPR)

SPR analyses were carried out using a multi-cycle injection strategy on a dual flowcell Biacore-X100 instrument (GE-Healthcare). Each binding curve was subtracted for the corresponding baseline, accounting for nonspecific binding (<2% of RU_{max}), and the data were analyzed using the BIAevaluation software. β2GpI was immobilized (1000-5000 RU) on a carboxymethylated-dextran chip (CM5) and increasing concentrations of αT solutions were injected in the mobile phase. In the affinity mode, K_d of αT-β2GpI complex was obtained by plotting the value of RU_{max}, measured at the steady state, as a function of [αT] and fitting the data points to **eq. 2**, describing a 1:1 binding model (**Suppl. Data**). Measurements were also performed by reversing the interacting system, i.e. by immobilizing αT on the sensor chip (500 RU) and injecting β2GpI solutions in the mobile phase (**23**) (**Fig. S2, Suppl. Data**). To study fibrinogen-β2GpI interaction, fibrinogen-bound CM5 sensor chip was challenged with incremental concentrations of β2GpI and the data points were interpolated with **eq. 2**. SPR measurements were carried out in HBS, containing 3mM EDTA, 0.05% polyoxyethylene sorbitan (HBS-EP$^+$).

Preparation of β2GpI and αT derivatives

Fully deglycosylated β2GpI was prepared by treating plasma purified β2GpI (0.5mg/ml) with peptide-*N*-glycosidase F (PNGase-F) (Roche, Germany) at an enzyme:substrate ratio of 1:50(w/w) in 0.1M NH_4HCO_3, pH 7.9, 0.1%(v/v) Rapigest (Waters, MO, USA) for 24 h at 37°C. The reaction was quenched with 4% aqueous TFA and analysed by RP-HPLC, SDS-PAGE (4-12% acrylamide), after

Coomassie- and fuxin-based staining, and high-resolution mass spectrometry (HR-MS) on a Xevo G2-S Q-TOF instrument (Waters) (**Fig. S3_A, Suppl. Data**). Nicked β2GpI (β2GpI*) was prepared by treating purified β2GpI (22μM, 0.5ml) for 2h at 37°C with human plasmin at an enzyme:substrate ratio of 1:50 (w/w) in 20mM Tris-HCl, pH 7.5, containing 150mM NaCl, 0.3mM CaCl$_2$. β2GpI* was purified by heparin-sepharose affinity chromatography and further dialyzed to eliminate excess salt. The purity and chemical identity of β2GpI* was established by SDS-PAGE, RP-HPLC and HR-MS under reducing and nonreducing conditions, yielding mass values fully consistent with the hydrolysis of the single peptide bond K317-T318 in β2GpI domain V (**Fig. S4_A, Suppl. Data**).

Recombinant wild-type human α-thrombin (rαT), prethrombin-2 (rPre2) and the inactive thrombin S195A mutant (rS195A) were expressed in *E. coli*, as detailed elsewhere (**19,24**), whereas Ala-mutants at αT exosites were expressed in HEK293 human kidney cells and purified as described (**25**) (**Fig. S5, Suppl. Data**). β$_T$-Thrombin (β$_T$T) was prepared by proteolysis of mature αT (7μM) with trypsin (35nM) (EC-3.4.21.4, Promega Biosciences, CA, USA) for 3h at 37 °C (**26**). To avoid (auto)proteolytic degradation of β$_T$T, a 10-fold molar excess of PPACK and tosyl-lysyl chloromethyl ketone was added to selectively inhibit αT and trypsin, respectively. The chemical identity and purity (>85%) of the final β$_T$T preparation were carefully established by RP-HPLC, SDS-PAGE, and high-resolution MS (**Fig. S6, Suppl. Data**).

Kinetics of substrate hydrolysis by αT

Chromogenic substrate S2238

αT-catalyzed hydrolysis of the chromogenic substrate S2238 (D-Phe-Pip-Arg-pNA) (Chromogenix, Sweden) was monitored at 25°C by measuring the release of pNA at 405nm on a Victor-3 microplate reader (Perkin-Elmer, CA, USA). The initial velocity of pNA release was plotted against substrate concentration and interpolated with the Michaelis-Menten equation to yield the values of k$_{cat}$ and K$_m$ as fitting parameters (**15**).

Fibrinogen

The specificity constants, k$_{catA}$/K$_{mA}$ and k$_{catB}$/K$_{mB}$, relative to the release of fibrinopeptides A (FpA) and B (FpB) from fibrinogen by αT were determined by carefully following the method of Shafer and co-workers (**27**). Briefly, desalted human fibrinogen, Fb, (Sigma) (0.35μM) in HBS, containing 0.1% PEG-8000, was reacted at 37°C with human αT (300pM). At fixed time intervals, acid-quenched aliquots were centrifuged to eliminate fibrin and uncleaved fibrinogen. The supernatant was lyophilized, dissolved in guanidinium hydrochloride (6M), and analyzed by RP-HPLC to quantify FpA and FpB release. From the plot of FpA or FpB concentration *vs.* time, the

values of the corresponding specificity constants were determined as fitting parameters by interpolating the data points with **eq. 6** and **7**, respectively (**Suppl. Data**).

PAR1(38-60)

The specificity constant, k_{cat}/K_m, relative to the hydrolysis of the synthetic peptide PAR1(38-60) was determined as previously detailed (**28**). Briefly, PAR1(38-60) in HBS, containing 0.1% PEG-8000, was reacted at 25°C with human αT (100 pM). At fixed time intervals, acid-quenched aliquots were analyzed by RP-HPLC to quantify the time-course release of PAR1(42-60) fragment. From kinetic data, the values of the corresponding specificity constant for αT cleavage was determined as a fitting parameter by interpolating the data points with **eq. 8** (**Suppl. Data**).

Computational methods

Protein structures were visualized with the ViewerPro 4.2 software (Accelerys Inc., USA). Electrostatic potential calculations were carried out using APBS (**29**) and BLUUES (**30**) program. Calculations were performed using a solvent dielectric of 78.14 and a protein dielectric of 2.0 at 298K in 145mM NaCl. Final electrostatic maps were constructed by subtracting the protein self-energies from the calculated map using the dxmath utility in APBS. Electrostatic calculations and docking simulations did not take into account the contribution of glycan chains. Docking of αT into β2GpI structure was performed using the ClusPro-2.0 software (https://cluspro.bu.edu/login.php) (**31**), starting from the structure of β2GpI (1c1z) (**6**) and (D)-phenylalanyl-prolyl-arginyl chloromethyl ketone(PPACK)-inhibited thrombin (1ppb) (**16**), after removing the inhibitor coordinates. The "van der Waals+electrostatics" option was used for docking simulations.

Turbidimetric measurements

Human fibrinogen (Sigma, cat. F4129) was desalted on an in-house packed Sephadex G10 column (0.8x15cm), eluted (0.3ml/min) with HBS, 0.1% PEG-8000. Fibrin generation was started by adding human αT to a solution of freshly desalted fibrinogen. The time course of clot formation was followed by continuously recording at 37°C, on a Jasco V-630 spectrophotometer, the turbidity of the solution, expressed as the intensity decrease of transmitted light (or the absorbance increase) at 350nm, due to scattering of fibrin fibers (**32**). The clotting curves were analyzed to extract the values of A_{max} and t_c, where A_{max} is the maximum absorbance value obtained when fibrin generation is complete, and t_c is the clotting time determined as the intercept with the *time* axis of the tangent line to the flex point of the clotting curve.

The plasmid containing the cDNA of prethrombin-2 (Pre2) was a generous gift of Prof.

Huntington (Cambridge University). The recombinant inactive mutant rS195A, obtained by single-point mutagenesis, was expressed in *E. coli*, subjected to *in vitro* disulphide oxidative refolding, activation by ecarin, and characterized as previously detailed (**44,45**). $β_T$-thrombin ($β_T$T) was obtained by proteolysis of human αT (7μM) with bovine pancreas trypsin (35nM) for 3 hours at 37°C in HBS, and characterized as previously detailed (**46,43**). The concentrations of thrombin solutions were determined by measuring the absorbance at 280nm, using an absorptivity coefficient of 66390 $M^{-1} \cdot cm^{-1}$. For the concentration of ProT solutions, the absorptivity coefficient of 109790$M^{-1} \cdot cm^{-1}$ was used.

RESULTS AND DISCUSSION

Probing β2GpI-αT interaction

Dynamic light scattering (DLS)

A first qualitative indication of αT-β2GpI interaction was obtained by DLS analysis, carried out in triplicate in two different sets of experiments (**Fig. 1A**). The hydrodynamic diameter (D_H) of αT was reproducibly measured as **6.50±1.20nm**, with a percent polydispersity (%Pd) of **18.6**, indicating that αT preparation was approximately monodisperse (**22**). Purified β2GpI displayed a D_H value of **8.72±2.42nm** with a higher %Pd (**25.0**), consistent with the extensive glycosylation (**1**) and high conformational heterogeneity of β2GpI elongated structure (**6-9**).

When αT and β2GpI were mixed at equimolar concentration (18μM), a slightly smaller D_H of **7.52±1.56nm** was reproducibly measured, with an even lower **%Pd** (**19.3**), compared to that of β2GpI alone (**25.0**). Notably, a mixture of *noninteracting proteins* of different size and polydispersity should yield a %Pd value much greater than that of the more polydispersed protein alone (**22**). Therefore, the results of DLS analysis are consistent with a picture of αT-β2GpI interaction whereby αT binds to β2GpI and reduces the size and conformational heterogeneity of the protein by forming a complex in which β2GpI becomes more ordered around αT. This interpretation is consistent with DLS analysis of peptide binding to calmodulin (CaM), where peptide-CaM interaction reduced both the D_H value and %Pd of the protein (**33**).

Fluorescence spectroscopy

A more quantitative estimate of αT-β2GpI interaction was obtained by measuring the decrease of αT fluorescence intensity at 330nm after addition of incremental concentrations of β2GpI (**Fig. 1B**). At saturating β2GpI concentrations (300nM), a **~12%** decrease of fluorescence was reproducibly measured and interpolation of the data points with **eq. 1** (**Suppl. Data**), describing 1:1 tight binding, yielded a K_d of **50±8nM**. The fluorescence change associated with αT-β2GpI coupling is likely

caused by alterations in the environment of Trp-residues, occurring mainly in αT where six of the nine Trp-residues present in the enzyme structure are moderately or highly solvent exposed and therefore amenable to interact with β2GpI. At variance, Trp-residues in β2GpI are shielded from the solvent (apart from Trp316 in domain V) and their fluorescence is strongly quenched (**Fig. 1B, Inset**) by stacking interactions onto internal disulfide bridges (**6,7,34**).
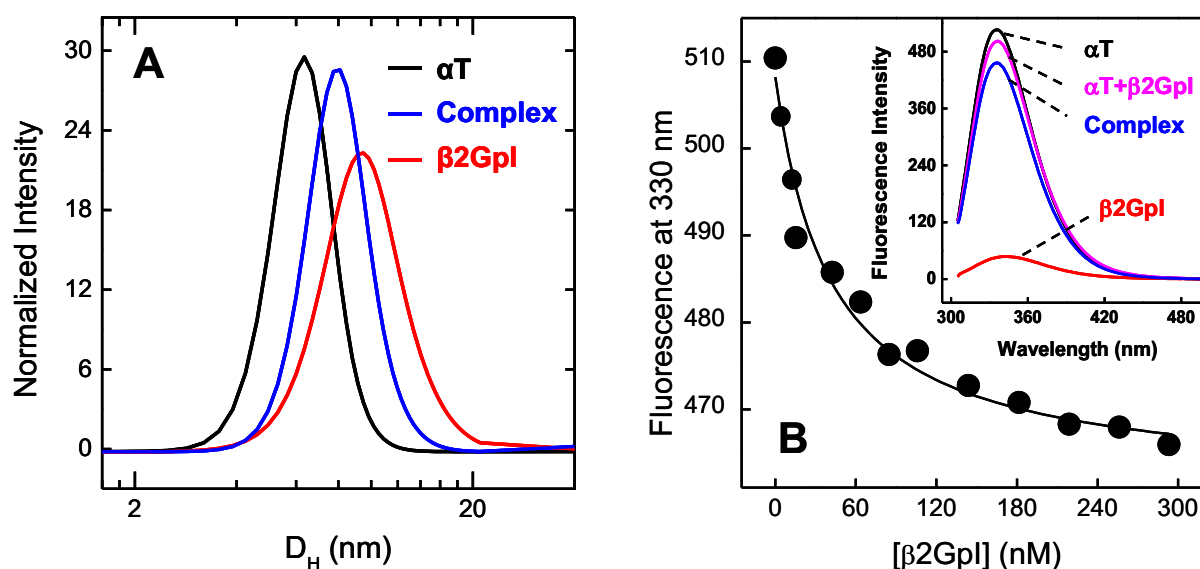

Figure 1. Probing β2GpI-αT interaction by dynamic light scattering (A) and fluorescence spectroscopy (B). (**A**) DLS analysis of 4μM β2GpI (—) and αT (—) alone or in equimolar mixture (—). Measurements were conducted equilibrating samples for 40min at 25°C in HBS, pH 7.4. (**B**) To a solution of αT (60nM) in HBS were added aliquots (2-10μl) of a β2GpI stock solution (11μM). The samples were excited at 295nm and emission intensity was recorded at 330 nm. After subtracting the fluorescence of β2GpI alone, the data points were interpolated with **eq. 1** (**Suppl. Data**) and a K_d = **50±8nM** was estimated. (**Inset**) Fluorescence spectra of αT (60nM, —) and β2GpI (300nM, —) in the isolated and mixed form (—). The theoretical sum-spectrum is also reported (—). At each β2GpI concentration, the fluorescence of αT-β2GpI mixture was subtracted for the contribution of β2GpI alone at the same concentration to yield the fluorescence change associated with the formation of the Complex.

Surface plasmon resonance (SPR)

SPR measurements were performed by immobilizing either β2GpI or αT on the sensor chip (**Fig. 2**), as detailed in the **Suppl. Data**. In the first set of experiments, β2GpI was covalently immobilized on a CM5 chip, *via* the amine coupling chemistry, and then incremental concentrations of αT were injected in the mobile phase (**Fig. 2A,B**). As described in the **Suppl. Data** (**Fig. S7**), it is expected that most of β2GpI molecules are anchored onto the sensor chip through the lower face of domain V, containing >3-fold higher percentage of reactive Lys-residues, compared to the rest of the protein (**1**). SPR data were analyzed according to the one-site binding model (**eq. 2, Suppl. Data**),

yielding a **K$_d$ = 43±5nM**, identical to that estimated by fluorescence measurements in solution. In the second set of experiments, the interacting system was reversed, i.e. αT was covalently reacted at the active site with the bivalent reagent biotinyl-PPACK and anchored to a NeutrAvidin-coated C1 chip through the biotin-avidin capture strategy, as recently described (**23**) (**Fig. 2C,D**). Incremental concentrations of β2GpI were then injected in the mobile phase and, after data fitting as above, only a slightly higher **K$_d$ of 100±8nM** was determined. The results of DLS, fluorescence and SPR analyses concurrently indicate that β2GpI in solution exists in a conformation fully competent for binding to αT.
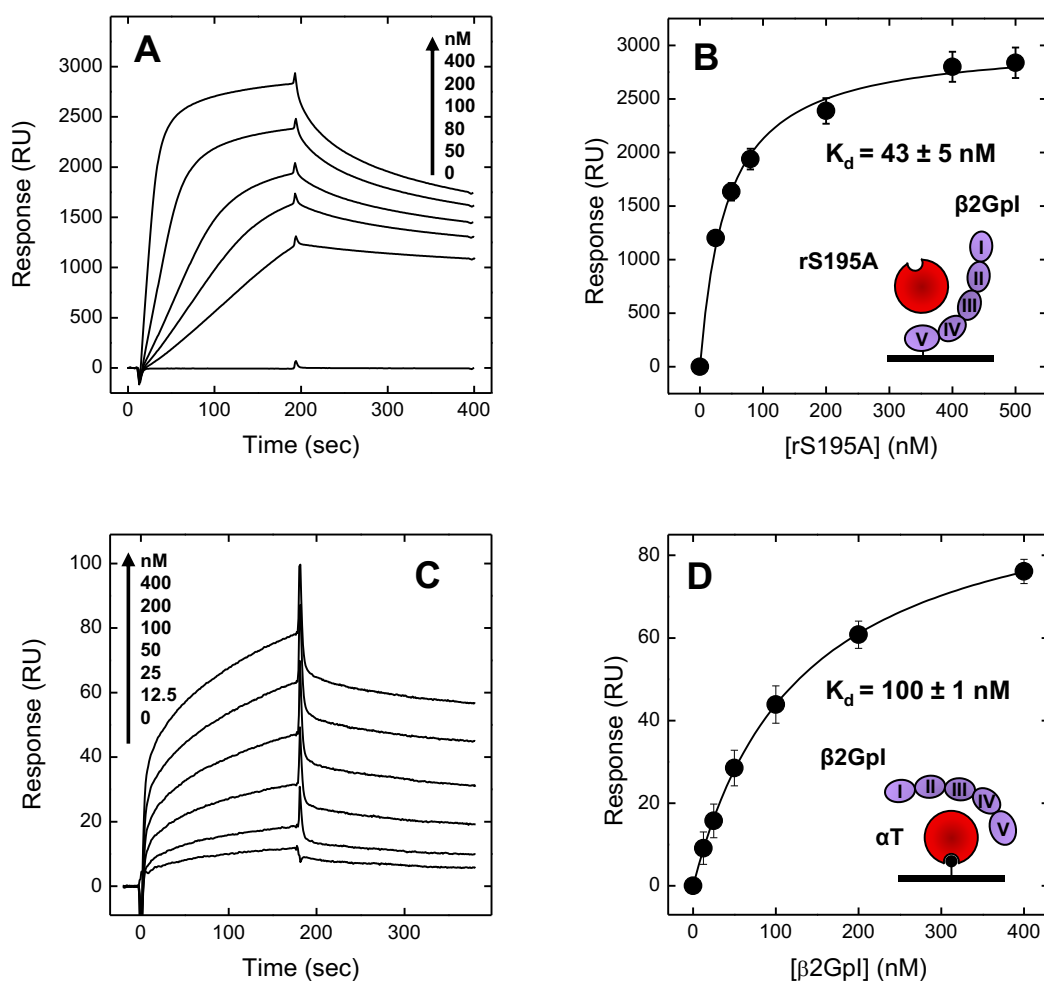
Figure 2. Probing β2GpI-αT interaction by surface plasmon resonance (**A, B**). Binding of rS195A to β2GpI immobilized on a CM5 sensor chip. (**A**) Sensograms relative to rS195A binding. (**B**) Plot of RU$_{max}$ *versus* rS195A concentration (●). Fitting of data points with **eq. 2** (**Suppl. Data**) yielded a K$_d$ value of **43±4nM**. (**C, D**) Binding of β2GpI to αT, immobilized on a NeutrAvidin-coated CM1 sensor chip (**see Methods**). (**C**) Sensograms relative to β2GpI binding. (**D**) Plot of RU$_{max}$ *versus* β2GpI concentration (●). Fitting of data points with **eq. 2** (**Suppl. Data**) yielded a K$_d$ of **100±4nM**. All measurements were carried out at 25°C in HBS-EP$^+$, pH 7.5. Each data point represents the average of three different runs performed on different plasma samples. The standard deviations are shown as error bars.

The role of ionic interactions and the effect of salt type in β2GpI-αT binding

The role of ionic interaction in αT-β2GpI complex formation was probed by measuring the affinity of αT for β2GpI at increasing NaCl concentrations. The Debye-Hückel theory indeed predicts that if the binding of two interacting proteins is driven by ionic interactions then increasing salt concentrations should weaken the affinity through unspecific screening of charges on the interacting protein surfaces (**35**). SPR data in **Fig. 3A** indicate that this is actually the case, as the affinity of the inactive S195A mutant thrombin for immobilized β2GpI decreased by **32-fold** going from 50 to 400mM NaCl. Notably, the S195A mutant can be considered as a pseudo-wild type enzyme. Indeed, this mutant is inactive due to the replacement of the catalytic Ser195 with Ala, but it retains the molecular recognition properties of natural αT (**19,24**). A more quantitative estimate of the contribution of ionic interactions was obtained as reported by Bode and co-workers for studying the salt-dependent interaction of αT with the bivalent inhibitor haemadin (**36**). The standard free energy change of binding, $\Delta G°_b = RT \cdot \ln K_d$, was partitioned into an ionic ($\Delta G°_I$) and a non-ionic component ($\Delta G°_\Phi$), as follows: $\Delta G°_b = \Delta G°_I + \Delta G°_\Phi$ (**36**). The values of $\Delta G°_b$, obtained from experimental dissociation constant values (K_d), were plotted against the square root of the ionic strength (I) (**Fig. 3B**) and the data points interpolated with **eq. 3** (**Suppl. Data**), yielding $\Delta G°_\Phi$ = **-8.2±0.1**kcal/mol and $\Delta G°_{I°}$ = **-7.3±0.9**kcal/mol. In this analysis, $\Delta G°_\Phi$ is the value of $\Delta G°_b$ extrapolated at I→∞ and $\Delta G°_{I°}$ is the value of $\Delta G°_I$ extrapolated at I→0. These data suggest that ionic interactions make up to **47%** of the total binding energy at zero ionic strength (**$\Delta G°_b$ = -15.5kcal/mol**), thus confirming the importance of charged interactions in αT-β2GpI binding. The effect of salt was further quantified according to the counter-ion condensation (CC) theory of protein-polyelectrolyte interaction, following the method that Olson and co-workers used for studying αT binding to heparin (**37**) (**Fig. 3C**). According to the CC theory, the binding of a positively charged protein to a negative polyelectrolyte, in the presence of NaCl, can be regarded as an ion exchange-like process, whereby protein binding is driven by the entropically favorable release of cations (i.e. Na^+) bound to the polyelectrolyte, whereas the displacement of anions (i.e. Cl^-) from the positive protein only marginally contributes. The values of $\log K_d$ are plotted *versus* $\log[Na^+]$ and the data points interpolated with the linear equation $\log K_d = A_0 + \Gamma_{salt} \cdot \log[Na^+]$, where A_0 is the value of $\log K_d$ extrapolated at $\log[NaCl] = 0$ and Γ_{salt} is the slope of the straight line. Notably, A_0 represents the non-ionic contribution to binding, as it is calculated at 1M NaCl, where the contribution of ionic interactions to the binding energy is virtually zero due to charge-screening effects. On the other hand, Γ_{salt} represents a thermodynamic measure of the effect of salt concentration on binding equilibria. Assuming that this effect is solely due to ionic interactions, then Γ_{salt} gives the number of Na^+-ions released upon protein-protein interaction and can be expressed as $\Gamma_{salt} = Z \cdot \psi$, where Z is the number

of ionic interactions involved in binding while ψ is the fraction of a cation bound to the polyelectrolyte per unit charge and depends on the charge density of the polyelectrolyte (ψ = 0.8 for heparin). From the parameters of the straight line in **Fig. 3C**, it was possible to estimate the non-ionic contribution to the binding energy of αT-β2GpI interaction as **ΔG°Φ = -7.5kcal/mol**, comparable to that determined by the Debye-Hückel theory and infer that **2** intermolecular salt bridges can be formed in the αT-β2GpI complex. The latter value is close to that determined by Beglova and co-corkers for the binding of the recombinant β2GpI domain V to the heparin-derived pentasaccharide fondaparinux (Z = 2.5) (**38**).
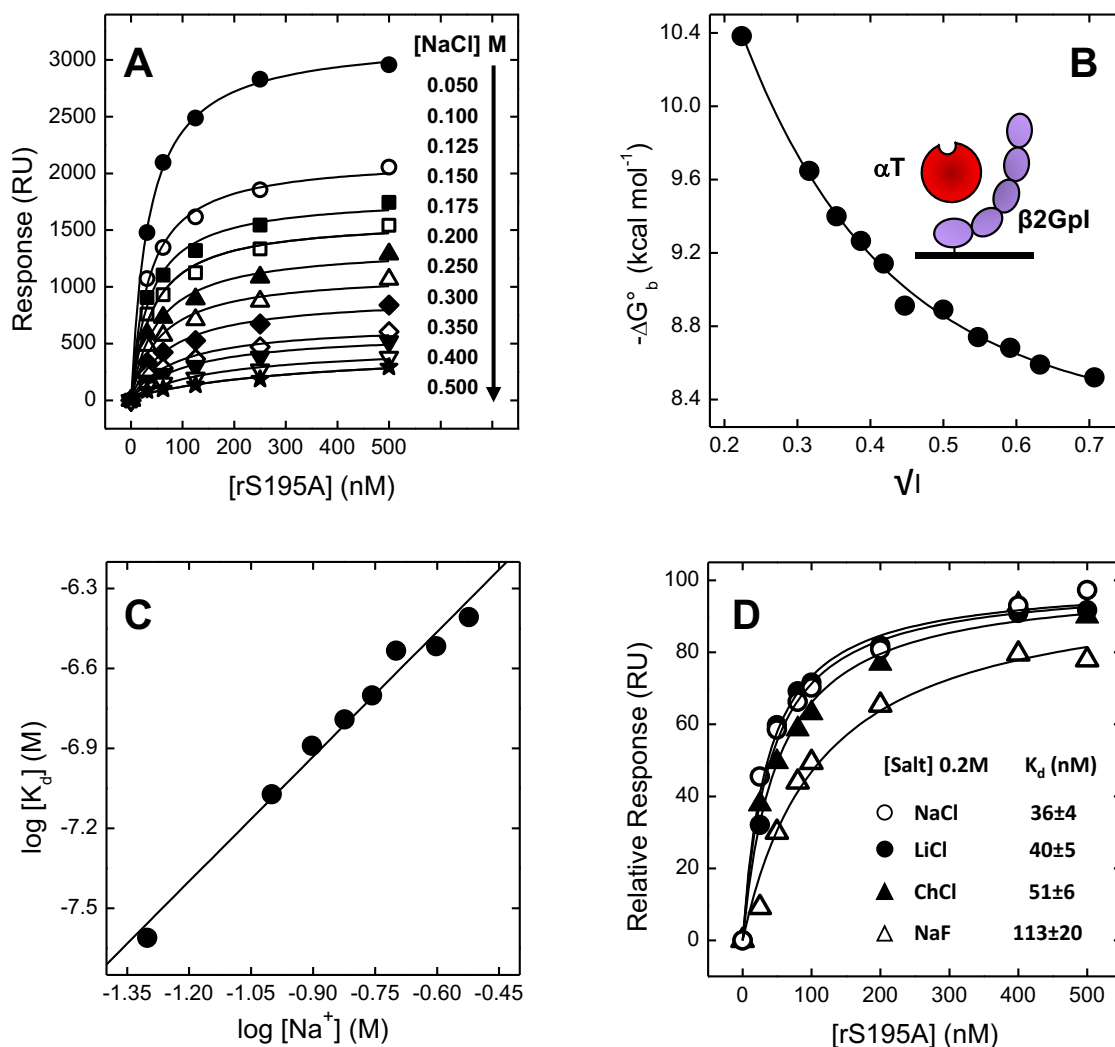

Figure 3. Effect of ionic strength and salt type on β2GpI-αT interaction. (**A**) SPR analysis of the effect of increasing NaCl concentration on the binding of rS195A to immobilized β2GpI. The binding data were interpolated with **eq. 2** (**Suppl. Data**) to estimate the K_d value at each [NaCl]. (**B**) Plot of the binding energies ($\Delta G°_b$) of rS195A-β2GpI interaction against the square root of the ionic strength, √I. $\Delta G°_b$ values were calculated from the K_d values determined in **panel A**: $\Delta G°_b = RT \cdot \ln K_d$. The data points (●) were interpolated with **eq. 3** (**Suppl. Data**), with best-fit parameters: $\Delta G°_\Phi = $ **-8.2±0.1**kcal/mol, $\Delta G°_{I°} = $ **-7.3±0.9**kcal/mol, and α = **3.1±0.4**. (**C**) Salt dependence of the affinity of αT for β2GpI, as determined by SPR measurements. The data points were fitted to the equation logK_d

= A_0 + $\Gamma_{salt} \cdot \log[Na^+]$, with best-fit parameters A_0 = **-5.53M** and Γ_{salt} = **1.6±0.2**. (**D**) Effect of the salt type on the affinity of rS195A for immobilized β2GpI. Measurements were carried out at constant concentration (i.e. 0.2M) of different salts. After data fitting with **eq. 2**, the reported K_d values were obtained. All measurements were carried out at 25°C in HBS-EP$^+$, pH 7.5.

αT is a sodium-activated enzyme, whereby Na$^+$ binds to a specific site (K_d=18mM at 25°C) and induces structural changes in αT (**15,39**), which more efficiently cleaves procoagulant substrates, like fibrinogen and PAR1, than the anticoagulant substrate PC zymogen (**12**). The possible role of salt type was investigated by measuring the affinity of rS195A for immobilized β2GpI at constant ionic strength (0.2M) in the presence of salts (i.e. ChCl, NaCl, LiCl and NaF) having different cation (Ch$^+$>>Na$^+$>Li$^+$) and anion (Cl$^-$>F$^-$) size. SPR data in **Fig. 3D** indicate that with ChCl and LiCl the affinity remained essentially constant (within the error of the SPR technique) compared to NaCl, and was only slightly reduced with NaF, thus arguing against a specific contribution of cation/anion effect in αT-β2GpI interaction.

The role of glycosylation in β2GpI-αT interaction

Both αT and β2GpI are N-glycosylated proteins, with the carbohydrate chain moiety contributing for approximately 7 and 20% of the total protein weight, respectively (**1,16**). To study the role of glycosylation in αT-β2GpI interaction, the corresponding deglycosylated proteins were produced and their affinities measured by SPR (**Fig. 4**). Deglycosylated β2GpI (d-β2GpI) was obtained in high yields (>85%) by treating plasma purified β2GpI with PNGase-F glycosidase (**Fig. S3_A**). For αT, the deglycosylated form (d-αT) was obtained as the expression product of human αT cDNA in *E. coli*, after disulfide oxidative refolding and ecarin activation (**Fig. S3_B**) (**19,24**) SPR data indicate that deglycosylation of β2GpI only marginally (i.e. <2-fold) reduced the affinity of the protein for immobilized natural αT (**Fig. 4A**) Likewise, deglycosylation of αT did not alter the affinity for the immobilized natural β2GpI (**Fig. 4B**). These findings provide evidence that (de)glycosylation does not significantly influence β2GpI-αT interaction.
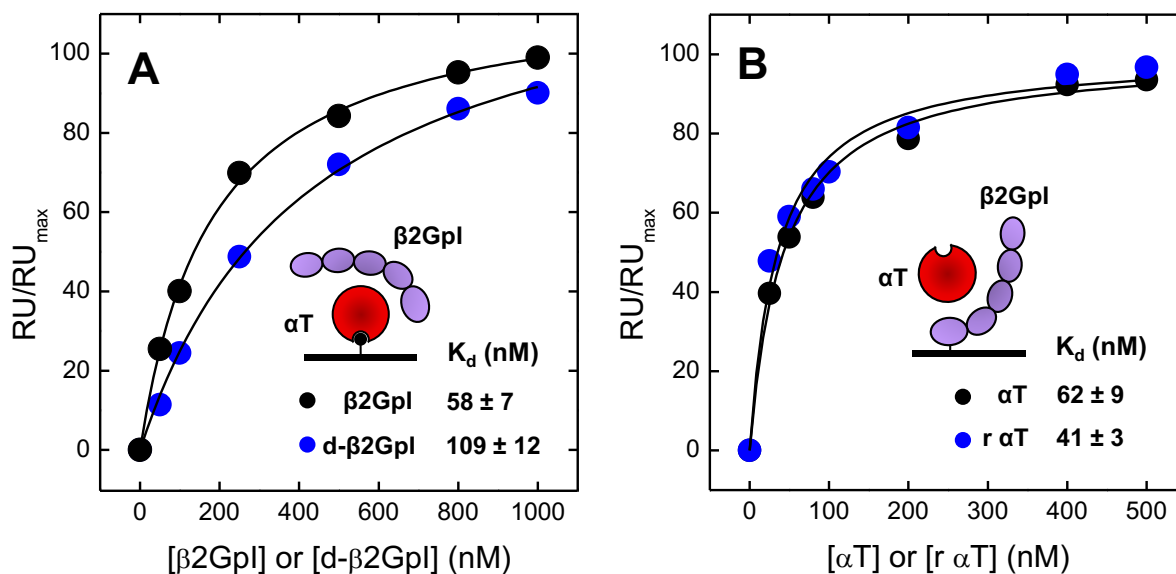
Figure 4. Effect of glycosylation on β2GpI-αT interaction. (**A**) Effect of deglycosylation of β2GpI. SPR analysis of the binding of β2GpI (●) and d-β2GpI (●) to immobilized natural/glycosylated αT. (**B**) Effect of deglycosylation of -T. SPR analysis of the binding of αT (●) and r-αT (●) to immobilized natural/glycosylated β2GpI. All measurements were carried out at 25°C in HBS-EP⁺, pH 8.0. K_d values were obtained by fitting the data points with **eq. 2** (**Suppl. Data**).

Mapping of the binding sites on αT

The role of αT active site and recognition exosites in β2GpI binding was assessed by measuring the effect of β2GpI on the efficiency of substrate hydrolysis by αT or by selectively introducing incremental structural perturbations at a given site of the protease and then measuring the affinity change of the perturbed αT species for β2GpI. A strong decrease in affinity was taken as an indication that the perturbed site was relevant for the interaction of αT with β2GpI.

Active site

The involvement of αT active site was directly probed by measuring the efficiency of hydrolysis of the specific chromogenic substrate S2238 in the presence or absence of β2GpI (4μM). The data shown in **Fig. 5A** indicate that β2GpI did not alter the kinetic constants, K_m and k_{cat}, for substrate hydrolysis. These results provide straight evidence that β2GpI did not affect the accessibility nor the efficiency of αT catalytic machinery and strongly suggest that the protease active site is not involved in binding to β2GpI. The role of αT active site in β2GpI interaction was further probed by SPR, challenging a β2GpI-loaded sensor chip with PPACK-inhibited αT (αT-PPACK) or with the recombinant prethrombin-2 zymogen (Pre2). Notably, PPACK covalently reacts with Ser195 and His57 in the catalytic pocket and extensively penetrates in the S1, S2, and S3 substrate binding sites (**16**). On the other hand, Pre2 structure shows major perturbations in the Na⁺-binding site and

activation domain, leading to disruption of the catalytic site which becomes also occluded by the partial collapse of the surrounding insertion loops, whereas the exosites remain functional (**40**). SPR data (**Fig. 5B**) show that both αT-PPACK and Pre2 retain the affinity of native αT for immobilized β2GpI, thus indicating that neither the occupancy of αT catalytic cleft nor disruption of protease active site do not compromise binding to β2GpI.

Exosites

Binding of thrombin Ala-mutants to β2GpI

Twelve single Ala-mutants of αT were produced in HEK293 human kidney cells and purified to homogeneity (**25**) (**Fig. S5A, Suppl. Data**), while their affinity for immobilized β2GpI was determined by SPR. Our data indicate that Ala-shaving of hydrophobic (Phe/Leu) or charged (Arg/Lys) amino acids at exosite-I only slightly altered, either positively or negatively, the K_d for the binding to β2GpI (<1.5-fold) (**Fig. S5B, Suppl. Data**). Similar results were obtained with Arg/Lys→Ala mutants at exosite-II and the only substitution that caused a significant change in the affinity was D178A, which rather surprisingly enhanced by ~4-fold the affinity of αT for β2GpI compared to the natural enzyme (**Fig. S5B, Suppl. Data**). For a correct interpretation of these data, it should be considered that the net effect of a charged-to-neutral amino acid exchange on ligand-protein interaction is the result of compensatory (often opposing) effects that the mutation has on the ligand binding energetics, but also on the local protein environment at the mutation site (**41**). These effects are difficult to predict and can be rationalized only when a reliable model of the ligand-protein complex is available. The poor sensitivity of αT-β2GpI binding to Ala-mutations, however, does not rule out the possibility that αT exosites are involved in β2GpI binding. Instead, these data suggest that the perturbation introduced by single-charge ablation might be too small to cause large affinity loss, as already observed in other thrombin interacting systems, where multiple Arg/Lys→Ala or even charge-reversal mutations (Arg/Lys→Asp/Glu) are needed to elicit significant changes in affinity (**36,42,43**). Electrostatic potential calculations, indeed, show that this is actually the case, as the estimated change of surface potential after mutation is small, on average **6.9±2.8%** for exosite-I and **6.3±2.6%** for exosite-II (**Fig. S5C, Suppl. Data**).
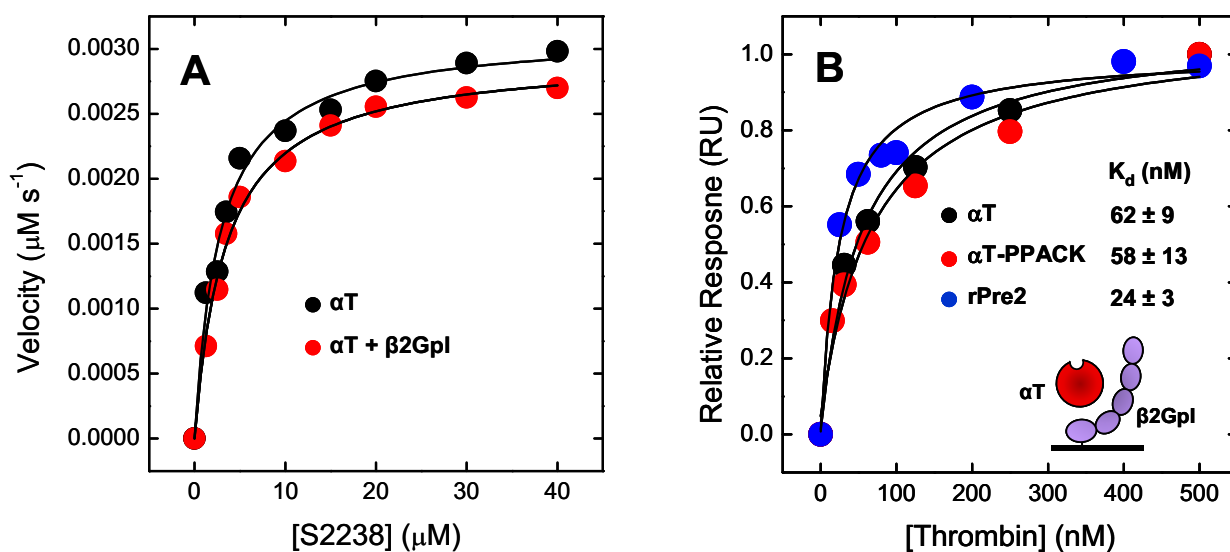
Figure 5. The role of αT active site in β2GpI-αT interaction. (**A**) Effect of β2GpI on the hydrolytic activity of αT. The initial rate of pNA release from S2238 by αT (50pM) was measured at 405nm in HBS, 0.1% PEG at 25°C in the absence (●) or in the presence (●) of 4μM β2GpI. The data points were interpolated with the Michaelis-Menten equation, with best-fit parameters: - β2GpI, k_{cat} = **62±5s⁻¹, K_m = 2.8±0.3μM, k_{cat}/K_m = 22.4 μM⁻¹·s⁻¹**; +β2GpI, **k_{cat} = 60±4s⁻¹, K_m = 3.4±0.3μM, k_{cat}/K_m = 21.5μM⁻¹·s⁻¹**. (**B**) Effect of active-site occupation/perturbation on αT thrombin binding to β2GpI. SPR analyses of the binding of natural αT (●), PPACK-inhibited αT (●) and recombinant Pre2 zymogen (●). All measurements were carried out at 25°C in HBS-EP⁺, pH 8.0. The data points were interpolated with **eq. 2** (**Suppl. Data**), yielding the corresponding K_d values, as reported.

Effect of exosite-specific ligands on aT-β2GpI interaction

Given the relative insensitivity of exosite electrostatics to point-mutations, we decided to more strongly perturb αT through the binding of negatively charged ligands that electrostatically couple with and cover a much larger area on the enzyme surface. Hence we devised a SPR competition experiment (**Fig. 6**) where S195A (250nM) was incubated with increasing concentrations of a given exosite-specific ligand and then injected over the β2GpI-sensor chip. The C-terminal peptide segment 268-282 of the αT platelet receptor, GpIbα, was used as a specific exosite-II ligand (**K_d=3μM**) (**43,44**), while hirugen (**K_d=1μM**) and HD1 aptamer (**K_d=0.5μM**) were used as exosite-I binders (**17**). Notably, GpIbα(268-282) reduced up 70%, in a dose-dependent manner, the RU$_{max}$ of αT binding to β2GpI (**Fig. 6A,B**). This effect was taken as an indication that the peptide in solution can compete with immobilized β2GpI for interacting with αT and that the protease exosite-II is involved in binding to β2GpI. Intriguingly, addition of incremental concentrations of exosite-I specific ligands, i.e. hirugen and HD1, also significantly reduced the RU$_{max}$ of αT binding to immobilized β2GpI (**Fig. 6B**). The data were analyzed using the SPR competition model recently reported by Gamsjaeger and co-workers (**45**), describing the competition of two ligands (one of which is immobilized on the

sensor chip) for the same receptor in the mobile phase. Interpolation of the data points with **eqs. 4 and 5** (**Suppl. Data**) yielded values of $K_d^{\alpha T}$ (i.e. the K_d for the binding of αT to chip-bound β2GpI) and K_d^L (i.e. the K_d for the binding of αT to an exosite-specific ligand in the mobile phase) that were comparable to those estimated by direct binding measurements, thus supporting the validity of the competition model used.

At a first glance, these findings would suggest that, besides exosite-II, also exosite-I participates in β2GpI interaction. Nevertheless, our data can be also explained by the negative allosteric linkage existing between αT exosites, whereby the binding of a ligand at exosite-I can perturb long range exosite-II structure and decrease the affinity of that site for a specific ligand and *vice versa* (**46-48**). Hence, the decrease of SPR signal measured with hirugen or HD1 does not imply a direct involvement of exosite-I in β2GpI interaction and might be caused by an indirect effect that the binding of these ligands at exosite-I have on the affinity of exosite-II for β2GpI. Clearly, this further complicates a straightforward interpretation of the data reported in **Fig. 6B** and prompted us to device alternative strategies for more precisely addressing the role of αT exosites.
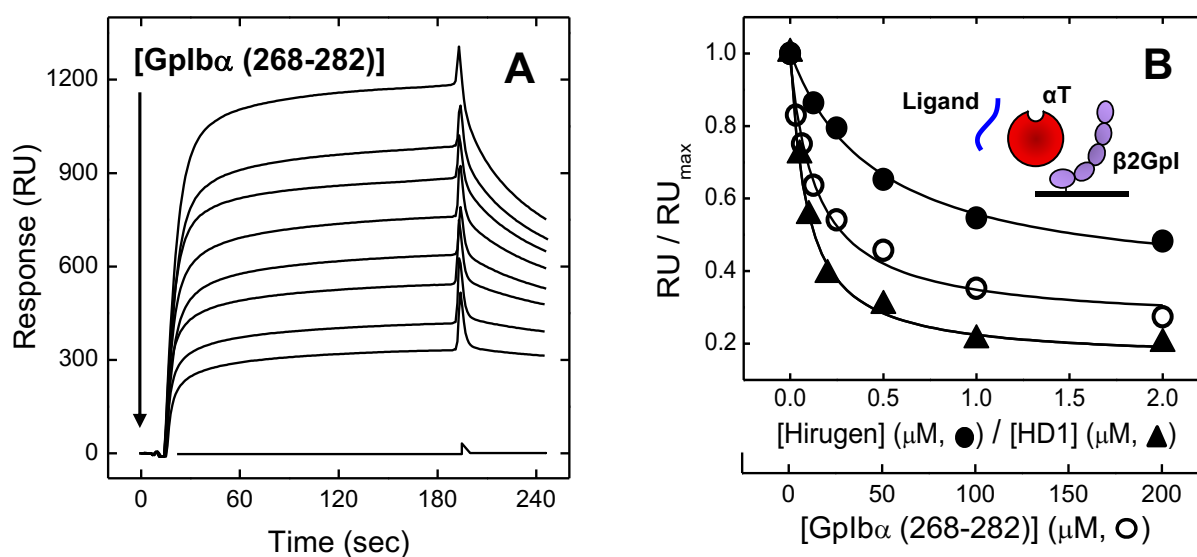

Figure 6. Effect of exosite occupation on the affinity of αT for β2GpI. (A) Sensograms relative to the binding of rS195A (250nM) to immobilized β2GpI in the presence of increasing concentrations of the exosite II-specific ligand GpIbα(268-282). **(B)** Plot of RU/RU_{max} values at increasing concentrations of Hirugen (●), GpIbα(268-282) (○), and HD1 aptamer (▲). The data points were interpolated with **eq. 4** (**Suppl. Data**), describing the competition of two ligands for the same receptor site. The following best-fit parameters were obtained: **Hirugen, $K_d^{\alpha T}$ = 15±3nM and K_d^L = 1.5±0.4μM; HD1, $K_d^{\alpha T}$ = 11±2nM and K_d^L = 170±10μM; GpIbα(268-282), $K_d^{\alpha T}$ = 12±3nM and K_d^L = 0.5±0.1μM**, where $K_d^{\alpha T}$ is the K_d for the binding of αT to the immobilized β2GpI, while K_d^L is the K_d for the binding of αT to the ligand peptide (L) in the mobile phase. All measurements were carried out at 25°C in HBS-EP+, pH 7.4.

Displacement of fluoresceine-labelled hirugen ([F]-hirugen) from αT exosite-I

To reduce the ambiguity in interpreting the effect of exosite-I blockage in β2GpI binding, the ability of β2GpI to displace [F]-hirugen from αT exosite-I was investigated (**Fig. 7**). In the first step, [F]-hirugen was titrated with S195A, and a K_d of **30±8nM** was estimated, consistent with previous work (**17,23,46**). In the second step, increasing concentrations of β2GpI were added to the solution of S195A, previously saturated with [F]-hirugen. Only **12%** of the initial fluorescence of [F]-hirugen was recovered at saturating β2GpI concentration (3μM). In the third step, [F]-hirugen still bound to S195A was displaced by adding increasing concentrations of unlabelled hirugen. As expected, the initial fluorescence characteristic of free [F]-hirugen was almost fully recovered. Our results indicate that naïve hirugen, *but not* β2GpI, is able to displace the majority of [F]-hirugen molecules from thrombin exosite-I, thus providing strong, albeit indirect, evidence that αT exosite-I is not involved in binding to β2GpI.
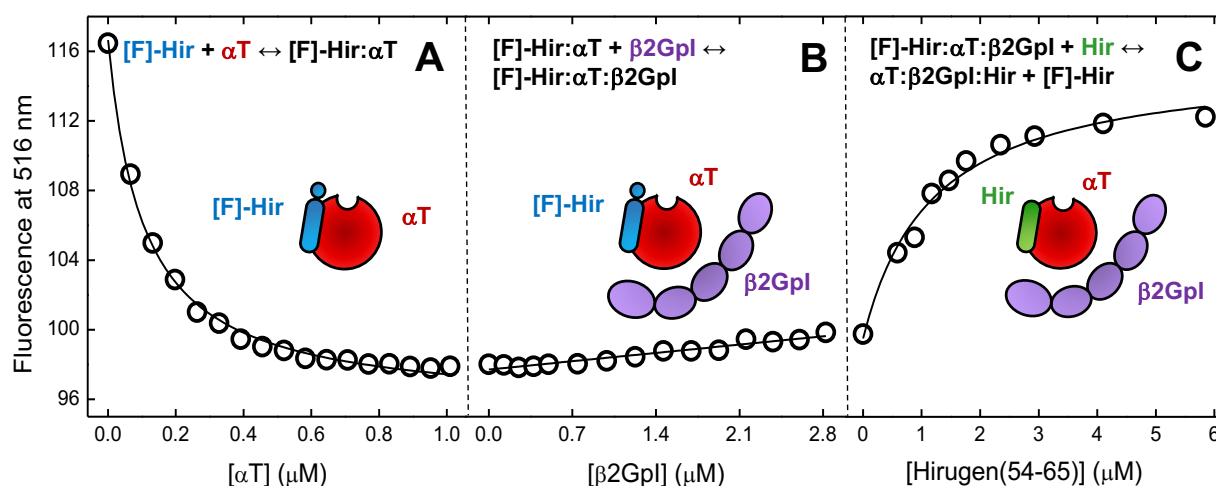

Figure 7. Competition of fluoresceinated hirugen and β2GpI for αT exosite I. Fluorescence competition measurements for the binding of αT and β2GpI to [F]-hirugen. (**A**) Binding of rS195A to [F]-hirugen (60nM). The data points were interpolated with **eq. 1** (**Suppl. Data**), yielding **K_d=30±8nM**. (**B**) Displacement of [F]-hirugen from the complex with rS195A, as obtained in panel **A**, by adding incremental concentrations of β2GpI. A moderate increase of fluorescence (~10%) was observed, suggestive of only a partial displacement of [F]-hirugen by β2GpI. (**C**) Displacement of [F]-hirugen from rS195A by adding incremental concentrations of *unlabelled* hirugen. A marked increase of fluorescence (~90%) was measured as the result of complete displacement from αT exosite-I of [F]-hirugen that was still bound to the enzyme in the presence of β2GpI. Samples in HBS, containing 0.1% PEG-8000 were excited at 25°C at 492nm and the fluorescence of [F]-hirugen, bound to or released from S195A, was recorded at 516nm (**Suppl. Data**).

Binding of thrombin derivatives to β2GpI

The role of exosites in αT-β2GpI interaction was further investigated by SPR using αT derivatives, i.e. prothrombin (ProT) and β_T-thrombin (β_TT), having the exosites variably compromised (**Fig. 8A**). Notably, both ProT and β_TT have been already exploited for mapping αT binding site in other interacting systems (**13,17,23**). ProT is the physiological inactive precursor of mature αT and is composed of a γ-carboxyglutamic acid(Gla)-domain, two kringle domains, and a protease domain. As reported for Pre2, the Na^+-binding site, the activation domain and the insertion loops surrounding the catalytic pocket in ProT are compromised, while exosite-I is only slightly altered compared to αT structure (**49**). At variance with Pre2, exosite-II reactivity in ProT is abolished due to masking of the kringle-2 domain. β_TT is a non-physiological nicked species of αT (**Fig. S6, Suppl. Data**), resulting from limited proteolysis of the mature enzyme with trypsin at the single peptide bond Arg77a-Asn78 in the exosite-I, which is selectively disrupted in β_TT, whereas the catalytic site and exosite-II remain fully functional (**26**). SPR data (**Fig. 8B**) indicate that masking of exosite-II reactivity, as in ProT, causes a drop (7-fold) in the affinity of αT for immobilized β2GpI, whereas killing of exosite-I, as in β_TT, did not alter the binding strength. These results further support our conclusion that exosite-II is the hot spot on αT for binding to β2GpI.
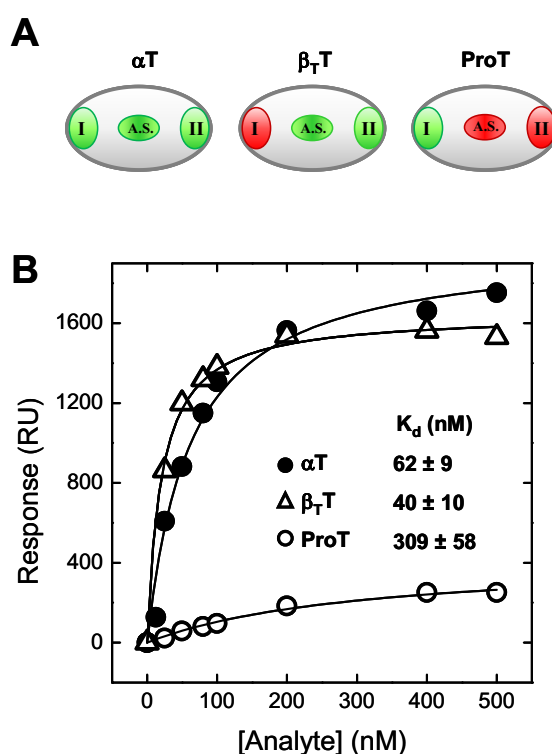

Figure 8. Effect of selective perturbation of exosites on the affinity of αT for β2GpI. (**A**) Schematic representation of the protease-domain of mature α-thrombin (αT), β_T-thrombin (β_TT), and prothrombin (ProT). The active site (AS) and exosite-I (I) and exosite-II (II) are colored according to the conformational/functional state they assume in the different thrombin derivatives, compared to αT (see text); *green*: unperturbed or only slightly perturbed; *red*: heavily perturbed. (**B**) SPR analysis

of the binding of αT, $β_T$T, and ProT to a β2GpI-sensor chip. The values of RU_{max} were plotted *versus* the concentration of thrombin derivatives and the data points were interpolated with **eq. 2** (**Suppl. Data**), yielding the corresponding K_d values, as indicated. All measurements were carried out at 25°C in HBS-EP$^+$, pH 7.4.

Effect of β2GpI on fibrinogen and PAR1 hydrolysis

αT exploits exosite-I for binding to either fibrinogen in or PAR1 and for properly orienting these substrates in the protease active site for efficient cleavage (**11,13,17**). Hence, to probe the effect of β2GpI on the functional state of exosite-I, beyond simple binding, we evaluated whether physiological β2GpI concentrations (4μM) alter the efficiency with which αT releases fibrinopeptides (FpA and FpB) from fibrinogen (**Fig. 9A**) and cleaves PAR1(38-60) (**Fig. 9B**). Notably, the latter peptide reproduces the substrate binding properties of the extracellular domain of PAR1 on platelets, as it contains both the exosite-I binding sequence and the scissile bond R^{41}-S^{42} for αT (**28**). The kinetic data relative to fibrinopeptides generation were analysed within the framework of the Shafer's model (**27**), whereby a highly specific cleavage at the Aα chain leads to the rapid release of FpA and formation of fibrin I monomers that aggregate to form fibrin I protofibrils. A second cleavage by αT at the Bβ chain of the fibrin I monomers then leads to the slower release of FpB and formation of fibrin II protofibrils, which then aggregate to form the fibrin clot. The values of the specificity constants (k_{cat}/K_m) for the release of FpA and FpB, extracted form the kinetic data in **Fig. 9A,** were found to be identical to those reported earlier (**27**) and, more importantly, independent of β2GpI addition. Likewise, the k_{cat}/K_m value of PAR1(38-60) hydrolysis by αT was identical to that previously estimated (**18,28**) and remained essentially constant after addition of 4μM β2GpI (**Fig. 9B**). The relative insensitivity to β2GpI of αT-mediated cleavage of two exosite-I binders like fibrinogen and PAR1 provides evidence that exosite-I plays a minor (if any) role in αT-β2GpI recognition.
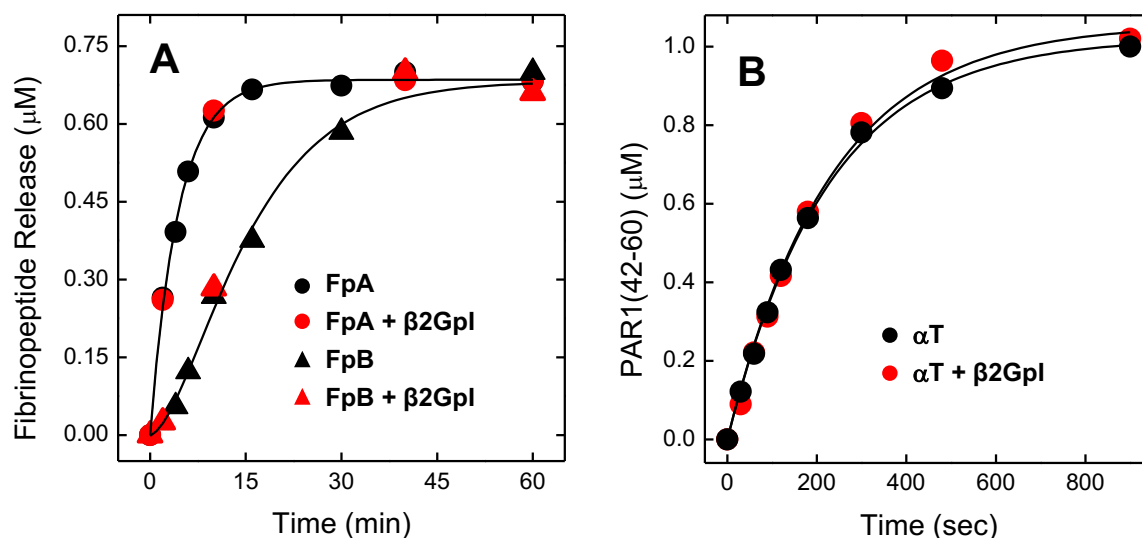
Figure 9 Effect of β2GpI on the efficiency of fibrinogen and PAR1 hydrolysis by αT. (**A**) Time course analysis of fibrinopeptides release. Release of FpA (●, ●) and FpB (▲,▲) from human fibrinogen (0.35μM) by αT (0.3nM) in the absence (●, ▲) or in the presence (●, ▲) of 4μM β2GpI. Experiments were carried out at 37°C in HBS. Fibrinopeptides were quantified by RP-HPLC. Interpolation of the data points relative to FpA and FpB release with **eq. 6** or **eq. 7** (**Suppl. Data**), respectively, yielded kinetic constant values as $k'=3.74\pm0.12\cdot10^{-3}$ s^{-1} and $k''=1.11\pm0.38\cdot10^{-3}$ s^{-1}, from which the values of the apparent specificity constants were obtained as $k_{catA}/K_{mA} = 12.5\pm0.6 s^{-1}\cdot\mu M^{-1}$ and $k_{catB}/K_{mB} = 3.7\pm0.8 s^{-1}\cdot\mu M^{-1}$. (**B**) Time course analysis of PAR1(38-60) cleavage by αT in the absence (●) or in the presence (●) of 4μM β2GpI. The time course release of PAR(42-60) fragment was quantified by RP-HPLC and the data points were fitted with **eq. 8** (**Suppl. Data**) to yield the following k_{cat}/K_m values: **-β2GpI, k_{cat}/K_m = 4.5\pm0.2x10^7 M^{-1}\cdot s^{-1}$; +β2GpI, k_{cat}/K_m = 4.3\pm0.3 x 10^7 M^{-1}\cdot s^{-1}$**.

Mapping of the binding sites on β2GpI

Considered that formation of αT-β2GpI complex is significantly contributed by ionic interactions (**Fig. 3**) and that the highly positive αT exosite-II is involved in binding, we sought for large negative spots on β2GpI structure as putative binding sites for αT. Domains I, III and V were all discarded as they are positively charged at the plasma pH (pI: 8.8, 8.2, and 8.9). Although highly basic, D-V displays an asymmetric distribution of charges, whereby the upper surface is predominantly negative whereas the lower surface is strongly positive (**see Fig. 11A**). The possible involvement of domain II (pI: 4.7) was also ruled out as the six acidic residues present in the sequence are dispersed on the domain surface, do not form a sufficiently large negative patch, and are partially compensated by basic amino acids nearby (**6,7**). At variance with D-II, D-IV (pI: 5.6) contains the segment [222]**D**GP**EEIE**[228], which forms a large continuous region of uncompensated negative charges on β2GpI surface (**6,7**) and thus it may function as a linear epitope for αT binding.

The peptide β2GpI(219-232), [219]YSL**DGPEEIE**STKL[232], was synthesized and its affinity for

αT measured by fluorescence spectroscopy. As already observed with full-length β2GpI (**Fig. 1B**), the synthetic peptide β2GpI(219-232) reduced αT fluorescence intensity (**Fig. 10A**), even tough to a lower extent compared to β2GpI (**Fig. 10B**), and bound to the protease with similar affinity (K$_d$ = **85±15nM**). However, the binding was not specific, as the synthetic peptide analogue R-β2GpI(219-232), having the randomized sequence **D**LYIPSL**E**GKT**E**S**E**, reproduced the fluorescence changes induced by the natural peptide (**Fig. 10B**). These results suggest that the two peptides and β2GpI likely cover overlapping regions on αT surface, even though the details of ionic interactions they establish with αT might be different. This interpretation is in keeping with the data in **Fig. 3**, showing that αT-β2GpI binding is influenced by ionic interactions, which are intrinsically unspecific in nature (**35**). Indeed, charge-charge interactions are formed by long, flexible amino acids (Asp, Glu, Lys, Arg) that often form dynamic ionic networks on proteins, whereby the loss of binding energy caused by disruption of a specific salt bridge at the complex interface can be compensated by the formation of novel electrostatic interactions nearby, with minimal structural/energetic perturbation (**35**).
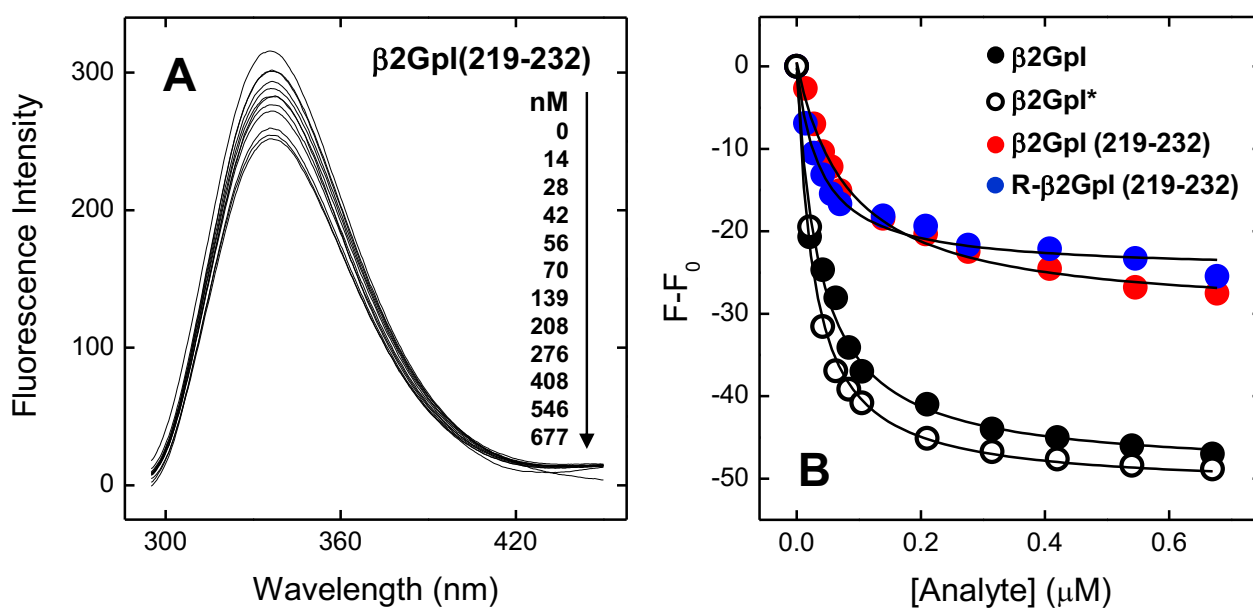

Figure 10. Binding of β2GpI(219-232) and nicked β2GpI* to αT. (**A**) Fluorescence spectra of αT in the presence of increasing concentrations of β2GpI(219-232) peptide. At each β2GpI(291-232) concentration, the fluorescence of αT-β2GpI peptide mixture was subtracted for the contribution of β2GpI peptide alone at the same concentration, to yield the fluorescence change associated with complex formation. (**B**) Plot of the fluorescence change of αT *vs.* the concentration of the peptideβ2GpI(219-232) (●), the sequence-randomized peptide R-β2GpI(219-232) (●), full-length β2GpI (●), and the plasmin-nicked species β2GpI* (○). To a solution of αT (60nM) were added aliquots (2-5μl) of analyte, i.e. β2GpI or β2GpI peptides. The samples were excited at 295nm and the emission intensity was recorded at 330nm. After subtracting the fluorescence of the analyte alone, the data points were interpolated with **eq. 1** (**Suppl. Data**) to yield K$_d$ values: β2GpI(219-232), **K$_d$ = 85±15nM**; R-β2GpI(219-232), **K$_d$ = 49±6nM**; β2GpI, **K$_d$ = 50±8nM;** β2GpI*, **K$_d$ = 45±5nM.**

Following the site-specific perturbation strategy we have exploited above for mapping the binding sites on αT, we decided to probe the role of β2GpI D-V by measuring the affinity of the nicked species β2GpI* for αT, where β2GpI* is generated by proteolysis with plasmin during fibrinolysis *in vivo* and corresponds to the natural protein having the single peptide bond Lys317-Thr318 in D-V cleaved (**1,4**). Notably, the electropositive face of D-V (**Fig. 11A**) binds to negatively charged molecular targets, i.e. anionic phospholipids, heparin and cellular receptors (**1,4,50,51**), mainly through the positive segment [282]KNKEKK[287], connecting strands βC and βD, and the C-1terminal flexible loop [308]KEHSSLAFWK↓TDASDVKPC[326], containing the cleavage site for plasmin (↓). Notably, after proteolysis the loop 308-326 remains linked to the protein core by the two disulphide bonds Cys281-Cys306 and Cys288-Cys326. NMR analysis of intact and nicked recombinant D-V reveals that even though peptide bond cleavage does not induce global unfolding of D-V it locally alters the conformation of the loop 308-326, which becomes much more flexible, and strongly perturbs the electrostatic potential of D-V, due to the generation of an additional positive and negative charge at the cleaved peptide bond (**52**) (**see Fig. S4_D, Suppl. Data**). As a result, β2GpI* displays much reduced capacity of binding to anionic phospholipids and heparin (**50)**. Hence, β2GpI* can be taken as a suitable probe for studying the role of D-V electropositive region in β2GpI interacting systems. In this study, β2GpI* was prepared by proteolysis of plasma β2GpI with plasmin, purified to homogeneity (>95%) according to Goto and co-workers (**52**), and thoroughly characterized by RP-HPLC, SDS-PAGE, and HR-MS (**Fig. S4A, Suppl. Data**). Interestingly, the fluorescence quantum yield of β2GpI* was reduced by ~30% compared to the intact protein (**Fig. S4B, Suppl. Data**), fully consistent with the interpretation that (partial) unfolding of the nicked loop 308-326 alters the conformation/environment of the single Trp316 next to the cleavage site. Importantly, fluorescence binding data in **Fig. 10B** indicated that intact β2GpI and nicked β2GpI* bind to αT with identical affinities, thus suggesting that the phospholipid/heparin binding site in D-V is not likely to be involved in the interaction with αT.
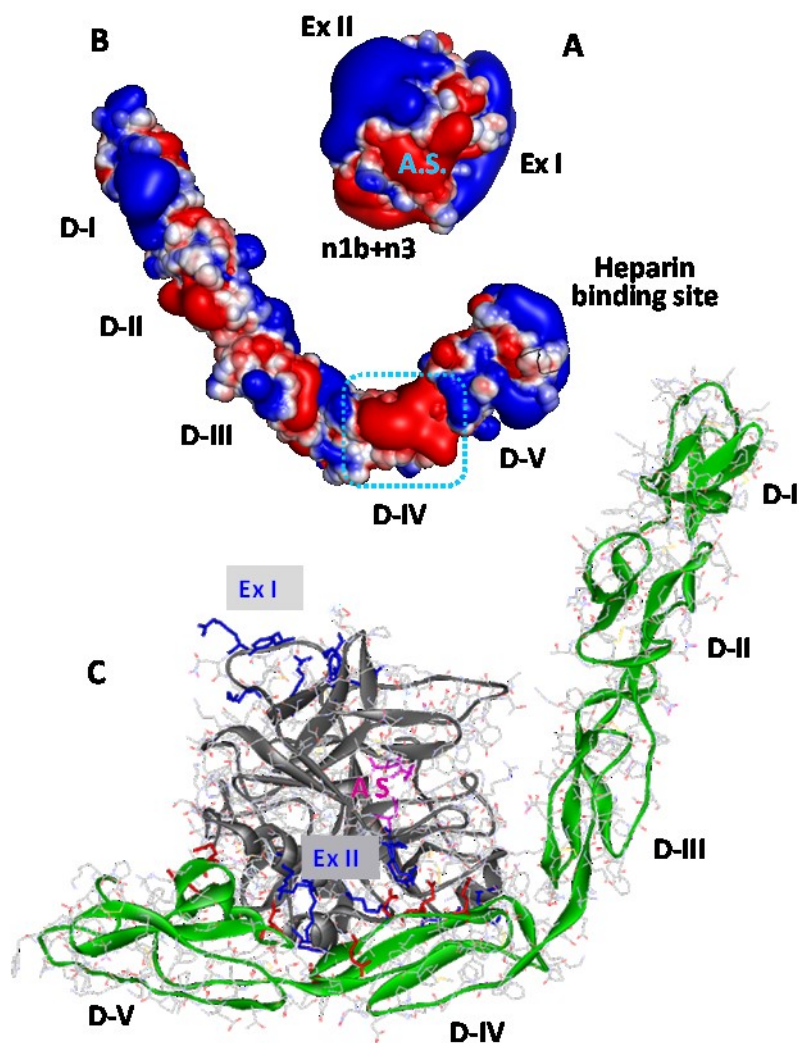
Figure 11 Theoretical Model of αT-β2GpI interaction Surface electrostatic properties of αT (**A**) and β2GpI (**B**). The protein surfaces are color-coded according to their electrostatic potential, from -1kcal/mol/e⁻ (deep red) to +1kcal/mol/e⁻ (deep blue). Calculations were performed using the program APBS (**29**), run on the X-ray structure of β2GpI (1c1z) and des-PPACK αT (1ppb). (**A**) In αT structure (top view) e, the negatively charged active site, A.S., (H57,D102,S195) is surrounded by a "ring" of negative amino acids (E39,D60e,E61,D63,E97a,E146,E192,E217,D221a), protruding from the protease insertion loops and flanked by the positive regions defining exosite-I (F34,K36,R67,R73,Y76,R77a,K81) and exosite-II (R93,R101,R126,R165,K169,R233,K235,K236,K240), which are positioned almost opposite to the active site. Calculations reveals the presence of an additional negative region in αT, formed by n1b+n3 patches (E14e,E14h,D14l, E164,D186a,E186b,D222) (**16**). (**B**) For β2GpI (side view), a large electronegative surface can be identified in the region spanning D-IV (D217,D222,E225,E226,E228) and the upper face of D-V (E259,E265,D275), whereas the lower face of D-V, i.e. the heparin binding site, is strongly electropositive. (**C**) Ribbon drawing of the complex formed by αT (grey) and β2GpI (green), as obtained by ClusPro-2.0 (model_01). The position of αT active site and exosites I and II are indicated, along with some (partially) uncompensated basic amino acids (blue) in αT exosite-II (R93,R101,R126,K236) and acidic uncompensated residues (red) in β2GpI (E217,E225,E226,E275). The model suggests that αT active site and exosite-I are not involved in β2GpI interaction and are accessible for ligand binding.

Modelling β2GpI-αT interaction

To interpret on structural grounds the effects of β2GpI on αT functions, we first investigated the electrostatic properties of the two proteins (**Fig. 11A,B**) and then produced a theoretical model of αT-β2GpI complex (**Fig. 11C**). Electrostatic potential calculations highlight the unique and asymmetric surface electrostatics of αT (**16,53**), with two positively charged patches, i.e. exosite-I and -II, flanking the enzyme active site, which conversely has a strong negative potential and is surrounded by a "negative ring" of acidic residues, also denoted as the n1a negative patch (**16**), in the insertion loops shaping the substrate binding sites. Another large negative region comprises the outer surface of the loops 180 and 220 (i.e. the n1b patch), shaping the Na^+-binding site, and the C-terminal helix of the A-chain (i.e. the n3 patch) (**16**). The negative electrostatic potential of this region is likely overestimated, as the software we used for calculations did not consider the contribution of the Na^+-cation bound to αT. Asymmetric distribution of charges is also common to β2GpI, where a large electronegative surface can be identified in the hook-shaped region spanning the upper face of domains IV and V, whereas the lower face of domain V is highly electropositive (**6,7**). Hence, both αT and β2GpI contain either positive and negative regions where amino acids with uncompensated charges display high electrostatic potential and thus may function as potent attractors for complex formation.
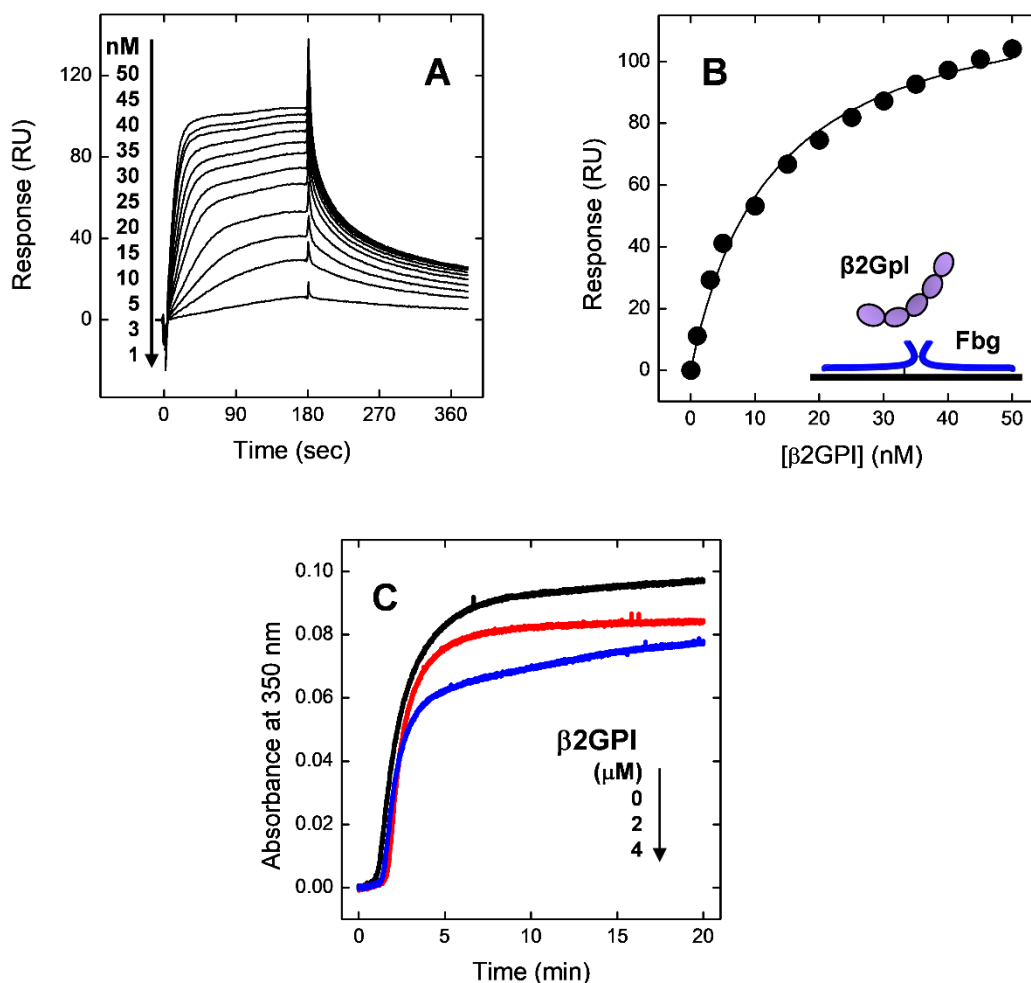
Figure 12. SPR analysis (A, B) of β2GpI-fibrinogen interaction and turbidimetric analysis of the effect of β2GpI on fibrin generation. (**A, B**) Binding of fibrinogen to β2GpI immobilized on a CM5 sensor chip. Sensograms (**A**) and plot (**B**) of RU_{max} *versus* fibrinogen concentration (●). Fitting of data points with **eq. 2 (Suppl. Data)** yielded $K_d = \textbf{13±2nM}$. All measurements were carried out at 25°C in HBS-EP$^+$, pH 7.4. (**C**) Effect of β2GpI of fibrin generation. Representative clotting curves for the generation of fibrin in the presence of increasing β2GpI concentrations: 0, ━; 2, ━; 4, ━ μM. To a human fibrinogen solution (0.35μM) in HBS, pH 7.4, at 25°C was added αT (1nM), with or without β2GpI (4μM) and the time course increase of turbidity (Abs at 350nm) was recorded.

The theoretical model of the αT-β2GpI complex (**Fig. 11C**) was generated starting from the structure of full-length β2GpI and des-PPACK αT, using the "van der Waals+electrostatics" option, as implemented in the on-line version of the automated docking algorithm ClusPro-2.0 (**31**), without imposing any geometric/energetic constraint. Briefly, the server performs three computational steps as follows: (1) rigid-body docking; (2) hierarchical clustering to select and rank near-native docked conformations; and (3) refinement of selected structures. The ranking method is based on the hypothesis that clusters of near-native structures are located in broad energy funnels, such that the

most likely models of the complex are represented in the most populated clusters. As from the default output of ClusPro, the 10 top-ranked models were analyzed and the representative structures (models 00 and 01) of the two most populated clusters (containing 157 and 131 members, respectively) were considered as possible candidates for αT-β2GpI complex (**Fig. S8, Suppl. Data**). Model_00 indicates that the highly electropositive lower face of D-V, i.e. the phospholipid/heparin binding site encompassing the loop-regions 282-287 and 308-326, might interact with a negative region extending over the n1b+n3 patches in αT (see above), while leaving the active site and both exosites unmasked. This model, however, was discarded as it contradicts our experimental data demonstrating that αT exosite-II interacts with β2GpI (**Figs. 6,8**) and, conversely, that the phospholipid/heparin binding site in β2GpI D-V is not involved in binding to αT (**Fig. 10B**). Hence, model_01 (representing the second most populated cluster) was selected as best representative of αT-β2GpI complex (**Fig. 11C**). This model captures the shape and electrostatic complementarity existing between αT and β2GpI structures, whereby the highly electropositive exosite-II on the convex αT surface interacts with the electronegative concave surface in β2GpI, shaped by D-IV and part of D-V, while leaving the active-site region and exosite-I fully accessible for binding (**see the legend to Fig. 11C**). This picture nicely agrees with the experimental data reported in this work, highlighting the salt dependence of αT-β2GpI interaction (**Fig. 3**) and indicating that the positive exosite-II is the hot spot on αT for binding to β2GpI (**Figs. 6, 8**) whereas the protease active site (**Fig. 5**) and exosite-I (**Figs. 7-9**) are not involved in complex formation. Consistent with the results of deglycosylation experiments (**Fig. 4**), the model also argues against a direct involvement of the carbohydrate chains in αT-β2GpI interaction, as these point to different directions in the complex or are too far for productive binding. Intriguingly, model_01 also seems to account for unexpected results, such as the increased affinity (~4-fold) of the D178A αT mutant for β2GpI (**Fig. S5**, **Suppl. Data**). D178 is intramolecularly salt bridged to R165 and R233 at the periphery of exosite-II in αT structure (**16**) and in the docking complex with β2GpI it points toward the negative surface of D-IV, at 7-8Å distance from the uncompensated E225 and E226 (**Fig. 11C**). Hence, if it is assumed that αT structure is not altered by D178A mutation, it is conceivable to propose that ablation of the negative charge at position 178 might increase the affinity of αT for β2GpI by either strengthening the resulting positive electrostatic potential of the protease at the mutated site and, concomitantly, by alleviating the electrostatic repulsion of D178 with the negative region of D-IV. Of note, in models 03, 04, 08, and 09 αT assumes different orientations on β2GpI structure, but nevertheless the interacting regions we have observed in model_01 are roughly conserved.

Overall, although our model snugly fits with the experimental data herein reported, it is important to emphasize that the model awaits structural verification by direct experiments, e.g. X-

ray, NMR, or small angle X-ray scattering techniques.

Effect of β2GpI on fibrin structure

The lack of any relevant effect of β2GpI on fibrinogen hydrolysis (see above) suggests that the prolongation of the clotting time induced by β2GpI in our previous fibrin clotting assays (**19**) cannot be ascribed to the alteration in the efficiency of fibrinopeptides release. These considerations prompted us to investigate the alternative possibility that β2GpI directly binds to fibrinogen and alters the structure of the ensuing fibrin clot through a mechanism not dependent on the effect that β2GpI might exert on αT-induced hydrolysis of fibrinogen. To this aim, SPR measurements were performed by challenging a β2GpI-bound CM5 sensor chip with incremental concentrations of fibrinogen. Strikingly, our data (**Fig. 12A,B**) indicate that fibrinogen binds to immobilized β2GpI with high affinity (**K_d = 13±2nM**). Thereafter, the effect of $β_2$GpI on the time-course generation of fibrin was studied by turbidimetry at 350nm (**Fig. 12C**), yielding different clotting curves in the absence and presence of β2GpI. Specifically, the clotting time (t_c) remained essentially constant, whereas the A_{max} value, i.e. the maximum turbidity measured when the final fibrin clot is formed, was reduced by **~20%** with 4μM β2GpI.

Typically, a fibrin clotting curve displays: i) a lag phase, ii) a linear rise, and iii) a plateau (**32**). The lag phase (i) corresponds to the time necessary for the longitudinal elongation of protofibrils deriving from fibrin monomers, after removal of fibrinopeptides; thereafter, the rapid linear rise in turbidity (ii) results from lateral aggregation of those protofibrils that have reached a certain threshold length to aggregate; finally, the turbidity reaches a plateau (iii) when most of protofibrils have been transformed into fibers (**32**). Noteworthy, the value of A_{max} provides key geometric parameters of fibrin, as it is proportional to the square of the average diameter of the fibers (**32**). In the light of these considerations, the relative invariance of the lag phase is consistent with the observation that β2GpI does not alter the rate of fibrinopeptides release (**Fig. 9A**), whereas the decrease of A_{max} indicates that β2GpI affects lateral aggregation of fibrin, inducing the formation thinner fibers, which generate a less intense turbidimetric signal (**Fig. 12C**).

CONCLUSIONS

Although the involvement of β2GpI in the pathogenesis of APS is widely accepted, the physiological function of this protein is still unclear and in the last three decades both procoagulant and anticoagulant functions *in vitro* have been reported (**4**). To accomplish these functions, β2GpI interacts with different target systems, including negatively charged membranes of activated platelets, coagulation factor XI zymogen, von Willebrand factor, plasminogen and tissue plasminogen activator, platelet factor 4, and lipoprotein receptors (**54-59**). Recently, we added another piece to the puzzle of β2GpI functions (**19**) and showed that this protein prolongs fibrin clotting time in Ecarin Clotting Time (ECT) and Thrombin Time (TT) assays on β2GpI-deficient plasma and inhibits αT-induced platelets aggregation in several different experimental settings, including impedence aggregometry on whole blood, transmittance aggregometry on gel-filtered platelets, and immunocytofluorimetry for measuring PAR1 cleavage on platelet membranes. In the same study, we demonstrated that β2GpI does not alter the efficiency with which αT activates the anticoagulant PC, regardless of TM addition (**19**). Hence, we proposed that β2GpI may function as a physiological anticoagulant by interacting with αT and selectively inhibiting the procoagulant functions (i.e. normal fibrin generation and platelets aggregation) of the protease without affecting its unique anticoagulant activity (i.e. aPC generation). This hypothesis is in keeping with several lines of clinical evidences, whereby reduced β2GpI levels are found in patients with stroke and thrombotic disorders (**60,61**), whereas high circulating levels of β2GpI reduce the risk of myocardial infarction (**62**). Furthermore, there is a positive correlation between the presence of auto-antibodies against β2GpI and thrombotic manifestations in APS patients (**1-4**).

To shed light on the mechanism underlying the effects of β2GpI on αT functions, in the present study we first carefully established, by DLS and fluorescence spectroscopy (**Fig. 1**) and SPR (**Fig. 2**), that β2GpI forms a stable complex with αT (K_d = 50-100nM) and then mapped the binding sites on αT (**Figs. 5-9**) mainly using the site specific perturbation strategy, whereby a decrease in the αT-β2GpI affinity caused by perturbation (i.e. amino acid exchange, ligand binding, proteolysis, etc.) of a given site on αT was taken as an indication that the perturbed site was directly involved in binding. The possible involvement of αT active site in β2GpI interaction was ruled out by enzymatic activity measurements (**Fig. 5A**), showing that physiological β2GpI concentrations did not alter the efficiency of S2238 hydrolysis by αT, and by SPR measurements (**Fig. 5B**), indicating that neither blockage of αT active site with PPACK nor disruption of the catalytic pocked, as in the Pre2 zymogen, compromised binding to β2GpI. The involvement of exosite-II was highlighted by SPR measurements, using the save exosite-II binder GpIbα(268-282) which was able to compete with β2GpI for binding to αT (**Fig. 6**). Accordingly, masking of exosite-II, as in the ProT zymogen,

strongly reduced the affinity of αT for β2GpI (**Fig. 8**). Intriguingly, even exosite-I binders, like hirugen and HD1 aptamer, competed with β2GpI in binding to αT (**Fig. 6B**). However, this result was interpreted as arising from an indirect effect generated by the negative allosteric coupling existing between the two exosites (**46-48**). This interpretation was corroborated by three lines of evidence: firstly, β2GpI failed to displace fluoresceinated hirugen from αT exosite-I (**Fig. 8**); secondly, selective disruption of exosite-I by proteolysis, as in β$_T$-Thrombin, did not alter the affinity for β2GpI (**Fig. 9**); thirdly, β2GpI did not affect the efficiency with which αT cleaves two exosite-I specific ligands/substrates like fibrinogen and PAR1(38-60) (**Fig. 9**). Although our data concurrently indicate that exosite-II is the hot spot on αT for β2GpI binding, some promiscuous binding at exosite-I can not be ruled out, especially at high protein local concentrations *in vivo* (i.e. on the activated platelets surface) or when exosite-II is occupied. Thereafter, starting from the knowledge that charge-charge interactions significantly contribute to αT-β2GpI association and that the strongly positive exosite-2 of thrombin is involved in binding, we identified the negatively charged segment [222]**DGPEEIE**[228] in β2GpI D-IV as a putative binding site for αT. Indeed, the corresponding synthetic peptide β2GpI(219-232) binds to αT with an affinity only 2-fold lower than that of the full-length β2GpI. Importantly, the theoretical docking model of αT-β2GpI complex reported in **Fig. 11C** well agrees with all the experimental data reported in this study and sets the basis for future mutagenesis work and direct structural determination.

The proposed model also bears important implications for understanding the effect of β2GpI on αT functions. First of all, the involvement of exosite-II explains in a straightforward way how β2GpI impairs αT-mediated platelets aggregation (**19**). GpIbα is responsible of anchoring αT on the platelet surface through exosite-II binding, thus orienting the protease exosite-I and active site for efficient binding to and cleavage of PAR1 (**18**). Notably, αT-GpIbα interaction is the rate limiting step in the pathway leading to platelets activation, in the sense that impairment of αT-GpIbα interaction by an interfering molecule can inhibit platelet aggregation even though the molecule does not directly influence PAR1 hydrolysis. Hence, the co-localization of αT and β2GpI on the platelet surface (**1,4,11,13,17**) and the competition of β2GpI and GpIbα(268-282) for binding to αT exosite-II (**Fig. 6**) suggest that β2GpI may function as a scavenger of the protease, thus preventing αT binding to GpIbα and the resulting platelet aggregation mediated by PAR1 cleavage. The concomitant shielding of exosite-II and exposure of αT active site and exosite-I in the β2GpI-αT complex nicely explains apparently puzzling data whereby β2GpI inhibits αT-mediated cleavage of PAR1 on intact platelets (**19**) without impairing PAR1(38-60) hydrolysis by αT (**Fig. 9B**). Likewise, the accessibility of αT active site and exosite-I in the β2GpI-αT complex is fully consistent with the observation that β2GpI does not interfere with αT-mediated hydrolysis of PC to generate aPC either in the absence or

presence of TM, a cofactor that tightly binds to αT exosite-I and brings PC zymogen in close proximity for accelerating aPC generation (**10**).

Particular attention deserves the interpretation of the effect that β2GpI plays on fibrin generation in plasma clotting assays. In our previous work (**19**), we showed that β2GpI prolongs the clotting time, t_c, in clinical tests such as ECT and TT on β2GpI-deficient plasma, suggesting that the protein interferes with the αT-catalyzed conversion of fibrinogen to fibrin. Notably, t_c corresponds to the time necessary to increase, above a certain threshold, the turbidity signal (Abs at 671nm) generated by the newly formed fibrin. Nonetheless, kinetic measurements reported in **Fig. 9A** clearly demonstrate that β2GpI does not alter the rate of fibrinopeptides release from purified fibrinogen and this is fully consistent with our structural model (**Fig. 11C**) showing that β2GpI does not mask the reactivity of αT active-site and exosite-I, which is actually the fibrinogen binding site on αT (**11,13,17**). These findings indicate that the apparent increase of t_c, caused by β2GpI in plasma clotting assays, should not be ascribed to the inhibition of fibrinogen hydrolysis by αT and prompted us to explore the possibility that β2GpI may directly bind to fibrinogen and alter fibrin generation through a mechanism independent from αT proteolysis. Strikingly, SPR data in **Fig. 12A,B** indicate that β2GpI tightly interacts with fibrinogen, while turbidimetric analysis provides clear-cut evidence that β2GpI dose dependently induces the generation of fibrin fibers having a smaller diameter compared to those obtained without β2GpI (**Fig. 12C**). Hence, the prolongation of t_c value induced by β2GpI (**19**) more likely reflects the inhibition of the lateral aggregation of fibrin oligomers rather than the impairment of fibrinogen hydrolysis by αT.

In conclusion, by combining molecular modelling with biochemical/biophysical techniques, in this work we produced a coherent structural model of αT-β2GpI complex which allows to rationalize at the molecular level the effects of β2GpI on αT functions. These results will contribute to elucidate the role of the multifunctional protein β2GpI in the physiology of normal coagulation and, hopefully, to understand the pathogenetic mechanisms underlying the thrombotic effects of anti-β2GpI autoantibodies in APS.

REFERENCES

1. de Groot, P. G. and Meijers, J. C. (2011) Beta2-glycoprotein I: Evolution, structure and function. *J. Thromb. Haemost.* **9**, 1275-1284.

2. Meroni, P. L., Borghi, M. O., Raschi, E. and Tedesco, F. (2011) Pathogenesis of antiphospholipid syndrome: Understanding the antibodies. *Nat. Rev. Rheumatol.* **7**, 330-339.

3. Rand, J. H. (2003) The antiphospholipid syndrome. *Annu. Rev. Med.* **54**, 409-424.

4. Miyakis, S., Giannakopoulos, B. and Krilis, S. A. (2004) Beta 2 glycoprotein I--function in health and disease. *Thromb. Res.* **114**, 335-346.

5. Ninivaggi, M., Kelchtermans, H., Lindhout, T. and de Laat, B. (2012) Conformation of beta2glycoprotein I and its effect on coagulation. *Thromb. Res.* **130 Suppl 1**, S33-6.

6. Schwarzenbacher, R., Zeth, K., Diederichs, K., Gries, A., Kostner, G. M., Laggner, P. and Prassl, R. (1999) Crystal structure of human beta2-glycoprotein I: Implications for phospholipid binding and the antiphospholipid syndrome. *EMBO J.* **18**, 6228-6239.

7. Bouma, B., de Groot, P. G., van den Elsen, J. M., Ravelli, R. B., Schouten, A., Simmelink, M. J., Derksen, R. H., Kroon, J. and Gros, P. (1999) Adhesion mechanism of human beta(2)-glycoprotein I to phospholipids based on its crystal structure. *EMBO J.* **18**, 5166-5174.

8. Hammel, M., Kriechbaum, M., Gries, A., Kostner, G. M., Laggner, P. and Prassl, R. (2002) Solution structure of human and bovine beta(2)-glycoprotein I revealed by small-angle X-ray scattering. *J. Mol. Biol.* **321**, 85-97.

9. Agar, C., van Os, G. M., Morgelin, M., Sprenger, R. R., Marquart, J. A., Urbanus, R. T., Derksen, R. H., Meijers, J. C. and de Groot, P. G. (2010) Beta2-glycoprotein I can exist in 2 conformations: Implications for our understanding of the antiphospholipid syndrome. *Blood.* **116**, 1336-1343.

10. Esmon, C. T. (2005) The interactions between inflammation and coagulation. *Br. J. Haematol.* **131**, 417-430.

11. Di Cera, E. (2003) Thrombin interactions. *Chest.* **124**, 11S-7S.

12. Di Cera, E. (2007) Thrombin as procoagulant and anticoagulant. *J. Thromb. Haemost.* **5 Suppl 1**, 196-202.

13. Huntington, J. A. (2005) Molecular recognition mechanisms of thrombin. *J. Thromb. Haemost.* **3**, 1861-1872.

14. De Filippis, V., Colombo, G., Russo, I., Spadari, B. and Fontana, A. (2002) Probing the hirudin-thrombin interaction by incorporation of noncoded amino acids and molecular dynamics simulation. *Biochemistry.* **41**, 13556-13569.

15. De Filippis, V., De Dea, E., Lucatello, F. and Frasson, R. (2005) Effect of Na$^+$ binding on the conformation, stability and molecular recognition properties of thrombin. *Biochem. J.* **390**, 485-492.

16. Bode, W., Turk, D. and Karshikov, A. (1992) The refined 1.9-A X-ray crystal structure of D-phe-pro-arg chloromethylketone-inhibited human alpha-thrombin: Structure analysis, overall

structure, electrostatic properties, detailed active-site geometry, and structure-function relationships. *Protein Sci.* **1**, 426-471.

17. Bock, P. E., Panizzi, P. and Verhamme, I. M. (2007) Exosites in the substrate specificity of blood coagulation reactions. *J. Thromb. Haemost.* **5 Suppl 1**, 81-94.

18. De Candia, E., Hall, S. W., Rutella, S., Landolfi, R., Andrews, R. K. and De Cristofaro, R. (2001) Binding of thrombin to glycoprotein ib accelerates the hydrolysis of par-1 on intact platelets. *J. Biol. Chem.* **276**, 4692-4698.

19. Pozzi, N., Acquasaliente, L., Frasson, R., Cristiani, A., Moro, S., Banzato, A., Pengo, V., Scaglione, G. L., Arcovito, A., De Cristofaro, R. and De Filippis, V. (2013) beta2 - glycoprotein I binds to thrombin and selectively inhibits the enzyme procoagulant functions. *J. Thromb. Haemost.* **11**, 1093-1102.

20. De Filippis, V., Quarzago, D., Vindigni, A., Di Cera, E. and Fontana, A. (1998) Synthesis and characterization of more potent analogues of hirudin fragment 1-47 containing non-natural amino acids. *Biochemistry.* **37**, 13507-13515.

21. Artenjak, A., Leonardi, A., Krizaj, I., Ambrozic, A., Sodin-Semrl, S., Bozic, B. and Cucnik, S. (2014) Optimization of unnicked beta2-glycoprotein I and high avidity anti-beta2-glycoprotein I antibodies isolation. *J. Immunol. Res.* **2014**, 195687.

22. Murphy, R. M. (1997) Static and dynamic light scattering of biological macromolecules: What can we learn? *Curr. Opin. Biotechnol.* **8**, 25-30.

23. Sokolov, A. V., Acquasaliente, L., Kostevich, V. A., Frasson, R., Zakharova, E. T., Pontarollo, G., Vasilyev, V. B. and De Filippis, V. (2015) Thrombin inhibits the anti-myeloperoxidase and ferroxidase functions of ceruloplasmin: Relevance in rheumatoid arthritis. *Free Radic. Biol. Med.* **86**, 279-294.

24. Li, W., Johnson, D. J., Adams, T. E., Pozzi, N., De Filippis, V. and Huntington, J. A. (2010) Thrombin inhibition by serpins disrupts exosite II. *J. Biol. Chem.* **285**, 38621-38629.

25. Pozzi, N., Chen, Z., Pelc, L. A., Shropshire, D. B. and Di Cera, E. (2014) The linker connecting the two kringles plays a key role in prothrombin activation. *Proc. Natl. Acad. Sci. U. S. A.* **111**, 7630-7635.

26. Hofsteenge, J., Braun, P. J. and Stone, S. R. (1988) Enzymatic properties of proteolytic derivatives of human alpha-thrombin. *Biochemistry.* **27**, 2144-2151

27. Ng, A. S., Lewis, S. D. and Shafer, J. A. (1993) Quantifying thrombin-catalyzed release of fibrinopeptides from fibrinogen using high-performance liquid chromatography. *Methods Enzymol.* **222**, 341-358.

28. Ayala, Y. M., Cantwell, A. M., Rose, T., Bush, L. A., Arosio, D. and Di Cera, E. (2001) Molecular mapping of thrombin-receptor interactions. *Proteins.* **45**, 107-116.

29. Baker, N. A., Sept, D., Joseph, S., Holst, M. J. and McCammon, J. A. (2001) Electrostatics of nanosystems: Application to microtubules and the ribosome. *Proc. Natl. Acad. Sci. U. S. A.* **98**, 10037-10041.

30.   Fogolari, F., Corazza, A., Yarra, V., Jalaru, A., Viglino, P. and Esposito, G. (2012) Bluues: A program for the analysis of the electrostatic properties of proteins based on generalized born radii. *BMC Bioinformatics.* **13 Suppl 4**, S18-2105-13-S4-S18.

31.   Comeau, S. R., Gatchell, D. W., Vajda, S. and Camacho, C. J. (2004) ClusPro: An automated docking and discrimination method for the prediction of protein complexes. *Bioinformatics.* **20**, 45-50

32.   Weisel, J. W. and Nagaswami, C. (1992) Computer modeling of fibrin polymerization kinetics correlated with electron microscope and turbidity observations: Clot structure and assembly are kinetically controlled. *Biophys. J.* **63**, 111-128. doi:S0006-3495(92)81594-1 [pii]

33.   Papish, A. L., Tari, L. W. and Vogel, H. J. (2002) Dynamic light scattering study of calmodulin-target peptide complexes. *Biophys. J.* **83**, 1455-1464.

34.   Pozzi, N., Banzato, A., Bettin, S., Bison, E., Pengo, V. and De Filippis, V. (2010) Chemical synthesis and characterization of wild-type and biotinylated N-terminal domain 1-64 of beta2-glycoprotein I. *Protein Sci.* **19**, 1065-1078.

35.   Bertonati, C., Honig, B. and Alexov, E. (2007) Poisson-boltzmann calculations of nonspecific salt effects on protein-protein binding free energies. *Biophys. J.* **92**, 1891-1899.

36.   Richardson, J. L., Fuentes-Prior, P., Sadler, J. E., Huber, R. and Bode, W. (2002) Characterization of the residues involved in the human alpha-thrombin-haemadin complex: An exosite II-binding inhibitor. *Biochemistry.* **41**, 2535-2542.

37.   Olson, S. T., Halvorson, H. R., and Björk, I. (1991) Quantitative characterization of the thrombin-heparin interaction. Discrimination between specific and nonspecific binding models. *J. Biol. Chem.* **266**, 6342-6352.

38.   Kolyada, A., De Biasio, A., and Beglova, N. (2013) Identification of the binding site for fondaparinux on beta2-glycoprotein I. *Biochim. Biophys. Acta.* **1834**, 2080-2088.

39.   Lechtenberg, B. C., Johnson, D. J., Freund, S. M. and Huntington, J. A. (2010) NMR resonance assignments of thrombin reveal the conformational and dynamic effects of ligation. *Proc. Natl. Acad. Sci. U. S. A.* **107**, 14087-14092.

40.   Pozzi, N., Chen, Z., Zapata, F., Pelc, L. A., Barranco-Medina, S. and Di Cera, E. (2011) Crystal structures of prethrombin-2 reveal alternative conformations under identical solution conditions and the mechanism of zymogen activation. *Biochemistry.* **50**, 10195-10202.

41.   Verespy III, S., Mehta, A .Y., Afosah, D., Al-Horani, R. A., Desai, U. R. (2016) Allosteric partial inhibition of monomeric proteases. Sulphated coumarins induce regulation, not just inhibition, of thrombin. *Sci. Rep.* **6**, 24043.

42.   Alexander, K. S., Fried, M. G. and Farrell, D. H. (2012) Role of electrostatic interactions in binding of thrombin to the fibrinogen gamma' chain. *Biochemistry.* **51**, 3445-3450.

43.   Lechtenberg, B. C., Freund, S. M. and Huntington, J. A. (2014) GpIbα interacts exclusively with exosite II of thrombin. *J. Mol. Biol.* **426**, 881-893.

44.   De Cristofaro, R. and De Filippis, V. (2003) Interaction of the 268-282 region of glycoprotein ibalpha with the heparin-binding site of thrombin inhibits the enzyme activation of factor VIII. *Biochem. J.* **373**, 593-601.

45.   Gamsjaeger, R., Kariawasam, R., Bang, L. H., Touma, C., Nguyen, C. D., Matthews, J. M., Cubeddu, L. and Mackay, J. P. (2013) Semiquantitative and quantitative analysis of protein-DNA interactions using steady-state measurements in surface plasmon resonance competition experiments. *Anal. Biochem.* **440**, 178-185.

46.   Fredenburgh, J. C., Stafford, A. R. and Weitz, J. I. (1997) Evidence for allosteric linkage between exosites 1 and 2 of thrombin. *J. Biol. Chem.* **272**, 25493-25499.

47.   Malovichko, M. V., Sabo, T. M. and Maurer, M. C. (2013) Ligand binding to anion-binding exosites regulates conformational properties of thrombin. *J. Biol. Chem.* **288**, 8667-8678.

48.   Lancellotti, S., Rutella, S., De Filippis, V., Pozzi, N., Rocca, B., De Cristofaro, R. (2008) Fibrinogen Elongated γ-Chain Inhibits Thrombin-Induced Platelet Response, Hindering the Interaction with Different Receptors. *J. Biol. Chem.* **283**, 30193-30204.

49.   Pozzi, N., Chen, Z., Gohara, D. W., Niu, W., Heyduk, T. and Di Cera, E. (2013) Crystal structure of prothrombin reveals conformational flexibility and mechanism of activation. *J. Biol. Chem.* **288**, 22734-22744.

50.   Guerin, J., Sheng, Y., Reddel, S., Iverson, G. M., Chapman, M. G., and Krilis, S. A. (2002) Heparin inhibits the binding of beta 2-glycoprotein I to phospholipids and promotes the plasmin-mediated inactivation of this blood protein. *J. Biol. Chem.* **277**, 2644-2649.

51.   Beglov, D., Lee, C.-J., De Biasio, A., Kozakov, D., Brenke, R., Vajda, S., and Beglova, N. (2009) Structural insights into recognition of beta2-glycoprotein I by the lipoprotein receptors. *Proteins.* **77**, 940-949.

52.   Hoshino, M., Hagihara, Y., Nishii, I., Yamazaki, T., Kato, H., and Goto, Y. (2000) Identification of the phospholipid-binding site of human beta(2)-glycoprotein I domain V by heteronuclear magnetic resonance. *J. Mol. Biol.* **304**, 927-939.

53.   Pozzi, N., Zerbetto, M., Acquasaliente, L., Tescari, S., Frezzato, D., Polimeno, A., Gohara, D. W., Di Cera, E., and De Filippis, V. (2016) Loop Electrostatics Asymmetry Modulates the Preexisting Conformational Equilibrium in Thrombin. *Biochemistry.* **55**, 3984-3994.

54.   Schousboe, I. (1980) Binding of beta2-glycoprotein I to platelets: Effect of adenylate cyclase activity. *Thromb. Res.* **19**, 225-237.

55.   Shi, T., Iverson, G. M., Qi, J. C., Cockerill, K. A., Linnik, M. D., Konecny, P. and Krilis, S. A. (2004) Beta 2-glycoprotein I binds factor XI and inhibits its activation by thrombin and factor XIIa: Loss of inhibition by clipped beta 2-glycoprotein I. *Proc. Natl. Acad. Sci. U. S. A.* **101**, 3939-3944.

56.   Hulstein, J. J., Lenting, P. J., de Laat, B., Derksen, R. H., Fijnheer, R. and de Groot, P. G. (2007) beta2-glycoprotein I inhibits von willebrand factor dependent platelet adhesion and aggregation. *Blood.* **110**, 1483-1491.

57. Lopez-Lira, F., Rosales-Leon, L., Martinez, V. M. and Ruiz Ordaz, B. H. (2006) The role of beta2-glycoprotein I (beta2GPI) in the activation of plasminogen. *Biochim. Biophys. Acta.* **1764**, 815-823.

58. Bu, C., Gao, L., Xie, W., Zhang, J., He, Y., Cai, G. and McCrae, K. R. (2009) Beta2-glycoprotein i is a cofactor for tissue plasminogen activator-mediated plasminogen activation. *Arthritis Rheum.* **60**, 559-568.

59. Sikara, M. P., Routsias, J. G., Samiotaki, M., Panayotou, G., Moutsopoulos, H. M. and Vlachoyiannopoulos, P. G. (2010) Beta2-glycoprotein I (beta2GPI) binds platelet factor 4 (PF4): Implications for the pathogenesis of antiphospholipid syndrome. *Blood.* **115**, 713-723.

60. Brighton, T. A., Hogg, P. J., Dai, Y. P., Murray, B. H., Chong, B. H. and Chesterman, C. N. (1996) Beta 2-glycoprotein I in thrombosis: Evidence for a role as a natural anticoagulant. *Br. J. Haematol.* **93**, 185-194.

61. Lin, F., Murphy, R., White, B., Kelly, J., Feighery, C., Doyle, R., Pittock, S., Moroney, J., Smith, O., Livingstone, W., Keenan, C. and Jackson, J. (2006) Circulating levels of beta2-glycoprotein I in thrombotic disorders and in inflammation. *Lupus.* **15**, 87-93.

62. de Laat, B., de Groot, P. G., Derksen, R. H., Urbanus, R. T., Mertens, K., Rosendaal, F. R. and Doggen, C. J. (2009) Association between beta2-glycoprotein I plasma levels and the risk of myocardial infarction in older men. *Blood.* **114**, 3656-3661.

SUPPLEMENTARY MATERIALS

Experimentals

Reagents

Natural human α-thrombin (αT) and prothrombin (ProT) were purchased from Haematologic Technologies (Essex Junction, VT, USA). Hirugen [54]GDFEEIPEEY(PO$_3$H)LQ[65], N$^\alpha$-fluoresceinated hirugen ([F]-hirugen), GpIbα(268-282) peptide, GDEGDTDLY(PO$_3$H)DY(PO$_3$H)Y(PO$_3$H)PEE, from platelet receptor GpIbα and PAR1(38-60) [38]LDPR↓SFLLRNPNDKYEPFWEDDE[60] were synthesised in our laboratory by the solid phase strategy on a PS3 automated synthesizer (Protein Technologies, AZ, USA) using the fluorenylmethyloxycarbonyl-chemistry, as described (**1**). The synthetic peptides were purified by semi-preparative RP-HPLC and characterized by high-resolution mass spectrometry on a Xevo G2-S Q-TOF instrument (Waters), yielding experimental mass values in agreement with the expected amino acid composition within 1-2 ppm. The thrombin inhibitor (D)-Phe-Pro-Arg-chloromethyl ketone (PPACK) was from Merck (Germany). Salts, solvents and reagents were of analytical grade and purchased from Sigma (St Louis, MO, USA).

Purification and characterization of β2GpI from human plasma

Purification of β2GpI from human plasma was carried out following essentially the perchloric acid precipitation method of (**2**), as recently modified (**3-5**) (**Fig. S1**). Pooled plasma (80ml) from A$^+$- and 0$^+$-blood group healthy donors was thawed at 4°C, diluted 1:1 (v/v) with phosphate buffered saline (PBS) and added dropwise under gentle stirring with a 60% (v/v) perchloric acid solution at 4°C up to 0.285M final concentration. The suspension was centrifuged at 10,000 g for 15min at 4°C. The supernatant containing β2GpI was withdrawn, the solution pH adjusted to 8.0 with 1M NaOH, and dialysed overnight at 4°C against 20mM Tris-HCl buffer, pH 8.0, 30mM NaCl with a 14-kDa cut-off membrane (Sartorius AG, Germany). Aliquots (1ml) of the dialysed solution were loaded onto a (1x5cm) HiTrap Heparin-sepharose colum (GE-Healthcare, USA), equilibrated with the same buffer (buffer A) and eluted with 20mM Tris-HCl buffer, pH 7.4, containing 350mM NaCl (buffer B) from 0 to 65% of buffer B in 40 min at a flow-rate of 2 ml/min (**Fig. S1A**). Fractions were collected and analyzed by SDS-PAGE (4-12 % acrylamide) (**Fig. S1B**) to identify the presence of β2GpI, migrating as a 50-kDa band. β2GpI-containing fractions were pooled, dialysed overnight at 4°C against 20mM Tris-HCl buffer, pH 7.4, 0.15M NaCl and stored at -20°C for subsequent analysis. The purity of β2GpI preparation was established by SDS-PAGE (4-12% acrylamide), followed by Coomassie blue staining, (**Fig. S1C**) and RP-HPLC (**Fig. S1D**) on an analytical (4.6x150mm) C4 column (Grace-Vydac, MD, USA) eluted with a linear acetonitrile-0.078%-TFA gradient from 20 to 50% in 30min at a flow-rate of 0.8ml/min. The molecular mass of purified β2GpI was determined at

low resolution on a 4800 MALDI TOF/TOF instrument (Applied Biosystems, CA, USA) (**Fig. S1E**) and at high resolution on a Xevo G2-S Q-TOF mass spectrometer (Waters, MO, USA). Densitometric analysis of the electrophoretic bands in **Fig. S1C** was carried out with a Geliance-600 Chem-Imaging system (Perkin-Elmer, USA) and the Image-J software (www.imagej.nih.gov), yielding a purity **>98%.** The concentration of β2GpI solutions was determined by measuring the absorbance at 280 nm, using a molar absorptivity value of 47.250 $M^{-1}cm^{-1}$. This procedure allowed us to obtain β2GpI preparations free of C1 inhibitor, a plasma serine protease inhibitor which might be co-purified with β2GpI (**3**).

Dynamic light scattering (DLS) measurements

In DLS analysis, the time-dependent fluctuations of scattered light from molecules of different size in solution is measured and from the rate of these fluctuations the translational diffusion coefficient (D) is determined. The hydrodynamic radius (R_H), defined as the radius of a hard sphere that diffuses at the same rate as that of the molecule considered, is then derived from the Stokes-Einstein equation, $R_H = kT/6\pi\eta D$, where k is the Boltzmann constant, T is the absolute temperature and η is the solution viscosity (**6**). From DLS analysis, it is possible to calculate the per cent polydispersity (%Pd), a parameter describing the width of the particle size distribution of a protein in a given sample. Notably, %Pd is given by the equation %Pd = $\sqrt{PdI}$ x 100, where PdI is defined as the polydispersity index, PdI = σ^2/Z^2_D. Assuming a Gaussian distribution of a single size population of particles, σ is the standard deviation of the distribution and Z_D is the Z average size, i.e. the intensity-weighed mean hydrodynamic size of the ensemble collection of particles (**7**).

DLS measurements were performed at 25°C on a Zetasizer-Nano-S instrument (Malvern Instruments, UK) at a fixed angle (i.e. 173°) from the incident light (i.e. a He–Ne 4mW laser source at 633 nm). Polystyrene cuvettes (1-cm pathlength, 100μl) (Hellma, Switzerland) were used for all measurements. Each measurement consisted of a single run (15s). The refractive index (n) and viscosity (η) of the protein solutions were taken as **1.450 and 0.887cP**, respectively at 25°C. Scattering data were analyzed with the Nano-6.20 software and expressed as percentage intensity size distribution, as described.

Fluorescence

Fluorescence binding measurements were carried out at 25°C in 20 mM Hepes, pH 7.4, 0.15M NaCl and 0.1% PEG-8000 on a Jasco (Tokyo, Japan) FP-6500 spectrofluorimeter, using excitation/emission slits of 3/5 nm.. Aliquots (2-10μl) of full-length β2GpI or β2GpI peptides 219-232 and 219-229 were added to an αT solution (150nM, 1.5ml). Samples were excited at 280 or

295nm and the spectra of β2GpI or β2GpI peptides were subtracted from those of the corresponding complexes. The data points were interpolated with **eq. 1**, describing tight-binding interaction, to obtain the dissociation constant, K_d, of the complex as a fitting parameter.

$$[\Delta F] = [\Delta F]_{max} \cdot \frac{([R]_T + [L]_T + K_d) + \sqrt{([R]_T + [L]_T + K_d)^2 - 4 \cdot [R]_T [L]_T}}{2 \cdot [R]}$$ **(eq. 1)**

In fluorescence competition measurements, aliquots (5μl) of thrombin S195A mutant (20μM) stock solution were incrementally added to a solution of [F]-hirugen (60nM, 1.5ml). Samples were excited at 492nm and the decrease of fluorescence intensity of [F]-hirugen was recorded at 516 nm as a function of thrombin concentration. The data points were interpolated with **eq. 1**. After [F]-hirugen was saturated with thrombin (i.e. when there was no change in fluorescence emission), increasing concentrations of competing β2GpI (5-10μl aliquots, 40μM stock solution) were added. Finally, to this solution were added incremental concentrations of *unlabelled* hirugen (2-5μl aliquots, 900μM stock solution).

Notably, in binding experiments, the receptor R is αT whereas the ligand L is the intact β2GpI protein (**Fig. 1**) or the synthetic β2GpI peptides (**Fig. 10**), and RL is αT-β2GpI complex. The corresponding signals ΔF and ΔF_{max} are the changes in the fluorescence intensity of αT measured at intermediate and saturating β2GpI concentrations, respectively. In competition experiments (**Fig. 6**), R and L are [F]-hirugen and αT, respectively, and RL is the [F]-hirugen-□αT complex. ΔF and ΔF_{max} are the changes of fluorescence intensity of [F]-hirugen measured at intermediate and saturating αT concentrations, respectively. The dissociation constant, K_d, of the complex was obtained as a fitting parameter.

Surface plasmon resonance (SPR)

SPR measurements were carried out at 25 °C using a carboxymethylated-dextran chip (CM5) on a dual flowcell Biacore-X100 instrument (GE-Healthcare), using the amide coupling chemistry at pH 4.0. Increasing concentrations of PPACK-inhibited wild-type or mutant thrombin solutions (70 μl) were injected over the β2GpI-coated sensor chip at a flow rate of 30 μl/min, with a contact time of 200 sec, in 10 mM Hepes, pH 7.5, 150 mM NaCl, 3 mM EDTA, 0.05% polyoxyethylene sorbitan (HBS-EP⁺). Binding measurements were also performed by reverting the interacting system, i.e. by immobilizing α-thrombin on the sensor chip and injecting β2GpI in the mobile phase. Briefly, using the amide coupling chemistry, a carboxymethylated C1 sensor chip was first derivatized at pH 5.0 with NeutrAvidin (Pierce Biotechnology, IL). Thereafter, human plasma α-thrombin (10μl, 20μM)

was reacted with the bivalent reagent biotinyl-Σ-aminocaproyl-(D)-Phe-Pro-Arg-chloromethylketone (Biotinyl-PPACK) (Bachem, Switzerland) (2 μl, 0.6 mM) to covalently block thrombin active site, while leaving the biotinyl moiety available for interacting with the immobilized NeutrAvidin (**Fig. S2**). A Biotinyl-PPACK-thrombin solution (100 μl, 0.4 μM) was then loaded for 700 sec on the NeutrAvidin-coated C1 chip at a flow rate of 10 μl/min. Finally, aliquots (70 μl) of β2GpI solutions at increasing concentrations were injected over the NeutrAvidin sensor chip saturated with Biotinyl-PPACK-thrombin. Notably, NeutrAvidin (pI=6.3) was used as an excellent alternative to avidin (pI = 10) for minimizing nonspecific binding.

Each binding curve was subtracted for the corresponding baseline obtained on the reference flow cell and accounting for nonspecific binding, which was found <2% of RU_{max}. The dissociation constant (K_d) relative to the binding of the ligand (L), i.e. αT or β2GpI, to the immobilized receptor (R), i.e. β2GpI or αT, was obtained as a fitting parameter by plotting the value of the response units at the steady state (RU_{eq}), after reaching equilibrium at each ligand concentration, and fitting the data points to **eq. 2**, describing the one-site binding model (**8**):

$$RU_{eq} = RU_{max} \cdot \frac{[L]_F}{[L]_F + K_d}$$

(eq. 2)

where RU_{max} is the RU value at saturating L concentrations and $[L]_F$ is the concentration of the free ligand in equilibrium with the receptor-ligand (RL) complex present on the sensor chip surface. When $[R] \ll K_d$, then $[L]_F$ can be approximated to $[L]_T$, i.e. the total ligand concentration in the mobile phase. Data analysis was performed using the BIAevaluation software.

The effect of ionic strength on αT-β2GpI interaction

The effect of ionic strength (I) increase on the affinity of S195A mutant α-thrombin (rS195A) for immobilized β2GpI was treated according to the Debye-Hückel theory, modified to take into account deviations occurring at higher ionic strength (**9**). Because of the instability of αT at low ionic strength, it was not possible to obtain reliable binding data at [NaCl] < 50 mM (**9**). The standard free energy change of complex formation (referred to in this paper as binding energy) is given by: $\Delta G°_b$ = RT·lnK_d, where R is the gas constant, 1.987 cal/(mol·K), T is the absolute temperature (298.15 K), and K_d is the dissociation constant of the rS195A-β2GpI complex at each I value, calculated form the SPR data in **Fig. 3A**. The binding energy ($\Delta G°_b$) can be partitioned into an ionic component ($\Delta G°_I$) and a nonionic component ($\Delta G°_\Phi$), according to the equation: $\Delta G°_b = \Delta G°_I + \Delta G°_\Phi$, where $\Delta G°_I$ accounts for all energy contributions involving charged amino acids, while $\Delta G°_\Phi$ accounts for all

other effects, e.g. hydrophobic, van der Waals, and polar interactions. From the modified Debye-Hückel theory, the ionic strength dependence of $\Delta G°_b$ can be estimated by the equation (**9**):

$$\Delta G°_b = \Delta G°_\phi + \Delta G°_{I°} \cdot \frac{\exp(-\alpha\sqrt{I})}{1+\alpha\sqrt{I}}$$

(eq. 3)

where $\Delta G°_{I°}$ is the value of $\Delta G°_I$ at $I \rightarrow 0$ and α is a constant that is proportional to the distance between the interacting charges and generally increases for a decrease of the binding strength. From the interpolation of data points in the plot of $\Delta G°_b$ against the square root of I (**Fig. 3B**) the values of $\Delta G°_\Phi$, $\Delta G°_{I°}$ and α can be obtained as fitting parameters. For $I \rightarrow \infty$, $\Delta G°_b$ approaches to $\Delta G°_\Phi$, which is the lower asymptote of the curve described by **eq. 3**. For $I \rightarrow 0$, $\Delta G°_b$ approaches the value of $\Delta G°_\Phi + \Delta G°_{I°}$.

SPR competition experiments

When the injected ligand (L) [i.e. Hirugen, HD1 aptamer, or GpIbα(268-282)] was expected to compete with immobilized β2GpI for the specific binding to exosite I or II of αT in the mobile phase, the data of RU_{eq} were fitted to **eq. 4** (**10**):

$$RU_{eq} = RU_{max} \cdot \frac{[\alpha T]_F}{[\alpha T]_F + K_d^{\alpha T}}$$

(eq. 4)

where $K_d^{\alpha T}$ is the dissociation constant relative to the binding of αT to chip-bound β2GpI and $[\alpha T]_F$ is the residual αT concentration in the free, unbound state in the presence of increasing concentrations of the competitor ligand peptide, L. Notably, $[\alpha T]_F$ cannot be approximated to $[\alpha T]_T$ and is expressed as a function of $[\alpha T]_T$, $[L]_T$, and K_d^L by **eq. 5** (**10**):

$$[\alpha T]_F = [\alpha T]_T - \frac{([L]_T + [\alpha T]_T + K_d^L) + \sqrt{([L]_T + [\alpha T]_T + K_d^L)^2 - 4 \cdot [\alpha T]_T \cdot [L]_T}}{2}$$

(eq. 5)

where $[\alpha T]_T$ and $[L]_T$ are the total concentrations of injected αT and L, respectively, and K_d^L is the dissociation constant relative to the binding of αT to L in the mobile phase. Substituting $[\alpha T]_F$, derived from **eq. 5,** into **eq. 4** and considering that $[\alpha T]_T$ and $[L]_T$ are known quantities, $K_d^{\alpha T}$ and K_d^L can be calculated as fitting parameters.

Kinetics of fibrinopeptides release by αT

The release of fibrinopeptides A (FpA) and B (FpB) in the presence or absence of 4μM β2GpI was followed using the method previously reported (**11**). Human fibrinogen, Fb, (Sigma, MO, USA) was desalted on a G25 HiTrap column (GE Healthcare, USA) eluted with HBS, containing 0.1% PEG-8000, at a flow-rate of 1.0ml/min. The concentration of desalted fibrinogen solutions was determined by measuring the absorbance at 280nm ($\varepsilon^{0.1\%} = 1.50$ mg^{-1}·cm^{-2}). Briefly, aliquots (0.9 ml, 0.39 μM) of freshly prepared fibrinogen solution in HBS were added with 0.1ml each of human αT solution (3.0 nM) in HBS to a final concentration of 0.35 μM and 300 pM, respectively. The concentration of thrombin stock solutions was determined spectrophotometrically at 280 nm ($\Sigma^{0.1\%}$ =1.83 mg^{-1}·cm^{-2}). Proteolysis reactions were conducted at 37 °C and blocked at fixed time points with 0.2 ml of 12%(v/v) formic acid. Fibrin and acid precipitated fibrinogen were eliminated by centrifugation at 10,000 g for 5 min at 4 °C. The supernatant (1ml) was withdrawn, lyophilized, and dissolved in 6 M guanidinium hydrochloride aqueous solution (170 μl). Fibrinopepides were separated and quantified by reverse-phase HPLC (RP-HPLC), injecting 100μl of the guanidinium solution onto a (4.6 x 250mm; 5 μM, 300 Å) C18 column (Grace-Vydac, MD, USA) equilibrated in 40mM ammonium phosphate buffer, pH 3.1, and eluted with an acetonitrile gradient from 0 to 17% in 15 min and from 17 to 40% in 15 min at a flow rate of 1 ml/min, recording the absorbance of the effluent at 205 nm. The amount of FpA and FpB released was determined by integrating the area under the chromatographic peaks, using molar absorptivities at 205 nm of 4.4 x 10^4 or 5.12 x 10^4 M^{-1}·cm^{-1}, while the recovery of FpA and FpB was approximately 95% or 90% of that expected from the initial fibrinogen concentration. A biocompatible Bio-410 HPLC system (Perkin-Elmer, CA, USA), connected to a ISS-100 autosampler, was used for all analyses.

The specificity constant k_{catA}/K_{mA} for the release of FpA was determined by interpolating the data points in **Fig. 9A** to **eq. 6**:

$$[FpA]_t = [FpA]_\infty \cdot (1 - e^{-k't})$$

(eq. 6)

where $[FpA]_t$ and $[FpA]_\infty$ is the concentration of FpA at time t and ∞, respectively, and k′ is the observed kinetic constant for FpA release, obtained as a fitting parameter. Under pseudo-first order conditions, i.e. when [Fb α-chain] >> [αT], and low substrate concentration, i.e. when [Fb] < 0.1·K_{mA}, then the observed kinetic constant k′ is expressed by the equation k′ = (k_{catA}/K_{mA})·[αT] and k_{cat}/K_m can be easily derived as k_{catA}/K_{mA} = k′/[αT]. Provided that the K_m of FpA release (K_{mA}) at 37°C, pH 7.4, 0.15M NaCl is 7.2μM (**11**), the concentrations of both Fb and αT used in this work

fully satisfy the conditions reported above. Indeed, [Fb α-chain] = 0.70μM >> [αT] = 300pM and [Fb] = 0.35μM < 0.1·K_{mA}.

The data points relative to the time-dependent release of FpB in **Fig. 9A** were interpolated with **eq. 7**:

$$[FpB]_t = [FpB]_\infty \cdot (1 + \alpha \cdot e^{-k't} - \beta \cdot e^{-k''t})$$

(eq. 7)

where k′ is the observed kinetic constant for FpA release calculated from **eq. 6** and k″ is the observed kinetic constant for the release of FpB, while α= k″/(k′-k″) and β= k′/(k′-k″). As for FpA release, at the αT and Fb concentrations used in this work, the kinetic data can be treated under pseudo-first order an low substrate conditions, whereby k″ = (k_{catB}/K_{mB})·[αT] and (k_{catB}/K_{mB}) = k″/[αT].

Kinetics of PAR1(38-60) hydrolysis by αT

Hydrolysis of the synthetic peptide PAR1(38-60) (1 μM, 3 ml) [38]LDPR↓SFLLRNPNDKYEPFWEDDE[60] by αT (100 pM) was carried out at 25 °C in HBS, containing 0.1% PEG-8000 in the absence and in the presence of 4 μM□β2GpI. At time intervals of 0, 0.5, 1, 1.5, 2, 3, 5, 8, 15 min, aliquots (360 μl) were taken and added with 4% (v/v) aqueous/TFA (10 μl). Acid-quenched aliquots were loaded (350 μL) onto a Vydac C18 column (300 Å, 5 μm, 4.6 x 250 mm), eluted with a linear acetonitrile-0.078% TFA gradient from 10-45% in 40 min. The release of the C-terminal PAR1(42-60) fragment was quantified by integrating the area under the chromatographic peak corresponding to PAR1(42-60) fragment, having approximately the same molar extinction coefficient of the parent peptide PAR1(38-60).

The kinetic data reported in **Fig. 9B** were interpolated with **eq. 8**, describing a pseudo-first order reaction:

$$[P]_t = [P]_\infty \cdot [1 - \exp(-k_{obs}t)]$$

eq. 8

where [P]$_\infty$ is the concentration of the product fragment PAR1(42-60) after all the substrate PAR1(38-60) has been cleaved, and k_{obs} is the observed kinetic constant for PAR1(38-60) hydrolysis, obtained as a fitting parameter. As for the release of FpA, and provided that the K_m of PAR1(38-60) hydrolysis by αT at 25°C is 7.6±0.6μM (**12**), the concentrations of PAR1(38-60) and αT used in this work fully satisfy the conditions of a pseudo-first order reaction, i.e. [PAR1(38-60)] = 1 μM >> [αT] = 100 pM, and low substrate concentration, i.e. [PAR1(38-60)] = < 0.2·K_m. Hence, the kinetic

constant k_{obs} can be expressed as $k_{obs} = (k_{cat}/K_m) \cdot [\alpha T]$ and the specificity constant $s = k_{cat}/K_m$ can be easily derived as $s = k_{obs}/[\alpha T]$.
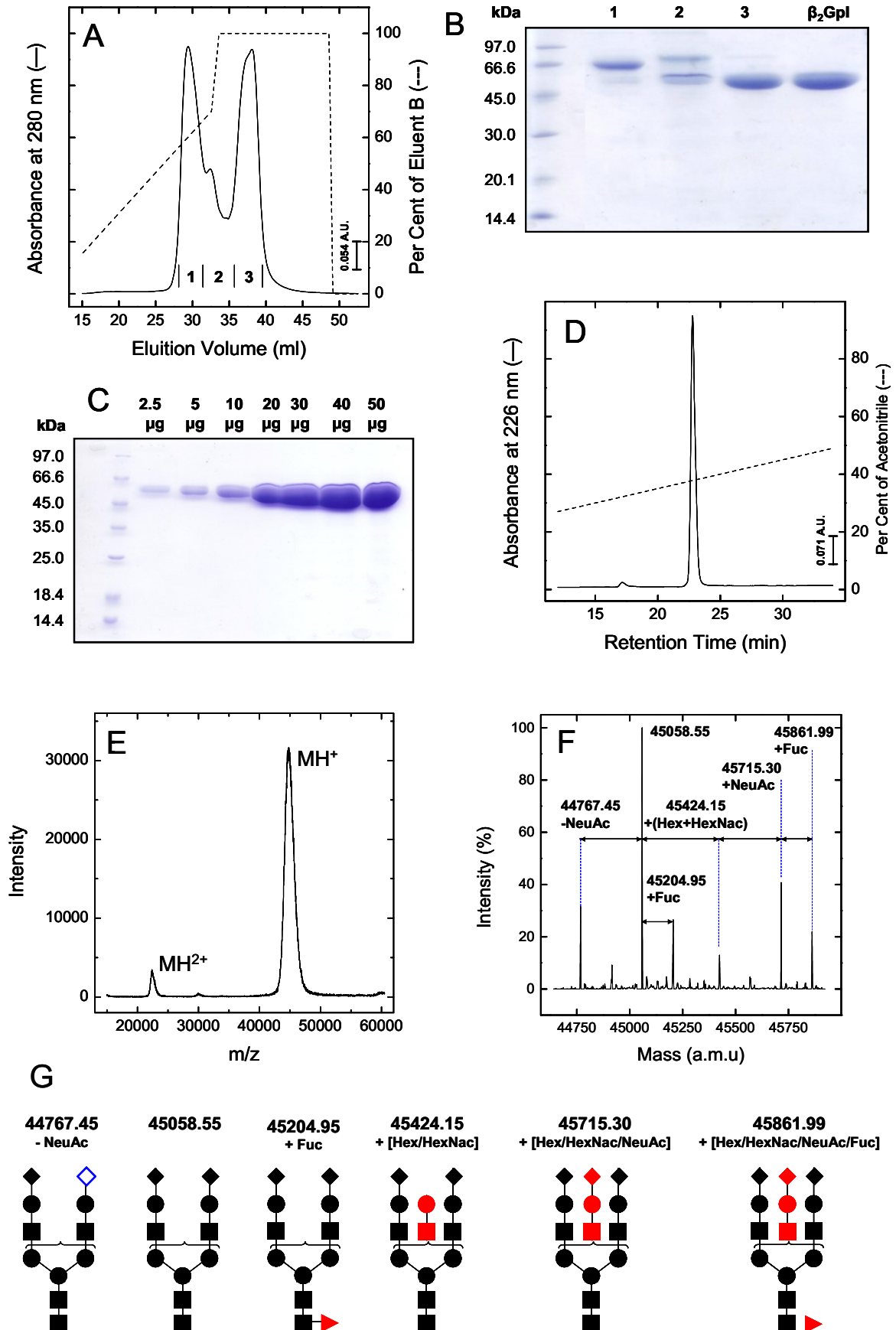
Figure S1. Purification and characterization of β2GpI from human plasma. (**A**) Heparin-sepharose affinity chromatography. After perchloric acid precipitation and centrifugation, an aliquot (1ml) of the supernant solution containing β2GpI was fractionated on a HiTrap heparin-sepharose column eluted with a linear gradient of buffer B (---) at a flow-rate of 2 ml/min. (**B**) SDS-PAGE (4-12% acrylamide) analysis of 20-μl aliquots corresponding to the fractions eluted from Heparin-sepharose column in panel A. (**C**) SDS-PAGE (4-12% acrylamide) analysis of increasing amounts (2.5-50μg) of purified β2GpI. (**D**) RP-HPLC analysis of purified β2GpI, as in panel A. An aliquot (50μl) was loaded onto an analytical (4.6x150mm) column eluted with a linear acetonitrile-0.078%TFA gradient (---) at a flow-rate of 0.8 ml/min. (**E**) Low-resolution mass spectrum of purified β2GpI. Measurements were carried out on a 4800 MALDI TOF/TOF instrument (Applied Biosystems), yielding an average mass value of **44990** a.m.u and **22495** a.m.u. for the MH^+ and MH^{2+} molecular ions, respectively. (**F**) High-resolution mass spectrum of purified β2GpI. Measurements were carried out on a Xevo G2S Q-TOF instrument (Waters), yielding the average mass values as indicated. Heterogeneity of molecular masses arise from the natural glycosylation processing of β2GpI in vivo, generating variably trimmed carbohydrate chains on $β_2$GpI. The major component has an experimental molecular mass of **45058.5±1.0** a.m.u., corresponding to the experimental mass of deglycosylated β2GpI peptide chain (**36239.2±0.7** a.m.u.), processed at the four glycosylation sites on β2GpI (Asn143, Asn164, Asn174, Asn234) according to the most common N-glycosylation pattern in humans: $-(GlcNAc)_2-(Man)_3-(GlcNAc)_2-(Man)_2-(NeuAc)_2$ (**2204.78 a.m.u.**) yielding a theoretical average mass of **45058.3** a.m.u. for the fully glycosylated β2GpI, identical to that determined experimentally. (**G**) Proposed glycosylation pattern for the minor β2GpI species in the MS of panel F. Hex: Mannose (Man) or Galactose (Gal) (●, 162 a.m.u.); Fuc: Fucose (▶, 146 a.m.u.); GlcNAc: N-acetylglucosamine (■, 203 a.m.u.); NeuAc: N-acetylneuraminic acid (♦, 291 a.m.u.). Starting from the mass of the major component, added sugars are coloured in red (filled symbols), whereas removed sugars are in blue (empty symbols). The present analysis does not allow to identify which of the four carbohydrate chains in β2GpI contains additional sugar moieties.
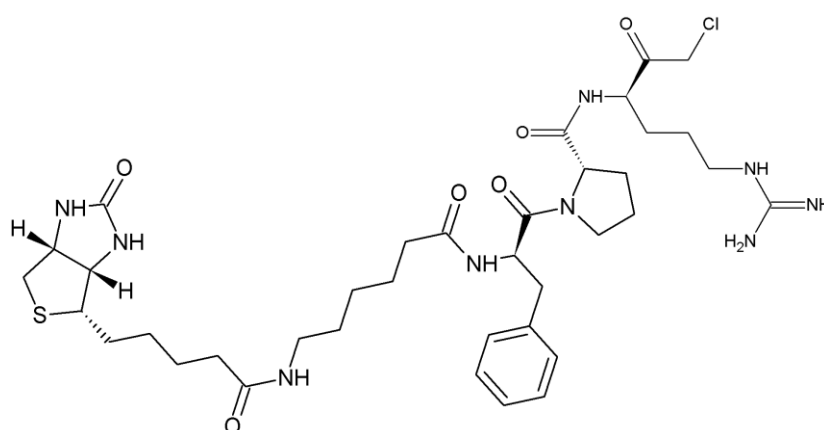
Figure S2. Structure of the bivalent reagent biotinyl-Σ-aminocaproyl-(D)-Phe-Pro-Arg-chloromethylketone (Biotinyl-PPACK).
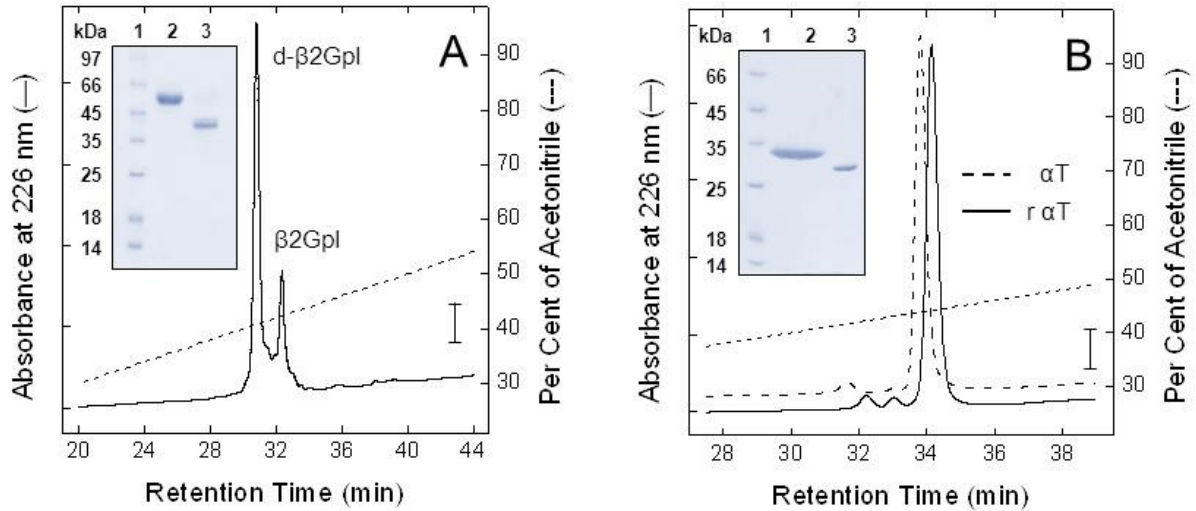
Figure S3. Production of the deglycosylated form of β2GpI and αT. (**A**) RP-HPLC analysis and reducing SDS-PAGE (4-12% acrylamide) (**Inset**) of the deglycosylation reaction of natural β2GpI with PNGase-F. The protein material, eluted in correspondence of the peaks labeled as β2GpI and d-β2GpI, was collected, analyzed by mass spectrometry (MS), and found to correspond to the fully glycosylated (β2GpI) or deglycosylated (d-β2GpI) forms, with molecular masses of **45057.8±1.0** and **36239.2±0.7** a.m.u., respectively. (**C**) RP-HPLC analysis and SDS-PAGE (**Inset**) of natural/glycosylated human thrombin (αT) and recombinant deglycosylated αT (rαT), expressed in *E. coli*. The molecular masses of αT and rαT were determined as **36442.6±0.6** and **33820.7±0.8** a.m.u., respectively. Samples were loaded onto a Grace-Vydac C4 analytical column (4.6x150mm, 5μm granulometry) eluted (0.8ml/min) with a linear 0.078%-TFA acetionitrile gradient (---). The protein material eluted in correspondence of the chromatographic peaks was collected and analyzed by high-resolution MS on a Xevo G2S instrument (Waters).
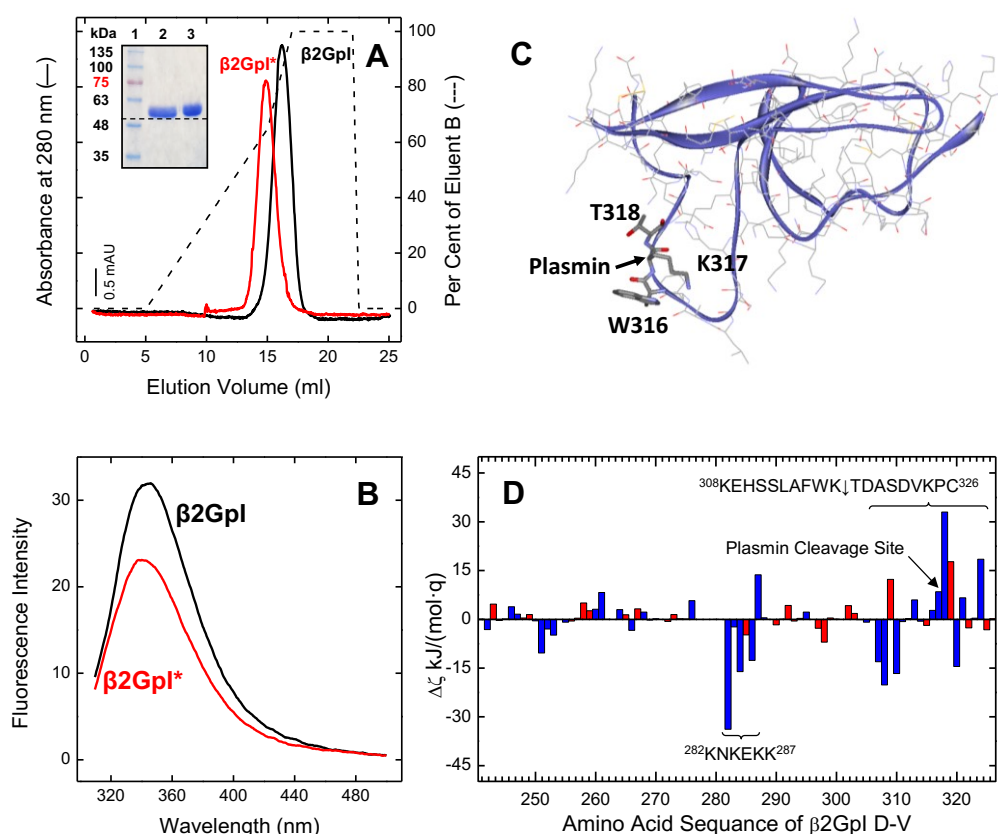
Figure S4. Purification and characterization of the nicked β2GpI*. (**A**) β2GpI* was prepared by treating plasma purified β2GpI (1mg/ml) for 2h at 37°C with human plasmin at an enzyme:substrate ratio of 1:50 (w/w) in 20mM Tris-HCl, pH 7.5, containing 150mM NaCl (buffer A), and 0.3mM CaCl$_2$. Under these conditions, proteolysis reaction occurred quantitatively at a single peptide bond. The reaction mixture (0.5mg) was loaded onto a HiTrap heparin-sepharose column (GE-Healthcare), equilibrated with buffer A and eluted (1ml/min) with a linear gradient (---) of buffer A containing 0.35M NaCl. Notably, β2GpI* was eluted earlier than the intact protein, in agreement with the lower affinity of β2GpI* for heparin. LC-MS analysis of β2GpI*, under reducing and non-reducing conditions, allowed us to unequivocally establish that proteolysis occurred exclusively at the K317-T318 bond. (**Inset**) SDS-PAGE analysis (4-10% acrylamide) under reducing conditions of aliquots (5μg) of β2GpI* (lane 2) and intact β2GpI (lane 3), as eluted form the heparin-sepharose column; lane 1, molecular weight protein standards. As expected, reduced β2GpI* (1-317) migrates slightly faster than β2GpI (1-326). (**B**) Fluorescence spectra of β2GpI and β2GpI* at 25°C. Protein samples (100nM) were excited at 295nm. The lower signal intensity of β2GpI* is consistent with partial unfolding of Trp316 in the C-terminal loop 308-326 upon cleavage. (**C**) Ribbon-drawing of D-V in β2GpI (1c1z). The plasmin cleavage site is indicated by an arrow. (**D**) Histogram reporting the variations of the electrostatic potential for each amino acid (*i*) of D-V in β2GpI* and β2GpI structure ($\Delta\zeta_i = \zeta_{i,D-V*} - \zeta_{i,D-V}$). Blue and red bars refer to changes, expressed as the absolute value, of positive and negative electrostatic potential, respectively. The data indicate that, upon peptide bond cleavage, there is a net decrease of the positive potential and an increase of the negative potential in the loop regions 282-287 and 308-326. Electrostatic calculations were carried out using the BLUUES program, run on the structure of D-V and D-V*. The coordinates of D-V are those of the corresponding segment in the X-ray structure of full-length intact β2GpI (1c1z), while those of D-V* were obtained by simulating the cleavage of the peptide bond K317-T318 and then minimizing the

structure with the AMBER99 force field, as implemented in the MOE suite (The Chemical Computing Group, Montreal, Canada).
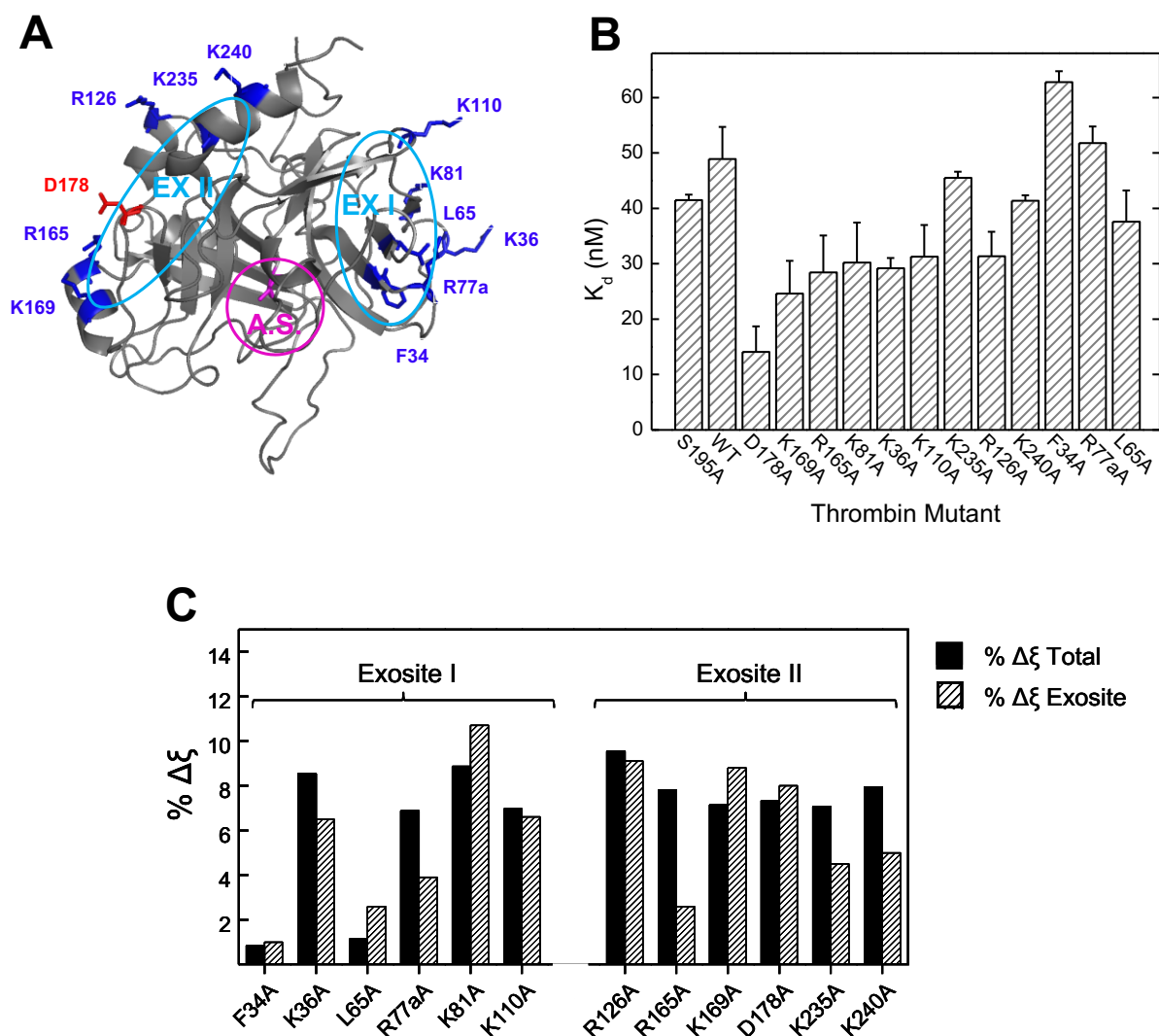
Figure S5. Effect of Ala-mutations at αT exosites on β2GpI-αT interaction. (**A**) Ribbon-drawing representation (grey) of αT structure (1ppb). The basic amino acids (Lys or Arg) and the acidic D178 which have been muted to Ala at thrombin exosites are coloured in blue and red, respectively. The approximate position of the active site (magenta) and exosite I and II (cyan) are indicated by circles. (**B**) Bar-plot of the K_d values of Ala-mutants of αT for immobilized β2GpI. K_d values were obtained by plotting RU_{max} values as a function of increasing concentrations of thrombin mutants and fitting the data points with **eq. 2**. All measurements were carried out at 25°C in HBS-EP$^+$, pH 8.0. K_d values were the average of three measurement, with standard deviations represented by error bars. (**C**) Effect of Ala-mutations on the variation of αT electrostatic potential of. Differences in ζ values between each αT mutant and the wild-type enzyme were calculated at the atomic level and reported as the percent variation over the total αT electrostatic potential (grey bars) or considering only the surface potential generated by the positively charged amino acids forming exosite-I or exosite–II (black bars), as indicated.
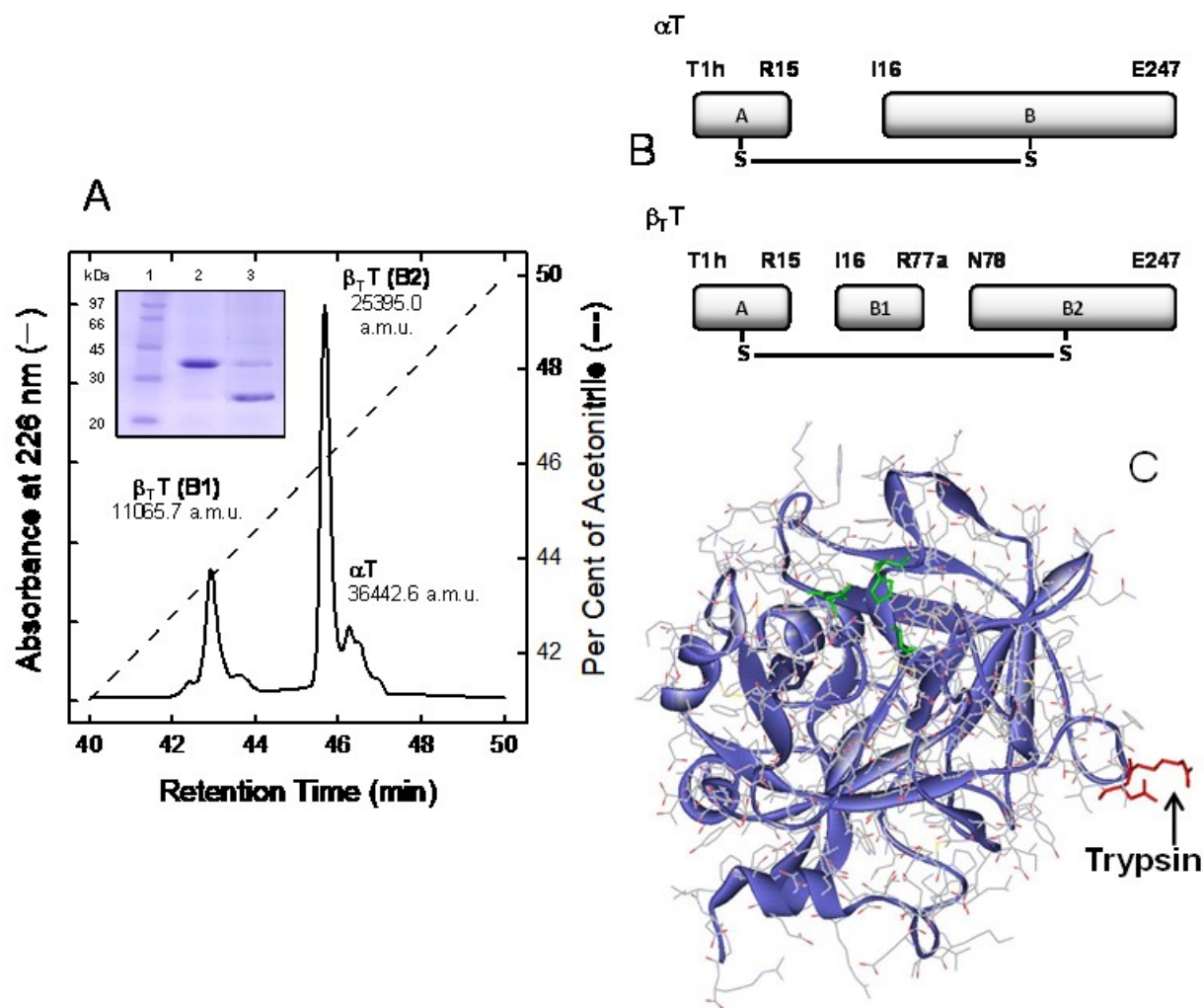
Figure S6. Production and characterization of β$_T$-thrombin (β$_T$T). (A) RP-HPLC analysis of the proteolysis reaction of αT with trypsin. After 3-h reaction, an aliquot (40μl, 10μg) was loaded, under nonreducing conditions, onto a Grace-Vydac C4 analytical RP-column (4.6x150 mm), eluted with an acetonitrile-0.1%TFA gradient (---) at a flow rate of 0.8 ml/min. The chemical identity of the protein material eluted from the column was established by MS, yielding mass values in agreement with those of the proteolytic fragments forming β$_T$T, as schematized in **panel B**. (**Inset**) SDS-PAGE (4-12% acrylamide) analysis under reducing conditions of the proteolysis reaction of αT with trypsin. After 40min, aliquots (12μl, 3μg) of the reaction mixture were analyzed: lane 1, molecular weight protein standards; lane 2, proteolysis mixture at t = 0 min; lane 3, proteolysis mixture at t = 40 min. (**B**) Schematic representation of the polypeptide chain topology in αT and β$_T$T. β$_T$T(B1) corresponds to fragment 16-77a of αT B-chain (11065.7±0.8 a.m.u.), while β$_T$T(B2) corresponds to fragment 78-247 of the B-chain (23395.0±1.2 a.m.u.), linked through a disulfide bridge to the A-chain. In β$_T$T, under nondenaturing conditions, β$_T$T(B1) and β$_T$T(B2) fragments form a noncovalent complex, which instead dissociates during RP-HPLC analysis, under denaturing condition, as in panel A. (**C**) The trypsin cleavage site in αT. The tryptic cleavage of the peptide bond Arg77a-Asn78 (coloured in red) leads to disruption of exosite-I structure and molecular recognition properties (**13**). The catalytic amino acids (H57, D102 and S195) are indicated in green. The ribbon drawing was generated on the coordinates of deriving from the X-ray structure of αT (1ppb) (**14**) using the ViewerPro 4.2 software (Accelerys Inc., USA).

112
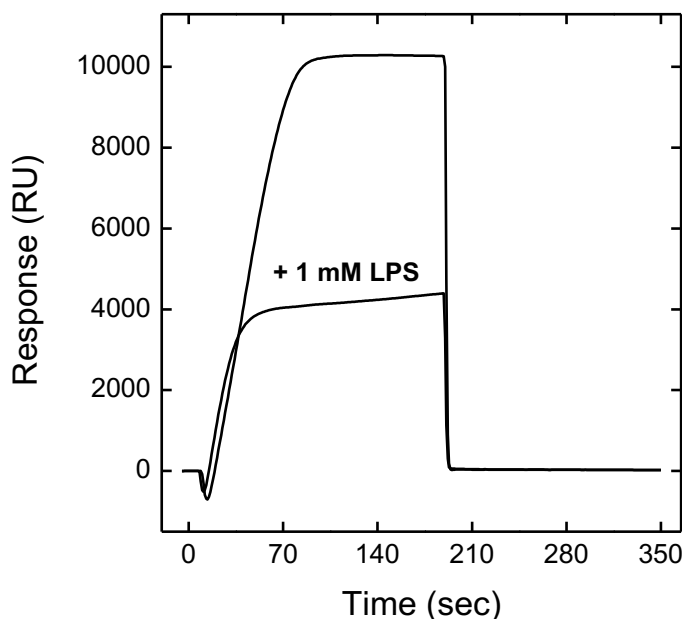
Figure S7. Effect of lipopolysaccharide (LPS) on the immobilization efficiency of β2GpI on the dextran carboxymethylated sensor chip. Purified β2GpI (50 μg/ml) in 10 mM ammonium acetate buffer pH 4.5 was injected for 180 sec at a flow rate of 5 μl/min on a CM5 chip. Final levels of 10272 RU were obtained in the absence of LPS, whereas in the presence of 1mM LPS a value of only 4364 RU was obtained. The marked decrease of derivatization yield, that we measured in the presence of LPS, is consistent with the hypothesis (see main text) that most of β2GpI molecules are anchored onto the sensor chip through the lower face of domain V, containing >3-fold higher percentage of reactive Lys-residues, compared to the rest of the protein. Indeed, LPS is a highly negatively charged molecule that specifically binds to the highly positive lower region of β2GpI domain V (**15**), thus reducing the interaction with the negative surface of dextran carboxymethylated sensor chip. Notably, a similar strategy has been recently reported for defining the most likely orientation of immobilized αT in binding to coagulation factor V (**16**).
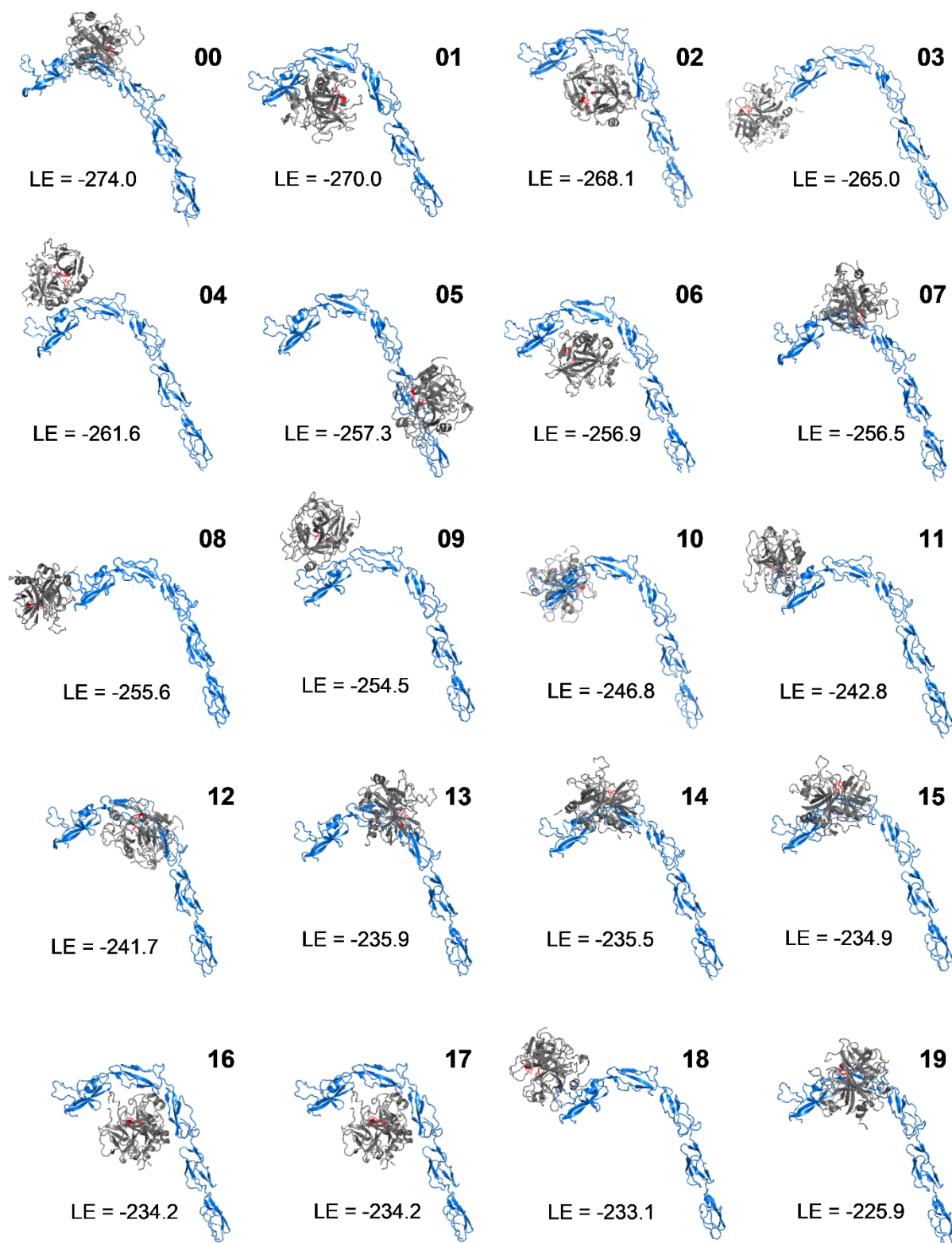
Figure S8. Schematic representation of the 20 theoretical models corresponding to the structure of αT-β2GpI complex. The models were produced with the automated program ClusPro-2.0 (**17**), starting for the coordinates of des-PPACK αT (1ppb) (**14**) and β2GpI (1c1z) (**18**), and ranked according to the population of their corresponding clusters, i.e. the number of members (M) forming that cluster. The structure of αT (grey) and β2GpI (blue) are shown as ribbon drawing. The position of β2GpI domains (I – V) are indicated in the model_00. The orientation of β2GpI was kept constant

and the active site on αT was highlighted in red. As obtained from ClusPro default output, only the models representative of the 10 largest clusters were considered. In all models, the active-site region of αT was disclosed and fully accessible to ligand binding, consistent with the experimental data in **Figs. 2D and 5B**. In seven models (01, 03, 04, 05, 07, 08 and 09) exosite-II was identified as the region of αT responsible for binding to β2GpI, in agreement with our findings showing that exosite-II is a hot spot in αT-β2GpI interaction (**Figs. 6, 8**). In three models (00, 02, and 06) the negative patch around the Na⁺-binding site (n1b+n3) was found to interact with the positively charged heparin binding site in β2GpI D-V. Interestingly, exosite-I was not involved in any of the top 10 models, consistent with data in **Figs. 7-9**. When β2GpI was being analyzed, it was found that in five models (01, 03, 04, 08 and 09), D-IV and (part of) D-V were directly involved in αT binding. In three models (00, 02, and 06) only D-V was involved, whereas in only one model (07) the binding site was localized in D-II.

References

1   De Filippis, V., Quarzago, D., Vindigni, A., Di Cera, E. and Fontana, A. (1998) Synthesis and characterization of more potent analogues of hirudin fragment 1-47 containing non-natural amino acids. *Biochemistry.* **37**, 13507-13515.

2   Wurm, H. (1984) Beta 2-glycoprotein-I (apolipoprotein H) interactions with phospholipid vesicles. *Int. J. Biochem.* **16**, 511-515.

3   Cucnik, S., Krizaj, I., Rozman, B., Kveder, T. and Bozic, B. (2004) Concomitant isolation of protein C inhibitor and unnicked beta2-glycoprotein I. *Clin. Chem. Lab. Med.* **42**, 171-174.

4   Pozzi, N., Acquasaliente, L., Frasson, R., Cristiani, A., Moro, S., Banzato, A., Pengo, V., Scaglione, G. L., Arcovito, A., De Cristofaro, R. and De Filippis, V. (2013) beta2 - glycoprotein I binds to thrombin and selectively inhibits the enzyme procoagulant functions. *J. Thromb. Haemost.* **11**, 1093-1102.

5   Artenjak, A., Leonardi, A., Krizaj, I., Ambrozic, A., Sodin-Semrl, S., Bozic, B. and Cucnik, S. (2014) Optimization of unnicked beta2-glycoprotein I and high avidity anti-beta2-glycoprotein I antibodies isolation. *J. Immunol. Res.* **2014**, 195687.

6   Murphy, R. M. (1997) Static and dynamic light scattering of biological macromolecules: What can we learn? *Curr. Opin. Biotechnol.* **8**, 25-30.

7   Arzenvsek, D. (2010) Dynamic light scattering and application to proteins in solutions. Seminar, Department of Physics, University of Ljubljana. , 1-18

8   Gesellchen, F., Zimmermann, B. and Herberg, F. W. (2005) Direct optical detection of protein-ligand interactions. *Methods Mol. Biol.* **305**, 17-46.

9   Richardson, J. L., Fuentes-Prior, P., Sadler, J. E., Huber, R. and Bode, W. (2002) Characterization of the residues involved in the human alpha-thrombin-haemadin complex: An exosite II-binding inhibitor. *Biochemistry.* **41**, 2535-2542.

10   Gamsjaeger, R., Kariawasam, R., Bang, L. H., Touma, C., Nguyen, C. D., Matthews, J. M., Cubeddu, L. and Mackay, J. P. (2013) Semiquantitative and quantitative analysis of protein-DNA interactions using steady-state measurements in surface plasmon resonance competition experiments. *Anal. Biochem.* **440**, 178-185.

11   Ng, A. S., Lewis, S. D. and Shafer, J. A. (1993) Quantifying thrombin-catalyzed release of fibrinopeptides from fibrinogen using high-performance liquid chromatography. *Methods Enzymol.* **222**, 341-358.

12   Ayala, Y. M., Cantwell, A. M., Rose, T., Bush, L. A., Arosio, D. and Di Cera, E. (2001) Molecular mapping of thrombin-receptor interactions. *Proteins.* **45**, 107-116.

13   Hofsteenge, J., Braun, P. J. and Stone, S. R. (1988) Enzymatic properties of proteolytic derivatives of human alpha-thrombin. *Biochemistry*. **27**, 2144-2151

14   Bode, W., Turk, D. and Karshikov, A. (1992) The refined 1.9-A X-ray crystal structure of D-phe-pro-arg chloromethylketone-inhibited human alpha-thrombin: Structure analysis, overall structure, electrostatic properties, detailed active-site geometry, and structure-function relationships. *Protein Sci.* **1**, 426-471.

15   Agar, C., van Os, G. M., Morgelin, M., Sprenger, R. R., Marquart, J. A., Urbanus, R. T., Derksen, R. H., Meijers, J. C. and de Groot, P. G. (2010) Beta2-glycoprotein I can exist in 2 conformations: Implications for our understanding of the antiphospholipid syndrome. *Blood.* **116**, 1336-1343.

16   Corral-Rodriguez, M. A., Bock, P. E., Hernandez-Carvajal, E., Gutierrez-Gallego, R. and Fuentes-Prior, P. (2011) Structural basis of thrombin-mediated factor V activation: The Glu666-Glu672 sequence is critical for processing at the heavy chain-B domain junction. *Blood.* **117**, 7164-7173.

17   Comeau, S. R., Gatchell, D. W., Vajda, S. and Camacho, C. J. (2004) ClusPro: An automated docking and discrimination method for the prediction of protein complexes. *Bioinformatics.* **20**, 45-50

18   Schwarzenbacher, R., Zeth, K., Diederichs, K., Gries, A., Kostner, G. M., Laggner, P. and Prassl, R. (1999) Crystal structure of human beta2-glycoprotein I: Implications for phospholipid binding and the antiphospholipid syndrome. *EMBO J.* **18**, 6228-6239.

CHAPTER 3.1

Noncanonical Proteolytic Activation of Human Prothrombin by Subtilisin from *Bacillus subtilis* may Shift the Procoagulant-Anticoagulant Equilibrium Toward Thrombosis

Giulia Pontarollo[1], Laura Acquasaliente[1], **Daniele Peterle**, Roberta Frasson, Ilaria Artusi and Vincenzo De Filippis

Department of Pharmaceutical and Pharmacological Sciences, University of Padova, Via F. Marzolo 5, Padova, 35131, Italy

[1]Both authors equally contributed to this work

INTRODUCTION

Blood coagulation is a finely regulated physiological process which culminates with the factor Xa-mediated conversion of the prothrombin (ProT) zymogen to the active α-thrombin (αT) enzyme, which in turn is responsible for the generation of insoluble fibrin and activation of platelets *via* the GpIbα–PAR1 pathway (**1,2**). ProT (~72 kDa) is a vitamin K-dependent glycoprotein produced in the liver and circulating at a relatively high plasma concentration (0.1 mg/ml) (**3**). The domain architecture of ProT (**Fig. 4**) comprises a Gla domain (residues 1-46), a kringle-1 (residues 65-143) and kringle-2 (residues 170-248) domain, and a chymotrypsin-like protease domain (residues 285-579), connected by three intervening linker regions (Lnk-1, -2, and -3) (**4**). Isolated factor Xa (FXa) has low intrinsic ProT-converting activity, but when it is assembled in the presence of Ca^{2+} with cofactor Va in the prothrombinase complex on the platelet surface its ability to activate ProT is increased by about five orders of magnitude (**5**). FXa cleaves ProT in a concerted manner at two sites, i.e. Arg271 and Arg320, but the order of peptide bond cleavage is highly context dependent. On the platelet surface, FXa first cleaves ProT at Arg271 generating the inactive precursor prethrombin-2 (Pre2), which is attacked by FXa at Arg320 to generate the active αT species, formed by the polypeptide chains Thr272-Arg320 and Ile321-Glu579 (**6**). The N-terminal chain undergoes further autoproteolytic cleavage at Arg284-Thr285 to yield the mature αT (**Fig. 4**). At variance, on the membrane of red blood cells, FXa first cleaves ProT at Arg320, generating the catalytically active

meizothrombin, and then at Arg271 to generate the mature αT (**7**) (**Fig. 4**). Notably, αT is formed by the A-chain (residues 285-320) and the B-chain (residues 321-579), connected by the disulphide bridge Cys293-Cys439, and differs from the immediate zymogen Pre2 only in the cleaved Arg320-Ile321 bond and for the absence of the fraying N-terminal segment Thr272-Arg284 (**8**).

It is widely accepted that the route to ProT activation follows the classical mechanism of trypsinogen activation established earlier by the seminal work of Bode and Huber (**9**), whereby cleavage of the Arg320-Ile321 allows the formation of a critical salt bridge between the positive N^{α}-ammonium group of the newly generated Ile321-Val322-segment and the negative side-chain of Asp524. This electrostatic coupling triggers a large conformational change leading to the formation/stabilization of the substrate binding sites and oxyanion hole required for catalysis. According to the model, the effect of salt bridging is mainly conformational (**10**), as the zymogen exists in unfavourable conformational equilibrium between inactive (E*) and active (E) forms, and Ile321-Asp524 salt bridge formation is thought to stabilize the active E form (**11**). For the different zymogens, the pre-existing E $\leftrightarrow$ E* equilibrium is variably shifted to the E* form with equilibrium constants (K_{eq}) ranging from 10^8 (trypsinogen) (**12**) to 7 (tissue plasminogen activator) (**13**). For Pre2, a K_{eq} of 10 has been recently determined (**14**). An indirect, albeit stringent, proof of the existence of the E $\leftrightarrow$ E* equilibrium in ProT is that protein binding to thrombin precursors can effectively stabilize the active E form, as demonstrated in the case of staphylocoagulase (SC) (**15**) and von Willebrand factor binding protein (vWbp) (**10**), two proteins secreted from the virulent Gram-positive bacterium *S. aureus* exploiting a molecular mimicry mechanism to orient their N-terminal Ile1-Val2 dipeptide into the Asp524 cavity, thus leading to non-proteolytic activation of ProT.

Proteolytic conversion of ProT to meizothrombin or αT can be also performed by exogenous non-physiological activators, such as serine and metallo-proteases present in the snake venom (**16**) or secreted by bacterial cells (**17-21**). The best characterized proteolytic activator of this group is ecarin, a zinc-protease isolated from the venom of the viper *Echis carinatus*, that cleaves ProT at the same peptide bond as FXa, i.e. Arg320-Ile321, generating meizothrombin which is ultimately converted to αT after autolysis at Arg284 (**16**), thus resulting in systemic thrombus formation. Nonetheless, little is known about the role that bacterial proteases, possibly released in the bloodstream during infection, might play in inducing blood coagulation by directly activating ProT *via* proteolysis. This issue is particularly important as sepsis, caused by either Gram-positive and Gram-negative bacteria, is frequently complicated by coagulopathies and, in about one third of these cases, by disseminated intravascular coagulation (DIC), a hypercoagulable state often leading to multiple organ failure and death (**22**).

In the present study, we describe the results of experiments designed to investigate the ability

of subtilisin to proteolytically activate ProT and trigger fibrin generation and platelets aggregation. Subtilisin (EC 3.4.21.14) (**23**) is a serine protease (27.3 kDa) secreted by *Bacillus subtilis*, a facultative aerobe Gram-positive bacterium which is found in the gastrointestinal tract of humans, lacks obvious pathogenicity (**24**) and becomes virulent only in immunodeficient subjects (**25**). Subtilisin is the prototype member of the subtilase family, the second largest family of serine proteases (after the chymotrypsin clan) identified till date and known members (either pathogenic or non-pathogenic) span across eubacteria, archaebacteria, eukaryotes and viruses (**26**). Subtilisins exhibit broad substrate specificity, with a preference to cleave after hydrophobic residues, even though cleavage at basic amino acids are not rare (**27**). Our results show that addition of subtilisin (50 nM - 2 μM) to whole blood samples is able to bypass the coagulation cascade and induce blood clot formation by directly activating ProT through zymogen cleavage at Arg271-Thr272 and Ala470-Asn471 peptide bonds. The resulting thrombin-like species, hereafter denoted as σPre2, is able to proteolytically convert fibrinogen into fibrin and to aggregate platelets. Notably, the raise of thrombin-like activity is caused by the alternative cleavage at Ala470-Asn471 bond and subsequent formation of the Asn471-Asp524 intramolecular salt bridge. These findings establish a new paradigm for the proteolytic activation of ProT. Furthermore, our data widen the current notion that bacterial infections are positively correlated to thrombotic risk and suggest that even non-virulent bacteria, such as *B. subtilis*, can shift the delicate procoagulant-anticoagulant equilibrium towards thrombosis.

EXPERIMENTALS

Reagents

Human αT, ProT, PC, and rabbit TM were purchased from Haematologic Technologies (Essex Junction, VT). Subtilisin (EC 3.4.21.62) from *Bacillus subtilis*, ecarin from *Echis carinatus*, human plasma fibrinogen, *p*-aminobenzamidine (PABA), trifluoroacetic acid (TFA), (D)-Phe-Pro-Arg-chloromethyl ketone (PPACK), and potassium cyanate (KCNO) were purchased from Sigma (St. Louis, MO, USA). Recombinant human Pre2 was expressed in *E. coli*, renatured and purified as previously detailed (**34,35**), while αT was obtained from Pre2 after ecarin activation. Sequencing-grade bovine trypsin was from Promega (Medison, WI). Chromogenic substrates S2238, S2366 and S2765 were purchased from Chromogenix (Badform, MA). (D)-Phe-Pip-Arg-OH (FPR), hirugen [54]GDFEEIPEEY*LQ[65] (**53**), hirudin N-terminal domain 1-47, Hir(1-47) (**71**), biotinyl-PEG-GpIbα(GDEGDTDLY*DY*Y*PEE) (**44**), and PAR1(38-60) [8]LDPR↓SFLLRNPNDKYEPFWEDDE[60] (**52**) were synthesised in our laboratory by the solid phase strategy, using the fluorenylmethyloxycarbonyl-chemistry on a PS3 automated synthesizer (Protein Technologies, AZ), purified by RP-HPLC and chemically characterized by high-resolution mass

spectrometry. Notably, Y* stands for tyrosine phosphate. Reagents for electrophoresis were from Sigma or Bio-Rad (Hercules, CA). All other salts, solvents and reagents were of analytical grade and purchased from Sigma or Merck (Darmstadt, Germany).

Limited proteolysis of ProT and Pre2 by subtilisin

ProT or Pre2 (0.1 mg/ml) were reacted with subtilisin (0.05 μg/ml) at different temperatures in 5 mM Tris-HCl, pH 7.4, 0.15 M NaCl, 0.1% PEG-8000 (TBS), containing 5 mM CaCl$_2$. At time intervals, aliquots of proteolysis mixtures were taken and the protein component precipitated overnight at -20°C with 10% ice-cold trichloroacetic acid (TCA) in acetone. After centrifugation, the protein pellet was dissolved with nonreducing sample loading buffer, sonicated for 10min, analyzed by nonreducing SDS-PAGE (4-12% acrylamide) and then Coomassie stained. Alternatively, aliquots of the proteolysis mixture were taken and analyzed for hydrolytic activity on the chromogenic substrate S2238 (see below). For Pre2, the kinetics of proteolysis was monitored by either nonreducing SDS-PAGE (4-14% acrylamide) and RP-HPLC. plasmid containing the cDNA of prethrombin-2 (Pre2) was a generous gift of Prof. Huntington (Cambridge University). The recombinant inactive mutant rS195A, obtained by single-point mutagenesis, was expressed in *E. coli*, subjected to *in vitro* disulphide oxidative refolding, activation by ecarin, and characterized as previously detailed (**44,45**). β$_T$-thrombin (β$_T$T) was obtained by proteolysis of human αT (7μM) with bovine pancreas trypsin (35nM) for 3 hours at 37°C in HBS, and characterized as previously detailed (**46,43**). The concentrations of thrombin solutions were determined by measuring the absorbance at 280nm, using an absorptivity coefficient of 66390 M^{-1}·cm^{-1}. For the concentration of ProT solutions, the absorptivity coefficient of 109790M^{-1}·cm^{-1} was used. The relative intensity of the Pre2 gel bands, after Coomassie staining, was estimated by densitometric analysis, using a Geliance-600 Chem-Imaging system (Perkin-Elmer, Norwalk, CA) and the Image-J software (www.imagej.nih.gov). RP-HPLC analyses were performed on a Grace-Vydac (Columbia, MD) C4 (4.6 x 150mm) analytical column, connected to a Jasco (Tokyo, Japan) 1500 HPLC system. The chromatographic peaks corresponding to intact Pre2 were integrated using the software Borwin. The densitometric or chromatographic data were fitted to equation 1, describing a pseudo-first order reaction (**36**):

$$[S] = [S_0] \cdot e^{-kt}$$

(eq. 1)

where [S$_0$] and [S] is the Pre2 concentration at the beginning of the reaction and after time t, respectively, and k is the observed kinetic constant for hydrolysis, obtained as a fitting parameter. Under pseudo-first order conditions, the specificity constant (s = k$_{cat}$/K$_m$) for the hydrolysis of Pre2

by subtilisin was derived as s = k/[E], where [E] is the protease concentration.

Identification of the subtilisin cleavage sites on ProT and Pre2

The cleavage sites were identified by electroblotting the protein bands, generated from ProT and Pre2, onto an Immobilon membrane (Merck-Millipore, Billerica, MA) and N-terminal sequencing on an automated Procise sequencer (Applied Biosystems, Foster City, CA). Blotting was performed at 4°C in 10 mM 3-cyclohexylamino-1-propanesulfonate, pH 10.5, at 50 Volt for 3 h. Alternatively, the gel bands were excised and subjected to *in situ* peptide mass fingerprint with trypsin as described (**72**). After extraction of the tryptic peptides from the gel, the proteolytic mixture was loaded onto a Grace-Vydac (Hesperia, CA) C4 (1 x 10mm) microbore column connected to an Agilent (Santa Clara, CA) 1290 UHPLC system. The column was eluted at a flow-rate of 50 μl/min, with a linear aqueous acetonitrile-0.1% formic acid gradient, from 15 to 65% in 30 min. The effluent from the column was analysed on-line by high-resolution mass spectrometry (MS), with respect to mass values and amino acid sequence data. Using a different approach, aliquots of the proteolysis mixture with subtilisin, conducted at 10°C in TBS without PEG-8000, were taken and analyzed by LC-MS to obtain the accurate mass values of the proteolytic fragments. Analyses were performed in the positive ion mode, using a Waters (Milford, MO, USA) Xevo-G2S Q-TOF mass spectrometer and the software programs MassLynx4.1 and BioPharmaLynx for data acquisition or analysis.

Purification of σPre2

For micro-preparative purposes, ProT (0.1 mg/ml, 300 μg) was treated with subtilisin (0.05 μg/ml) for 24 h at 10°C in TBS, containing 5mM $CaCl_2$. The reaction mixture was then fractionated on a HiTrap (0.7 x 2.5cm) heparin-sepharose column (GE Healthcare, Little Chalfont, UK) equilibrated with TBS, containing 0.25 M NaCl, and then eluted with the same buffer, containing 1 M NaCl. The material eluted in correspondence of the major chromatographic peak was collected, stored at -20°C and used for subsequent analyses. The chemical identity and homogeneity σPre2 was confirmed by non-reducing SDS-PAGE, RP-HPLC, and high-resolution MS analysis, as described above.

Spectroscopic characterization of σPre2

Protein concentration was determined by UV-absorption at 280 nm on a Jasco V-630 spectrophotometer, using a molar absorptivity value (Σ^M_{280nm}) of 67161 $M^{-1} \cdot cm^{-1}$ or 66424 $M^{-1} \cdot cm^{-1}$ for commercial and recombinant αT, respectively, and 99360 $M^{-1} \cdot cm^{-1}$ and 67871 $M^{-1} \cdot cm^{-1}$ for ProT or Pre2/σPre2. The active-site concentration of αT was also determined by titration with hirudin (**41**)

and found identical (± 5%) to that determined spectrophotometrically. Far-UV CD spectra were recorded on a Jasco J-810 spectropolarimeter, equipped with a Peltier temperature control system. The spectra were recorded in a 1-mm cell, at a scan-speed of 10 nm/min, with a response time of 16sec, and resulted from the average of four accumulations after baseline subtraction. CD data were expressed as the mean residue ellipticity $[\theta] = \theta_{obs} \cdot MRW/(10 \cdot l \cdot c)$, where θ_{obs} is the observed signal in degrees, MRW is the mean residue weight of recombinant αT (115.03 Da) and Pre2/σPre2 (114.98 Da), l is the cuvette pathlength in cm, and c is the protein concentration in g/ml. Fluorescence spectra were recorded on a Jasco FP-6500 spectropolarimeter, equipped with Peltier temperature control system, in a 1-cm pathlength cuvette (2 ml internal volume) at a scan speed of 200 nm/min using excitation and emission slits of 5 and 10 nm, respectively. Measurements were carried out at least in duplicate at 25±0.1°C and the spectra were subtracted for the corresponding baselines.

Fluorescence binding measurements

For measuring the binding of Na$^+$, incremental volumes of a solution containing 15 nM recombinant αT or σPre2 in TBS, pH 8.0, 1 M choline chloride, were withdrawn and then restored with the corresponding volumes of a solution containing 15 nM αT or σPre2 in TBS, pH 8.0, 1 M NaCl, such that the ionic strength and enzyme concentration were held constant at 1 M and 15 nM, respectively, while the Na$^+$ concentration was increased (**38**). Samples were excited at 280 nm (25±0.1°C) and the fluorescence intensity was recorded at the λ_{max} as vs. [NaCl]. The equilibrium dissociation constants of PABA ($\Sigma^M_{293nm} = 15 \times 10^3$ M$^{-1}\cdot$cm^{-1}), FPR ($\Sigma^M_{257nm} = 200$ M$^{-1}\cdot$cm^{-1}), Hir(1-47) ($\Sigma^M_{280nm} = 2920$ M$^{-1}\cdot$cm^{-1}) and hirugen ($\Sigma^M_{280nm} = 418$ M$^{-1}\cdot$cm^{-1}) for αT or σPre2 were obtained by adding, under gentle magnetic stirring (30 s), incremental volumes (2-10 μl) of ligand stock-solutions in 20 mM HEPES, pH 7.4, 0.15 M NaCl, 0.1% PEG-8000 (w/v) (HBS) to αT or σPre2 solutions in the same buffer. At each ligand concentration, samples were incubated for 2 min at 37°C and excited at 280nm, using an excitation/emission slit of 5 and 10 nm. The emission intensity was recorded at the protein λ_{max}, after subtracting the corresponding spectra of the ligands alone. Fluorescence data were corrected for sample dilution, which was always < 2% at the end of the titration. Photobleaching was almost eliminated, even after prolonged light exposure, by using a 1-cm pathlength quartz cuvette (2 ml) with two frosted walls that are able to diffuse the incident light inside the sample, thus preventing photodegradation of Trp-residues. To prevent inner filter effect (IFE), the optical density of the solution was kept always lower than 0.05 units both at λ_{ex} and λ_{em} (**38**). For PABA binding, samples were excited at 336 nm and the emission was recorded at 375 nm, after baseline subtraction and correction for IFE (**35**). For all ligands tested, except Hir(1-47) binding to αT, the data points were interpolated with **eq. 2**, describing the single-site binding model (**38**):

$$\Delta F = \Delta F_{max} \cdot \frac{[L]}{K_d + [L]}$$

<div align="right">(**eq. 2**)</div>

In the case of Hir(1-47)-αT interaction, fluorescence data were fitted to **equation 3**, describing the tight-binding model (**38**):

$$\Delta F = \Delta F_{max} \cdot \frac{b + \sqrt{b^2 - 4[R][L]}}{2[R]}$$

<div align="right">(**eq. 3**)</div>

with $b = ([R] + [L] + K_d)$

where R and L are the total enzyme and ligand concentrations, respectively, while RL is the enzyme-ligand complex. ΔF and ΔF_{max} are the changes of fluorescence intensity measured at intermediate or saturating ligand concentrations. The dissociation constant, K_d, of the complex was obtained as a fitting parameter.

Surface plasmon resonance (SPR)

SPR measurements were carried out at 25°C on a dual flowcell Biacore-X100 instrument (GE-Healthcare). A carboxymethylated C1 sensor chip was first derivatized at pH 5.0 with NeutrAvidin (Pierce Biotechnology, Rockford, IL). The NeutrAvidin-coated chip was then loaded for 700 sec at a flow rate of 10 μl/min with a solution (100 μl, 0.4 μM) of the synthetic peptide Biotinyl-PEG-GpIbα(268-282). Notably, NeutrAvidin (pI = 6.3) was used as an excellent alternative to avidin (pI = 10) for minimizing nonspecific binding (**53,72**) Finally, aliquots (100 μl) of αT and σPre2 solutions at increasing concentrations were injected over the NeutrAvidin sensor chip saturated with Biotinyl-PEG-GpIbα(268-282) (**Fig. S1**) at a flow rate of 10μl/min, with a contact time of 350 sec, in 10 mM HEPES, pH 7.4, 150 mM NaCl, 3 mM EDTA, 0.05% polyoxyethylene sorbitan (HBS-EP⁺). Each binding curve was subtracted for the corresponding baseline obtained on the reference flow cell and accounting for nonspecific binding, which was found < 2% of RU_{max}.

The dissociation constant (K_d) relative to the binding of αT or σPre2 to immobilized Biotinyl-PEG-GpIbα(268-282) was obtained as a fitting parameter by plotting the value of the response units at the steady state (RU_{eq}) vs. αT or σPre2 concentration and interpolating the data points with **eq. 4**:

$$RU_{eq} = RU_{max} \cdot \frac{[L]}{K_d + [L]}$$

(eq. 4)

where L is the concentration of αT or σPre2 and RU_{eq} and RU_{max} are the response units, measured at the steady state, at intermediate and saturating [L] (**73**). The binding data were analyzed using the BIAevaluation software.

Enzymatic activity assays

Chromogenic substrates

Hydrolytic activity of αT and σPre2 was determined at 37°C in HBS on the chromogenic substrates S2238 (D-Phe-Pip-Arg-pNA), S2366 (pyroGlu-Pro-Arg-pNA) and S2765 (Arg-Gly-Arg-pNA) by measuring the release of p-nitroaniline (pNA) at 405nm ($\Sigma^M_{405nm} = 9920$ M$^{-1}\cdot$cm^{-1}). The kinetic constants (k_{cat} and K_m) for substrate (S) hydrolysis were determined by the standard Michaelis-Menten treatment (**53**):

$$[v_0] = \frac{k_{cat}[E][S]}{K_M + [S]}$$

(eq. 5)

where E is the enzyme concentration and v_0 is the initial rate of substrate hydrolysis, calculated when < 10% of product was generated.

Fibrinopeptides release

The kinetics of fibrinopeptide A (FpA) and B (FpB) release by αT or σPre2 was followed as earlier reported (**53**). Briefly, human fibrinogen (Fb) ($\Sigma^M_{280nm} = 5.1\cdot10^5$ M$^{-1}\cdot$cm^{-1}) was desalted on an in-house packed (8x125mm) G10 fast-flow column (GE Healthcare, USA) eluted with HBS, pH 7.4, at a flow-rate of 0.3 ml/min. Freshly prepared Fb (0.35 µM) was reacted at 37°C with σPre2 (30 nM) or human αT (300 pM) and at fixed time points proteolysis mixtures were added with formic acid (2% v/v final concentration) to block the proteolysis reaction and induce precipitation of unreacted Fb. After centrifugation (10.000 g for 5 min at 4°C), the supernatant (1.0 ml) was withdrawn, lyophilized, dissolved in 6 M guanidinium hydrochloride solution (170 µl) and injected (100 µl) onto

a RP-HPLC (4.6 x 250mm) C18 column (Grace-Vydac, Columbia, MD). The column was equilibrated with 40mM ammonium phosphate buffer, pH 3.1, and eluted with an acetonitrile gradient. The absorbance of the effluent was recorded at 205 nm and the amount of FpA (Σ^M_{205nm} = $4.40 \cdot 10^4$ $M^{-1} \cdot cm^{-1}$) and FpB (Σ^M_{205nm} = $5.12 \cdot 10^4$ $M^{-1} \cdot cm^{-1}$) released was determined by integrating the area under the chromatographic peaks. A biocompatible Bio-410 HPLC system (Perkin-Elmer, Norwalk, CT), connected to a ISS-100 autosampler, was used for all analyses.

The specificity constants, k_{catA}/K_{mA} and k_{catB}/K_{mB}, for the release of FpA or FpB by αT or σPre2 were determined by interpolating the data points to equations **6** and **7**, respectively (**55**):

$$[FpA]_t = [FpA]_\infty \cdot (1 - e^{-k't})$$

(eq. 6)

$$[FpB]_t = [FpB]_\infty \cdot (1 + \alpha \cdot e^{-k't} - \beta \cdot e^{-k''t})$$

(eq. 7)

where $[FpA]_t$ or $[FpB]_t$ and $[FpA]_\infty$ or $[FpB]_\infty$ are the concentration of FpA or FpB at time t and ∞, respectively, and k′ and k″ are the observed kinetic constants for FpA or FpB release, obtained as fitting parameters. Under pseudo-first order conditions and low substrate concentration, the specificity constants could be easily determined k_{catA}/K_{mA} = k′/[E] and k_{catB}/K_{mB} = k″/[E], where [E] is the protease concentration.

PAR1(38-60) hydrolysis

Hydrolysis of the synthetic peptide PAR1(38-60) (1 µM) by αT (100 pM) or σPre2 (10 nM) was carried out at 25°C in HBS. At time points, aliquots (360 µl) were taken, acid quenched (10 µl, 4% aqueous TFA) and loaded (350 µL) onto a Grace-Vydac (4.6 x 250 mm) C18 column. The column was eluted with a linear acetonitrile-0.078% TFA gradient from 10-45% in 40 min and the release of PAR1(42-60) (Σ^M_{205nm} = 95870 $M^{-1} \cdot cm^{-1}$) (**53**) was quantified by integrating the area under the chromatographic peak. The kinetic data were interpolated with **equation 8**, describing a pseudo-first order reaction:

$$[P]_t = [P]_\infty \cdot [1 - \exp(-k_{obs} \cdot t)]$$

(eq. 8)

where $[P]_\infty$ is the concentration of the fragment PAR1(42-60) when the proteolysis reaction was complete and k_{obs} is the observed kinetic constant for PAR1(38-60) hydrolysis, obtained as a fitting parameter. As for the release of fibrinopeptides, under pseudo-first order conditions and low

substrate concentration, k_{cat}/K_m could be derived as $k_{obs}/[E]$.

Protein C activation

The generation of active PC (aPC) by αT or σPre2 (E) in the presence of thrombomodulin (TM), was monitored by recording the release of pNA (P′) from the substrate S2366 (S), according to the well-established reaction **scheme 1** (**54**):

$$E + PC \rightleftarrows EPC \rightleftarrows E + aPC$$

$$+$$

$$P + P' + aPC \rightleftarrows aPCS \rightleftarrows S$$
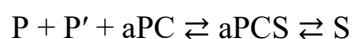
Scheme 1

The reaction was carried out at 37°C in HBS, containing 5 mM $CaCl_2$. The time course of pNA release was monitored by continuously recording the absorbance increase at 405 nm and the progress curves were analyzed as described (**54**) to extract the specificity constants (k_{cat}/K_m) of PC hydrolysis by αT or σPre2.

Inhibition of thrombin hydrolytic activity by PPACK.

The irreversible inhibition of αT or σPre2 (E) by PPACK (I) can be modelled by the reaction in **scheme 2** (**40**):

$$E + I \underset{k_{-1}}{\overset{k_1}{\rightleftarrows}} EI^* \overset{k_2}{\rightarrow} EI$$
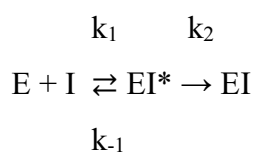
Scheme 2

where E reversibly binds I to form the encounter complex, EI*, that irreversibly converts into the stable EI complex, with a rate constant k_2. K_{EI^*} is the equilibrium dissociation constant of the noncovalent complex, $K_{EI^*} = k_{-1}/k_1$, where k_1 and k_{-1} are the association and dissociation rate constants, respectively. Under rapid equilibrium ($k_2 \ll k_{-1}$), the reaction simplifies to a one-step irreversible process (**40,74**):

$$k_a$$

$$E + I \rightarrow EI$$
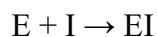
Scheme 3

where $k_a = k_2/K_{EI^*}$ is the second-order rate constant for the formation of the nondissociating complex EI. Under pseudo first-order conditions, the observed rate constant, k_{obs}, can be extracted from **equation 9**:

$$\frac{v_t}{v_0} = \frac{[E]_t}{[E]_0} = \exp(-k_{obs} \cdot t)$$

(eq. 9)

where $k_{obs} = k_{on} \cdot [I]_0$, while v_t and v_0 are the initial rates of substrate hydrolysis by the enzyme at a fixed inhibitor concentration, $[I]_0$, at time t and zero, respectively. Considered that complete inhibition of both αT and σPre2 occurred in a relatively short time range (90-240 sec), accurate estimates of v were obtained in a continuous assay, from the first derivative of the progress curves of pNA generation (i.e. from the slope of the tangent line at each t value).

Fibrin generation and platelet aggregation

Fibrin generation was started by adding αT or σPre2 (50 nM) to a freshly desalted Fb solution (0.44 μM) in HBS at 37°C, while the time course clot formation was followed by continuously recording the solution absorbance at 350 nm (i.e. the turbidity) on a Jasco V-630 spectrophotometer. From the clotting curve, the values of S_m, t_m, t_c, and ΔA_{max} were extracted as described in **Fig. 10B** and **Table 3 (35)**. When fibrin generation was induced in human plasma samples (diluted 1:1 with HBS) at 37°C, the absorbance change was recorded at 671 nm.

Platelet aggregation was determined in whole blood or in gel-filtered platelets by multiple electrode aggregometry (MEA), using a multiplate analyzer (Dynabyte, Munich, Germany). The area under the aggregation curve (AUC) was determined over 10-min reaction time. Citrate-treated venous blood samples were taken from three healthy donors: one male and two females, 28–35 years of age, and non-smokers. The donors gave written informed consent for participation in this study, which was approved by the institutional ethics committee of the Padua University Hospital. Platelets were isolated by loading platelet-rich plasma (PRP) samples onto a (1.5 x 25cm) Sepharose 2B gel-filtration column (GE-Healthcare), equilibrated with HBS, containing0.2% bovine serum albumin, 5.5 mM glucose, and 5 mM KCl. PRP was prepared by centrifugation of blood samples (800 r.p.m. for 15 min at 4°C). Platelet counts were determined using an automated Hematology Analyser XP-300 (Sysmex Co., Kobe, Japan).

N-terminal carbamylation

To assess the susceptibility of the N-terminal to chemical modification by KCNO (0.2 M), σPre2 (1 μM) or αT (1 μM) were incubated in HBS at 37°C. In a discontinuous assay, at different time points the reactions were stopped by dilution and the residual amidolytic activity was determined by S2238 hydrolysis. Control experiments without KCNO were conducted in parallel. The relative rate of substrate hydrolysis was plotted as a function of the reaction time with KCNO and the data points were analyzed as reported above for the irreversible thrombin inhibition by PPACK to obtain the pseudo-first order association rate constant, k_{on}.

The extent of carbamylation of the N-termini in αT and σPre2, was comparatively estimated by automated Edman sequencing, after 1-h reaction with KCNO at 37°C (**60**). An identical amount (100 pmoles) of purified αT A- and B-chain or σPre2 NT and CT fragments were loaded on a Procise sequencer (Applied Biosystems). Prior to analysis, these chains/fragments were subjected to disulphide bond reduction and carboxamidomethylation with dithiothreitol and iodoacetamide (**75**) and subsequent purification by RP-HPLC. As a reference, sequence analyses were performed on the corresponding species deriving from αT and σPre2 samples which were not treated with KCNO. The area of the chromatographic peak corresponding to the phenylthiohydantoin(PTH)-derivative of the N-terminal amino acid in each untreated species was the 100% reference value that was used to estimate the % carbamylation of KCNO-treated samples.

RESULTS AND DISCUSSION

Limited proteolysis of ProT by subtilisin

The data in **Fig. 1A** indicate that addition of an aliquot of the proteolysis mixture of ProT with subtilisin to a solution of the αT-specific chromogenic substrate S2238 (**28**) results in the release of pNA, as documented by the absorbance increase at 405 nm (ΔA_{405}). The initial rate (v_0) of S2238 hydrolysis strongly increases with the incubation time of ProT with subtilisin, reaching a maximum after 3-5h and then slightly decreasing at longer reaction times (**Fig. 1B**). Notably, under identical experimental conditions, subtilisin did not cleave S2238. These results provide clear-cut evidence that cleavage of ProT zymogen by subtilisin generates thrombin-like species displaying significant catalytic activity. To identify the subtilisin cleavage sites on ProT, non-reducing SDS-PAGE analysis of the proteolysis reaction was conducted at 37°C in the 1-300 min time range (**Fig. 2A**). The protein bands were electrotransferred onto Immobilon membrane and sequenced by automated N-terminal Edman degradation. Alternatively, the gel bands were excised, *in situ* digested with trypsin, and subjected to peptide mass fingerprint analysis by high-resolution LC-MS/MS. Using a different approach, the proteolysis mixture was analyzed by RP-HPLC and the fractions were characterized by

MS/MS (**Fig. 2B**). The results of these chemical analyses are summarized in **Table 1** and schematically reported in **Fig. 4A**.
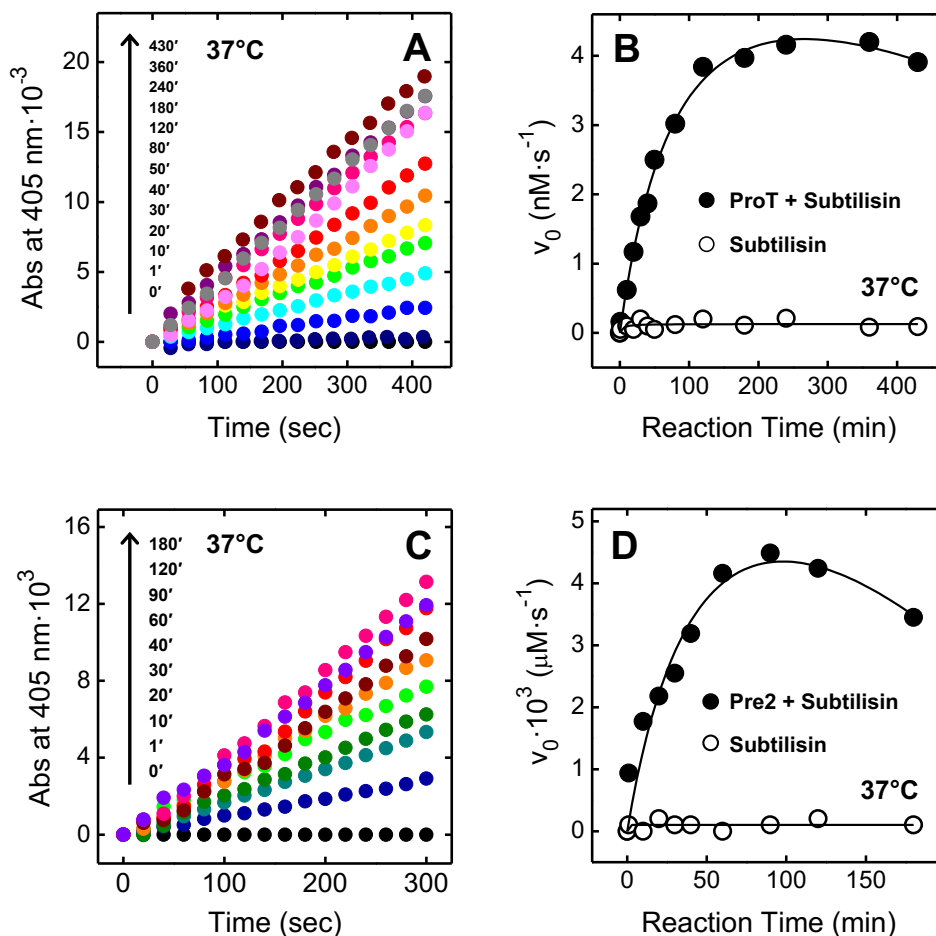
Figure 1. Time-course expression of thrombin-like hydrolytic activity during proteolysis of ProT (A, B) and Pre2 (C, D) by subtilisin. (**A**) ProT (0.1 mg/ml, 350 μl) was treated in TBS added with 5 mM CaCl$_2$ at 37°C with subtilisin (0.05 μg/ml) at an enzyme:ProT ratio of 1:2000 (w/w). At increasing time points, an aliquot (28 μl) of the proteolysis mixture was added to a solution of the chromogenic substrate S2238 (20 μM) in HBS. The time-course release of pNA was monitored at 37°C by recording the absorbance increase at 405 nm. The slope of the straight lines was taken as the initial velocity, v_0, of S2238 hydrolysis by the active thrombin-like species. (**B**) (●) Plot of v_0 as a function of the reaction time of ProT with subtilisin at 37°C. (○) Control measurements: S2238 (20μM) was incubated at 37°C with subtilisin (0.05 μg/ml) in the absence of ProT. (**C**) Pre2 was treated under identical experimental conditions as in panel A. At time points, aliquots (15μl) of the proteolysis mixture were taken and tested for activity on S2238 substrate. (**D**) (●) Plot of v_0 as a function of the reaction time of Pre2 with subtilisin at 37°C. (○) Control measurements were carried out as in panel A. The fitting curves are only intended to help the reader to follow the data points.

Under limited proteolysis conditions (subtilisin:ProT ratio of 1:2000 w/w) at 37°C subtilisin rapidly attacked ProT, migrating in nonreducing SDS-PAGE (4-12% acrylamide) with an apparent molecular weight of about 72 kDa (**Fig. 2A**). ProT was (almost) completely degraded after 10-min reaction, and four major bands were generated at 55, 35, 25, and 12 kDa. The 55-kDa band corresponds to fragment Met152-Glu579(247) and is generated by cleavage at Ala151-Met152 bond in the linker-1 region, i.e. the cleavage site-1 (CS-1) (**Fig. 4**). Of note, the numbers in parenthesis refer to the αT sequence numbering. This fragment contains the K2- and Pre2-domain, and therefore it is equivalent to Prethrombin-1 (Pre1), Ser156-Glu579(247), an intermediate resulting from the cleavage of ProT by factor Xa at Arg155 (**29**). The 35-kDa band originates from cleavage of ProT or Pre1 at Arg271-Thr272 bond in the liker-2 region, i.e. the cleavage site-2 (CS-2), and corresponds to the sequence of Pre2, Thr272-Glu579(247), a key physiological intermediate during αT generation (**6,29**). Albeit unusual, the cleavage at Arg271 should not be surprising. Subtilisin, indeed, has a preference for large uncharged residues at the primary specificity site (P1), but hydrolysis at peptide bonds containing Lys or Arg at P1 are also frequent (**27**). The two bands at 25 and 12 kDa result from the cleavage at the peptide bond Ala470(149a)-Asn471(149b) in the 148-loop of Pre2, denoted as cleavage site-3 (CS-3) (**Fig. 4**). Specifically, the 25-kDa band corresponds to the N-terminal fragment Thr272-Ala470(149a) of Pre2, denoted as NT, whereas the 12-kDa band corresponds to the C-terminal fragment Asn471(149b)-Glu579(247), denoted as CT (**Fig. 4A**, **Table 1**). RP-HPLC and MS analysis of the same proteolysis reaction (10 min at 37°C) (**Fig. 2B** and **Table 1**) confirmed the chemical identity of the proteolytic fragments reported in the SDS-PAGE and allowed us to identify the presence of minor, transient species that are further degraded by subtilisin at longer reaction times, i.e. K2-NT (38298.4 a.m.u.), F1 (21732.6 a.m.u.), and K2 (13093.5 a.m.u). Whereas K2-NT and F1 appeared as distinct bands in the SDS-PAGE, K2 likely co-migrated with CT (12348.4 a.m.u.), as their molecular weight differs by only 5%. Notably, when electrophoresis was run on a 14%-acrylamide gel, that better resolves low-molecular weight species, K2 and CT bands could be separated (**Fig. S2**). Noteworthy, NT and CT fragments are quite resistant to further proteolysis and accumulate at longer reaction times (up to 5 h), whereas other ProT segments, once formed, are rapidly degraded to small fragments not visible in the electrophoresis gel (**Fig. 2A**).
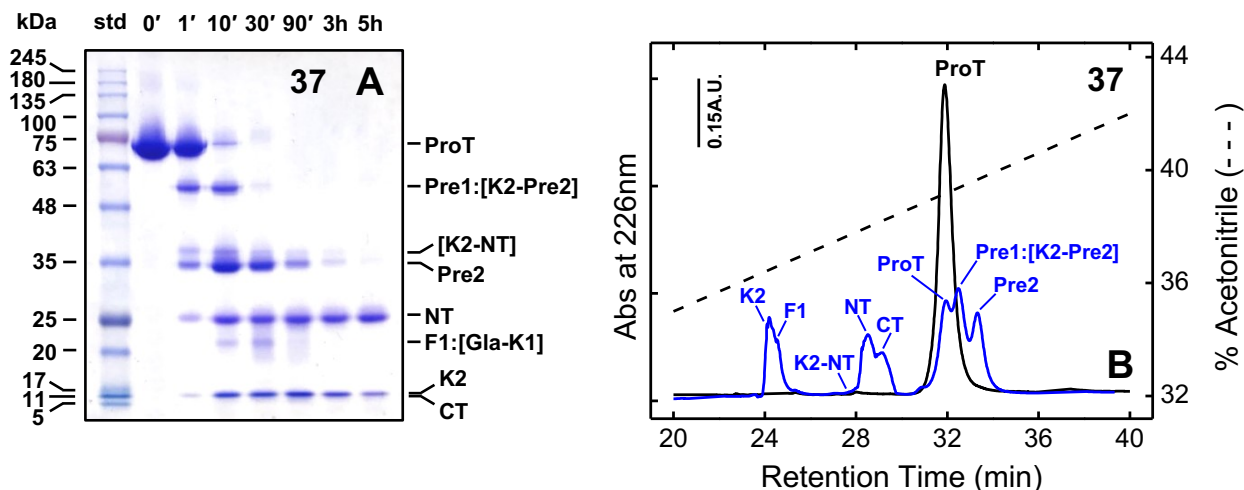
Figure 2. **Time-course analysis of the proteolysis reaction of ProT by subtilisin.** (**A**) Nonreducing electrophoretic analysis of the time-course reaction of ProT (0.1 mg/ml) with subtilisin (0.05 μg/ml) at 37°C. At time points, aliquots (100 μl, 10 μg) of the proteolysis mixtures were precipitated with cold TCA, analyzed by SDS-PAGE (4-12% acrylamide) and Coomassie stained. Std: molecular weight protein standards. (**B**) RP-HPLC analysis of the proteolysis reaction of ProT with subtilisin at 37°C after 1-min (—) and 10-min (—) reaction. Aliquots (20 μg) of the reaction mixtures were loaded onto a C4 analytical column, eluted with an aqueous acetonitrile-0.1% TFA gradient (---). The chemical identity of material eluted in correspondence of the major peaks was established by high-resolution MS and mass values are reported in **Table 1**.

Despite the broad specificity of subtilisin (**27**) and the large number of potential cleavage sites in ProT sequence, under controlled proteolysis, the protease attacks the zymogen at only three sites, i.e. CS-1, CS-2 and CS-3 (**Fig. 4A,B**). The unique susceptibility of ProT to subtilisin can be explained on the basis of the zymogen structure (**4**) (**Fig. 4B**) and the general structural requirements for limited proteolysis. Peptide bond cleavage, indeed, is only partially dictated by sequence and accessibility properties of the cleavage sites and, to a much greater extent, by their conformational flexibility (**30**). Notably, the subtilisin cleavage sites in ProT perfectly match with the regions of highest segmental flexibility of the zymogen, as deduced from the B-factor plot of the crystallographic structure in the solid state (**4**) and single-molecule FRET studies in solution (**31**) (**Fig. 4C**). In particular, CS-1 and CS-2 are embedded in the highly dynamic inter-domain linker regions, while CS-3 is in the highly flexible 148-loop of Pre2 domain (**4,32**) (**Fig. 4**), corresponding to the autolysis loop in the mature αT (**33**). Of note, the structure of ProT we used here is that of the zymogen deletion mutant, ProTΔ(154-167), solved at 2.2-Å resolution and lacking 14 amino acids in the linker-2 region while retaining the conformational properties of the wild-type ProT in the extended conformation (**29,31**).

A key aspect that emerges by comparing the time-course increase of hydrolytic activity at 37°C (**Fig. 1B**) with the progression of the proteolysis reaction (**Fig. 2A**) is that cleavage of Pre2 at CS-3 is instrumental for the onset and increase of thrombin-like hydrolytic activity.

Limited proteolysis of rPre2 by subtilisin

To investigate the kinetics of proteolytic zymogen activation by subtilisin solely at CS-3 site, we performed limited proteolysis experiments on the smallest inactive αT precursor, Pre2. Recombinant human Pre2 (rPre2) was expressed in *E. coli*, subjected to disulphide oxidative renaturation and purified to homogeneity by heparin-sepharose affinity chromatography, as described (**34,35**). Limited proteolysis reaction of rPre2 was carried out under experimental conditions identical to those used for ProT. The rate of S2238 hydrolysis (v_0) at 37°C strongly increased in the 0-90 min time range and then decreased at longer reaction times, likely because of further proteolytic degradation (**Fig. 1C,D**).

Cleavage of Pre2 by subtilisin was monitored by non-reducing SDS-PAGE (**Fig. 3A-D**) and RP-HPLC (**Fig. 3F**) in the temperature range 5-37°C. Non-glycosylated, intact rPre2 migrates as a 33-kDa band and in all trials two major bands were generated at 22 and 13 kDa (**Fig. 3A-D**). These bands were identified by automated Edman sequencing of the electroblotted gel bands or by *in situ* trypsin digestion of the gel bands followed by LC-MS/MS analysis of the tryptic fragments. As already established with ProT (**see Fig. 2**), these fragments correspond to the non-glycosylated NT and CT fragments of Pre2, respectively, resulting from specific cleavage at the Ala470(149a)-Asn471(149b) bond, in the region of highest segment mobility of Pre2 (**32**). Comparison of the proteolysis reactions of ProT (**Fig. 2A**) and rPre2 (**Fig. 3A**), both carried out at 37°C, reveals that the rate of Pre2 degradation is significantly higher compared with ProT and that the resulting NT and CT fragments from rPre2 are less stable to further proteolysis. This difference can be accounted for by: i) the lower number of subtilisin cleavages sites present on Pre2 structure compared with ProT; ii) the lack of glycosylation at Asn60g, that in the natural glycosylated ProT is expected protect the zymogen from subtilisin cleavage (**30**); iii) the possible shielding of the 148-loop operated by the N-terminal F1-region, which in the solution structure of ProT has been proposed to fold back on the Pre2 domain (**31**).
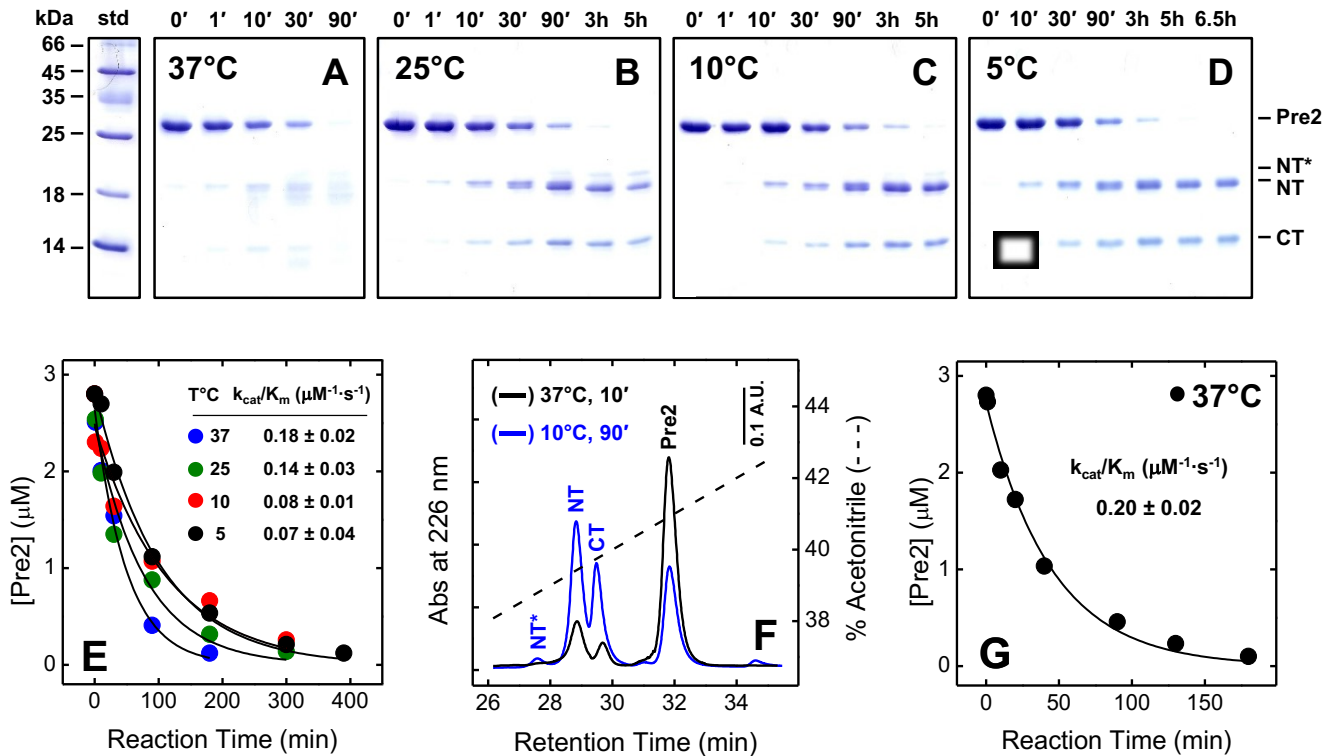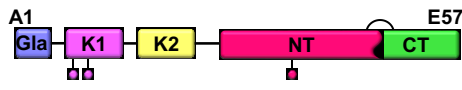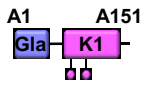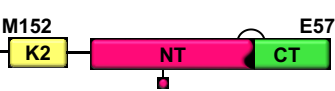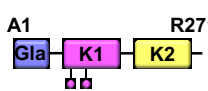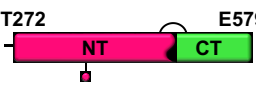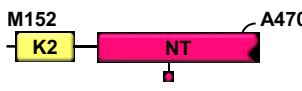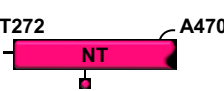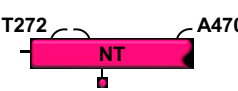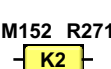
Figure 3. Time-course analysis of the proteolysis reaction of Pre2 by subtilisin. (**A-D**) Electrophoretic analysis of the time course reaction of Pre2 (2.8 μM) with subtilisin (1.8 nM). In all experiments, Pre2 (0.1 mg/ml) was reacted at the indicated temperatures in TBS, containing 5mM CaCl₂, with subtilisin at an ezyme:Pre2 ratio of 1:2000 (w/w). At time points, aliquots (50 μl, 5 μg) of the proteolysis mixtures were precipitated with cold TCA, analyzed by SDS-PAGE (4-14% acrylamide) under nonreducing conditions, and Coomassie stained. Std: molecular weight protein standards. (**E**) Kinetics of the of subtilisin-catalyzed proteolysis of Pre2, as determined by densitometric analysis of residual intact Pre2 in the gels reported in panels A-D. The data points were fitted with **eq. 1**, yielding k_{cat}/K_m values as indicated. (**F**) Representative RP-HPLC plots of the proteolysis reaction of Pre2 with subtilisin after 10-min reaction at 37°C (—) and after 90 min at 10°C (—). Aliquots (20 μg) of the reaction mixtures were loaded onto a C4 analytical column, eluted with a linear aqueous-0.1%-TFA gradient (---). The chemical identity of the protein material eluted from the chromatographic peaks was established by N-terminal sequencing and LC-MS/MS analysis as follows: Pre2, prethrombin-2; NT, fragment Thr272-Ala470; CT, fragment Asn471-Glu579; NT*, fragment NT nicked at the peptide bond Tyr316-Ile317. (**G**) Kinetics of subtilisin-catalyzed proteolysis of Pre2 at 37°C monitored by RP-HPLC. The concentration of residual intact Pre2 at different reaction times was estimated by integrating the area of the chromatographic peak of Pre2, as in panel F. After data fitting with **eq. 1**, the k_{cat}/K_m value was estimated, as reported.

As expected, the cleavage rate decreased at temperatures < 37°C, while the specificity of peptide bond cleavage by subtilisin significantly increased, such that at 10 or 5°C the protease hydrolyzed Pre2 virtually at the most flexible site, i.e. the Ala149a-Asn149b bond. Only at longer reaction times, a very minor band was progressively generated, corresponding to the nicked NT* species, resulting from hydrolysis of the peptide bond Tyr14j-Ile14k in the fraying N-terminal region

of Pre2 (**Table 1**). At each time point, the residual amount of intact Pre2 was estimated by densitometric analysis of the electrophoretic bands (**Fig. 3E**) and a specificity constant (k_{cat}/K_m) for the hydrolysis of the Ala149a-Asn149b bond at 37°C was estimated as 0.18 ± 0.02 $\mu M^{-1}\cdot s^{-1}$. Interestingly, when proteolysis of rPre2 at 37°C was monitored by RP-HPLC, identical results were obtained ($k_{cat}/K_m = 0.20\pm0.02$ $\mu M^{-1}\cdot s^{-1}$) (**Fig. 3F,G**).

Table 1: Mass Values of the protein fragments generated by limited proteolysis of ProT with Subtilisin[a]

Major Species	Mass (a.m.u.)	Minor Species	Mass (a.m.u.)
ProT	72344.6 (72339.7)[b]	F1	21732.6 (21731.0)
Pre1	50628.9 (50626.8)	F1-K2	34808.0 (34806.2)
Pre2	37553.0 (37551.5)	K2-NT	38298.4 (38296.7)
NT	25222.6 (25221.5)	NT*	25240.8 (25239.5)
K2	13093.5 (13093.3)		
CT	12348.4 (12348.1)		

[a] Proteolysis was conducted at 37°C in TBS, pH 7.4, 5 mM $CaCl_2$. After 10-min reaction, the proteolysis mixture was fractionated by RP-HPLC (Fig. 2B) and the peptide material analysed by high-resolution MS. [b] The theoretical mass values are reported in parenthesis and the error on mass determination was always lower than 60 ppm
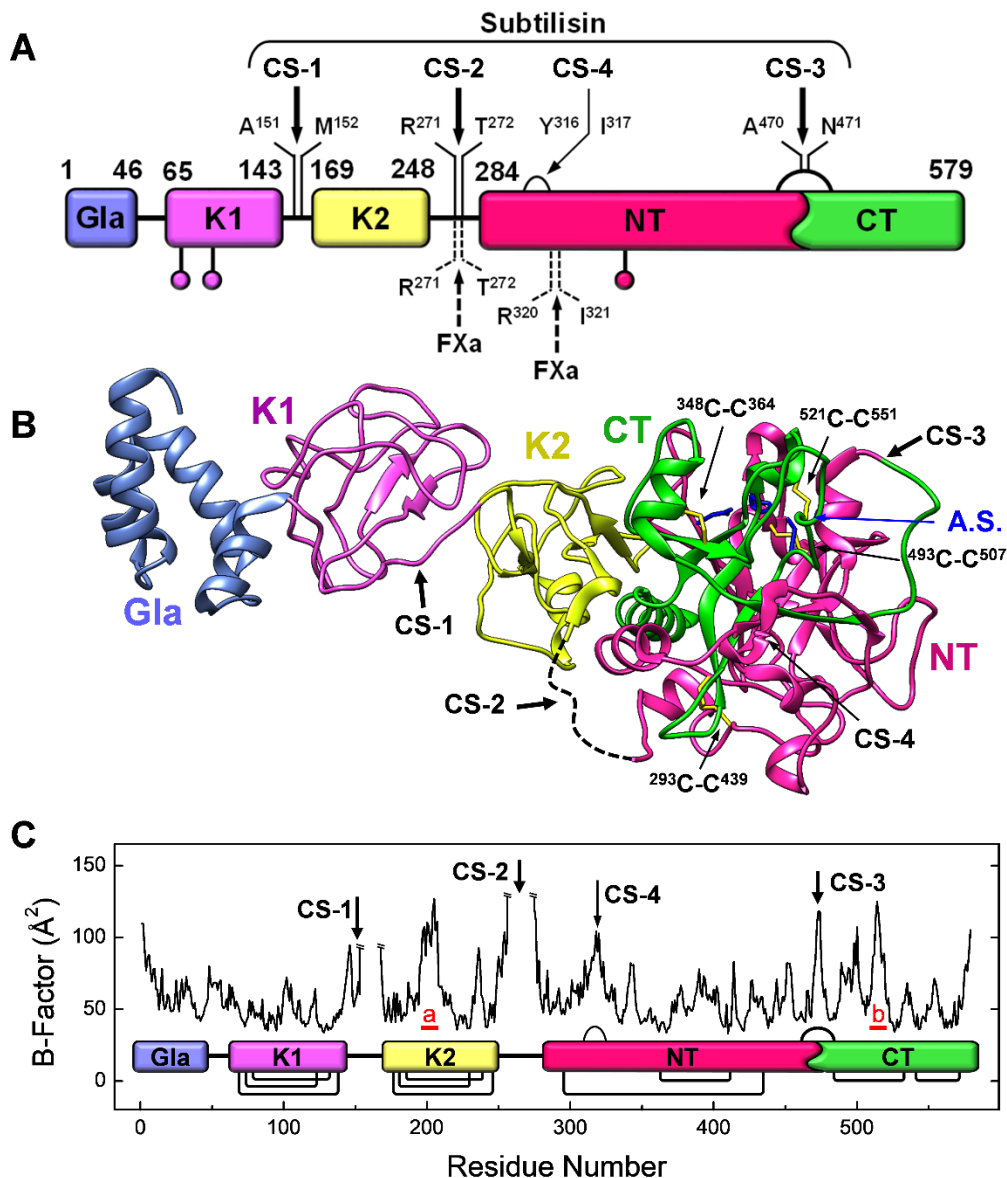
Figure 4. Schematic representation of the subtilisin cleavage sites (CS) on ProT. (**A**) Domain architecture of ProT. The numbers identify the N- and C-terminal ends of the zymogen domains, according to the ProT sequence numbering: Gla, γ-carboxyglutamic acid rich domain; K1, kringle-1 domain; K2, kringle-2 domain; Pre2, prethrombin-2 domain; NT and CT are the N- and C-terminal fragments of Pre2 deriving from cleavage of Pre2 by subtilisin. Non-physiological cleavage sites by subtilisin are on the top side of ProT sequence while physiological cleavage sites by factor Xa are on the bottom side. (**B**) Ribbon drawing of the structure of ProT deletion mutant des(154-167), ProTΔ(154-167) (5edm.pdb) lacking 14 amino acids in the linker-2 region connecting K1- and K2- domains (**4**). Dashed lines represent unresolved linker regions in the X-ray structure. The cleavage sites are indicated by arrows, while SS bonds in Pre2 domain are in yellow. The amino acids forming the active site (A.S.) are in blue. (**C**) B-factor flexibility plot of ProTΔ(154-167). The minor cleavage at CS-4 is indicated by a thinner arrow. Sequences marked in red and identified with small letters (a and b) correspond to those regions in ProTΔ(154-167) which, albeit displaying substantial conformational flexibility, are not cleaved by subtilisin. Segment *a* encompasses the sequence Ala197-His205, which is embedded in a short α-helical secondary structure in the zymogen and therefore it is expected to be quite protected from proteolysis (**30**). Segment *b* spans the sequence

[512]PDEGKRGD[519], contributing to the Na+-binding site in mature αT, is highly charged and for this reason it does not meet the substrate specificity requirements for subtilisin cleavage (**26,27**). Protein structures were visualized with the ViewerPro 4.2 software (Accelerys Inc., USA) and the B-factor plot was generated using What-If software (**76**).

Purification of σPre2

To minimize the presence of residual uncleaved Pre2, proteolysis of ProT with subtilisin was carried out for 24 h at 10°C. Taking advantage of the heparin-binding properties of thrombin exosite-II, the proteolysis mixture was fractionated by Heparin-sepharose affinity chromatography (**Fig. 5A**). The fractions were analysed by non-reducing SDS-PAGE (**Fig. 5A, Inset**) and chemically characterized by LC-MS/MS. The material eluting as a single chromatographic peak at 0.75M NaCl (i.e. fraction F3) split into two bands at 25 and 12 kDa in non-reducing SDS-PAGE. These bands were identified as the NT and CT fragments of Pre2.
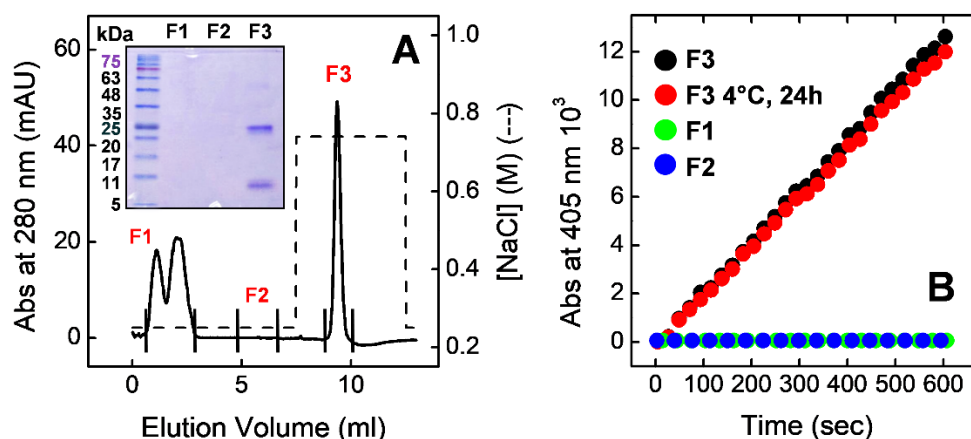
Figure 5. Purification and storage stability of σPre2. (**A**) Purification of σPre2 by heparin-sepharose affinity chromatography. For micro-preparative purposes, a ProT solution (300 μg, 0.1 mg/ml) was treated for 24 h at 10°C with subtilisin (0.05 μg/ml) in TBS, added with 5 mM CaCl$_2$. The reaction mixture was loaded onto a HiTrap (0.7 x 2.5cm) Heparin-Sepharose column, which was equilibrated with TBS and then eluted with a gradient of NaCl (---). The material eluted in correspondence of fractions F1 to F3 (200 μl) was precipitated with cold TCA for subsequent electrophoretic and functional analyses. (**Inset**) SDS-PAGE (4-14% acrylamide) of the fractions eluted from the affinity column, under non-reducing conditions and Coomassie staining. (**B**) Hydrolytic activity of the fractions eluted from Heparin-Sepharose column. Aliquots (60 μl) of F1 (●), F2 (●), and F3 (●) fractions, as in panel A, were immediately added to a S2238 solution (20 μM) in HBS and the time course release of pNA was monitored at 37°C by recording the absorbance increase at 405 nm. The storage stability of σPre2 was evaluated after incubation of F3 fraction for 24 h at 4°C (●).

The unretained material (i.e. fractions F1 and F2) contained only short peptides (**Fig. 5A, Inset**), not visible in the SDS-PAGE and deriving from further proteolytic degradation of K1 and K2 domains. Only the material eluting with F3, but not that eluting in correspondence of F1 or F2, was able to release pNA from S2238 (**Fig. 5B**). Furthermore, the hydrolytic activity of F3 remained constant even after 24-h storage at 4°C (**Fig. 5B**). Altogether, these results provide evidence that hydrolysis of ProT by subtilisin ends up with the generation of a stable and functional complex (hereafter denoted as σPre2) which is formed by the NT and CT fragments, held together by non-covalent forces (**Fig. 4B,C**). For preparative purposes, σPre2 was also prepared from recombinant Pre2 incubated for 15 h at 5°C, using the same zymogen-protease molar ratio as at 37°C (not shown).

Conformational characterization of σPre2

The CD spectrum of αT displays low ellipticity values and two unusual distinct minima at 210 and 228 nm, which are significantly red-shifted compared with those typical of the α-helix structure (208 and 222 nm) (**Fig. 6A**). As already pointed out in our earlier work (**36**), the peculiar far-UV CD spectrum of αT also results from the spectroscopic contribution in the far-UV region of the aromatic amino acids and SS bonds present in the thrombin sequence (9 Trp, 11 Tyr, 11 Phe, and 4 cystines) that masks the conformational contribution of the peptide bond chromophores embedded in secondary structure elements. Such effects become more important for those proteins displaying low signal intensity and are most prominent in systems where aromatic groups are clustered in the protein structure (**36**). The CD spectrum of intact Pre2 (**Fig. 6A**) differs from that of mature αT by both shape and intensity. These spectral changes reflect the conformational transition underlying the conversion of Pre2 to αT and are likely contributed also by rearrangement of some aromatic amino acids, occurring during zymogen activation (**Fig. 6C**). After hydrolysis of the peptide bond Ala149a-Asn149b, the minimum at 226 nm, characteristic of the intact zymogen, is conserved in the spectrum of σPre2, whereas the band of Pre2 at 211 nm becomes more intense and blue-shifted to 208 nm in σPre2. These spectral changes suggest that proteolysis likely induces (partial) unfolding of the region encompassing the autolysis loop.

At variance with CD, the fluorescence spectrum of Pre2 is almost superimposable to that of mature αT, with a λ_{max} value at 334 nm, whereas the emission of σPre2 is remarkably reduced and red-shifted to 340 nm (**Fig. 6B**). Both these spectral features are compatible with the flexibilization and exposure of some Trp-residues in σPre2 (**37**), in agreement with the partial unfolding of σPre2 deduced from CD spectra.
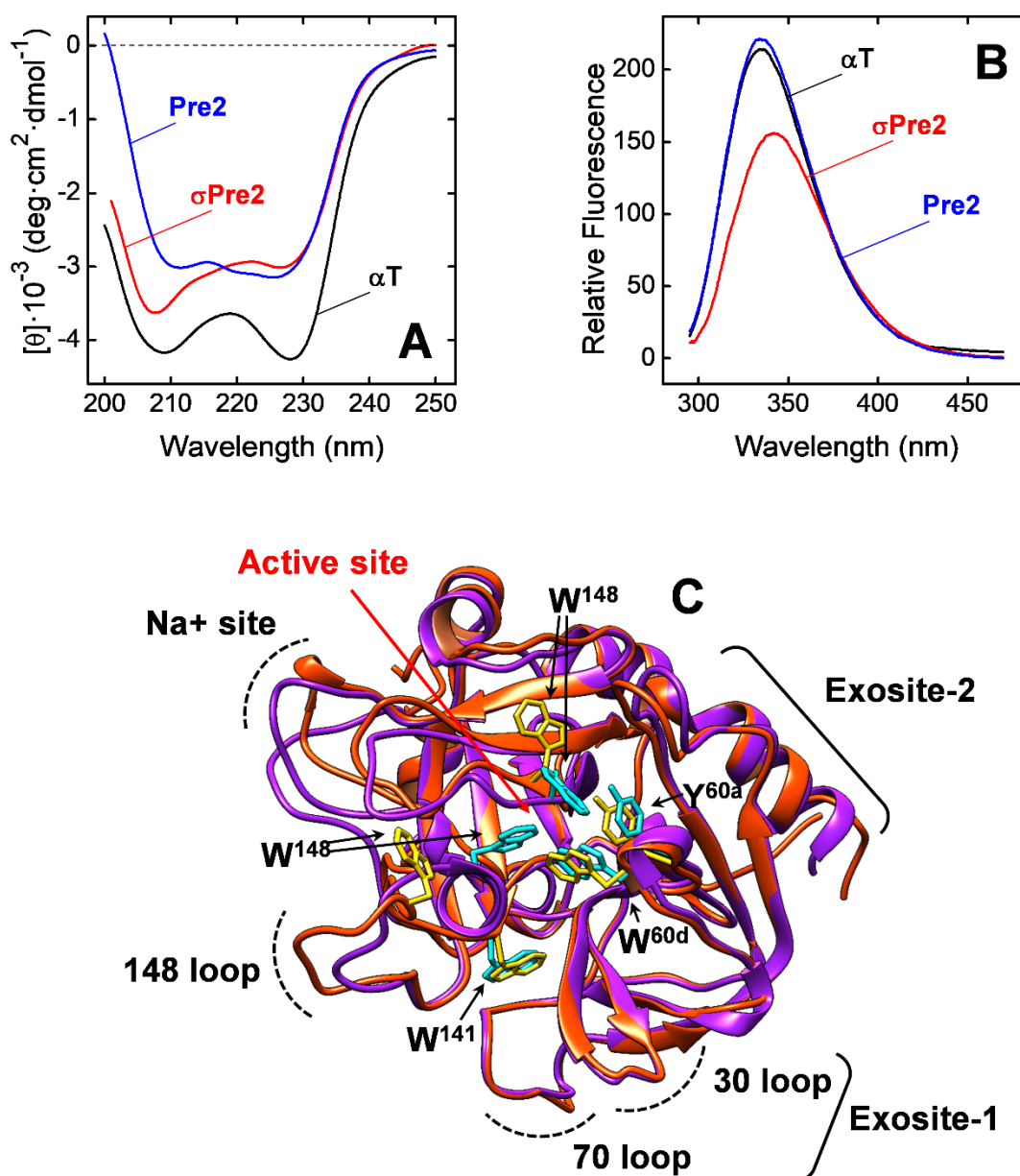
Figure 6. Spectroscopic characterization of σPre2, Pre2, and αT. Far-UV CD (**A**) and fluorescence (**B**) spectra of purified σPre2 (——), Pre2 (——), and αT. CD spectra were recorded at a protein concentration of 4 μM in PBS. Fluorescence spectra were taken at a protein concentration of 30 nM in TBS, pH 8.0, containing 0.2 M ChCl, after exciting the protein samples at 280 nm. The λ_{max} value of αT and Pre2 (334 nm) is shifted to 340 nm in σPre2. All measurements were carried out at 25°C and the resulting spectra were corrected for the corresponding base lines. (**C**) Ribbon drawing superposition of Pre2 (3sqe, purple) and αT (1ppb, orange red). Relevant amino acids side chains are coloured cyan for Pre2 and yellow for αT structure. The approximate position of relevant thrombin regions are indicated. The aromatic cluster formed by Trp148, Trp215, Trp60d and Tyr60a is evident in the structure of Pre2 (cyan).

Probing the structure of σPre2 by fluorescence and SPR binding measurements

The conformation of key regions in σPre2 (i.e. the Na$^+$-site, the active-site region and exosite-1 and -2) was investigated by site-specific ligand binding, measuring the affinity of ligands which are known to specifically bind at a given target site (**Fig. 7**). The decrease in binding strength, relative to αT, was taken as a strong indication that the conformation of that site was perturbed in σPre2.

Na$^+$-site.

The affinity of Na$^+$ for αT and σPre2 was determined by measuring the change of fluorescence intensity at the emission λ$_{max}$ (**Fig. 7A**). The binding of Na$^+$ to αT leads to an increase of the fluorescence signal, allowing to estimate a K$_d$ of 21 ± 3 mM at 25°C, identical to that reported earlier (**38**). Conversely, increasing salt concentrations induced a marked decrease of the fluorescence intensity in σPre2, along with a reduction of the affinity for Na$^+$ by about 20-fold, compared with αT. These results clearly indicate that the Na$^+$-binding site in σPre2 is heavily compromised and suggest that ion binding to σPre2 is irrelevant at physiological Na$^+$ concentrations.

Active site

The active-site region was probed by measuring the affinity of σPre2 and αT for inhibitors having different size and affinity for thrombin, and mapping different sub-sites in the protease catalytic region, i.e. p-aminobenzamidine (PABA), the tripeptide (D)-Phe-Pip-Arg-OH (FPR), (D)-Phe-Pro-Arg-chloromethyl ketone (PPACK), and the hirudin N-terminal domain 1-47 [Hir(1-47)]. PABA is a positively charged small molecule, selectively binding to Asp189, which is located at the bottom of the primary substrate specificity site S1 of chymotrysin-like proteases (**39**). At variance, FPR extensively penetrates into thrombin subsites, orienting Arg3 side-chain into the S1 site, the pipecolyl-moiety (Pip2) towards the S2 site (shaped by Tyr60a and Trp60d), and (D)-Phe1 in the apolar S3 site (formed by Leu99, Ile 174, and Trp215) (**33**). PPACK, the chloromethyl-ketone analogue of FPR, is the most specific affinity label for thrombin, such that even small changes in the conformation of the substrate recognition sites and/or protease catalytic amino acids dramatically reduces the inhibitory potency (**33,40**). The catalytic Ser195 γO atom in the αT active site attacks the ketone-group of the inhibitor to form the hemiketal anion, which reacts with the nucleophile His57 εN at the chloromethyl-group to release the chloride ion leaving group (**33**). This results in irreversible inhibition of αT by covalent cross-linking. Hir(1-47) is a potent and specific inhibitor of αT that binds to the S2 and S3 sites and covers the loop regions surrounding the active site, i.e. the autolysis loop, the 60-loop shaping the S2 site, and the 180- and 220-loop forming the Na$^+$-binding site (**41,42**).
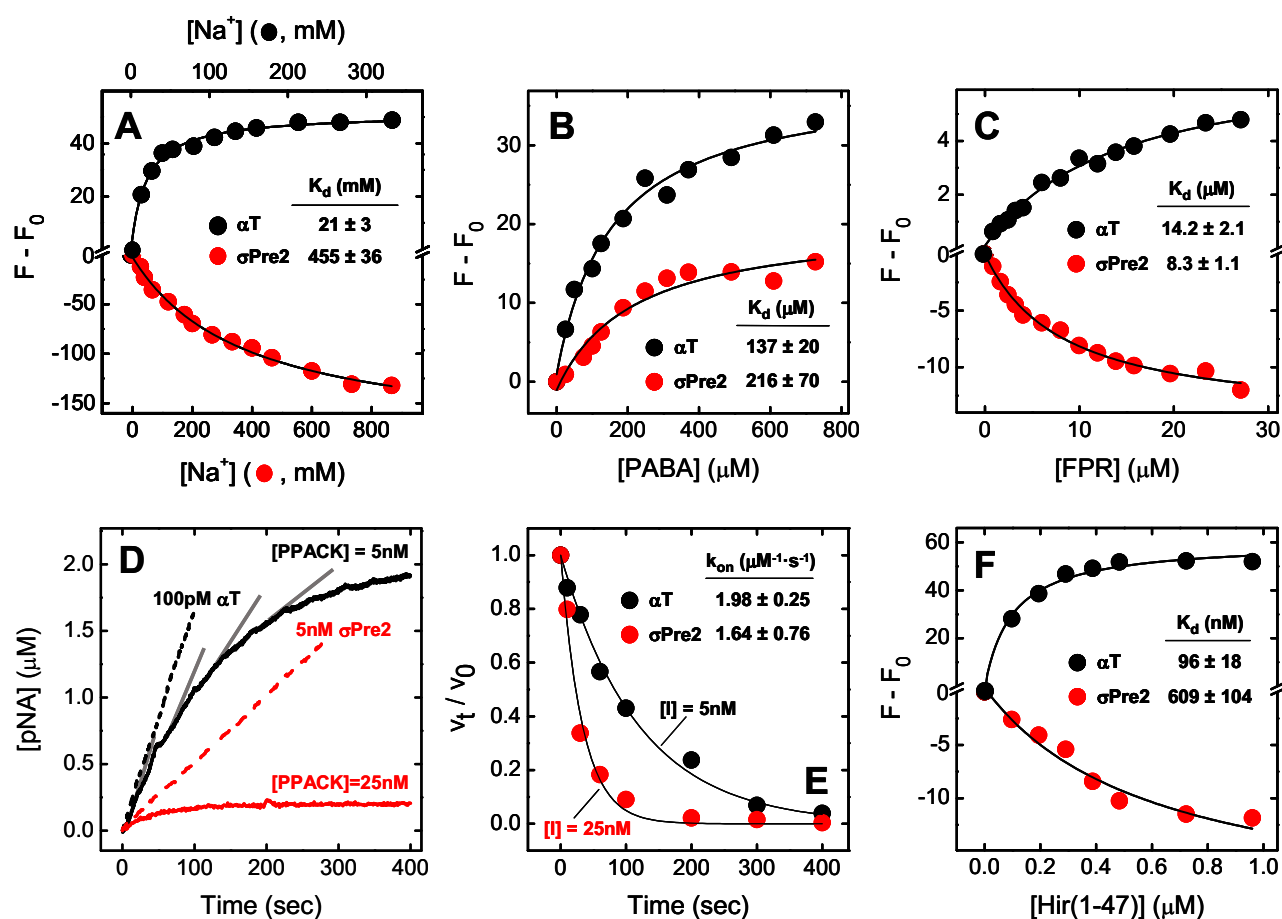
Figure 7. Probing the structure of the Na$^+$-site (A) and active site (B - F) of σPre2 (●) and αT (●). (**A**) Fluorescence measurements of sodium binding to σPre2 and αT. Samples (15 nM, 1.5 ml) of σPre2 and αT in TBS, pH 8.0, containing increasing concentrations of NaCl, were excited at 280 nm and constant temperature (25 ± 0.1°C). The fluorescence intensity was recorded at the emission λ$_{max}$ of the proteins, i.e. 334 nm for αT and 340 nm for σPre2. The data are expressed as F – F$_0$, where F$_0$ is the fluorescence intensity in the absence of NaCl. The data points were interpolated with **eq. 2** yielding the K$_d$ values for Na$^+$ binding, as indicated. The ionic strength was kept constant at 1 M with ChCl. (**B**) Fluorescence binding of PABA to σPre2 and αT. Increasing concentrations of PABA were added to protein samples (200 nM, 1.5 ml). Excitation wavelength was at 336nm, while the fluorescence intensity was recorded at 375 nm. K$_d$ values were obtained by fitting the data points to **eq. 2**, describing the one-site binding model. Fluorescence binding of FPR (**C**) and Hir(1-47) (**F**) to σPre2 and αT. To a solution of σPre2 or αT (100 nM, 1.5 ml) were added increasing concentrations of ligands and protein samples were excited at 280 nm, with FPR, or at 295 nm, with Hir(1-47). The fluorescence intensity was recorded at the emission λ$_{max}$ of αT (334 nm) or σPre2 (340 nm). The data points relative to the binding of FPR to σPre2 and αT, and those of Hir(1-47) binding to σPre2 were interpolated with **eq. 2**, whereas the binding of Hir(1-47) to αT were fitted to **eq. 3**, describing the tight binding model. (**D, E**) Inhibition of αT and σPre2 by PPACK. (**D**) Progress curves of pNA generation by αT (black lines) and σPre2 (red lines) in the absence (dashed lines) and presence (continuous lines) of PPACK. Aliquots (400 μl) of αT or σPre2 stock solutions were added at 37°C in HBS, pH 7.4 to a solution of substrate (20 μM) and PPACK, as indicated. At each time point, the rate of pNA release (v) was estimated from the slope of the tangent lines (grey) to the progress curve. (**E**) Plot of v$_t$/v$_0$ vs. time. The data points were interpolated with **eq. 10** to yield the values of k$_{obs}$ and k$_{on}$ for PPACK inhibition of αT and σPre2.

Whereas the binding of PABA was monitored by measuring the increase of the ligand quantum yield, the affinity of FPR and Hir(1-47) was determined by recording the fluorescence changes that the ligands evoked in σPre2 or αT. For PPACK inhibition, the pseudo-first order association rate constant, k_{on}, for αT and σPre2 was determined by measuring the time-dependence decrease in the rate of substrate hydrolysis at a fixed inhibitor concentration, where k_{on} is the best parameter for quantifying the potency of covalent inhibition (**40,43**). Our data indicate that σPre2 binds to small reversible inhibitors, i.e. PABA and FPR, with an affinity identical (± 1.7-fold) to that of mature αT (**Fig. 7B,C**). Likewise, αT and σPre2 are irreversibly inhibited by PPACK with the same association rate constant ($k_{on} = 1.6 – 2.0\ \mu M^{-1}\cdot s^{-1}$) (**Fig. 7D,E**). Conversely, the affinity of σPre2 for the larger inhibitor Hir(1-47) was reduced by > 6-fold (**Fig. 7F**).

From the comparison of inhibitors structures and their binding mode thrombin, it emerges that the geometry of the catalytic site and substrate recognition sites of αT are largely conserved in σPre2, whereas the conformation of the regions surrounding the protease active site is perturbed in the nicked species.

Exosite 1 and 2

The conformational state of σPre2 exosites was probed by exosite-specific binders. Hirugen, i.e. the C-terminal segment 54-65 of hirudin HV1, was used as a safe exosite-I ligand (**38**), while the C-terminal peptide segment 268-282 of the αT receptor on platelets, glycoprotein Ibα (GpIbα), was used as a specific exosite-II binder (**44,45**). The affinity of hirugen for σPre2 decreased by about 9-fold compared with αT (**Fig. 8A**), suggesting that the structure of exosite-1 in σPre2 is significantly perturbed. Contrary to what observed with mature αT in our recent work (**38**), incubation of σPre2 with saturating concentrations of hirugen did not enhance the affinity of the nicked species for Hir(1-47). In fact, a similar K_d value for the binding of Hir(1-47) to σPre2 was obtained either in the absence ($K_d = 0.61\pm0.10\mu M$) or presence ($K_d = 0.54\pm0.14\mu M$) of hirugen (unpublished results). This is a clear-cut indication that in σPre2 the positive allosteric linkage, coupling exosite-1 to the opening of active site, is essentially lost (**46,47**). The affinity of σPre2 or αT for GpIbα(268-282) was measured by immobilizing the synthetic peptide Biotinyl-PEG-GpIbα(268-282) (**Fig. S1**) onto a neutravidin-coated C1 sensor chip (**see Methods**) and injecting increasing concentrations of σPre2 or αT (**Fig. 8B**). SPR data in **Fig. 8B-D** indicate that σPre2 and αT share similar affinity for GpIbα(268-282), suggesting that αT exosite-2 is not significantly altered in the subtilisin-nicked species.

A general trend emerging from the binding measurements is that different ligands [i.e. Na^+, FPR, Hir(1-47), and hirugen], mapping different regions on thrombin, induce similar but opposite fluorescence changes in σPre2 and αT (**Fig. 7A-C,F** and **Fig. 8A**), whereby all the ligands tested

increase the fluorescence intensity of αT and, instead, decrease that of σPre2. This is a clear-cut indication that the conformational changes induced by ligand binding in σPre2 are intrinsically different from those triggered in αT structure. Nevertheless, for a correct interpretation of these results, experimental determination of σPre2 structure is needed.
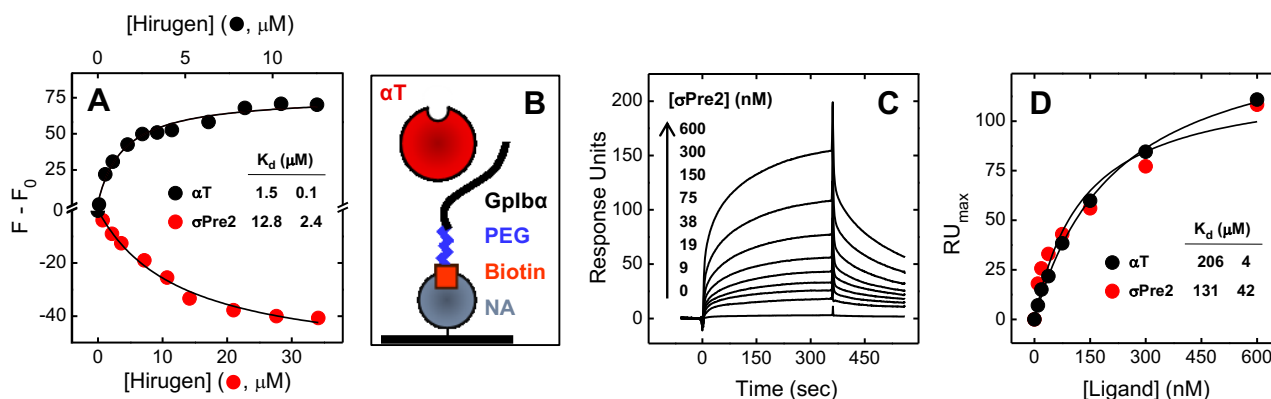
Figure 8. Probing the structure of exosite-1 (A) and 2 (B - D) of σPre2 (●) and αT (●). (A) Binding of hirugen to σPre2 and αT. Solutions (1.5 ml) of σPre2 (150 nM) or αT (50 nM) were added with increasing hirugen concentrations. The protein samples were excited at 280 nm and the fluorescence intensity was recorded at the λ_{max} of the two enzymes, i.e. 334 nm for αT and 340 nm for σPre2. The data points were interpolated with **eq. 2**. All fluorescence measurements were carried out in HBS at 37°C. **(B - D)** Binding of GpIbα(268-282) to σPre2 and αT. **(B)** Scheme of Biotinyl-PEG-GpIbα(268-282) peptide anchoring onto a Neutravidin-coated C1 sensor chip. **(C)** SPR sensograms relative to the binding of σPre2 to immobilized Biotinyl-PEG-GpIbα(268-282). **(H)** Plot of RU_{max} vs. the concentration of σPre2 or αT injected in the mobile phase. SPR measurements were carried out at 25°C in HBS-EP⁺ and K_d values were obtained by fitting the data points to **eq. 4**.

Functional characterization of σPre2

To better characterize the substrate specificity of σPre2 compared with mature αT, the two species were separately incubated with substrates specific for αT (S2238) (**28**), aPC (S2366) (**48**), or factor Xa (S2765) (**49**). The results in **Fig. 9A** clearly indicate that the specificity of σPre2 is qualitatively identical to that of αT, both cleaving the thrombin-specific substrate S2238 with the highest rate. Michaelis-Menten treatment of S2238 hydrolysis by σPre2 and αT reveals that σPre2 hydrolyzes S2238 with an efficiency (k_{cat}/K_m) 165-fold lower than αT and, importantly, this was mainly due to a selective decrease (by 124-fold) of the catalytic constant (k_{cat}), whereas the Michaelis constant (K_m) was only slightly increased (by 1.4-fold) (**Fig. 9B** and **Table 2**). For αT, K_m can be approximated to the dissociation constant (K_d) of the enzyme-substrate complex (**50**). Hence, the invariance of K_m strongly suggests that the substrate specificity sites in σPre2 are fully formed and recognize S2238 with an affinity identical to that of mature αT. This conclusion is fully consistent with the results of fluorescence and enzyme activity measurements, showing that FPR has the same affinity for αT and σPre2 (**Fig. 7C**) and that PPACK irreversibly inhibits the two enzymes with the

same k_{on} (**Fig. 7D,E**). These findings and the marked decrease of k_{cat}, we have measured for S2238 hydrolysis by σPre2, suggest that the catalytic events (following the early binding step) are altered in the nicked species. However, this should not be surprising. Indeed, although FPR-binding and PPACK-inhibition data provide strong indication that σPre2 strictly retains the precise stereochemistry and reactivity of the amino acids in the catalytic triad (i.e. His57, Asp102 and Ser195) of αT, these residues belong to physically distinct (albeit interacting) fragments in σPre2. In particular, His57 and Asp102 are located in the NT fragment, whereas Ser195 is in the CT fragment (**Fig. 4B**). This arrangement could therefore perturb the optimal coupling of the active-site amino acids during the catalytic reactions leading to peptide bond hydrolysis and product release, with a resulting decrease of k_{cat}.

The catalytic competence of σPre2 was also tested on more complex substrates, i.e. protein C (PC), fibrinogen (Fb) and PAR1, by measuring the efficiency of active PC (aPC) generation in the presence of the cofactor thrombomodulin (TM) (**Fig. 9C**), fibrinopeptides (FpA and FpB) release (**Fig. 9D**), and cleavage of PAR1(38-60) peptide (**Fig. 9E**). The corresponding kinetic parameters are reported in **Table 2**. Fb and PAR1 both interact with thrombin at either exosite-1 and active site (**1,2**). At variance, PC binds exclusively to the protease active site and TM accelerates thrombin-catalyzed PC hydrolysis by interacting with αT exosite-1 and properly orienting both the protease catalytic site and zymogen for efficient cleavage (**51**). Notably, PAR1(38-60) reproduces the substrate properties of the extracellular domain of PAR1 on platelets, as it contains both the exosite-1 binding sequence and the scissile bond R^{41}-S^{42} for αT (**52,53**). The efficiency with which αT or σPre2 converts PC zymogen to the active aPC was determined by a continuous assay, measuring pNA release from the aPC-specific substrate S2366 (**54**). Our data indicate that in the presence of TM σPre2 cleaves PC with an efficiency about **230-fold** lower than αT. The kinetics of fibrinopeptides release was analysed using the Shafer's model (**55**), according to which a highly specific cleavage at the Aα Fb chain by αT leads to the rapid release of FpA and formation of fibrin I monomers that aggregate to form fibrin I protofibrils. A second cleavage at the Bβ chain of the fibrin I monomers then leads to the slower release of FpB and formation of fibrin II protofibrils, which then aggregate to form the fibrin clot. The specificity constants (k_{cat}/K_m) relative to the release of FpA and FpB by σPre2 were determined as **300**- and **100-fold** lower, respectively, than those measured for αT (**53**). Likewise, the efficiency of PAR1(38-60) hydrolysis by σPre2 was reduced by almost 10^3**-fold**, compared with αT.
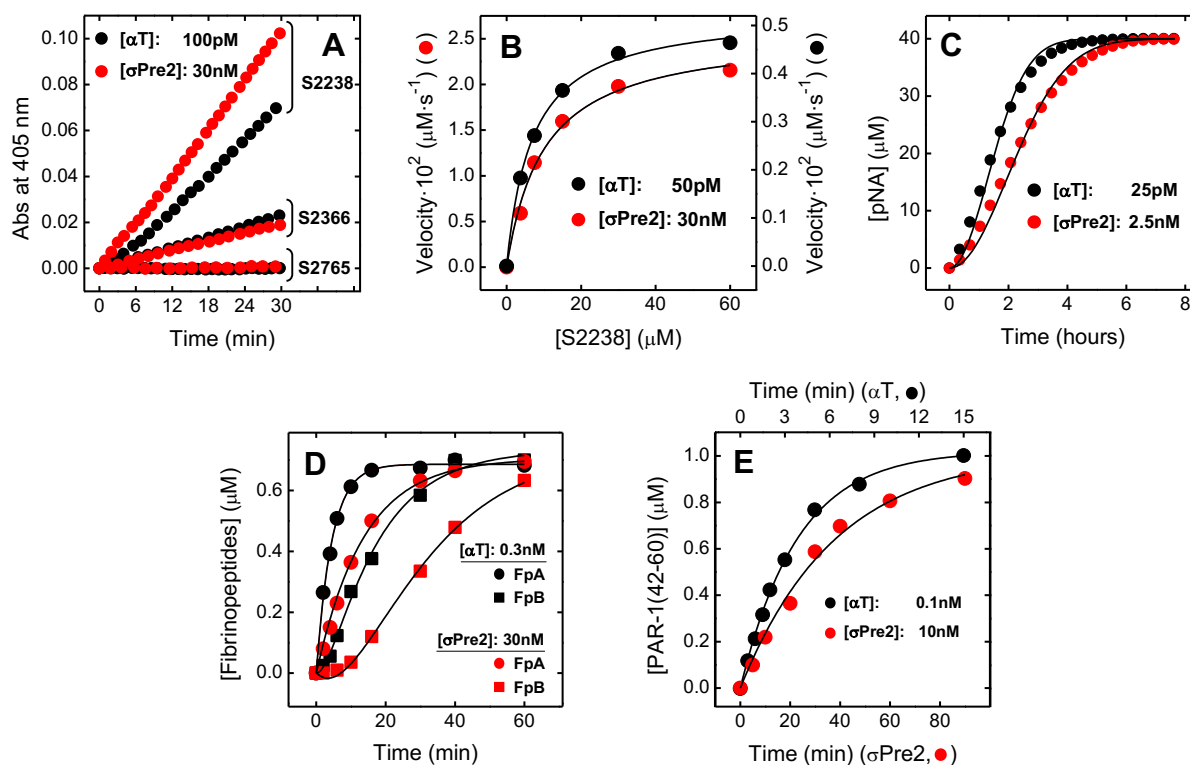
Figure 9. Substrate specificity and catalytic efficiency of σPre2 and αT on S2238, protein C, fibrinogen and PAR1(38-60). (**A**) Substrate specificity of σPre2. Purified σPre2 (●) (30 nM, final concentration) was added to solutions of chromogenic substrates (20 μM) in HBS at 37°C, each specific for αT (S2238), aPC (S2366), or factor Xa (S2765), and the release of pNA was monitored at 405 nm. For comparison, the activity of 100 pM human αT (●) on the same substrates is also reported. (**B**) Determination of the kinetic constants of S2238 hydrolysis by σPre2. The initial rate of pNA release from S2238 (20 μM) by σPre2 (30 nM, ●) and αT (50 pM, ●) was measured at 37°C in HBS, 0.1% PEG (200 μl, final volume). From the interpolation of the data points with the Michaelis-Menten equation (**eq. 5**) k_{cat} and K_m values were obtained as best-fit parameters (**Table 2**). (**C**) Active protein C (aPC) generation by αT (●) or σPre2 (●). To a solution of PC (50 nM) in HBS, pH 7.5, 5 mM CaCl$_2$ at 37°C in the presence of TM (10 nM) and S2366 (40 μM) were aliquots αT or σPre2, as indicated. The concentration of pNA released from S2366 by aPC was monitored at 405 nm in a continuous assay. The resulting progress curves were analyzed as in **ref. 54** (continuous lines), to extract the values of k_{cat}/K_m relative to PC activation by αT or σPre2 (**Table 2**). (**D**) Release of fibrinopeptides A and B from human fibrinogen. The release of FpA (●, ●) and FpB (■, ■) from human fibrinogen (0.35 μM) by σPre2 (30 nM) (●, ■) or αT (0.3 nM) (●, ■) was carried out at 37°C in HBS, and quantified by RP-HPLC (see Methods). Interpolation of the data points with **eq. 6** and **7**, yielded the apparent specificity constants (k_{cat}/K_m) of FpA and FpB release for σPre2 and αT (**Table 2**). (**E**) Cleavage of PAR1(38-60). The cleavage of PAR1(38-60) peptide (1 μM) by σPre2 (10 nM) (●) or αT (0.1 nM) (●) was carried out at 25°C in HBS. The time course of PAR1(42-60) fragment release was quantified by RP-HPLC and the data points were fitted with **eq. 8**, describing the kinetics of product formation under pseudo-first order conditions. For clarity, the lower and upper time scale refers to the experiment run with σPre2 (●) and αT (●), respectively. The estimated k_{cat}/K_m values are reported in **Table 2**.

Altogether, the results of ligand binding and enzymatic activity measurements indicate that, whereas the ligand binding properties of αT at exosite-2 and active site are retained in σPre2, molecular recognition at exosite-1 and Na$^+$-site is reduced by **10-** and **20-fold**, respectively. Furthermore, the decrease in the efficiency of substrate hydrolysis is even more pronounced (**100-1000 fold**), especially for those bivalent substrates interacting with the enzyme at both exosite-1 and active site, i.e. PAR1 and Fb. However, this is also true for PC activation in the presence of TM, where the cofactor tightly binds to exosite-1, which is compromised in σPre2 (**51**).

Table 2: Substrate specificity of σPre2 and αT [a].

	σPre2			αT		
	k_{cat} (s^{-1})	K_m (μM)	k_{cat}/K_m (μM^{-1}·s^{-1})	k_{cat} (s^{-1})	K_m (μM)	k_{cat}/K_m (μM^{-1}·s^{-1})
S2238	0.86 ± 0.04	10.0 ± 1.3	0.09 ± 0.01	106.6 ± 2.2	7.2 ± 0.5	14.8 ± 0.03
		k_{cat}/K_m (μM^{-1}·s^{-1})			k_{cat}/K_m (μM^{-1}·s^{-1})	
FbpA		0.042 ± 0.001			12.5 ± 0.6	
FbpB		0.036 ± 0.008			3.7 ± 0.8	
PAR1(38-60)		0.044 ± 0.005			43.3 ± 1.5	
		k_{cat}/K_m (mM^{-1}·s^{-1})			k_{cat}/K_m (mM^{-1}·s^{-1})	
PC		0.759 ± 0.004			173.8 ± 1.1	

[a] The kinetic constants relative to the hydrolysis of thrombin substrates were extracted by interpolating the data points in **Fig. 9**, as detailed in the Methods and legend to **Fig. 9**.

σPre2 induces fibrin generation and platelets aggregation

To address the possible relevance of subtilisin on the onset of thrombotic events during bacterial infections, we evaluated the effect of σPre2 on fibrin generation either with purified Fb and human plasma (**Fig. 10A**), as wells as the ability of subtilisin to directly generate fibrin in human plasma, *via* σPre2 formation (**Fig. 10B**). At last, the effect of σPre2 on platelets aggregation was studied either on gel-filtered platelets and in whole blood (**Fig. 10C,D**).

Fibrin generation

The time-course formation of fibrin from purified Fb or human plasma was monitored by recording the turbidimetric signal at 350 nm and 671 nm, respectively (**35,56**). The data in **Fig. 10A** and **Table 3** indicate that addition of σPre2 (50 nM) to a purified Fb solution (0.15 mg/ml, ~400 nM) or to diluted (1:2) human plasma ([Fb] = 3.5 μM) generated similar fibrin clotting curves converging to an identical A$_{max}$ value. However, in blood plasma, the t$_c$ value of σPre2 was prolonged by 1.6-fold compared with isolated Fb and the maximal rate of fibrin formation (S$_m$) was ~4-fold lower.

Notably, t_c corresponds to the time necessary for the longitudinal elongation of protofibrils, deriving from fibrin monomers after removal of fibrinopeptides. Importantly, the lag-phase of fibrin formation by σPre2, either with purified Fb and human plasma, was **100-200 fold** higher than that estimated with αT at the same concentration (50nM) (**Table 3**), reflecting the lower efficiency of fibrinopeptides release by σPre2 (**Fig. 9D**). Furthermore, a remarkable (~3-fold) increase of the A_{max} value was also observed with σPre2 (A_{max} = 0.21), compared with αT (A_{max} = 0.08), where A_{max} is the maximum turbidity measured when the final fibrin clot is formed and it is proportional to the square of the average diameter (d) of the fibers (**56**). The latter result indicates that the fibrin network generated by σPre2 is formed by fewer fibers that, however, are thicker than those produced by the more catalytically efficient αT at the same concentration.

At this point, the question arises as to whether subtilisin might function like ecarin, inducing the formation in human plasma of proteolytically active thrombin species which can clot fibrin. The data in **Fig. 10B** provide clear-cut answer to this question and demonstrate that addition of 0.25 IU of either subtilisin (2 μM, 50 nM) or ecarin (2.5 nM) to diluted (1:2) human plasma induced fibrin generation, even though with different time scales. Notably, 4 nM subtilisin was not able to induce plasma clotting in the time range explored (not shown). A clotting time, t_c, of 2.1 min was determined for ecarin (**see Fig. S3**), in agreement with our previous results (**35**), whereas a much longer lag-phase was estimated at either 2 μM (t_c = 2h) and 50 nM subtilisin (t_c = 14h) (**Table3**). Notwithstanding, the clotting curves in **Fig. 10B** document that even small subtilisin concentrations (50 nM) are able to clot fibrinogen in human plasma. The dramatic difference in the plasma clotting time, observed between subtilisin and ecarin, can be reasonably accounted for by several factors: i) the 20-fold lower specificity constant of subtilisin for CS-3 in Pre2 (k_{cat}/K_m = 0.18±0.02 μM^{-1}·s^{-1}) (**Fig. 3E,G**), compared with ecarin (k_{cat}/K_m = 4.1 μM^{-1}·s^{-1}) (**57**); ii) the 100-300 fold lower catalytic efficiency of the resulting nicked σPre2 species to hydrolyze Fb, compared with αT (**Fig. 9D**); iii) the presence of physiological serine proteinase inhibitors in human plasma (e.g. α$_2$-antitrypsin, antiplasmin, α$_1$-proteinase inhibitor) which may irreversibly inhibit subtilisin, without affecting ecarin function (**58**).

Platelet aggregation

The ability of σPre2 to agglutinate platelets was tested on whole blood (WB) and gel-filtered platelets (GFP) by Multiple Electrode Aggregometry (MEA) (**Fig. 10C**). This technique measures the increase of resistance, i.e. the impedance to the passage of alternate current in a medium between two platinum electrodes, which is caused by sticking of activated platelets on the electrodes (**59**). Addition of 50 nM σPre2 or 0.5 nM αT to WB or GFP yielded comparable aggregation curves, i.e. the time-dependent change of the plasma impedance expressed as relative Aggregation Units (AU).
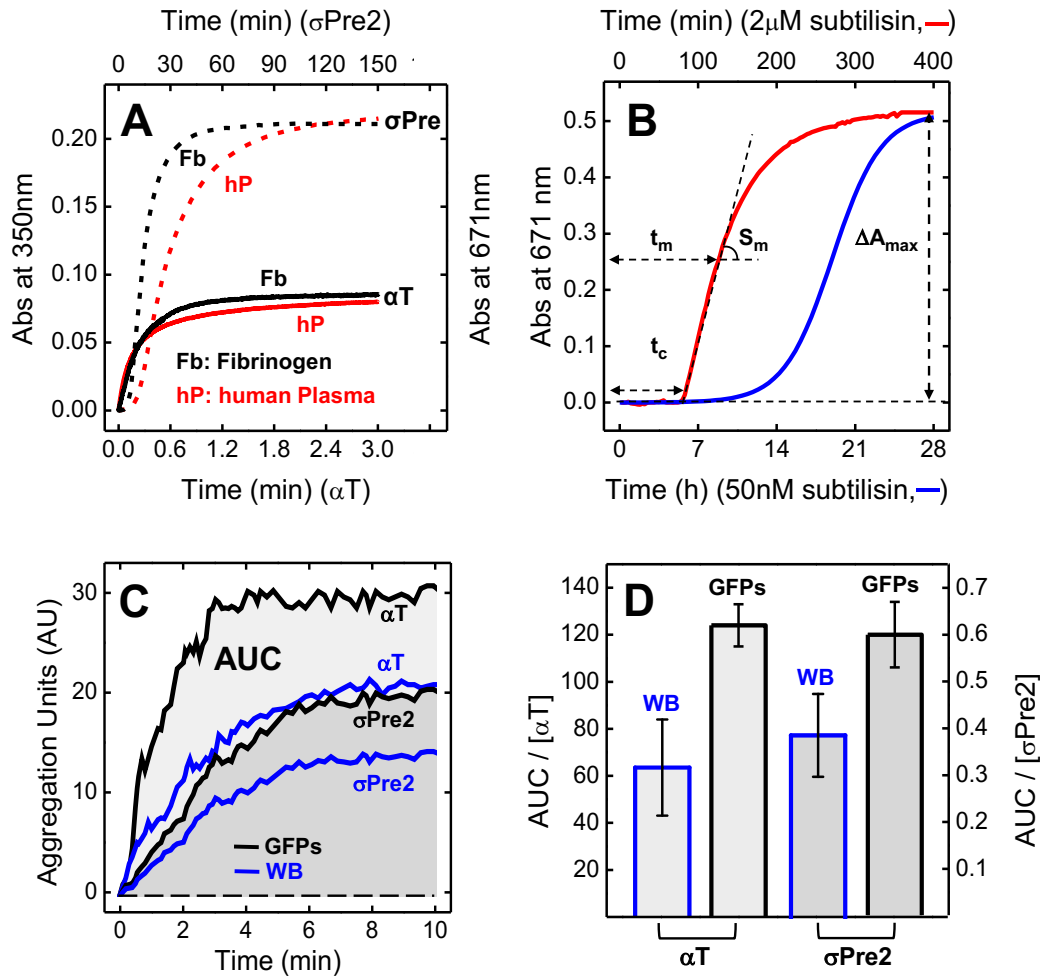
Figure 10. Fibrin generation and platelets aggregation induced by σPre2 and αT. (**A**) Turbidimetric analysis of fibrin generation induced by 50 nM σPre2 (dashed lines) or 50 nM αT (continuous lines) on purified fibrinogen (black lines) or diluted (1:2) human plasma (red lines). To a human fibrinogen solution (440 nM, 800 µl) in HBS at 37°C, containing 0.1% PEG-8000, was added αT (50 nM) or σPre2 (50 nM) and the time-course generation of fibrin was monitored by recording the absorbance increase of the solution at 350 nm. With human plasma samples, the absorbance change was recorded at 671 nm (right-handed scale). For clarity, the lower time scale (0-3 min) refers to the experiment run with αT, while the upper time scale (0-150 min) refers to the experiment run with σPre2. The absorbance scale for both experiments is the same (0-0.25 AU). (**B**) Turbidimetric analysis of fibrin generation induced by different concentrations of subtilisin (0.25 IU = 2µM, —) (50 nM, —) on diluted (1:2) plasma. From each clotting curve, the values of S_m, t_m, t_c, and ΔA_{max} were extracted, as indicated (**Table 3** and Methods). (**C**) Impedance aggregometry analysis of platelet aggregation induced by σPre2 or αT at 37°C in whole blood (WB, —) or gel filtered platelets (GFP, —). WB from healthy donors (300 µl; 160.000 platelets/µl) was diluted with HBS (320 µl), containing αT or σPre2 to a final concentration of 0.5 nM and 50 nM, respectively. A similar procedure was used with GFP (200.000 platelets/µl) (**D**) Histogram of the normalized platelets aggregation potency of σPre2 and αT expressed as AUC/[E] ratio, where [E] is the molar enzyme concentration. Each value is the average of single determinations on blood samples from three healthy donors. The error bars correspond to the standard deviation.

Notably, the more intense signal obtained with both σPre2 and αT on GFP reflects the higher platelets count of GFP (200.000/μl) compared with WB (160.000/μl). Integration of AU over time (10 min) gives the value of the Area Under the Curve (AUC), while the ratio AUC/[E] is taken as the platelets aggregation potency of σPre2 or αT, where [E] is the concentration of thrombin-like species. The histograms in **Fig. 10D** indicate that the aggregation potency of σPre2 on WB and GFP is approximately 150- and 200-fold lower than that of αT, respectively. The observation that nanomolar concentrations of σPre2 can still agglutinate platelets is consistent with site-specific binding data showing that peptide bond nicking does not appreciably perturb exosite-2, which is the binding site for thrombin on the platelets receptor GpIbα (**Fig. 8B-D**). On the other hand, the decrease of the aggregation potency is fully consistent with the marked reduction in the efficiency of PAR1(38-60) hydrolysis by σPre2 (**Fig. 9E**).

Table 3. Representative parameters for the fibrin clotting curves generated with isolated fibrinogen or human plasma by σPre2, αT, subtilisin, and ecarin. [a]

	S_m (AU·min^{-1}) [b]	t_m (min) [c]	t_c (min) [d]	ΔA_{max} (AU) [e]
Purified Fibrinogen [f]				
αT (50nM)	$234.0 \cdot 10^{-3}$	0.17	0.06	0.08
σPre2 (50 nM)	$15.8 \cdot 10^{-3}$	10.60	6.70	0.21
Human Plasma [g]				
αT (50 nM)	$8.2 \cdot 10^{-3}$	0.16	0.05	0.08
σPre2 (50 nM)	$4.1 \cdot 10^{-3}$	17.10	10.90	0.21
Human Plasma [g]				
Ecarin (2.5 nM)	$55.9 \cdot 10^{-3}$	2.40	2.10	0.41
Subtilisin (2μM)	$5.2 \cdot 10^{-3}$	125	82.0	0.52
Subtilisin (50nM)	$9.3 \cdot 10^{-4}$	1134	840.0	0.51

[a] The parameters of the fibrin clotting curves were extracted from the data reported in **Fig. 10A,B** and the experimental error was error was ± 10%. [b] S_m is the value of the maximal slope of the curve; [c] t_m is the time needed to reach S_m; [d] t_c is the clotting time and is calculated from the intercept point with the time axis of the tangent line to the curve at t_m; [e] ΔA_{max} is the maximal absorbance change when fibrin generation is complete. [f] In fibrin generation measurements, the concentration of purified fibrinogen was 400 nM. [g] The estimated concentration of fibrinogen in 1:2 diluted human plasma was 3.5 μM.

Molecular Mechanism of ProT/Pre2 activation by subtilisin

Our data clearly document that αT-like activity appears only after nicking of Ala149a-Asn149b bond and subsequent generation of a new N-terminal dipeptide segment, i.e. Asn149b-Val149c, on the CT fragment of σPre2. However, the molecular mechanism linking peptide bond cleavage to catalysis remains unknown. Notably, in a previous work (**36**), we used subtilisin as a probe of the conformational flexibility of the 148-loop in mature αT, in the absence and presence of Na^+, and found the same cleavage site as with ProT and Pre2. To gain more insights into the mechanism of zymogen activation, αT and σPre2 were subjected to carbamylation of the N-termini with potassium cyanate (KCNO), a reagent that at physiological pH almost exclusively reacts with the N-terminal α-amino groups of proteins and obliterates the positive charge at the N-terminus (R-NH_3^+) by forming a neutral ureido-group, according to the reaction: R-NH_2 + HNCO → R-$NHCONH_2$, where HNCO is the reactive isocyanic acid in equilibrium with cyanate (NCO^-) (**60**). Notably, at a given solution pH, the carbamylation rate is positively correlated with the amount and accessibility of the unprotonated N-terminal R-NH_2 group (**61,62**).

At time points, αT or σPre2 solutions (1 μM) were incubated in the absence or presence of KCNO (0.2 M) at 37°C and aliquots of these solutions were tested for enzymatic activity on S2238 substrate. The data in **Fig. 11A** indicate that, in the presence of cyanate, the relative rate of substrate hydrolysis by either αT (100 pM) and σPre2 (50 nM) decreased with time to different extents. Noteworthy, the reduction of the hydrolysis rate was stronger with σPre2 than with mature αT. After 1-h reaction with cyanate, for instance, the activity of αT was reduced by only < 10%, whereas that of σPre2 by > 50%. As a control, in the absence of KCNO, the rate of hydrolysis remained constantly high. When the effect of cyanate on αT or σPre2 function was analysed according to the irreversible inhibition model, used above for describing PPACK inhibition, (**42**), a 3-fold higher pseudo first-order inhibition rate constant (k_{on}) was estimated for σPre2 compared with αT (**Fig. 11A**). The extent of carbamylation of the N-termini in αT and σPre2 was estimated by automated Edman sequencing, after 1-h reaction with KCNO at 37°C and subsequent reduction and carboxamidomethylation of Cys-residues (see Methods). Edman degradation, indeed, starts only if the terminal N^α-amino group is available, and thus it allows a rough estimate of the % of molecules in a protein sample having free N-terminal ends. Our data indicate that the sequences of the A-chain in αT and that of NT fragment in σPre2 could not be detected, suggesting that in both enzymes the N-terminal end was quantitatively carbamylated and thus fully accessible in the structure of the two enzymes. Conversely, the B-chain was almost quantitatilely sequenced (> 90%), indicating that the N-terminal Ile16 in αT was deeply buried in the mature protease structure and thus protected from reaction with cyanate.
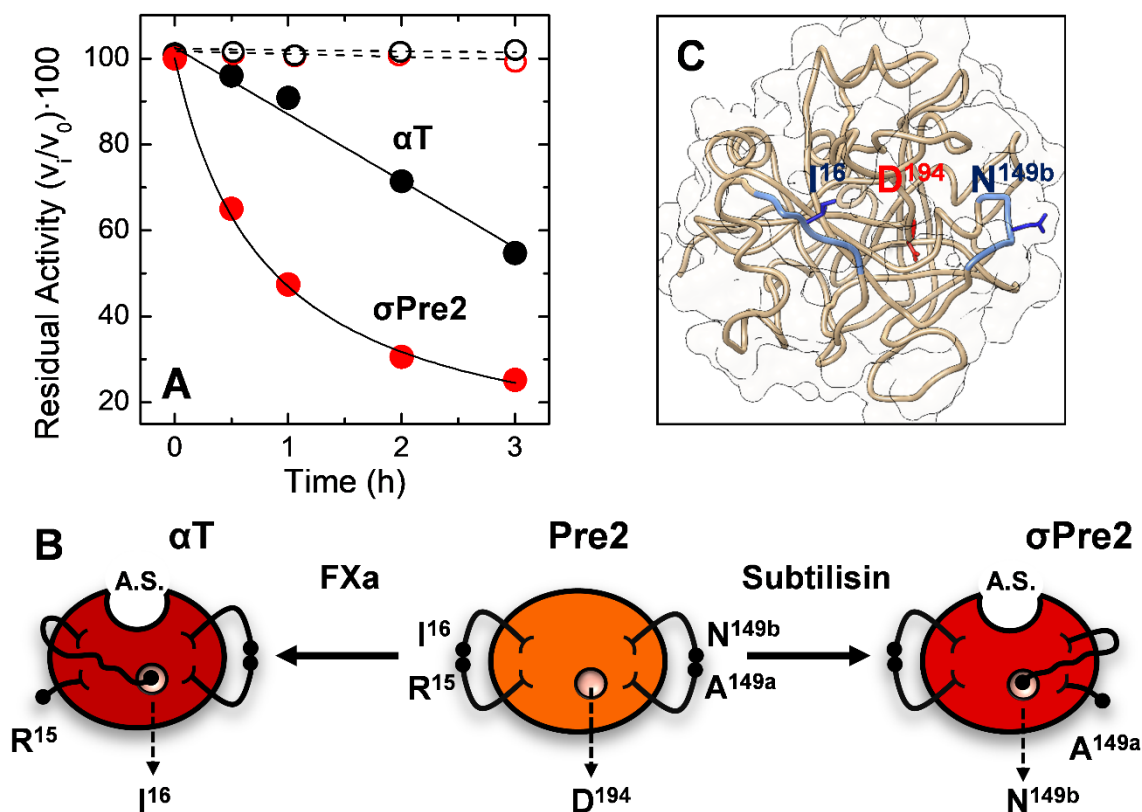
Figure 11. Mechanism of zymogen activation in σPre2 and αT. (**A**) Effect of time-course carbamylation of σPre2 on the rate of S2238 substrate hydrolysis. Time course hydrolysis of σPre2 (○, ●) and αT (○, ●) in the absence and presence of potassium cyanate. Solutions of σPre2 (1 μM) in HBS, pH 7.0 were incubated at 37°C in the absence (○) and presence (●) of 0.2 M KCNO. At the indicated time points, aliquots (40 μl; 50 nM final concentration) were taken and the initial rate (v_i) of S2238 (20 μM) hydrolysis was determined in HBS at 37°C. For comparison, the activity of αT (100 pM, final concentration) determined in the absence (○) and presence (●) of KCNO is also reported. The data are expressed as the percent residual activity, (v_i/v_0) x 100, where v_i and v_0 is the rate of hydrolysis determined at time t_i and 0, respectively. After interpolating the kinetic data with **eq. 9**, describing the irreversible enzyme inhibition under pseudo first-order conditions, the corresponding rate constants (k_{on}) were determined for σPre2 (4.8 x 10^{-2} $M^{-1} \cdot min^{-1}$) and αT (1.6 x 10^{-2} $M^{-1} \cdot min^{-1}$). (**B**) Schematic representation of the physiological and non-physiological Pre2 zymogen activation by factor Xa or bacterial subtilisin, respectively. After physiological cleavage of the peptide bond Arg15-Ile16 by FXa in Pre2, the newly generated dipeptide Ile16-Val17, swings into the 194-cleft and triggers substrate binding sites and oxyanion hole formation, required for catalysis. Likewise, after non-physiological cleavage by subtilisin at the peptide bond Ala149a-Asn149b in the exposed γ-loop of Pre2, the new N-terminal dipeptide Asn149b-Val149c can enter the 194-cleft and evoke zymogen activation. (**C**) Transparent surface representation of Pre2 showing Asp194 positioned at the bottom of a deep cleft in ProT structure (5edm.pdb) shaped by the two β-barrels of Pre2. The cleavage sites for FXa (Arg15-Ile16) and subtilisin (Ala149a-Asn149b) are also indicated.

At variance, in the case of CT in σPre2, only about 50% of the fragment molecules could be sequenced, thus suggesting that the N-terminal Asn149b was substantially exposed on the σPre2 structure. These findings are fully consistent with enzyme activity data showing that the rate constant of σPre2 inactivation by KCNO is 3-fold higher compared with αT (**Fig. 11A**) and indicate that Asn149b at the N-terminus of CT in σPre2 is, on average, much more exposed than Ile16 at the N-terminal end of the B-chain in αT.

A key aspect emerging from this work is that the raising of catalytic competence in σPre2 is not a fortuitous result of flexibilization of the 148-loop in Pre2, occurring after peptide bond cleavage, but of a precisely concerted conformational change which is inherently associated with the reactivity of the newly generated N-terminal Asn149b. Indeed, neutralization of the N-terminal positive charge, even with a small-sized carbamyl-group, hinders amidolytic activity of σPre2 (**Fig. 11A**). As already established for the zymogens of the trypsin family (**9**), as well as for the physiological activation of ProT by FXa (**6,7,15,33**), it is possible that the new positive N-terminal segment (Asn149b-Val149c-), formed after subtlisin cleavage of Pre2, binds to the negatively charged Asp194 and triggers a conformational transition very similar to that evoked by the Ile16-Val17-segment, which is generated after FXa cleavage at Arg15-Ile16 bond. Hence, nicking of Pre2 by an endogenous (FXa) or exogenous (subtilisin) protease, albeit occurring at two distinct sites on Pre2 structure, can trigger a common physiological mechanism of zymogen activation (**Fig. 11B**). Visual inspection of ProT (5edm) (**4**) or Pre2 (3sqe) (**32**) structure suggests that this may be actually the case (**Fig. 11C**), as both Asn149b in σPre2 and Ile16 in αT are located in unconstrained loop regions, which may become even more flexible after nicking, and (more importantly) at a comparable distance (~22 Å in αT and ~16 Å in σPre2) from the critical Asp194 side-chain. The proposed model of σPre2 activation accounts for the higher rate of carbamylation of Asn149b in σPre2, compared with that of Ile16 in αT (**Fig. 11A**). In αT structure, indeed, the NH_3^+-group of Ile16 is less amenable to react with cyanate as it is deeply buried in a hydrophobic environment, where it forms a high-energy salt bridge with the carboxylate of Asp194 (**33**). This salt bridge is likely weaker in σPre2 because the N-terminal amino-group of Asn is 10-fold less basic [pKa(Asn) = 8.72; pKa(Ile) = 9.76] (**60**) and 260-fold less hydrophobic than that of Ile [LogP(Asn) = -2.41; LogP(Ile) = -0.03] (**63**). The lower stability of the salt bridge between Asn149b and Asp194 is expected to reduce the residence time of Asn149b in the Asp194-cleft, and allow exposure of the N-terminal end, which becomes available for reacting with cyanate (**Fig. 11A**). In addition, weakening of Asn149b-Asp194 ionic interaction might also have a direct impact on the catalysis of σPre2, altering the efficiency with which electrostatic perturbation of Asp194 is transmitted long range to the active site. These considerations may also contribute to explain the marked decrease of k_{cat} we have measured for σPre2 compared with αT (**Fig. 9B**).

CONCLUSIONS

In the early 1900s it was shown that certain bacteria, especially staphylococci, are able to induce clotting of human blood (**64**) and, since the late '30s, fibrin deposition has been recognized as a common feature at the sites of bacterial infection (**65**). Very recently, fibrin generation has been proposed as a host defence mechanism of innate immunity to avoid systemic activation of coagulation, by segregating bacterial pathogens in a fibrin network at infection sites (**66**). On the other hand, activation of coagulation can also be seen as a smart evolutionary mechanism, whereby the pathogens exploit the host haemostatic system components to escape immune response and prevent their elimination from the blood by "self-entrapment" within a fibrin clot (**67**). Beyond these intriguing host-pathogen evolutionary strategies, the pathological activation of coagulation in infectious diseases is associated with high morbidity and mortality (**22,68**). Nonetheless, the molecular mechanisms linking bacterial infection to thrombosis have not been fully understood (**69**). It is generally accepted that coagulopathic complications in sepsis are mainly triggered by surface bacterial lipopolysaccharides (LPS) that interact with Toll-like receptors on monocytes and induce expression of tissue factor, thus activating the "extrinsic" pathway of thrombin generation (**66,69**). Intriguingly, LPS is present on Gram-negative bacteria, but it is absent on the surface of Gram-positive bacteria and infections from the latter group of pathogens are those that more frequently are complicated by severe coagulopathies (**68**). These observations indirectly suggest that other factors, different from LPS-induced activation of blood coagulation, should be considered for understanding the positive relation existing between sepsis and thrombosis. Mounting evidences, accumulated in the last decades, indicate that microbial pathogens can bypass the coagulation cascade and directly trigger ProT activation either by proteolytic (**17-21**) and non-proteolytic mechanisms (**10,15**). Whereas the non-proteolytic mechanism, leading *S. aureus* proteins SC and vWbp to conformationally activate ProT, has been elucidated in great detail (**10,15**), not many information are available on the mechanisms underlying the proteolytic conversion of ProT to thrombin-like active species and on the effect that the ensuing thrombin-like forms have on fibrinogen cleavage (**21**), fibrin generation and platelet aggregation (**20**). In addition, when available, literature data indicate that different proteases (e.g., serine-, cysteine-, or metallo-proteases) from different bacterial pathogens (e.g, Gram-positive or Gram-negative bacteria) convergently hydrolyze ProT at the canonical Arg320-Ile321 cleavage site for FXa, leading to the generation of meizothrombin/desF1-meizothrombin active species or even to the transient generation of mature αT, as in the case of gingipain, an Arg-specific cysteine-protease isolated from the pathogenic agent of periodontitis *Porphyromonas gingivalis* (**18**).

Our results show that addition of subtilisin (50 nM - 2 μM) is able to *bypass the coagulation cascade* and induce plasma clot formation and aggregate platelets by directly activating ProT through

zymogen cleavage at Ala151-Met152 and Arg271-Thr272 peptide bonds and at the non-canonical cleavage site Ala470-Asn471. The resulting σPre2 species proteolytically converts fibrinogen into fibrin (either in solution or in normal blood plasma) and aggregate platelets (either isolated or in whole blood). σPre2 was purified to homogeneity and thoroughly characterized in terms of chemical composition and conformational and functional properties, allowing us to safely conclude that σPre2 is constituted by NT and CT fragments forming a stable and functional fragment-complementing system, held together only by non-covalent interactions. Notably, the raise of thrombin-like activity is caused by the alternative cleavage at Ala149a-Asn149b bond and subsequent formation of the non-canonical Asn149b-Asp194 intramolecular salt bridge. These findings establish a new paradigm for the proteolytic activation of ProT, whereby nicking of Pre2 domain at different sites can evoke a common (physiological) mechanism of zymogen activation. The results reported in this work also indicate that proteases secreted by even non-virulent bacteria, such as *B. subtilis*, can shift the delicate procoagulant-anticoagulant equilibrium towards thrombosis and pave the way to further investigate the ability of other subtilisin-proteases (**70**), produced by known pathogenic bacteria (e.g., Shiga toxigenic *E. coli*, *Streptococcus pyogenes*, *Pseudomonas aeruginosa*, *Plasmodium falciparum*) and sharing high sequence similarity with subtilisin form *B. subtilis*, to affect blood coagulation.

REFERENCES

1. Roberts, H.R., Hoffman, M., and Monroe, D.M. (2006) A cell-based model of thrombin generation. *Semin. Thromb. Hemost.* **32 Suppl 1**, 32-38

2. Versteeg, H.H., Heemskerk, J.W., Levi, M., and Reitsma, P.H. (2013) New fundamentals in hemostasis. *Physiol. Rev.* **93**, 327-358

3. Butenas, S., van't Veer, C., and Mann, K.G. (1999) "Normal" thrombin generation. *Blood.* **94**, 2169-2178

4. Pozzi, N., Chen, Z., and Di Cera, E. (2016) How the linker connecting the two kringles influences activation and conformational plasticity of prothrombin. *J. Biol. Chem.* **291**, 6071–6082

5. Mann, K.G., Krishnaswamy, S., and Lawson, J.H. (1992) Surface-dependent hemostasis. *Semin. Hematol.* **29**, 213-226

6. Haynes, L.M., Bouchard, B.A., Tracy, P.B., and Mann, K.G. (2012) Prothrombin activation by platelet-associated prothrombinase proceeds through the prethrombin-2 pathway via a concerted mechanism. *J. Biol. Chem.* **287**, 38647-38655

7. Whelihan, M.F., Zachary, V., Orfeo, T., and Mann, K.G. (2012) Prothrombin activation in blood coagulation: the erythrocyte contribution to thrombin generation. *Blood.* **120**, 3837-3845

8. Fenton, J.W.,2nd, Fasco, M.J., and Stackrow, A.B. (1977) Human thrombins. Production, evaluation, and properties of alpha-thrombin. *J. Biol. Chem.* **252**, 3587-3598

9. Huber, R., and Bode, W. (1978) Structural basis of the activation and action of trypsin. *Acc. Chem. Res.* **11**, 114-122

10. Kroh, H.K., Panizzi, P., and Bock, P.E. (2009) von Willebrand factor-binding protein is a hysteretic conformational activator of prothrombin. *Proc. Natl. Acad. Sci. U.S.A.* **106**, 7786-7791

11. Pozzi, N., Vogt, A.D., Gohara, D.W., and Di Cera, E. (2012) Conformational selection in trypsin-like proteases. *Curr. Opin. Struct. Biol.* **22**, 421-431

12. Pasternak, A., Liu, X., Lin, T.Y., and Hedstrom, L. (1998) Activating a zymogen without proteolytic processing: mutation of Lys15 and Asn194 activates trypsinogen. *Biochemistry.* **37**, 16201-16210

13. Madison, E.L., Kobe, A., Gething, M.J., Sambrook, J.F., and Goldsmith, E.J. (1993) Converting tissue plasminogen activator to a zymogen: a regulatory triad of Asp-His-Ser. *Science.* **262**, 419-421

14. Vogt, A.D., Chakraborty, P., and Di Cera, E. (2015) Kinetic dissection of the pre-existing conformational equilibrium in the trypsin fold. *J. Biol. Chem.* **290**, 22435-22445

15. Friedrich, R., Panizzi, P., Fuentes-Prior, P., Richter, K., Verhamme, I., Anderson, P.J., Kawabata, S., Huber, R., Bode, W., and Bock, P.E. (2003) Staphylocoagulase is a prototype for the mechanism of cofactor-induced zymogen activation. *Nature.* **425**,535-539

16. Kini, R.M. (2003) Excitement ahead: structure, function and mechanism of snake venom phospholipase A2 enzymes. *Toxicon.* **42**, 827-840

17. Wegrzynowicz, Z., Heczko, P.B., Drapeau, G.R., Jeljaszewicz, J., and Pulverer, G. (1980) Prothrombin activation by a metalloprotease from *Staphylococcus aureus. J. Clin. Microbiol.* **12**, 138-139

18. Imamura, T., Banbula, A., Pereira, P.J., Travis, J., and Potempa, J. (2001) Activation of human prothrombin by arginine-specific cysteine proteinases (Gingipains R) from *Porphyromonas gingivalis. J. Biol. Chem.* **276**, 18984-18991

19. Chang, A.K., Kim, H.Y., Park, J.E., Acharya, P., Park, I.S., Yoon, S.M., You, H.J., Hahm, K.S., Park, J.K., and Lee, J.S. (2005) *Vibrio vulnificus* secretes a broad-specificity metalloprotease capable of interfering with blood homeostasis through prothrombin activation and fibrinolysis. *J. Bacteriol.* **187**, 6909-6916

20. Nitta, H., Kobayashi, H., Irie, A., Baba, H., Okamoto, K., and Imamura, T. (2007) Activation of prothrombin by ASP, a serine protease released from *Aeromonas sobria. FEBS Lett.* **581**, 5935-5939

21. Liu, C., Matsushita, Y., Shimizu, K., Makimura, K., and Hasumi, K. (2007) Activation of prothrombin by two subtilisin-like serine proteases from *Acremonium sp. Biochem. Biophys. Res. Commun.* **358**, 356-362

22. Levi, M., and Ten Cate, H. (1999) Disseminated intravascular coagulation. *N. Engl. J. Med.* **341**, 586-592

23. Smith, E.L., DeLange, R.J., Evans, W.H., Landon, M., and Markland, F.S. (1968) Subtilisin Carlsberg. V. The complete sequence; comparison with subtilisin BPN'; evolutionary relationships. *J. Biol. Chem.* **243**, 2184-2191

24. de Boer, A.S., and Diderichsen, B. (1991) On the safety of *Bacillus subtilis and B. amyloliquefaciens*: a review. *Appl. Microbiol. Biotechnol.* **36**, 1-4

25. Oggioni, M.R., Pozzi, G., Valensin, P.E., Galieni, P., and Bigazzi, C. (1998) Recurrent septicemia in an immunocompromised patient due to probiotic strains of *Bacillus subtilis. J. Clin. Microbiol.* **36**, 325-326

26. Siezen, R.J., and Leunissen, J.A. (1997) Subtilases: the superfamily of subtilisin-like serine proteases. *Protein Sci.* **6**, 501-523

27. Perona, J.J., and Craik, C.S. (1995) Structural basis of substrate specificity in the serine proteases. *Protein Sci.* **4**, 337-360

28. Vindigni, A., Dang, Q.D., and Di Cera, E. (1997) Site-specific dissection of substrate recognition by thrombin. *Nat. Biotechnol.* **15**, 891-895

29. Pozzi, N., Chen, Z., Pelc, L.A., Shropshire, D.B., and Di Cera, E. (2014) The linker connecting the two kringles plays a key role in prothrombin activation. *Proc. Natl. Acad. Sci. U.S.A.* **111**, 7630-7635

30.   Fontana, A., Zambonin, M., Polverino de Laureto, P., De Filippis, V., Clementi, A., and Scaramella, E. (1997) Probing the conformational state of apomyoglobin by limited proteolysis. *J. Mol. Biol.* **266**, 223-230

31.   Pozzi, N., Bystranowska, D., Zuo, X., and Di Cera, E. (2016) Structural architecture of prothrombin in solution revealed by single molecule spectroscopy. *J. Biol. Chem.* **291**, 18107-18116

32.   Pozzi, N., Chen, Z., Zapata, F., Pelc, L.A., Barranco-Medina, S., and Di Cera, E. (2011) Crystal structures of prethrombin-2 reveal alternative conformations under identical solution conditions and the mechanism of zymogen activation. *Biochemistry.* **50**, 10195-10202

33.   Bode, W., Turk, D., and Karshikov, A. (1992) The refined 1.9-A X-ray crystal structure of D-Phe-Pro-Arg chloromethylketone-inhibited human alpha-thrombin: structure analysis, overall structure, electrostatic properties, detailed active-site geometry, and structure-function relationships. *Protein Sci.* **1**, 426-471

34.   Li, W., Johnson, D.J., Adams, T.E., Pozzi, N., De Filippis, V., and Huntington, J.A. (2010) Thrombin inhibition by serpins disrupts exosite II. *J. Biol. Chem.* **285**, 38621-38629

35.   Pozzi, N., Acquasaliente, L., Frasson, R., Cristiani, A., Moro, S., Banzato, A., Pengo, V., Scaglione, G.L., Arcovito, A., De Cristofaro, R., and De Filippis, V. (2013) □2-Glycoprotein I binds to thrombin and selectively inhibits the enzyme procoagulant functions. *J. Thromb. Haemost.* **11**, 1093-1102

36.   De Filippis, V., De Dea, E., Lucatello, F., and Frasson, R. (2005) Effect of Na$^+$ binding on the conformation, stability and molecular recognition properties of thrombin. *Biochem. J.* **390**, 485-492

37.   Lakowicz, J. R. (2006) *Principles of fluorescence spectroscopy*, 3rd ed., Springer, New York

38.   Pozzi, N., Zerbetto, M., Acquasaliente, L., Tescari, S., Frezzato, D., Polimeno, A., Gohara, D.W., Di Cera, E., and De Filippis, V. (2016) Loop electrostatics asymmetry modulates the pre-existing conformational equilibrium in thrombin. *Biochemistry.* **55**, 3984-3994

39.   Evans, S.A., Olson, S.T., and Shore, J.D. (1982) *p*-Aminobenzamidine as a fluorescent probe for the active site of serine proteases. *J. Biol. Chem.* **257**, 3014-3017

40.   Kettner, C., and Shaw, E. (1981) Inactivation of trypsin-like enzymes with peptides of arginine chloromethyl ketone. *Methods Enzymol*. **90**, 826–842.

41.   Rydel, T.J., Tulinsky, A., Bode, W., and Huber, R. (1991) Refined structure of the hirudin-thrombin complex. *J. Mol. Biol.* **221**, 583-601

42.   De Filippis, V., Colombo, G., Russo, I., Spadari, B., and Fontana, A. (2002) Probing the hirudin-thrombin interaction by incorporation of noncoded amino acids and molecular dynamics simulation. *Biochemistry.* **41**, 13556-13569

43.   Walker, B., Wikstrom, P., and Shaw, E. (1985) Evaluation of inhibitor constants and alkylation rates for a series of thrombin affinity labels. *Biochem. J.* **230**, 645-650

44. De Cristofaro, R., and De Filippis, V. (2003) Interaction of the 268-282 region of glycoprotein Ibalpha with the heparin-binding site of thrombin inhibits the enzyme activation of factor VIII. *Biochem. J.* **373**, 593-601

45. Lechtenberg, B.C., Freund, S.M., and Huntington, J.A. (2014) GpIbα interacts exclusively with exosite II of thrombin. *J. Mol. Biol.* **426**, 881-893

46. Gandhi, P.S., Chen, Z., Mathews, F.S., and Di Cera, E. (2008) Structural identification of the pathway of long-range communication in an allosteric enzyme. *Proc. Natl. Acad. Sci. U.S.A.* **105**, 1832-1837

47. Lechtenberg, B.C., Johnson, D.J., Freund, S.M., and Huntington, J.A. (2010) NMR resonance assignments of thrombin reveal the conformational and dynamic effects of ligation. *Proc. Natl. Acad. Sci. U.S.A.* **107**, 14087-14092

48. Orthner, C.L., Kolen, B., and Drohan, W.N. (1993) A sensitive and facile assay for the measurement of activated protein C activity levels in vivo. *Thromb. Haemost.* **69**, 441-447

49. Nagai, K. and Thogerson, H.C. (1987) Synthesis and sequence-specific proteolysis of hybrid proteins produced in *Escherichia coli*. *Methods Enzymol.* **153**, 461-481

50. Wells, C.M., and Di Cera, E. (1992) Thrombin is a Na$^+$-activated enzyme. *Biochemistry.* **31**, 11721-11730

51. Pozzi, N., Barranco-Medina, S., Chen, Z., and Di Cera, E. (2012) Exposure of R169 controls protein C activation and autoactivation. *Blood.* **120**, 664–670

52. Lancellotti, S., Rutella, S., De Filippis, V., Pozzi, N., Rocca, B., and De Cristofaro, R. (2008) Fibrinogen-elongated gamma chain inhibits thrombin-induced platelet response, hindering the interaction with different receptors. *J. Biol. Chem.* **283**, 30193-30204

53. Acquasaliente, L., Peterle, D., Tescari, S., Pozzi, N., Pengo, V., and De Filippis, V. (2016) Molecular mapping of alpha-thrombin (alphaT)/beta2-glycoprotein I (beta2GpI) interaction reveals how □2GpI affects alphaT functions. *Biochem. J.* **473**, 4629-4650

54. Dang, Q.D., Vindigni, A, and Di Cera, E. (1995) An allosteric switch controls the procoagulant and anticoagulant activities of thrombin. *Proc. Natl. Acad. Sci. U.S.A.* **92**, 5977-5981

55. Ng, A.S., Lewis, S.D., and Shafer, J.A. (1993) Quantifying thrombin-catalyzed release of fibrinopeptides from fibrinogen using high-performance liquid chromatography. *Methods Enzymol.* **222**, 341-358

56. Weisel, J.W., and Nagaswami, C. (1992) Computer modeling of fibrin polymerization kinetics correlated with electron microscope and turbidity observations: clot structure and assembly are kinetically controlled. *Biophys. J.* **63**, 111-128

57. Morita, T. and Iwanaga, S. (1981) Prothrombin activator from *Echis carinatus* venom. *Methods Enzymol.* **80**, 303–311

58. Komiyama, T., Gron, H., Pemberton, P.A., and Salvesen, G.S. (1996) Interaction of subtilisins with serpins. *Protein Sci.* **5**, 874-882

59.   Toth, O., Calatzis, A., Penz, S., Losonczy, H., and Siess, W. (2006) Multiple electrode aggregometry: a new device to measure platelet aggregation in whole blood. *Thromb. Haemost.* **96**, 781-788

60.   Stark, G.R. (1965) Reactions of cyanate with functional groups of proteins. 3. Reactions with amino and carboxyl groups. *Biochemistry.* **4**, 1030-1036

61.   Persson, E., Kjalke, M., and Olsen, O.H. (2001) Rational design of coagulation factor VIIa variants with substantially increased intrinsic activity. *Proc. Natl. Acad. Sci. U.S.A.* **98**, 13583-13588

62.   Jiang, L., Botkjaer, K.A., Andersen, L.M., Yuan, C., Andreasen, P.A., and Huang, M. (2013) Rezymogenation of active urokinase induced by an inhibitory antibody. *Biochem. J.* **449**, 161-166

63.   Fauchere, J.L., Charton, M., Kier, L.B., Verloop, A., and Pliska, V. (1988) Amino acid side chain parameters for correlation studies in biology and pharmacology. *Int. J. Pept. Protein Res.* **32**, 269-278

64.   Loeb, B. (1903) The influence of certain bacteria on the coagulation of the blood. *Montreal Med. J.* **7**, 407-419

65.   Menkin, V. (1938) The role of inflammation in immunity. *Physiol. Rev.* **18**, 366-418

66.   Engelmann, B. and Massberg, S. (2013) Thrombosis as an intravascular effector of innate immunity. *Nat. Rev. Immunol.* **13**, 34-45

67.   Loof, T.G., Goldmann, O., Naudin, C., Mörgelin, M., Neumann, Y., Pils, M.C., Foster, S.J., Medina, E., and Herwald, H. (2015) *Staphylococcus aureus*-induced clotting of plasma is an immune evasion mechanism for persistence within the fibrin network. *Microbiology* **161**, 621-627

68.   Angus, D.C., and van der Poll, T. (2013) Severe sepsis and septic shock. *N. Engl. J. Med.* **369**, 840–851

69.   Opal, S.M., and Esmon, C.T. (2003) Bench-to-bedside review: functional relationships between coagulation and the innate immune response and their respective roles in the pathogenesis of sepsis. *Crit. Care.* **7**, 23-38

70.   Siezen, R.J., Renckens, B., and Boekhorst, J. (2007) Evolution of prokaryotic subtilases: genome-wide analysis reveals novel subfamilies with different catalytic residues. *Proteins* **67**, 681-694

71.   De Filippis, V., Quarzago, D., Vindigni, A., Di Cera, E., and Fontana, A. (1998) Synthesis and characterization of more potent analogues of hirudin fragment 1-47 containing non-natural amino acids. *Biochemistry.* **37**, 13507-13515

72.   Sokolov, A.V., Acquasaliente, L., Kostevich, V.A., Frasson, R., Zakharova, E.T., Pontarollo, G., Vasilyev, V.B., and De Filippis, V. (2015) Thrombin inhibits the anti-myeloperoxidase and ferroxidase functions of ceruloplasmin: relevance in rheumatoid arthritis. *Free Radic. Biol. Med.* **86**, 279-294

73. Valotteeau, C., Prystopiuk, V., Pietrocola, G., Rindi, S., Peterle, D., De Filippis, V., Foster, T.J., Speziale, P., and Dufrene, Y.F. (2017) The *Staphylococcus aureus* collagen-binding protein cna3 is a multifunctional adhesin. *ACS Nano* **11**, 2160-2170

74. Arcone, R., Chinali, A., Pozzi, N., Parafati, M., Maset, F., Pietropaolo, C., and De Filippis, V. (2009) Conformational and biochemical characterization of a biologically active rat recombinant Protease Nexin-1 expressed in *E. coli. Biochim. Biophys. Acta.* **1794**, 602-614

75. De Filippis, V., Russo, I., Vindigni, A., Di Cera, E., Salmaso, S., and Fontana, A. (1999) Incorporation of noncoded amino acids into the N-terminal domain 1-47 of hirudin yields a highly potent and selective thrombin inhibitor. *Protein Sci.* **8**, 2213-2217

76. Vriend, G. (1990) WHAT IF: A molecular modeling and drug design program. *J. Mol. Graph.* **8**, 52-56.

SUPPLEMENTARY MATERIALS
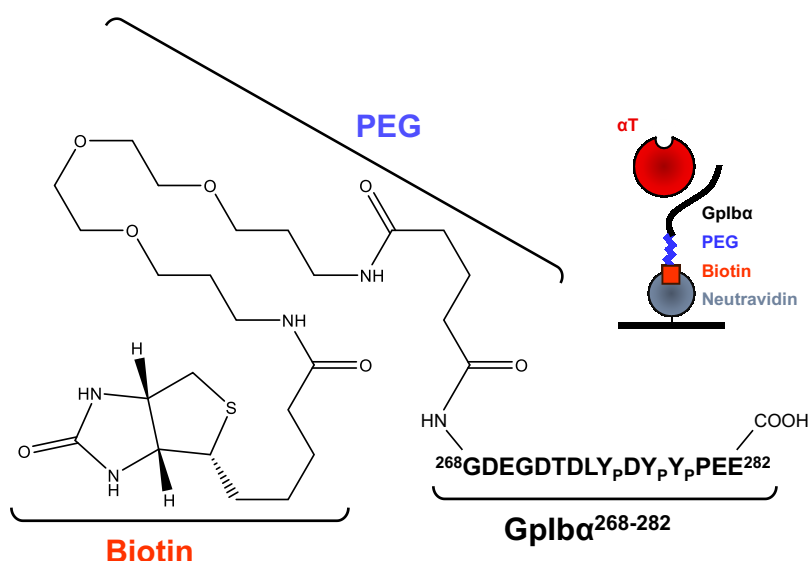
Figure S1. **Structure of the bivalent reagent biotinyl-PEG-[GpIbα(268-282)].**
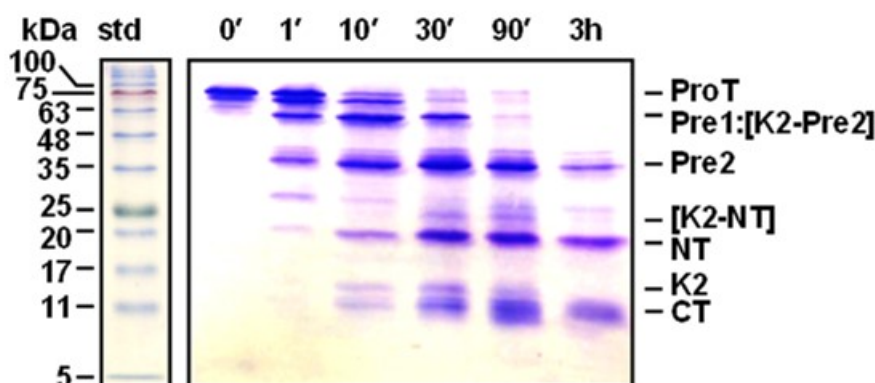
Figure S2. **Time course analysis of the proteolysis reaction of ProT by subtilisin.** Non-reducing electrophoretic analysis of the time-course reaction of ProT (0.1 mg/ml) with subtilisin (0.05 μg/ml) at 37°C. At time points, aliquots (100 μl, 10 μg) of the proteolysis mixtures were precipitated with cold trichloroacetic acid (TCA), analyzed by SDS-PAGE (4-14% acrylamide) and Coomassie stained. Std: molecular weight protein standards. The identity of the major bands are indicated: Pre1, Pre2, K2-NT, NT, K2, and CT. At variance with the SDS-PAGE analysis of Fig. 2A (nonreducing 12%-acrylamide), after 10-30 min reaction, the K2 and CT bands are resolved in the nonreducing 14%-acrylamide gel. At longer reaction times, the K2 band progressively disappears, due to further proteolysis, whereas CT remains stable in the time range explored.
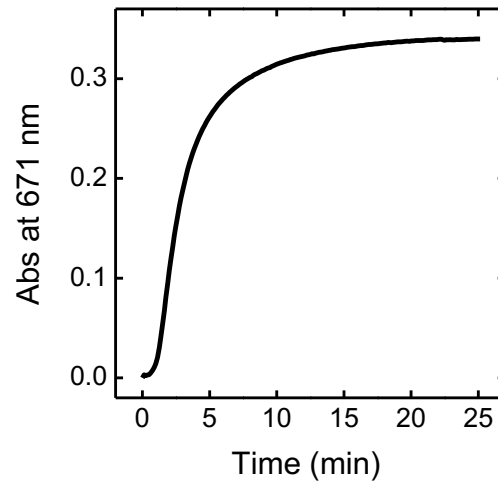
Figure S3. Fibrin generation induced by ecarin. The turbidimetric analysis was performed on 1:2 diluted human plasma at 37°C adding to a human fibrinogen solution (440 nM, 800 μl) ecarin (2.5 nM, 0.25 UI) and recording the absorbance increase of the solution at 671 nm. The characteristic parameters obtained from the ecarin clotting curve are reported in Fig. 10B of the main text.

CHAPTER 4.1

Human α-Synuclein Inhibits Platelets Aggregation by Interfering with the α-Thrombin-PAR1 Axis: Implications in Parkinson's Disease

INTRODUCTION

α-Synuclein (αSyn) is a small (140 amino acids; ~14 kDa) soluble protein, abundantly present in the presynaptic terminals and nuclei of neuronal cells in the central nervous system (CNS) (**1**). αSyn is highly conserved in vertebrates (**2**) and, when free in solution, it is intrinsically disordered (**3**). Although αSyn is not required for neuronal development or synapse formation, it binds to synaptic vesicles and has been suggested to modulate vesicle homeostasis and synaptic plasticity (**1,4**). Whereas the physiological role of αSyn has not yet firmly established (**5**), clinical evidences indicate that it is implicated in the pathogenesis of Parkinson's disease (PD) and the presence of intracytoplasmic deposits of αSyn aggregates (i.e. Lewy bodies) in the dopaminergic neurons of the brain *substantia nigra* is a key neuropathological hallmark of PD (**6**). αSyn primary structure comprises three distinct regions: the N-terminal region, NT (amino acids 1-60); the central region (61-95), also denoted as NAC region (Non-Amyloid β-Component); the C-terminal region 96-140 (CT) (**7**) (**Figure 1**). The NT region is highly electropositive positive (pI: 9.4) and comprises four 11-residue repeats, each centred on a variation of a KTKEGV core consensus sequence. Importantly, the positively charged NT is responsible for the lipid membrane binding properties of αSyn (**8**). Consistent with this model, αSyn has been shown to have the highest affinity for membranes containing anionic lipids (e.g. phospatidylserine), found on the surface of activated platelets. The NAC region is highly hydrophobic in nature and harbours three additional KTKEGV repeats. Moreover, NAC contains many strong β-forming amino acids (i.e. Thr and Val) and plays a crucial role in αSyn fibrillation and toxicity, shifting from a random coil to a β-sheet conformation in the amyloid aggregates (**9**). Finally, the CT region is strongly electronegative (pI: 3.1) and has a proline content about 3-fold higher than that of natural proteins. Notably, CT has been suggested as the interacting site for several different proteins on αSyn structure (**10**). Due to the intramolecular electrostatic repulsion of the negative amino acids and the secondary structure destabilizing effect of Pro-residues, CT is largely unfolded and remains disordered even in fibrillar aggregates (**11,12**).

A

B
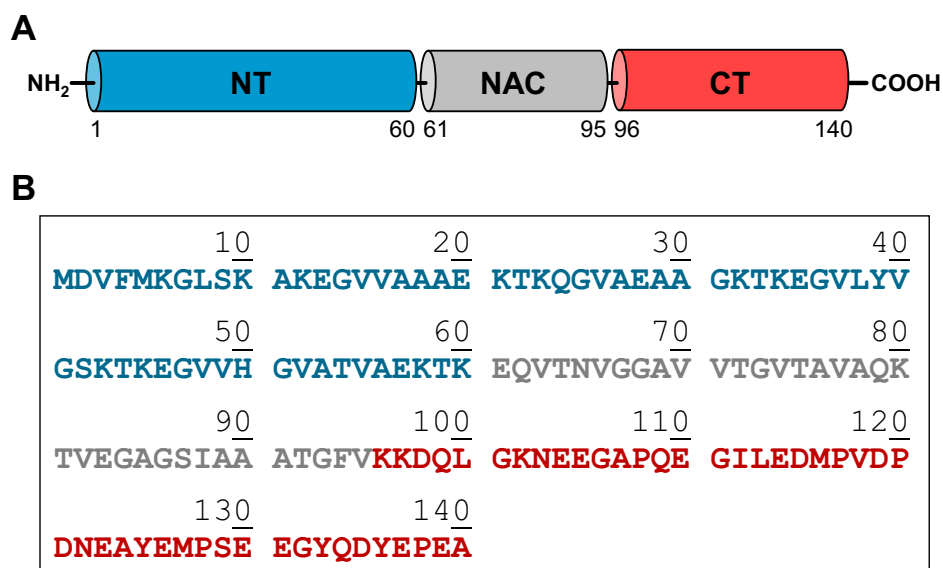
Figure 1. Domain architecture (A) and amino acid sequence (B) of human αSyn. NTD: the N-Terminal Domain region (amino acids 1-60) is positively charged (**pI: 9.4**) and assumes a helical conformation on lipid membrane surfaces (**8**). NAC: the Non-Amyloid β-Component (amino acids 61-95) is highly hydrophobic, has strong β-sheet conformational propensity, and mediates αSyn aggregation/fibrillation (**13**). CTD: the C-Terminal Domain (amino acids 96-140), is strongly negative (**pI: 3.1**) and has been proposed to inhibit αSyn aggregation/fibrillation by electrostatic repulsions (**11,12**).

Besides CNS, where αSyn is one of the most abundant proteins (**2**), significant expression levels of αSyn have been measured in human blood (~**1 μM**; ~**15 mg/l**), where it is found both in the soluble (i.e. plasma) and cellular fraction (i.e. erythrocytes, leukocytes, and platelets) **(2,14)**. Noteworthy, the vast majority (> 99%) of blood αSyn is stored in the erythrocytes, while the remainder is split between plasma (0.1%), platelets (0.2%), and peripheral mononuclear cells (0.05%) (**15,16**). While the higher absolute amount of αSyn in the erythrocytes can be simply accounted for by the far higher counts of red blood cells (4 – 6 x 10^6/μl) compared to platelets (1.5 - 4 x 10^5/μl), these are actually the main hosts of αSyn in the blood, containing 264±36 ng of αSyn *per* mg of total protein, compared to 131±23 ng of αSyn *per* mg of proteins in the erythrocytes (**14**).

Platelets are anuclear cells playing a pivotal role in hemostasis, i.e. the ensemble of coordinated biochemical processes enabling to close off damaged blood vessels, keep the blood in a fluid state, and restore vascular integrity. The hemostatic process can be conceptually divided into primary and secondary hemostasis, and fibrinolysis. However, these processes are activated simultaneously *in vivo*, albeit to varying degrees, according to the localization and extent of the vascular injury. Primary hemostasis entails the formation of the primary platelet plug at the site of vessel injury, while secondary hemostasis leads to a "burst" of α-thrombin (αT) and formation of insoluble, cross-linked fibrin clot. Finally, the fibrin clot is dissolved by plasmin during fibrinolysis,

to restore vascular integrity. Importantly, platelets are key players in all these events. During primary hemostasis, platelets adhere to and are activated by subendothelial matrix proteins (i.e. collagen and von Willebrand factor) that become exposed after vascular injury. Platelet adhesion triggers, *via* intracellular signaling, the release of potent platelet activators from the cytosol (thromboxane A_2) or dense granules (ADP and serotonin), thus amplifying activation and recruitment of additional platelets onto the primary plug. Activated platelets are essential for secondary hemostasis as they release key procoagulant factors from both dense granules (Ca^{+2} and polyphosphates) and α-granules (fibrinogen and factors V and XIII), and expose anionic phosphatidylserines (PS) on the plasma membrane, serving as a binding surface for coagulation factor complex assembly and activity during the amplification step of αT generation and propagation of the ensuing fibrin clot. Indeed, the exceedingly small amount of αT (nM) being generated through direct activation of prothrombin (ProT) by tissue factor-active factor VII complex on fibroblasts in the damaged subendothelium is not enough to produce a stable fibrin clot, yet it is capable of potently activating platelets and amplifying its own production on the PS-bearing platelet surface.

Central to platelets activation is the $P2Y_{12}$ receptor for ADP and the type-1 protease activated receptor (PAR1) for αT. Both $P2Y_{12}$ and PAR1 are seven transmembrane G-protein-coupled receptors (GPCRs) expressed on the platelet cell surface. However, these receptors signal platelets activation through different pathways. Stimulation of $P2Y_{12}$ receptor by ADP binding inhibits, *via* $G_{\alpha i2}$ protein activation, adenylyl cyclase resulting in a reduced concentration of cAMP (an inhibitor of platelet activation), elevation of cytosolic Ca^{2+} and platelets shape change. PAR1 signalling, instead, is triggered by αT cleavage, resulting in the exodomain removal and generation of a new N-terminus, which serves as a tethered ligand that folds back into the ligand-binding pocket of the receptor and activates $G_{\alpha 12}/G_{13}$, and $G_{\alpha q}$, leading to platelets shape change and granule secretion. Importantly, the synthetic peptide TRAP6 (H-Ser-Phel-Leu-Leu-Arg-Asn-NH_2), corresponding to the N-terminal segment of the tethered PAR1 region, is a potent and specific agonist of PAR1, independent of αT-induced receptor activation (**17**).

Even if still controversial, several clinical works reported that patients suffering from PD undergo a minor incidence of strokes, ischemic attacks and myocardial diseases (**18-21**). This intriguing protective effect of PD towards vascular disorders was addressed either to abnormalities in platelets (**22-24**) or to impaired agglutination (**25**). Moreover, it has been shown that exogenous αSyn is able to penetrate into resting platelets, bind to, and inhibit α-granule release (**26**). These observations and the co-localization of αSyn and αT on platelets surface in the amplification stage of αT generation, prompted us to investigate whether αSyn can affect αT-mediated activation of platelets.

EXPERIMENTALS

Reagents

Plasma αT (EC 3.4.21.5) and ProT were purchased from Haematologic Technologies (Essex Junction, VT, USA). Ecarin from *Echis carinatus* venom, human plasma fibrinogen, N^{α}-acetyl-tyrosinamide (Ac-Tyr-NH$_2$), N^{α}-acetyl-phenylalanylamide (Ac-Phe-NH$_2$), and *p*-aminobenzamidine (PABA) were purchased from Sigma (St. Louis, MO, USA). The chromogenic substrate (D)-Phe-Pip-Arg-*p*-nitroanilide (S2238) was from Chromogenix (Milan, Italy). Hirugen ([54]GDFEEIPEEY*LQ[65]), γ'–peptide [408]VRPEHPAETEY*DSLY*PEDDL[427] from elongated fibrinogen γ-chain splice variant (**27,28**), and the C-terminal synuclein peptide αSyn(103-140) were synthesised by standard solid-phase using the N^{α}-fluorenylmethyoxycaobonyl(Fmoc)-chemistry with a ChemMatrix resin (Matrix Innovation, Quebec, Canada), on a model PS3 automated synthesizer from Protein Technologies International (Tucson, AZ, USA). N^{α}-Fmoc-protected amino acids, solvents and reagents for peptide synthesis were purchased from Applied Biosystems (Forster City, CA, USA) or Bachem AG (Bubendorf, Switzerland). The crude peptides were purified to homogeneity by RP-HPLC on a C18 semi-preparative RP-HPLC column. The purified materials were characterized by high-resolution mass spectrometry with a Mariner ESI-TOF spectrometer from PerSeptive Biosystems (Stafford, TX, USA). The N-terminal domain of hirudin, HM2(1-47), was produced by limited proteolysis of full-length hirudin HM2 variant from *Hirudinaria manillensis* with bovine pancreas trypsin (Promega Biosciences, CA, USA) (**29**). ADP-test and TRAP-test solutions for Multiplate analyzer assays were purchased from Roche Diagnostics (Basel, Switzerland). Hirudin HM2 was a generous gift from Dr. G. Orsini (Farmitalia, Italy). Salts, solvents and other reagents were of analytical grade and purchased from Sigma or Fluka (Darmstadt, Germany).

Production and characterization of recombinant α-Synuclein (αSyn)

Recombinant human wild type and N-terminally 6xHis-tagged αSyn were produced as previously detailed (**30,31**). Briefly, BL21*(DE3)pLysS *Escherichia coli* cells were transformed, using the heat-shock method, with *p*RSET-B plasmid containing human αSyn gene and selected on a Luria-Bertani (LB) Agar Amp$^+$ (0.1 mg/ml) solid culture medium overnight. Transformed cells were grown at 37°C in LB Broth Amp$^+$ (0.05 mg/ml) and induced (O.D. = 0.6) with isopropyl β-D-1-thiogalactopyranoside (IPTG, 0.1mg/ml) under vigorous shaking. For wild-type αSyn, after 3-h induction with IPTG, bacteria were harvested by centrifugation (6.000 rpm, 15 min, at 4°C), and the pellet sonicated in 40 mM Tris-HCl, pH 8.0, 0.1 M NaCl (buffer A). After 10-min boiling, the

suspension was centrifuged at 12.000 rpm for 10 min at 4°C. The supernatant, containing soluble αSyn, was dialyzed overnight at 4°C against buffer A, containing 2 mM sodium ethylenediaminetetraacetate (EDTA). For 6xHis-tagged αSyn, after sonication in buffer A, the recombinant protein was purified by immobilized metal ion affinity chromatography (IMAC). The bacterial lysis supernatant (50 ml) was loaded onto a fast-flow Ni^{2+}-IMAC (1 x 3 cm) HiTrap column, using a model P-1 peristaltic pump (Pharmacia, Uppsala, Sweden) at a flow-rate of 0.1 ml/min. The flow-through was discarded and the column connected to an Äkta-purifier biochromatography system. After washing with buffer A (60 ml), 6xHis-tagged αSyn was eluted from the column (0.5 ml/min) with buffer A, pH 6.5, containing 0.4 M imidazole. The material eluted in correspondence of the major chromatographic peak was collected and dialyzed overnight at 4°C against 0.5 l of phosphate buffered saline, pH 7.4 (PBS). Both recombinant wild-type and 6xHis-tagged αSyn preparations were further purified by RP-HPLC on a C18 semi-preparative column (10 x 250 mm, 5μm, 300Å) from Grace-Vydac (Hesperia, CA, USA), eluted with a linear acetonitrile-0.078% trifluoroacetic acid (TFA) gradient at a flow rate of 1.5 ml/min. After lyophilisation, a small amount of the purified proteins were dissolved in water:acetonitrile (1:1 v/v), containing 1% formic acid, and characterized by HR-MS. To obtain purified αSyn in the monomeric state, the lyophilized wild-type protein (1 mg) was dissolved in 2 mM NaOH (100 μl) and 1 M NaOH (10 μl), up to pH 11.0. After centrifugation (15.000 rpm, 15 min), the supernatant was withdrawn and added with 0.1 M Tris-HCl, pH 7.0 (200 μl), down to pH 8.0 (**32**). Freshly dissolved αSyn samples were used for further spectroscopic and functional analyses.

Production of thrombin derivatives

The plasmid containing the cDNA of prethrombin-2 (Pre2) was a generous gift of Prof. James A. Huntington (University of Cambridge, UK). The recombinant inactive mutant rS195A, obtained by single-point mutagenesis, was expressed in *E. coli*, subjected to *in vitro* disulphide oxidative folding, activation by ecarin, and characterized as previously detailed (**33,34**). βT-thrombin (βTT) was obtained by proteolysis of human αT (7 μM) with bovine pancreas trypsin (35 nM) for 3 hours at 37°C in HBS, and characterized as previously detailed (**28,35**).

Hydrolysis of synthetic and natural thrombin substrates

The hydrolytic activity of αT was determined at 37°C in HBS on the chromogenic substrate S2238 (D-Phe-Pip-Arg-*p*NA), by measuring the release of *p*-nitroaniline (*p*NA) at 405nm (ε^M_{405nm} = 9.920 $M^{-1} \cdot cm^{-1}$) (**28,36**). The kinetics of fibrinopeptide A (FpA) and B (FpB) release by αT was followed as earlier described (**28,34**). Briefly, human fibrinogen (Fb) (ε^M_{280nm} = 5.1·10⁵ $M^{-1} \cdot cm^{-1}$) was desalted on an in-house packed (8 x 125 mm) G10 fast-flow column (GE Healthcare, USA) eluted with 20 mM HEPES, pH 7.4, 0.15 M NaCl, 0.1% PEG-8000 (w/v) (HBS), at a flow-rate of 0.3 ml/min. Freshly prepared Fb (0.35 μM) was reacted at 37°C with αT (300 pM) and at fixed time points proteolysis mixtures were added with formic acid (2% v/v final concentration) to block the proteolysis reaction and induce precipitation of fibrin and unreacted Fb. After centrifugation (10.000g for 5 min at 4°C), the supernatant (1.0 ml) was withdrawn, lyophilized, dissolved in 6 M Gnd-HCl (150 μl) and injected (100μl) onto a RP-HPLC (4.6 x 250mm) C18 column (Grace-Vydac, Columbia, MD). The column was equilibrated with 40 mM ammonium phosphate buffer, pH 3.1, and eluted with an acetonitrile gradient. The absorbance of the effluent was recorded at 205 nm and the amount of released FpA (ε^M_{205nm} = 4.40·10⁴ $M^{-1} \cdot cm^{-1}$) and FpB (ε^M_{205nm} = 5.12·10⁴ $M^{-1} \cdot cm^{-1}$) was determined by integrating the area under the chromatographic peaks. A biocompatible Bio-410 HPLC system (Perkin-Elmer, Norwalk, CT), connected to a ISS-100 autosampler, was used for all analyses. The specificity constants, $k_{cat,A}/K_{m,A}$ and $k_{cat,B}/K_{m,B}$, for the release of FpA or FpB by αT were determined by interpolating the data points with **equations 1** and **2**, respectively (**34**):

$$[FpA]_t = [FpA]_\infty \cdot (1 - e^{-k't})$$ (**eq. 1**)

$$[FpB]_t = [FpB]_\infty \cdot (1 + \alpha \cdot e^{-k't} - \beta \cdot e^{-k''t})$$ (**eq. 2**)

where $[FpA]_t$ or $[FpB]_t$ and $[FpA]_\infty$ or $[FpB]_\infty$ are the concentrations of FpA or FpB at time t and ∞, respectively, and k′ and k″ are the observed kinetic constants for FpA or FpB release, obtained as fitting parameters. Under pseudo-first order conditions and low substrate concentration, the specificity constants could be easily determined $k_{cat,A}/K_{m,A}$ = k′/[E] and $k_{cat,B}/K_{m,B}$ = k″/[E], where [E] is the protease concentration.

The hydrolysis of the synthetic peptide PAR1(38-60) (1 μM) by αT (150 pM) was carried out at 25°C in TBS. At time points, aliquots (360 μl) were taken, acid quenched (10 μl, 4% aqueous TFA) and loaded (350 μl) onto a Grace-Vydac (4.6 x 250 mm) C18 column. The column was eluted with a linear acetonitrile-0.078% TFA gradient from 10-45% in 40 min and the release of PAR1(42-60) (ε^M_{205nm} = 95.870 $M^{-1} \cdot cm^{-1}$) (**28,33,34**) was quantified by integrating the area under the

chromatographic peak. The kinetic data were interpolated with **equation 3**, describing a pseudo-first order reaction:

$$[P]_t = [P]_\infty \cdot [1 - \exp(-k_{obs} \cdot t)]$$

(eq. 3)

where $[P]_\infty$ is the concentration of the fragment PAR1(42-60) when the proteolysis reaction was complete and k_{obs} is the observed kinetic constant for PAR1(38-60) hydrolysis, obtained as a fitting parameter. As for the release of fibrinopeptides, under pseudo-first order conditions and low substrate concentration, k_{cat}/K_m could be derived as $k_{obs}/[E]$.

Fibrin generation assay

Fibrin generation was started by adding αT (1 nM) to a freshly desalted fibrinogen (Fb) solution (0.44 μM) in HBS at 37°C, while the time course of clot formation was followed by continuously recording the solution absorbance at 350 nm (i.e. the turbidity) on a double-beam V-630 Jasco (Tokyo, Japan) spectrophotometer (**28,33,34**). The effect of αSyn was estimated by first incubating a solution of αSyn at increasing concentrations with αT and then adding a desalted Fb solution.

Platelets aggregation assay

The effect of αSyn on platelets aggregation induced by αT, TRAP or ADP was measured in whole blood by Multiple Electrode Aggregometry (MEA), using a multiplate analyzer (Dynabyte, Munich, Germany) (**33,34,37**). Citrate-treated venous blood samples were taken from three healthy donors: one male and two females, 28–35 years of age, and non-smokers. The donors gave written informed consent for participation in this study, which was approved by the Institutional Ethics Committee of the Padua University Hospital. Monomeric samples of αSyn or αSyn(103-140) at increasing concentrations (0-20 μM) were pre-incubated with αT (6 nM) in 320 μl of HBS at 37°C. After 30 min, these solutions were mixed with whole blood (300 μl), and analysed by MEA over 10-min reaction time. At each αSyn concentration, the area under the aggregation curve (AUC) was determined for each donor and the average value expressed as %AUC, relative to the value determined in the absence of αSyn, (AUC$_0$) (**33,34**). To study the effect of αSyn or αSyn(103-140) on ADP- or TRAP-induced platelet aggregation, to 300 μl of whole blood sample was added an equal volume of αSyn or αSyn(103-140) solution (0-20 μM) in HBS and 20 μl of Multiplate ADP-Test or TRAP-Test solution (Roche Diagnostics, Switzerland). The aggregation curves were recorded and analyzed as reported above.

Spectroscopic methods

Ultraviolet (UV) absorption spectroscopy. The concentrations of protein/peptide solutions were determined by measuring the absorbance at 280 nm on a Jasco V-630 double-beam spectrophotometer, using a molar absorptivity value ($\varepsilon_M{}^{280}$) of 67.161 $M^{-1}\cdot cm^{-1}$ for plasma αT and $β_TT$, and 66.424 $M^{-1}\cdot cm^{-1}$ for recombinant rS195A; 99.360 $M^{-1}\cdot cm^{-1}$ for ProT; 5.960 and 4.470 $M^{-1}\cdot cm^{-1}$ for full-length αSyn and αSyn(103-140), respectively; 418 $M^{-1}\cdot cm^{-1}$ for hirugen; 68.000 $M^{-1}\cdot cm^{-1}$ at 492 nm for fluoresceinated hirugen; 3.355 $M^{-1}\cdot cm^{-1}$ for hirudin N-terminal domain Hir(1-47); 837 $M^{-1}\cdot cm^{-1}$ for fibrinogen γ'–peptide. The active-site concentration of αT was also determined by titration with hirudin (**38**) and found identical (±5%) to that determined spectrophotometrically. The concentration of PABA and S2238 solutions was measured spectrophotometrically, using ε_M = 548 $M^{-1}\cdot cm^{-1}$ at 336 nm and ε_M = 12.700 $M^{-1}\cdot cm^{-1}$ at 316 nm, respectively.

Dynamic light scattering (DLS). DLS measurements were performed at 37°C on a Zetasizer-Nano-S instrument (Malvern Instruments, UK) at a fixed angle (i.e. 173°) from the incident light (i.e. He–Ne 4 mW laser source at 633 nm). Polystyrene cuvettes (1-cm pathlength, 100 µl) (Hellma, Switzerland) were used for all measurements. Each measurement consisted of a single run (15 s). Scattering data were analyzed with the Nano-6.20 software and expressed as percentage of volume size distribution, from which the value of the hydrodynamic diameter (d_H) and percent polydisperisity (%PD) were extracted (**39,40**). In DLS analysis, the time-dependent fluctuations of scattered light from molecules of different size in solution is measured and from the rate of these fluctuations the translational diffusion coefficient (D) is determined. The value of d_H is then derived from the Stokes-Einstein equation, $d_H = 2\cdot kT/6\pi\eta D$, where k is the Boltzmann constant, T is the absolute temperature and η is the solution viscosity (**41**).

Fluorescence. Fluorescence binding measurements were carried out at 37°C in HBS, containing 0.1% PEG-8000 (w/v), on a Jasco FP-6500 spectrofluorimeter. Aliquots (2-10 µl) of αSyn or αSyn(103-140) in HBS were added, under gentle magnetic stirring, to an αT solution (70 nM) in the same buffer. At each ligand concentration, samples were incubated for 2 min at 37°C and excited at 295 nm, using an excitation/emission slit of 5 and 10 nm. The emission intensity was recorded at the λ_{max} of αT (334 nm), after subtracting the corresponding spectra of the ligands alone. Fluorescence data were corrected for sample dilution, which was always <2% at the end of the titration. Photobleaching was almost eliminated, even after prolonged light exposure, by using a 1-cm pathlength quartz cuvette (2 ml) with two frosted walls that are able to diffuse the incident light inside the sample, thus preventing photodegradation of Trp-residues. To prevent inner filter effect (IFE), the optical density of the solution was kept always lower than 0.05 units both at λ_{ex} and λ_{em}

(**42**). The data points were interpolated with **equation 4**, describing the single-site binding model R + L ↔ RL (**42**):

$$[\Delta F] = [\Delta F]_{max} \cdot \frac{[L]}{K_d + [L]}$$

(**eq. 4**)

A similar procedure and data analysis was used for measuring the affinity of site-specific ligands [i.e. S2238, Hir(1-47), PABA, hirugen and fibrinogen γ'–peptide] for αT in the presence of saturating αSyn or αSyn(103-140) concentrations (20 μM). For Hir(1-47) binding to αT (70 nM), fluorescence data were fitted to **equation 5**, describing the tight-binding model (**42**).

$$[\Delta F] = [\Delta F]_{max} \cdot \frac{([R]_T + [L]_T + K_d) + \sqrt{([R]_T + [L]_T + K_d)^2 - 4 \cdot [R]_T [L]_T}}{2 \cdot [R]}$$

(**eq. 5**)

where $[R]_T$ and $[L]_T$ are the total enzyme and ligand concentrations, respectively, while RL is the enzyme-ligand complex. ΔF and ΔF_{max} are the changes of fluorescence intensity measured at intermediate or saturating ligand concentrations. The dissociation constant, K_d, of the complex was obtained as a fitting parameter. When the binding of PABA was being studied, samples were excited at 336 nm and the emission of PABA was recorded at 375 nm, after baseline subtraction and correction for IFE, as detailed elsewhere (**28,33**).

Surface plasmon resonance (SPR). SPR analyses were carried out on a dual flow-cell Biacore X-100 instrument from GE Healthcare (Uppsala, Sweden). 6xHis-tag αSyn was noncovalently immobilized onto a Ni^{2+}-chelated nitrilotriacetate (NTA) carboxymethyldestrane sensor chip and incremental concentrations of rS195A were loaded. The Ni^{2+}-NTA/6xHis-αSyn chip was prepared as follows: the NTA chip was first washed (flow-rate: 30 μl/min) with 0.35 M EDTA, pH 8.3 (contact time: 700 sec) and then loaded with a 0.5 mM $NiCl_2$ solution (contact time: 400 sec); excess Ni^{2+} was removed by injecting 3 mM EDTA solution (contact time: 350 sec), whereas non-chelating NTA-groups were irreversibly blocked with ethanolamine, after NHS/EDC carboxylate activation (contact time: 800 sec); finally, a solution of 6xHis-tag αSyn (200 nM) was injected on the sensor chip (contact time: 400 sec) to yield a final immobilization level of 2194 response units (RU). The Ni^{2+}-NTA/6xHis-αSyn sensor chip was challenged (flow-rate: 30 μl/min; contact time: 350 sec) with increasing concentrations of inactive rS195A thrombin mutant, $β_T T$, and ProT. All measurements were carried out at 37°C in HBS-EP$^+$ buffer (10 mM HEPES, pH 7.4, 0.15 M NaCl, 50 μM EDTA, 0.005% v/v polyoxyethylene sorbitan). Between two consecutive runs, the regeneration of Ni^{2+}-NTA/6xHis-αSyn chip was achieved with HBS-EP$^+$ buffer, containing 2 M NaCl. Each sensogram was subtracted for the corresponding baseline, obtained on the reference flow cell and accounting for

nonspecific binding, i.e. typically less than 2% of RU_{max}. The binding data were analyzed using the BIAevaluation software. The dissociation constant (K_d) relative to the binding of αT to immobilized αSyn was obtained as a fitting parameter by plotting the RU value at the steady state (RU_{eq}) vs. αT concentration and interpolating the data points with **equation 6**, describing 1:1 binding model:

$$RU_{eq} = RU_{max} \cdot \frac{[L]}{K_d + [L]}$$

(eq. 6)

where L is the concentration of αT and RU_{eq} and RU_{max} are the RU values (measured at the steady state) at intermediate or saturating [L] (**28,34,43**)

Computational methods

Electrostatic potential calculations were performed using APBS (**44**) and BLUUES (**45**) software, which is based on the generalized Born models (**46**). For αT, calculations were run on the non-glycosylated X-ray structure of wild type αT (**1ppb**), after removal of the coordinates of the inhibitor (D)-Phe-Pip-Arg-chloromethylketone (PPACK), water molecules, and 4-(2-hydroxyethyl)-1-piperazineethanesulfonic acid (HEPES) (**47**). The coordinates of human PAR1 (**3vw7**) (**48**) and $P2Y_{12}$ receptor (**4ntj**) (**49**) bound to the inhibitors Vorapaxar and AZD1283, respectively, were considered. Notably, to facilitate crystallogenesis, T4 lysozyme (T4L) and the BRIL domain were inserted into the intracellular loop 3 in PAR1 and $P2Y_{12}R$, respectively. Notably, in the recombinant PAR1-T4L fusion protein the N-terminal exodomain (1-85) was missing. The coordinates of the bound inhibitor were virtually removed, along with the inserted structure of T4L and BRIL. To minimize artefactual charge perturbations, following virtual domain excision, the remaining N- and C-termini were acetylated or amidated. In our calculations, the electrostatic contribution of Na^+-ion bound to $P2Y_{12}R$ was not considered and a solvent dielectric of 78.14 and a protein dielectric of 2.0 at 298 K in 145 mM NaCl were used. Final electrostatic maps were constructed by subtracting the protein self-energies from the calculated map using the dxmath utility in APBS.

RESULTS AND DISCUSSION

Production, purification and characterization of recombinant monomeric αSyn

Recombinant human wild type αSyn and the corresponding N-terminally fused 6xHis-tag αSyn mutant were expressed by adding IPTG to BL21*(DE3)pLysS *Escherichia coli* cells, transformed with *p*RSET-B plasmid (**30,31**). After centrifugation, the bacterial pellet was re-suspended in buffer A (**see Methods**), the solution was sonicated and boiled for 10 min. After heat treatment, most of *E. coli* proteins precipitated whereas αSyn remained in solution, allowing to obtain an αSyn-enriched extract. This solution was then further purified by RP-HPLC. At variance, 6xHis-αSyn was purified by IMAC, after imidazole (0.4 M) elution, followed by RP-HPLC. In both cases, the purity of αSyn preparations was checked by SDS-PAGE (not shown) and RP-HPLC (**Fig. 2A**) (> 98%). The chemical identity of αSyn samples was established by high-resolution mass spectrometry and found in agreement with the protein amino acid composition, within 10 ppm mass accuracy (**Fig. 2A, Inset**). Both wild type and 6xHis-αSyn samples were divided into aliquots, lyophilized, and stored at -20°C for subsequent analyses.

With the aim to obtain monomeric αSyn preparations, different conditions were explored, including TBS, pH 7.4, alone or containing organic co-solvents (7% v/v DMSO), chemical denaturants (5 M Gnd-HCl), or at pH 8.0 after alkaline treatment (**see below**). The presence of protein aggregates was estimated from the shape of UV-absorption spectra (**Fig. 2B**), i.e. the ratio of the absorbance values at 275 and 250 nm (A_{275nm}/A_{250nm}) and from the relative intensity of the apparent fluorescence emission of αSyn solutions (F/F_0), recorded under different solvent conditions, at increasing protein concentrations (**Fig. 2C**). The A_{275nm}/A_{250nm} ratio is a sensitive measure of protein aggregation, as the intensity of the scattered light (I) exponentially increases at lower wavelengths (λ), as $I = f(1/\lambda^4)$. Likewise, the slope of the straight line of F/F_0 vs. [αSyn] is a signature of the presence of protein aggregates that more intensely scatter light, which is then recorded as the "apparent" fluorescence emission (**50**). The UV-absorption and fluorescence spectra of αSyn solutions were compared with those of a model compound solution, 4:2 (mol:mol) N^α-acetyl-Tyr-NH_2 / N^α-acetyl-Phe-NH_2 solution, recorded under identical conditions, which was taken as a model of Tyr and Phe spectroscopic properties αSyn monomer.
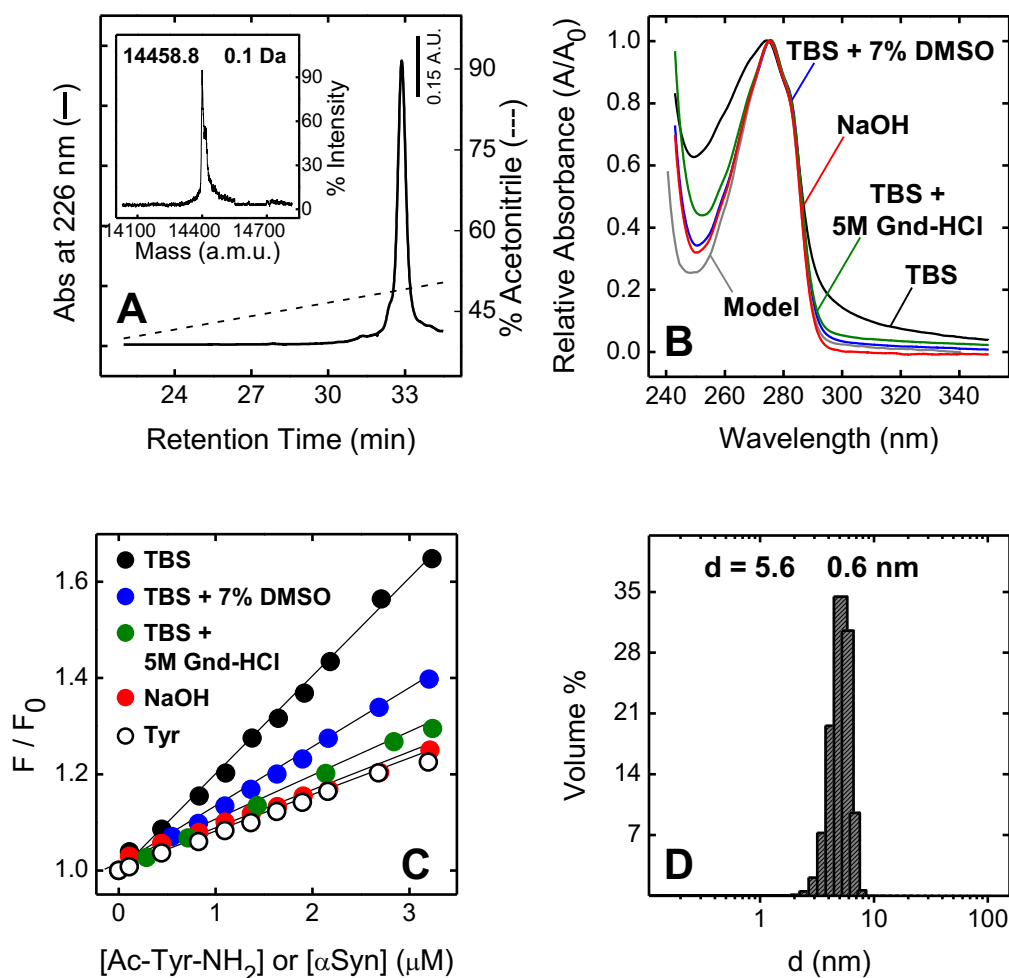
Figure 2. Purification and Characterization of monomeric αSyn. (**A**) RP-HPLC analysis of purified recombinant αSyn, using a semi-prepartive (1x25 cm) C18 column eluted with a linear 0.078% TFA-acetonitrile gradient (---). (**Inset**) MS analysis of RP-HPLC purified αSyn. (**B**) Near-UV absorption spectra of αSyn (**130 μM**) in different solvents (—) TBS: 5mM Tris-HCl, pH 8.0, 0.2 M NaCl, 0.1% PEG-8000 (v/w); (—) TBS-DMSO: TBS containing 7% (v/v) DMSO; (—) TBS-Gnd: TBS containing 5 M Gnd-HCl; (—) NaOH: αSyn was first dissolved in 100 μl of 2 mM NaOH and 10 μl of 1 M NaOH and then added with 200 μl of 0.1 M Tris-HCl pH 7.0 (**Methods**). UV-absorption spectra of αSyn samples at 25°C. The nominal αSyn concentration was the same under all experimental conditions and the spectra were normalized (A/A$_0$) for the absorbance intensity of αSyn in TBS (A$_0$) at the λ$_{max}$ (**275 nm**). As a control, the spectrum of Ac-Tyr-NH$_2$ and Ac-Phe-NH$_2$, mixed in the same molar ratio (**4:2**) as that present in αSyn (**Model**), is also reported (—). (**C**) Concentration-dependence of αSyn fluorescence intensity recorded at **25°C** under different solvent conditions, as reported above. αSyn samples were excited at 280nm and the fluorescence signal was recorded at the λ$_{max}$ (303nm). The data are expressed as F/F$_0$ ratio, where F and F$_0$ is the fluorescence signal of the buffer solvent in the presence or absence of increasing [αSyn]. For comparison, the data of Ac-Tyr-NH$_2$ (Tyr, ○) emission in TBS are also included. Linear interpolation of the fluorescence data yielded the following slope values: TBS, 0.201 ± 0.004; TBS-DMSO, 0.125 ± 0.001; TBS-Gnd, 0.092 ± 0.001; NaOH, 0.022 ± 0.001; Tyr, 0.073 ± 0.001. (**D**) DLS analysis at 37°C of purified αSyn (**50μM**) after alkaline treatment, as described above. The data are expressed as the volume size distribution and *d* is the average molecular diameter.

The spectra in **Fig. 2B** show that in TBS alone the r = A_{275nm}/A_{250nm} ratio of αSyn (**1.6**) is markedly lower than that estimated for the model compound solution (**r = 3.1**), containing N^α-acethyl-Tyr-NH$_2$ and N^α-acethyl-Phe-NH$_2$ in the 4:2 molar ratio, where aggregation effects are lacking. The latter result is indicative of the presence of αSyn aggregates in TBS, pH 7.4. Addition of 5 M Gnd-HCl to TBS increased the r value to **2.2**. Addition of 7% DMSO to TBS or after alkaline treatment (**see below**) yielded r = **2.9**, very close to that of the model compound solution. Notably, the alkaline treatment consisted in the dissolution of αSyn lyophilizate with NaOH solution, at pH 11.0, followed by addition of 0.1 M Tris-HCl, pH 7.0, to obtain a final solution pH of 8.0 (**32**). Consistent with previous work, the fluorescence data reported in **Fig. 2C** show that only alkaline treatment proved to effectively decrease the slope (m) of the straight line in the plot of F/F$_0$ vs. [αSyn], measured in TBS alone, to a value identical to that recorded for the model compound solution, where aggregation effects can be safely ruled out (**see the legend to Fig. 2**) (**32,50**).

The oligomeric state of αSyn preparation, after alkaline treatment, was confirmed by Dynamic Light Scattering (DLS) measurements, from which the hydrodynamic diameter (d$_H$) and the percent polydispersity (%PD) were extracted (**Fig. 2D**), where d$_H$ is the diameter of a hard sphere that diffuses at the same speed as the molecule being measured, while %PD is a parameter describing the width of the particle size distribution of a protein in a given sample (**28,40,51**). From DLS data in **Fig. 2D,** a d$_H$ = 56 ± 6 Å was estimated for αSyn, with a low %PD of 11.6% indicating that the protein solution was essentially monodispersed (**40,51**). The value of d$_H$ herein reported is lower than that estimated for a fully unfolded protein of 140 amino acids like αSyn (d$_H^U$ = 68 Å) (**52**), but compares favourably with that determined experimentally for monomeric αSyn by SAXS measurements (d$_H$ = 54 ± 2 Å) (**53**) and size-exclusion chromatography (d$_H$ = 55 ± 6 Å) (**54**). Actually, SAXS analysis yields the radius of gyration (R$_g$) of a protein, i.e. the root mean square distance from each atom of the protein to their centroid. For an unfolded protein, however, the R$_g$ value can be easily converted to the hydrodynamic radius (R$_H$) using the known relation: R$_g$/R$_H$ = 1.51 (**53,55**). Altogether, our results indicate that, after alkaline treatment, purified αSyn samples are largely in the monomeric/monodispersed state. Freshly prepared αSyn stock solutions were immediately used for subsequent functional/binding measurements (see below).
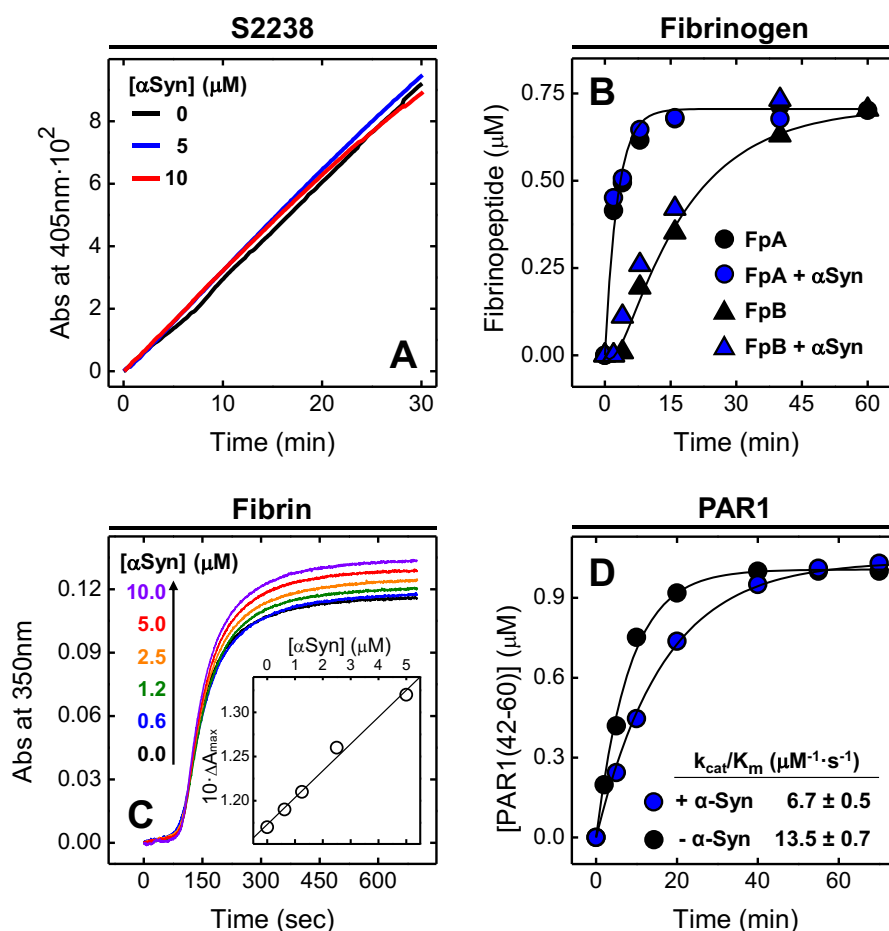
Figure 3. Effect of αSyn on αT-mediated hydrolysis of S2238, Fb, PAR1(38-60) and on fibrin generation. (**A**) αT-catalyzed hydrolysis of the chromogenic substrate S2238 in the presence of increasing αSyn concentrations. The hydrolytic activity was determined at 37°C in HBS by measuring the release of *p*-nitroaniline (*p*NA) at 405nm. (**B**) Release of FpA and FpB from desalted fibrinogen (0.35 μM) by αT (300 pM), in the absence or presence of αSyn (2 μM). Measurements were carried out at 37°C in HBS, and quantified by RP-HPLC (**see Methods**). Interpolation of the data points with **eq. 1 and 2**, yielded the apparent specificity constants (k_{cat}/K_m) of FpA and FpB release in the absence ($k_{cat,A}/K_{m,A}$ = 20.9±2.6 $\mu M^{-1} \cdot s^{-1}$; $k_{cat,B}/K_{m,B}$ = 2.9±0.8 $\mu M^{-1} \cdot s^{-1}$) and presence ($k_{cat,A}/K_{m,A}$ = 26.0±3.9 $\mu M^{-1} \cdot s^{-1}$; $k_{cat,B}/K_{m,B}$ = 2.8±0.8$\mu M^{-1} \cdot s^{-1}$) of αSyn. (**C**) Turbidimetric analysis of fibrin generation induced by αT in purified fibrinogen at increasing αSyn concentrations, as indicated. To a desalted fibrinogen solution (440 nM, 800 μl) in HBS at 37°C, containing 0.1% PEG-8000, was added αT (1 nM, final concentration) pre-incubated with increasing [αSyn] and the time-course generation of fibrin was monitored by recording the absorbance increase of the solution at 350 nm. From each clotting curve, the values of t_c, and ΔA_{max} were extracted. (**Inset**) Plot of ΔA_{max} vs. [αSyn]. (**D**) Cleavage of PAR1(38-60) by αT in the absence (●) or presence (●) of αSyn (15 μM). The cleavage of PAR1(38-60) peptide (1 μM) by αT (**150 pM**) was carried out at 25°C in 5 mM Tris-HCl pH 7.4, 0.15 M NaCl, 0.1% PEG-8000 (w/v) (TBS) and the time course of PAR1(42-60) fragment release was quantified by RP-HPLC. The data points were fitted with **eq. 3**, describing the kinetics of product formation under pseudo-first order conditions and yielding the values of specificity constant, k_{cat}/K_m, in the absence and presence of αSyn, as indicated.

The effect of αSyn and αSyn(103-140) on αT-catalyzed S2238 hydrolysis, fibrinopeptides release, and fibrin generation

The effect of full-length αSyn and the synthetic C-terminal peptide αSyn(103-140) on the catalytic activity of αT was first investigated using the chromogenic substrate (D)-Phe-Pip-Arg-*p*-nitroanilide (S2238), which is specific for αT (**56**). The kinetic data of *p*NA release clearly indicate that, up to 10 μM concentration, neither αSyn (**Fig. 3A**) nor αSyn(103-140) (**not shown**) appreciably affect αT catalytic function.

The same trend was observed by studying the effect of αSyn (2 μM) on the αT-catalysed hydrolysis of the physiological substrate fibrinogen (Fb), resulting in the release of fibrinopeptides (FpA and FpB) and fibrin clot formation (**Fig. 3B,C**). The kinetic data relative to fibrinopeptides generation were analysed within the framework of the Shafer's model (**57**), whereby a highly specific cleavage at the Aα chain leads to the rapid release of FpA and formation of fibrin-I monomers that aggregate to form fibrin-I protofibrils. A second cleavage by αT at the Bβ chain of fibrin-I monomers then leads to the slower release of FpB and formation of fibrin-II protofibrils, which then aggregate to form the fibrin clot. The values of the specificity constants (k_{cat}/K_m) for the release of FpA and FpB, extracted from the kinetic data in **Fig. 3B**, were found to be identical to those reported earlier (**34**) and, more importantly, independent from αSyn addition.

The time-course formation of fibrin clot, from purified Fb, was also monitored by recording the turbidity ($\tau = \ln10 \cdot A_{350}$) of a Fb solution (0.44 μM) after addition of αSyn (0–10 μM), where τ is the intensity decrease of transmitted light at 350 nm, which is caused by the scattering of light by fibrin fibers and is recorded as an apparent absorbance (A_{350}) (**58**). Typically, a fibrin clotting curve displays: i) a lag phase, ii) a linear rise, and iii) a plateau (**58,59**). The lag phase (i) corresponds to the time necessary for the longitudinal elongation of protofibrils, deriving from 20-25 fibrin monomers after removal of fibrinopeptides; thereafter, the rapid linear rise in turbidity (ii) results from lateral aggregation of those protofibrils that have reached a certain threshold length (0.5-0.6 μm) to aggregate and form thick fibers (length: 5-20 μm; diameter: 80-200 nm); finally, the turbidity reaches a plateau (iii) when most of protofibrils have been transformed into fibers, which then branch and assembly into the final fibrin network (**59**). From the resulting clotting curves, the values of A_{max} and t_c, can be extracted, where A_{max} is the maximum A_{350} value in the clotting curve when fibrin generation is complete, and t_c is the clotting time determined as the intercept with the time axis of the tangent line to the flex point (i.e. the point of maximum slope) of the clotting curve (**28,34,58**). Noteworthy, the value of A_{max} provides a key geometric parameter of fibrin structure, as it is proportional to the square of the average diameter of the fibers (**58**). From the fibrin clotting curves

in **Fig. 3C**, we can conclude that in the presence of αSyn (up to 10 μM) the clotting time remained essentially constant ($t_c = 109 \pm 2$ sec), whereas the A_{max} value was increased by > 15%. The relative invariance of t_c indicates that αSyn does not alter the lag phase of fibrin formation, consistent with the observation that αSyn does not affect fibrinopeptides release. On the other side, the increase of the A_{max} value indicates that αSyn perturbs lateral aggregation of fibrin and induces the formation fewer and thicker fibers, generating a more intense turbidimetric signal.

According to the "knobs-holes" interaction model of clot formation (**59**), longitudinal prolymerization of fibrin results from the interaction of the knobs ("A knobs") that are produced after FpA generation from the α-chain with the holes in the γ-chain ("a holes") of another fibrinogen molecule. At variance, lateral aggregation is promoted by the interaction of "B knobs", protruding from the β-chain of a Fb molecule after FpB cleavge, with the "b holes" in the β-chain of another Fb molecule and by the homophilic intermolecular binding of αC-domains, which are released from the central body of Fb after fibrinopeptides cleavage. Such "knob-hole" interactions are associated with the formation of numerous intermolecular salt bridges (**60**) and, as a direct consequence of the contribution of charge-charge interactions in fibrin formation, the geometry of fibrin fibers is heavily affected by ionic strength and ion type (**58,61**). Hence, it is not surprising that a highly charged protein like αSyn can participate in the process of fibrin polymerization and alter the structure of the ensuing fibrin fibers.

The effect of full-length αSyn and αSyn(103-140) on platelets aggregation and PAR1(38-60) hydrolysis

Multiple Electrode Aggregometry (MEA) was used to estimate the effect of full-length αSyn and αSyn(103-140) on platelets aggregation induced in whole blood at 37°C by αT, TRAP, or ADP (**Fig. 4**). MEA is a fast and convenient platelet-function-testing method which enables to measure aggregation in whole blood, i.e. the physiological environment where platelet function takes place *in vivo*. At variance, Light Transmisson Aggregometry techniques, traditionally used for measuring platelets agglutination, are performed on platelet-rich plasma in the absence of erythrocytes, leukocytes, and larger platelet subspecies that are likely to influence normal platelet aggregation (**37**). Furthermore, MEA takes place on the solid surface of the measure cell electrodes, resembling the physiological process of platelet adhesion and aggregation on the damaged vessel tissues (**62**). MEA relays on the measurement of the increase in impedance (i.e. the electric resistance to the passage of alternate current in a medium between two platinum electrodes) which is caused by sticking of activated platelets onto the electrodes (**37,63**). In non-clotted blood, quiescent/inactive platelets stick to the electrodes and self-organize in cell monolayers. After the addition of a platelet aggregant, such

as αT or ADP, platelets tightly adhere to the pre-existing monolayers on the electrodes, thus increasing blood electric impedance (**62**). Although MEA is specifically sensitive to the aggregation of platelets on the electrode surface, when blood samples are used, some red blood cells and leucocytes trapped in the platelet aggregate can be seen by scanning electron microscopy (**62,63**). Plasma fibrinogen and fibrin fibers, that can be generated by addition of αT to whole blood, might interact with activated platelets and increase the impedance signal (**64**). The time-dependent change of blood impedance is expressed as relative Aggregation Units (AU) (**Fig. 4A**), where 8 AU approximately correspond to 1 Ohm (Ω). Integration of AU over time (10 min) gives the value of the Area Under the Curve (AUC), which is taken as the best parameter of platelet function in MEA analysis (**37,62**).

The data in **Fig. 4A,B** show that that addition of full-length αSyn to whole blood samples reduced, in a concentration-dependent manner, the platelet aggregation potency (%AUC) of the synthetic hexapeptide SFLLRN-NH$_2$ (TRAP-6) up to **80%** in the Multiplate TRAP-test, where TRAP-6 is **the most potent** and specific agonist of PAR1, independent of αT-induced receptor activation (**65-67**). αSyn also inhibited platelets aggregation induced by αT up to 50%, at the highest concentrations tested (10-20 μM) (**Fig. 4C**). Consistent with this result, αSyn (15 μM) reduced by 2-fold the efficiency of PAR1(38-60) hydrolysis by αT (**Fig. 3D**). Notably, the latter peptide reproduces the substrate binding properties of the extracellular domain of PAR1 on platelets, as it contains both the exosite-I binding sequence and the scissile bond R^{41}-S^{42} for αT (**68**). Conversely to what observed with TRAP and αT, αSyn displayed only low anti-aggregating effect (20%) in the Multiplate ADP - test (**Fig. 4D**).

With the aim to identify the region(s) of αSyn responsible for the inhibition of platelet aggregation, we tested the ability of the synthetic peptide αSyn(103-140), to impair platelet agglutination triggered by TRAP, αT, or ADP (**Fig. 4**). In all these tests, αSyn(103-140) displayed weak, if any, platelet anti-aggregating potency (**5%**). These findings indicate that the negatively charged αSyn C-terminal peptide (pI: 3.1) alone was not able to promote significant inhibition of platelets aggregation and indirectly suggest that, instead, the highly positive N-terminal region of αSyn (pI: 9.4) might play an important role in impairing platelet aggregation. Recombinant αSyn(1-96) was expressed in *E. coli*, but direct measurement of anti-aggregating properties was impracticable due to the much higher tendency of this polypeptide to aggregate/precipitate, compared to full-length αSyn (**69**).
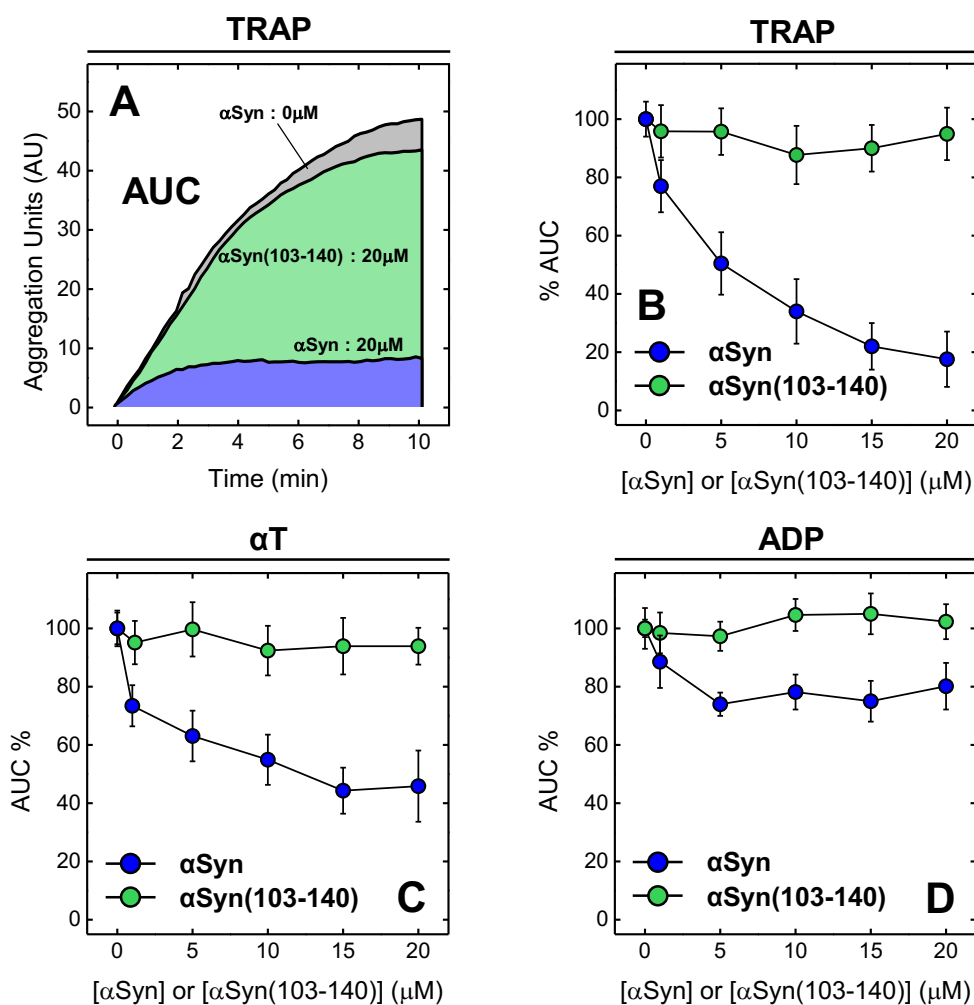
Figure 4. Effect of αSyn and αSyn(103-140) on the aggregation of platelets induced by TRAP, αT or ADP. (**A**) Representative impedance aggregometry curves of platelets aggregation induced by TRAP on whole blood in the absence (grey area) and presence of **20 μM** αSyn (blue area) or αSyn(103-140) (green area). (**B-D**) Impedance aggregometry analysis of platelet agglutination induced by **32 μM** TRAP-6 (**B**), **6 nM** αT (**C**), and **6.5 μM** ADP (**D**) on whole blood at 37°C at increasing concentrations of full-length αSyn (●) or αSyn(103-140) (●). At each αSyn concentration, the Area Under the Curve (%AUC) was calculated relative to the value determined in the absence of αSyn (AUC$_0$). Whole blood samples from healthy donors (300μl; 160.000 platelets/μl) were incubated with 300 μl of αSyn or αSyn(103-140) in HBS. Platelets agglutination was started by adding 20 μl of TRAP-6 or ADP stock solutions. When the effect of αSyn on αT-induce aggregation wa measured, protease solutions (320μl) were pre-incubated (30 min) with increasing αSyn concentrations and then added to blood samples (320μl). Each AUIC value is the average of single determinations on blood samples from three healthy donors. The error bars correspond to the standard deviation.
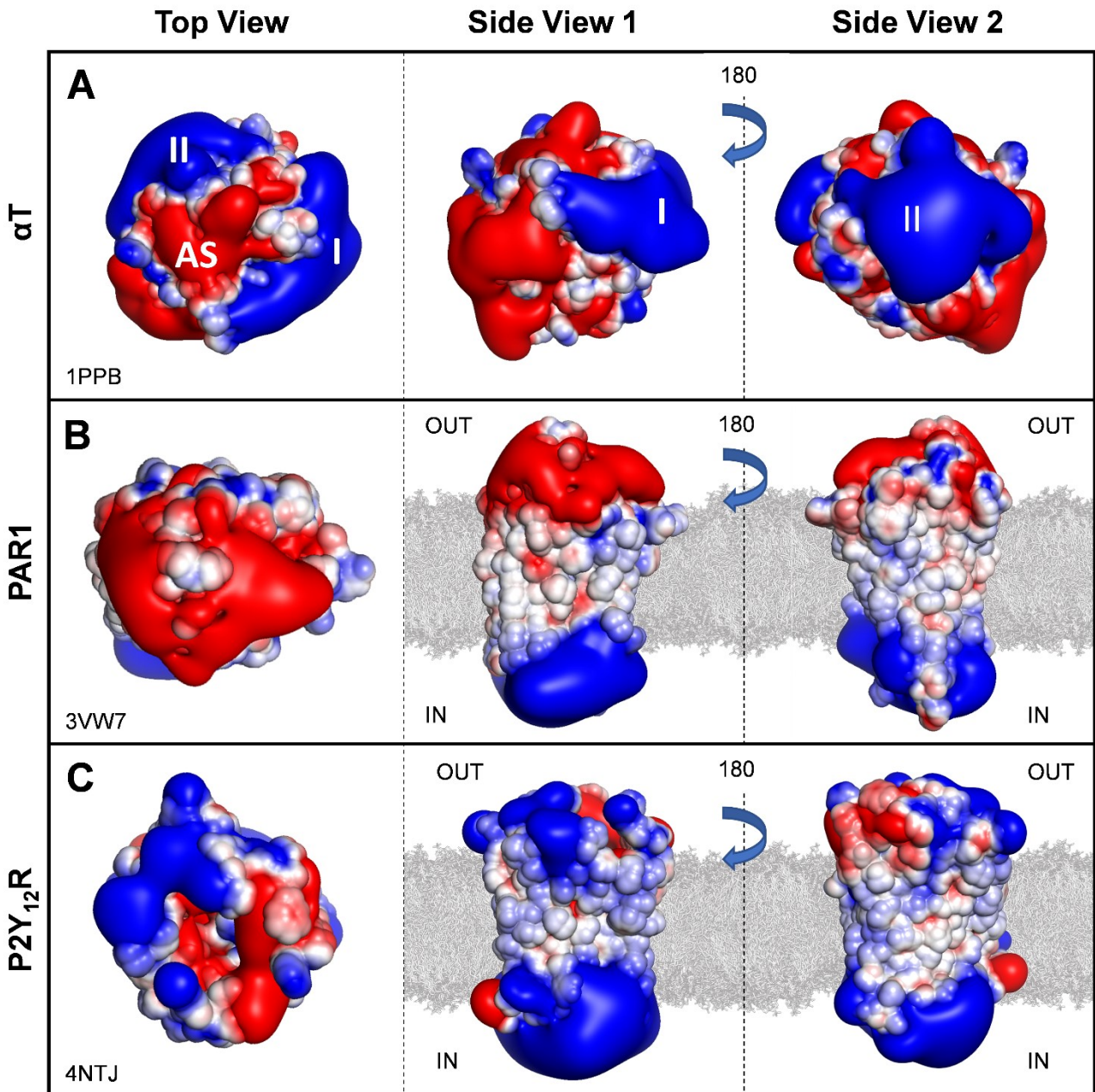
Figure 5. Surface electrostatic potential of αT, and platelet receptors PAR1 and P2Y$_{12}$R. Top and side view of surface electrostatic potential of αT (1ppb) (**A**), PAR1 (3vw7) (**B**), and ADP receptor P2Y$_{12}$R (**4ntj**) (**C**). The surface is coloured according to the electrostatic potential (blue, positive; red, negative) and expressed as kJ/(mol·q). Phospholipid double layer (grey) has been manually inserted. Calculations were carried out using the APBS software and images generated with the PyMOL software vs. 1.3 (DeLano Scientific, San Diego, CA, USA). (**A**) αT displays an asymmetrical potential with a strongly negative active site (AS) region flanked by the two electropositive exosites (I and II). (**B**) The structure of PAR1, lacking the negative exodomain 1-85, displays a highly polarized charged distribution, with highly negative the extracellular surface (OUT) and strongly positive intracellular surface (IN). As expected, the transmembrane region is essentially neutral. (**C**) A similar charge distribution is observed with P2Y$_{12}$R. In this case, however, the extracellular side is much less negative (more electropositive) than in PAR1. For P2Y$_{12}$R, the contribution of the receptor bound sodium cation (Na$^+$) was not taken into account during electrostatic calculations.

The results reported above prompted us to investigate the possible physicochemical determinants underlying the remarkably different effect of full-length αSyn on P2Y$_{12}$ receptor for ADP and PAR1 for αT. Provided that the positively charged N-terminal region of αSyn is crucial for platelets antiaggregating effect caused by both ADP and αT, we carried out surface electrostatic potential calculations on the crystallographic coordinates of P2Y$_{12}$ receptor and PAR1. As shown in **Fig. 5**, the extracellular region of PAR1 is highly negative and thus ready to interact with the positive N-terminal portion of αSyn. Conversely, the external regional of P2Y$_{12}$ receptor is much more positively charged and contains only a few negative spots. Hence, we propose that the more negative electrostatic potential of PAR1, compared to P2Y$_{12}$ receptor, can account for the higher inhibitory effect of αSyn on platelets activation induced by αT, compared to ADP.

Probing α-Synuclein binding to α-Thrombin by fluorescence spectroscopy and surface plasmon resonance

The interaction of αSyn with αT was monitored by two orthogonal techniques which are based on different physico-chemical observables: steady state intrinsic fluorescence (**70**)and Surface Plasmon Resonance (SPR) (**71**).

The fluorescence spectra in **Fig. 6A** indicate that addition of aSyn causes a decrease of the intrinsic fluorescence of αT, after excitation at 295 nm, compared to the theoretical sum-spectrum of isolated αT and αSyn, without appreciably changing the wavelength of maximal emission (λ_{max}). A quantitative estimate of αSyn-αT interaction was obtained by recording the decrease of αT fluorescence at 334 nm at increasing αSyn concentrations (**Fig. 6B**). At saturating αSyn concentrations (**20 μM**), a 10% decrease of αT fluorescence was reproducibly measured and interpolation of the data points with **eq. 4**, describing a stoichiometric 1:1 binding model, yielded an equilibrium dissociation constant (K$_d$) of **0.96 μM**. The fluorescence change associated with αSyn-αT coupling is likely caused by alteration in the environment of Trp-residues in αT, as αSyn contains only four Tyr-residues which does not (or only negligibly) absorb at 295 nm and therefore do not contribute to the emitted fluorescence (**72**). Notably, of the nine Trp-residues present in αT structure, six are moderately or highly solvent exposed and therefore amenable to interact with αSyn (**47**). Like full-length αSyn, addition of αSyn(103-140) reduces αT fluorescence by the same extent and binds to the protease with an identical affinity (**K$_d$ = 1.25 μM**). This finding indicates that the negatively charged C-terminal tail is the αT binding epitope on αSyn and that, conversely, the positive N-terminal region is not required for the interaction with the protease.
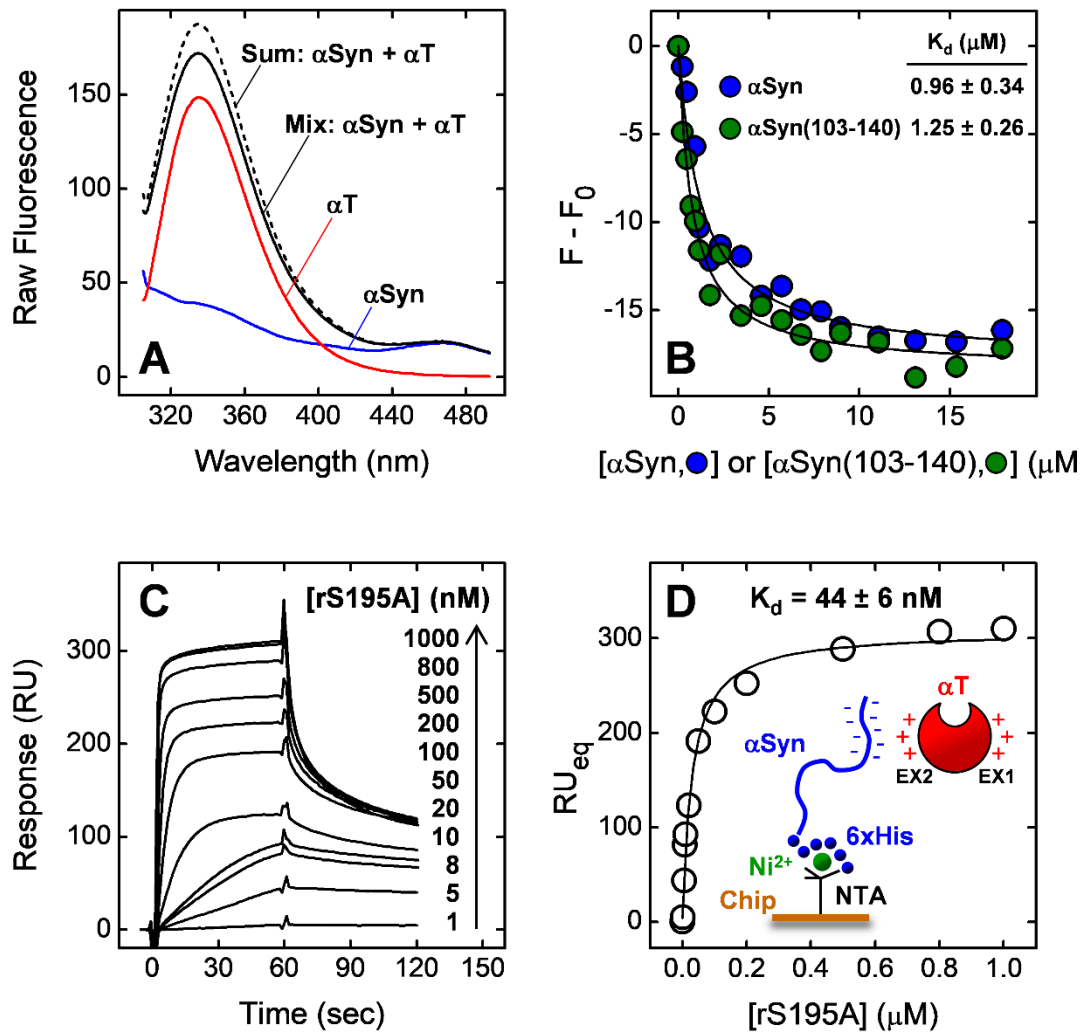
Figure 6. Probing αT-αSyn interaction by fluorescence spectroscopy and surface plasmon resonance. (**A**) Fluorescence spectra of isolated αSyn (20 μM, ▬) and αT (70 nM, ▬), and of the experimental complex containing the interacting proteins at the corresponding concentrations (▬). For comparison, the theoretical sum spectrum (---) is also reported. Emission spectra were recorded in HBS at 37°C, after excitation at 295 nm, and subtracted for the corresponding baseline. (**B**) Fluorescence binding measurements of αSyn interaction with αT. To a solution of αT (70 nM) in HBS at 37°C were added aliquots (2-20 μl) of full-length αSyn (●) and αSyn(103-140) (●). The samples were excited at 295, and the emission intensity was recorded at the λ_{max} of αT (334nm). Each spectrum was subtracted for the contribution of αSyn alone at the corresponding concentration and expressed as F - F₀, where F and F_0 are the fluorescence intensity in the presence or absence of αSyn derivatives. The data points were interpolated with **eq. 4**, yielding the K_d value as a fitting parameter. (**C, D**) SPR analysis of thrombin binding to immobilized αSyn. Recombinant wild-type 6xHis-αSyn was immobilized onto a Ni^{2+}-NTA sensor chip and increasing concentrations of rS195A thrombin mutant were injected in the mobile phase. (**C**) Sensograms relative to rS195A binding. (**D**) Plot of RU_{max} vs. rS195A concentration (○). Fitting of data points with **eq. 6** yielded the K_d value for the synuclein-thrombin complex, as indicated. All SPR measurements were carried out at **37°C** in HBS-EP⁺.

185

SPR measurements were carried out by first immobilizing the N-terminally fused 6xHis-tag αSyn onto a Ni^{2+}/NTA sensor chip, *via* non-covalent chelation, and then injecting incremental concentrations of αT in the mobile phase (**Fig. 6 C,D**). SPR data were analyzed according to the one-site binding model, yielding a K_d of 44 nM. Notably, the affinity of αT for immobilized αSyn, deduced from SPR measurements, was >20-fold higher than that estimated by fluorescence binding experiments. Overestimation of binding strength in protein-protein interactions is quite frequent in SPR measurements, compared to other spectroscopic binding measurements (e.g. fluorescence) (**28,71**), and is inherently associated to the beneficial lower loss of binding entropy (ΔS_b) occurring in a biphasic interacting system like SPR, where one of the two partners is in solution and the other is immobilized on the sensor chip. This is especially true for an intrinsically unfolded protein like αSyn, which becomes more rigid after immobilization on the sensor chip, with a resulting favorable reduction of ΔS_b during αSyn-αT complex formation. Intriguingly, the higher affinity of αT for immobilized αSyn in SPR analysis might have some relevance for *in vivo* binding studies, as αSyn is known to become ordered after binding to platelets membrane (**9**) (**see Introduction**).

Altogether, fluorescence and SPR measurements concurrently indicate that αSyn binds to αT with a moderate to high affinity, according to the binding system exploited. Furthermore, fluorescence data indicate that the negative C-terminal tail of αSyn is the binding epitope for αT.

Molecular mapping of α-Synuclein/α-Thrombin interaction

The active site and exosites 1 and 2 are the regions of αT responsible for the recognition of most physiological substrates/inhibitors (**73,74**). The role played by these hot spots in binding to αSyn was assessed by measuring the effect of saturating concentrations of αSyn (20 μM) on the affinity of selected ligands which are known to specifically bind at a given target site on αT structure. The decrease in binding strength for a specific ligand, covering a well-defined αT region, was taken as a strong indication that the targeted region on αT was involved in the binding of αSyn. Likewise, we measured the binding strength to αSyn of thrombin derivatives in which one of the key binding sites was selectively perturbed/killed (**28,33,35**).
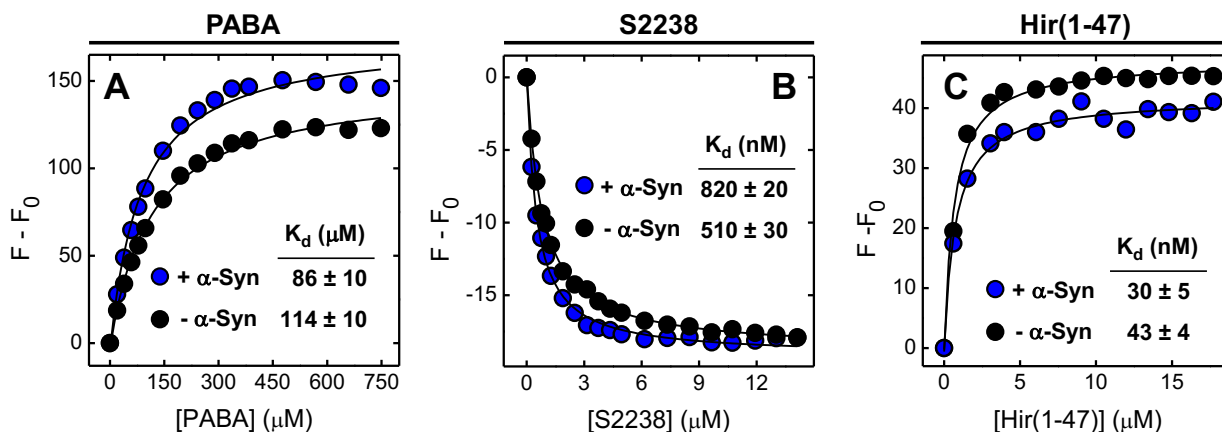
Figure 7. Molecular mapping of αSyn-αT interaction: the role of thrombin active site. Effect of αSyn on the affinity of the active-site ligands PABA (**A**), S2238 (**B**), or Hir(1-47) (**C**) for thrombin. Fluorescence binding measurements were carried out in HBS at 37°C by adding increasing ligand concentrations to thrombin solutions, in the absence or presence of saturating αSyn (20 μM). For the binding of PABA, samples (40nM) were excited at 336nm, the fluorescence intensity of the ligand was recorded at 375 nm and corrected for inner filter effect. With S2238 and Hir(1-47), protein samples (50 nM and 70 nM, respectively) were excited at 295nm and the fluorescence of thrombin was recorded at the emission λ_{max} of the enzyme (334nm). When the binding of S2238 to thrombin was being studied, the inactive rS195A mutant was used. The data points relative to the binding of PABA and S2338 were interpolated with **eq. 4**, describing a single-site interaction model, while the data for the binding of Hir(1-47) were fitted with **eq. 5**, describing a tight-binding model. After interpolation, the K_d values were obtained as fitting parameters, as indicated.

Active Site. To probe the possible involvement of αT active site in αSyn binding, the affinity of active-site binders, having incremental size [i.e. PABA, S2238, Hir(1-47)], for natural αT or the inactive rS195A mutant was measured by fluorescence spectroscopy. Notably, albeit inactive, this mutant stores all the molecular recognition properties of active αT (**28,33,42**). PABA (*p*-aminobenzamidine) is a small molecule that binds to the primary substrate specificity site, S1, of chymotrysin-like proteases with an increase of fluorescence quantum yield at 375 nm (**75**). S2238 (D-Phe-Pip-Arg-*p*NA) is a chromogenic substrate for active αT and extensively penetrates into the protease sub-sites S1, S2, and S3 (**47**). When the inactive rS195A was used, the affinity of S2238 for thrombin could be determined by measuring the decrease of Trp-fluorescence of thrombin due to fluorescence energy transfer with the pNA moiety of S2238 (**76,77**). Hir(1-47) encompasses the N-terminal domain of hirudin and displays potent and specific inhibitory activity for αT, interacting with the S2 and S3 sites and covering the loop regions surrounding the active site (**78**). Binding of Hir(1-47) to αT is associated to an increase of the protease fluorescence emission, likely caused by rigidification and partial shielding of some Trp-residues in αT (**38,42**). The data in **Fig. 7** indicate that αSyn (20 μM) only marginally alters the affinity of all the ligands/inhibitors tested for αT by 2-

3%, with respect to their binding free energy change (ΔG_b), thus suggesting that the protease active site is not involved in binding to αSyn.
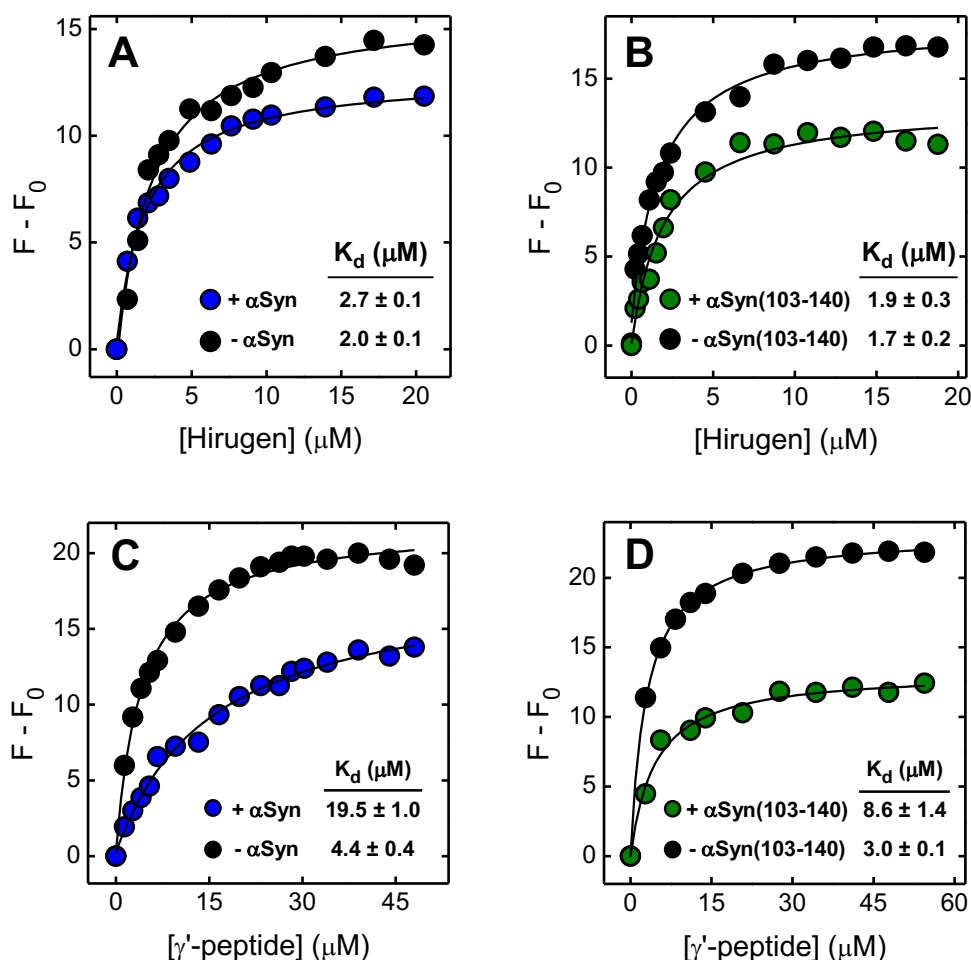
Figure 8. Molecular mapping of αSyn-αT interaction: the role of thrombin exosites. (**A, B**) The role of exosite 1. Effect of αSyn and αSyn(103-140) on the affinity of hirugen for thrombin exosite-1. Fluorescence measurements of hirugen binding to αT (70 nM) in the absence or presence of saturating concentrations (20 μM) of full-length αSyn (**A**) or αSyn(103-140) (**B**). (**C, D**) The role of exosite 2. Effect of αSyn and αSyn(103-140) on the affinity of γ′-peptide for thrombin exosite-2. Fluorescence measurements of γ′-peptide binding to αT (70 nM) in the absence or presence of saturating concentrations (20 μM) of full-length αSyn (**C**) or αSyn(103-140) (**D**). Protein samples in HBS at 37°C were excited at 295nm and the fluorescence intensity was recorded at 334 nm, after baseline subtraction. The data points were interpolated with **eq. 4** to obtain the K_d values, as indicated.

Exosites 1 and 2. The role of exosites was investigated by measuring the affinity of αT for exosite-specific peptide ligands in the absence and presence of 20 μM αSyn or αSyn(103-140). Hirugen, corresponding the C-terminal tail 54-65 of hirudin HV1 variant, was selected as a safe exosite-1 binder (**28,42,73**), whereas the γ′-peptide, corresponding to the 408-427 C-terminal tail of the fibrinogen elongated γ-chain splice variant, was used as a specific exosite-2 ligand (**27,79**).

Fluorescence binding measurements show that αSyn(103-140) and full-length αSyn decreased the affinity of the γ'-peptide for αT by about 3- and 4-fold (**Fig. 8 C,D**), without significantly affecting binding strength of hirugen (**Fig. 8 A,B**). These results indicate that exosite 2 is involved in the interaction with αSyn, whereas exosite 1 does not seem to play an important role.

Further support to the role of exosite 2 in αT-αSyn interaction derives from SPR analysis of the interaction of immobilized αSyn with thrombin species having the exosites variably compromised, i.e. the inactive zymogens prothrombin (ProT) and the nicked species β_T-thrombin (β_TT) (**Fig. 9**). ProT is the physiological precursor of mature αT and, going from the N- to the C-terminus, it is formed by the γ-carboxyglutamic acid rich Gla domain, the kringle 1 (K1) and kringle 2 (K2) domains, and the prethrombin 2 region (Pre2) (**80**). The recently solved crystallographic structure of ProT (**42**) reveals that, compared to αT, major perturbations occur in the Na^+-binding site, in the activation domain and in the insertion loops surrounding on the catalytic cleft. Importantly, exosite 1 structure seems to be only slightly altered in the zymogen relative to the mature enzyme whereas the reactivity of exosite 2 is completely abolished in ProT by the intramolecular tight binding of the K2 domain (**Fig. 9A**). β_TT results from the tryptic cleavage of mature αT at the single peptide bond Arg77a−Asn78, leading to disruption of exosite-1, whereas the catalytic site and exosite-2 fully retain the structural/functional properties of the corresponding regions in the mature αT (**81**) (**Fig. 9A**). Notably, the inactive S195A mutant was used in SPR measurements with immobilized 6xHis-tag αSyn, as the active αT cleaves the fused recombinant protein (but not the wild-type αSyn) at Lys6 (**unpublished results**). Analysis of binding data (**Fig. 9B**) reveals that disruption of exosite-1, as in β_TT, reduces the affinity for aSyn by only 1.5-fold, whereas masking of exosite-2, as in ProT, leads to a dramatic drop in binding strength by 37-fold.

The results of fluorescence and SPR measurements indicate that the highly negative C-terminal tail 103-140 of αSyn is responsible for the binding to αT exosite 2 which, of the two exosites, is the most strongly positive.
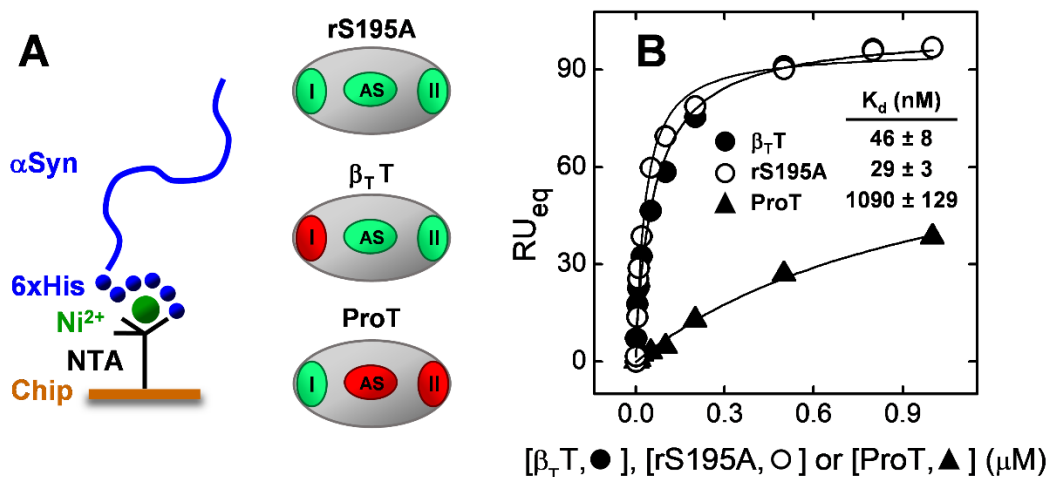
Figure 9. Effect of selective perturbation of thrombin exosites on the affinity for αSyn. (**A**) Schematic representation of the protease-domain of rS195A thrombin mutant, β_T-thrombin (β_TT), and prothrombin (ProT). The active site (AS) and exosite-1 (I) and exosite-2 (II) are colored according to the conformational/functional state they assume in the different thrombin derivatives, compared to αT (see text); *green*: unperturbed or only slightly perturbed; *red*: heavily perturbed. (**B**) SPR analysis of the binding of rS195A, β_TT, and ProT to 6xHis-αSyn immobilized on a Ni^{2+}-NTA sensor chip. The values of RU_{max} were plotted *versus* the concentration of thrombin derivatives and the data points were interpolated with **eq. 6**, yielding the corresponding K_d values as indicated. Measurements were carried out at 37°C in HBS-EP$^+$, pH 7.4.

CONCLUSIONS

αT is the key enzyme of the coagulation cascade, acting at the interface between coagulation, inflammation and cellular proliferation. On the other hand, human αSyn is a cerebral protein, mainly localized in the presynaptic terminals of neurons. Abnormal accumulation of cytoplasmic αSyn aggregates, both in neurons and glia, is the major determinant for the onset and progression of neurodegenerative disorders, such Parkinson's and Alzheimer's diseases. However, αSyn is also found in human blood; it is expressed in platelets and binds to the α-granules, from which it is released upon αT stimulation. Intriguingly, the co-localization of αT and αSyn on (or near) the platelets membrane surface led us to investigate the possible effect of αSyn on the functional axis involving αT and PAR1.

The results reported in this work actually indicate that αSyn predominantly inhibits platelets activation induced by thrombin, likely through binding to the negative extracellular region of PAR1. On the other hand, the negatively charged C-terminal region of αSyn can also directly interact with the positive exosite-2 on αT structure, thus impairing platelets activation. On this basis, we propose that αSyn may act as a negative regulator of platelets stimulation by αT, either functioning as a direct PAR1 inhibitor and a molecular scavenger of αT on platelets surface.

REFERENCES

1.   Clayton, D. F., and George, J. M. (1998) The synucleins: a family of proteins involved in synaptic function, plasticity, neurodegeneration and disease. *Trends Neurosci* **21**, 249-254

2.   Ueda, K., Fukushima, H., Masliah, E., Xia, Y., Iwai, A., Yoshimoto, M., Otero, D. A., Kondo, J., Ihara, Y., and Saitoh, T. (1993) Molecular cloning of cDNA encoding an unrecognized component of amyloid in Alzheimer disease. *Proc Natl Acad Sci U S A* **90**, 11282-11286

3.   Sandal, M., Valle, F., Tessari, I., Mammi, S., Bergantino, E., Musiani, F., Brucale, M., Bubacco, L., and Samori, B. (2008) Conformational equilibria in monomeric alpha-synuclein at the single-molecule level. *PLoS Biol* **6**, e6

4.   Lavedan, C., Buchholtz, S., Auburger, G., Albin, R. L., Athanassiadou, A., Blancato, J., Burguera, J. A., Ferrell, R. E., Kostic, V., Leroy, E., Leube, B., Mota-Vieira, L., Papapetropoulos, T., Pericak-Vance, M. A., Pinkus, J., Scott, W. K., Ulm, G., Vasconcelos, J., Vilchez, J. J., Nussbaum, R. L., and Polymeropoulos, M. H. (1998) Absence of mutation in the beta- and gamma-synuclein genes in familial autosomal dominant Parkinson's disease. *DNA Res* **5**, 401-402

5.   Iwai, A., Masliah, E., Yoshimoto, M., Ge, N., Flanagan, L., de Silva, H. A., Kittel, A., and Saitoh, T. (1995) The precursor protein of non-A beta component of Alzheimer's disease amyloid is a presynaptic protein of the central nervous system. *Neuron* **14**, 467-475

6.   Bisaglia, M., Tessari, I., Pinato, L., Bellanda, M., Giraudo, S., Fasano, M., Bergantino, E., Bubacco, L., and Mammi, S. (2005) A topological model of the interaction between alpha-synuclein and sodium dodecyl sulfate micelles. *Biochemistry* **44**, 329-339

7.   Uversky, V. N. (2007) Neuropathology, biochemistry, and biophysics of alpha-synuclein aggregation. *J Neurochem* **103**, 17-37

8.   Davidson, W. S., Jonas, A., Clayton, D. F., and George, J. M. (1998) Stabilization of alpha-synuclein secondary structure upon binding to synthetic membranes. *J Biol Chem* **273**, 9443-9449

9.   Ulmer, T. S., and Bax, A. (2005) Comparison of structure and dynamics of micelle-bound human alpha-synuclein and Parkinson disease variants. *J Biol Chem* **280**, 43179-43187

10.   Eliezer, D., Kutluay, E., Bussell, R., Jr., and Browne, G. (2001) Conformational properties of alpha-synuclein in its free and lipid-associated states. *J Mol Biol* **307**, 1061-1073

11.   Dedmon, M. M., Lindorff-Larsen, K., Christodoulou, J., Vendruscolo, M., and Dobson, C. M. (2005) Mapping long-range interactions in alpha-synuclein using spin-label NMR and ensemble molecular dynamics simulations. *J Am Chem Soc* **127**, 476-477

12.   Murray, I. V., Giasson, B. I., Quinn, S. M., Koppaka, V., Axelsen, P. H., Ischiropoulos, H., Trojanowski, J. Q., and Lee, V. M. (2003) Role of alpha-synuclein carboxy-terminus on fibril formation in vitro. *Biochemistry* **42**, 8530-8540

13.   Lucking, C. B., and Brice, A. (2000) Alpha-synuclein and Parkinson's disease. *Cell Mol Life Sci* **57**, 1894-1908

14. Barbour, R., Kling, K., Anderson, J. P., Banducci, K., Cole, T., Diep, L., Fox, M., Goldstein, J. M., Soriano, F., Seubert, P., and Chilcote, T. J. (2008) Red blood cells are the major source of alpha-synuclein in blood. *Neurodegener Dis* **5**, 55-59

15. Hashimoto, M., Yoshimoto, M., Sisk, A., Hsu, L. J., Sundsmo, M., Kittel, A., Saitoh, T., Miller, A., and Masliah, E. (1997) NACP, a synaptic protein involved in Alzheimer's disease, is differentially regulated during megakaryocyte differentiation. *Biochem Biophys Res Commun* **237**, 611-616

16. Shin, E. C., Cho, S. E., Lee, D. K., Hur, M. W., Paik, S. R., Park, J. H., and Kim, J. (2000) Expression patterns of alpha-synuclein in human hematopoietic cells and in Drosophila at different developmental stages. *Mol Cells* **10**, 65-70

17. Chung, A. W., Jurasz, P., Hollenberg, M. D., and Radomski, M. W. (2002) Mechanisms of action of proteinase-activated receptor agonists on human platelets. *Br J Pharmacol* **135**, 1123-1132

18. Korten, A., Lodder, J., Vreeling, F., Boreas, A., van Raak, L., and Kessels, F. (2001) Stroke and idiopathic Parkinson's disease: does a shortage of dopamine offer protection against stroke? *Mov Disord* **16**, 119-123

19. Levine, R. L., Jones, J. C., and Bee, N. (1992) Stroke and Parkinson's disease. *Stroke* **23**, 839-842

20. Scigliano, G., Musicco, M., Soliveri, P., Piccolo, I., Ronchetti, G., and Girotti, F. (2006) Reduced risk factors for vascular disorders in Parkinson disease patients: a case-control study. *Stroke* **37**, 1184-1188

21. Struck, L. K., Rodnitzky, R. L., and Dobson, J. K. (1990) Circadian fluctuations of contrast sensitivity in Parkinson's disease. *Neurology* **40**, 467-470

22. Barbeau, A., Campanella, G., Butterworth, R. F., and Yamada, K. (1975) Uptake and efflux of 14-C-dopamine in platelets: evidence for a generalized defect in Parkinson's disease. *Neurology* **25**, 1-9

23. Bonuccelli, U., Piccini, P., Del Dotto, P., Pacifici, G. M., Corsini, G. U., and Muratorio, A. (1990) Platelet monoamine oxidase B activity in parkinsonian patients. *J Neurol Neurosurg Psychiatry* **53**, 854-855

24. Rabey, J. M., Vered, Y., Shabtai, H., Graff, E., Harsat, A., and Korczyn, A. D. (1993) Broad bean (Vicia faba) consumption and Parkinson's disease. *Adv Neurol* **60**, 681-684

25. Sharma, P., Nag, D., Atam, V., Seth, P. K., and Khanna, V. K. (1991) Platelet aggregation in patients with Parkinson's disease. *Stroke* **22**, 1607-1608

26. Park, S. M., Jung, H. Y., Kim, H. O., Rhim, H., Paik, S. R., Chung, K. C., Park, J. H., and Kim, J. (2002) Evidence that alpha-synuclein functions as a negative regulator of Ca(++)-dependent alpha-granule release from human platelets. *Blood* **100**, 2506-2514

27. Lancellotti, S., Rutella, S., De Filippis, V., Pozzi, N., Rocca, B., and De Cristofaro, R. (2008) Fibrinogen-elongated gamma chain inhibits thrombin-induced platelet response, hindering the interaction with different receptors. *J Biol Chem* **283**, 30193-30204

28.   Acquasaliente, L., Peterle, D., Tescari, S., Pozzi, N., Pengo, V., and De Filippis, V. (2016) Molecular mapping of alpha-thrombin (alphaT)/beta2-glycoprotein I (beta2GpI) interaction reveals how beta2GpI affects alphaT functions. *Biochem J* **473**, 4629-4650

29.   Vindigni, A., De Filippis, V., Zanotti, G., Visco, C., Orsini, G., and Fontana, A. (1994) Probing the structure of hirudin from Hirudinaria manillensis by limited proteolysis. Isolation, characterization and thrombin-inhibitory properties of N-terminal fragments. *Eur J Biochem* **226**, 323-333

30.   Weinreb, P. H., Zhen, W., Poon, A. W., Conway, K. A., and Lansbury, P. T., Jr. (1996) NACP, a protein implicated in Alzheimer's disease and learning, is natively unfolded. *Biochemistry* **35**, 13709-13715

31.   Negro, A., Brunati, A. M., Donella-Deana, A., Massimino, M. L., and Pinna, L. A. (2002) Multiple phosphorylation of alpha-synuclein by protein tyrosine kinase Syk prevents eosin-induced aggregation. *Faseb j* **16**, 210-212

32.   Munishkina, L. A., Phelan, C., Uversky, V. N., and Fink, A. L. (2003) Conformational behavior and aggregation of alpha-synuclein in organic solvents: modeling the effects of membranes. *Biochemistry* **42**, 2720-2730

33.   Pozzi, N., Acquasaliente, L., Frasson, R., Cristiani, A., Moro, S., Banzato, A., Pengo, V., Scaglione, G. L., Arcovito, A., De Cristofaro, R., and De Filippis, V. (2013) beta2 - Glycoprotein I binds to thrombin and selectively inhibits the enzyme procoagulant functions. *J Thromb Haemost* **11**, 1093-1102

34.   Pontarollo, G., Acquasaliente, L., Peterle, D., Frasson, R., Artusi, I., and De Filippis, V. (2017) Non-canonical proteolytic activation of human prothrombin by subtilisin from Bacillus subtilis may shift the procoagulant-anticoagulant equilibrium toward thrombosis. *J Biol Chem* **292**, 15161-15179

35.   Sokolov, A. V., Acquasaliente, L., Kostevich, V. A., Frasson, R., Zakharova, E. T., Pontarollo, G., Vasilyev, V. B., and De Filippis, V. (2015) Thrombin inhibits the anti-myeloperoxidase and ferroxidase functions of ceruloplasmin: relevance in rheumatoid arthritis. *Free Radic Biol Med* **86**, 279-294

36.   De Filippis, V., De Dea, E., Lucatello, F., and Frasson, R. (2005) Effect of Na+ binding on the conformation, stability and molecular recognition properties of thrombin. *Biochem J* **390**, 485-492

37.   Toth, O., Calatzis, A., Penz, S., Losonczy, H., and Siess, W. (2006) Multiple electrode aggregometry: a new device to measure platelet aggregation in whole blood. *Thromb Haemost* **96**, 781-788

38.   De Filippis, V., Colombo, G., Russo, I., Spadari, B., and Fontana, A. (2002) Probing the hirudin-thrombin interaction by incorporation of noncoded amino acids and molecular dynamics simulation. *Biochemistry* **41**, 13556-13569

39.   Donnini, S., Finetti, F., Francese, S., Boscaro, F., Dani, F. R., Maset, F., Frasson, R., Palmieri, M., Pazzagli, M., De Filippis, V., Garaci, E., and Ziche, M. (2011) A novel protein from the

serum of Python sebae, structurally homologous with type-gamma phospholipase A(2) inhibitor, displays antitumour activity. *Biochem J* **440**, 251-262

40. Zavyalova, E. G., Protopopova, A. D., Kopylov, A. M., and Yaminsky, I. V. (2011) Investigation of early stages of fibrin association. *Langmuir* **27**, 4922-4927

41. Harding, S. E., and Jumel, K. (2001) Light scattering. *Curr Protoc Protein Sci* **Chapter 7**, Unit 7.8

42. Pozzi, N., Bystranowska, D., Zuo, X., and Di Cera, E. (2016) Structural Architecture of Prothrombin in Solution Revealed by Single Molecule Spectroscopy. *J Biol Chem* **291**, 18107-18116

43. Valotteau, C., Prystopiuk, V., Pietrocola, G., Rindi, S., Peterle, D., De Filippis, V., Foster, T. J., Speziale, P., and Dufrene, Y. F. (2017) Single-Cell and Single-Molecule Analysis Unravels the Multifunctionality of the Staphylococcus aureus Collagen-Binding Protein Cna. *ACS Nano* **11**, 2160-2170

44. Baker, N. A., Sept, D., Joseph, S., Holst, M. J., and McCammon, J. A. (2001) Electrostatics of nanosystems: application to microtubules and the ribosome. *Proc Natl Acad Sci U S A* **98**, 10037-10041

45. Fogolari, F., Corazza, A., Yarra, V., Jalaru, A., Viglino, P., and Esposito, G. (2012) Bluues: a program for the analysis of the electrostatic properties of proteins based on generalized Born radii. *BMC Bioinformatics* **13 Suppl 4**, S18

46. Bashford, D., and Case, D. A. (2000) Generalized born models of macromolecular solvation effects. *Annu Rev Phys Chem* **51**, 129-152

47. Bode, W., Turk, D., and Karshikov, A. (1992) The refined 1.9-A X-ray crystal structure of D-Phe-Pro-Arg chloromethylketone-inhibited human alpha-thrombin: structure analysis, overall structure, electrostatic properties, detailed active-site geometry, and structure-function relationships. *Protein Sci* **1**, 426-471

48. Zhang, C., Srinivasan, Y., Arlow, D. H., Fung, J. J., Palmer, D., Zheng, Y., Green, H. F., Pandey, A., Dror, R. O., Shaw, D. E., Weis, W. I., Coughlin, S. R., and Kobilka, B. K. (2012) High-resolution crystal structure of human protease-activated receptor 1. *Nature* **492**, 387-392

49. Zhang, K., Zhang, J., Gao, Z. G., Zhang, D., Zhu, L., Han, G. W., Moss, S. M., Paoletta, S., Kiselev, E., Lu, W., Fenalti, G., Zhang, W., Muller, C. E., Yang, H., Jiang, H., Cherezov, V., Katritch, V., Jacobson, K. A., Stevens, R. C., Wu, B., and Zhao, Q. (2014) Structure of the human P2Y12 receptor in complex with an antithrombotic drug. *Nature* **509**, 115-118

50. Giehm, L., Lorenzen, N., and Otzen, D. E. (2011) Assays for alpha-synuclein aggregation. *Methods* **53**, 295-305

51. Murphy, R. M. (1997) Static and dynamic light scattering of biological macromolecules: what can we learn? *Curr Opin Biotechnol* **8**, 25-30

52. Uversky, V. N. (1993) Use of fast protein size-exclusion liquid chromatography to study the unfolding of proteins which denature through the molten globule. *Biochemistry* **32**, 13288-13298

53. Uversky, V. N., Li, J., and Fink, A. L. (2001) Trimethylamine-N-oxide-induced folding of alpha-synuclein. *FEBS Lett* **509**, 31-35

54. Nath, A., Trexler, A. J., Koo, P., Miranker, A. D., Atkins, W. M., and Rhoades, E. (2010) Single-molecule fluorescence spectroscopy using phospholipid bilayer nanodiscs. *Methods Enzymol* **472**, 89-117

55. Damaschun, G., Damaschun, H., Gast, K., Gernat, C., and Zirwer, D. (1991) Acid denatured apo-cytochrome c is a random coil: evidence from small-angle X-ray scattering and dynamic light scattering. *Biochim Biophys Acta* **1078**, 289-295

56. Vindigni, A., Dang, Q. D., and Di Cera, E. (1997) Site-specific dissection of substrate recognition by thrombin. *Nat Biotechnol* **15**, 891-895

57. Higgins, D. L., and Vehar, G. A. (1987) Interaction of one-chain and two-chain tissue plasminogen activator with intact and plasmin-degraded fibrin. *Biochemistry* **26**, 7786-7791

58. Weisel, J. W., and Nagaswami, C. (1992) Computer modeling of fibrin polymerization kinetics correlated with electron microscope and turbidity observations: clot structure and assembly are kinetically controlled. *Biophys J* **63**, 111-128

59. Weisel, J. W., and Litvinov, R. I. (2013) Adaptation of fibrous biopolymers to recurring increasing strains. *Proc Natl Acad Sci U S A* **110**, 12164-12165

60. Kononova, O., Litvinov, R. I., Zhmurov, A., Alekseenko, A., Cheng, C. H., Agarwal, S., Marx, K. A., Weisel, J. W., and Barsegov, V. (2013) Molecular mechanisms, thermodynamics, and dissociation kinetics of knob-hole interactions in fibrin. *J Biol Chem* **288**, 22681-22692

61. Di Stasio, E., Nagaswami, C., Weisel, J. W., and Di Cera, E. (1998) Cl- regulates the structure of the fibrin clot. *Biophys J* **75**, 1973-1979

62. Koltai, K., Kesmarky, G., Feher, G., Tibold, A., and Toth, K. (2017) Platelet Aggregometry Testing: Molecular Mechanisms, Techniques and Clinical Implications. *Int J Mol Sci* **18**

63. Cardinal, D. C., and Flower, R. J. (1980) The electronic aggregometer: a novel device for assessing platelet behavior in blood. *J Pharmacol Methods* **3**, 135-158

64. Riess, H. (1986) [Fibrinolytic therapy of lung embolism]. *Fortschr Med* **104**, 667-670

65. Kinlough-Rathbone, R. L., Perry, D. W., Guccione, M. A., Rand, M. L., and Packham, M. A. (1993) Degranulation of human platelets by the thrombin receptor peptide SFLLRN: comparison with degranulation by thrombin. *Thromb Haemost* **70**, 1019-1023

66. Scarborough, R. M., Naughton, M. A., Teng, W., Hung, D. T., Rose, J., Vu, T. K., Wheaton, V. I., Turck, C. W., and Coughlin, S. R. (1992) Tethered ligand agonist peptides. Structural requirements for thrombin receptor activation reveal mechanism of proteolytic unmasking of agonist function. *J Biol Chem* **267**, 13146-13149

67. Vu, T. K., Wheaton, V. I., Hung, D. T., Charo, I., and Coughlin, S. R. (1991) Domains specifying thrombin-receptor interaction. *Nature* **353**, 674-677

68. Ayala, Y. M., Cantwell, A. M., Rose, T., Bush, L. A., Arosio, D., and Di Cera, E. (2001) Molecular mapping of thrombin-receptor interactions. *Proteins* **45**, 107-116

69. Liu, H., Liu, W., Wu, Y., Zhou, Y., Xue, R., Luo, C., Wang, L., Zhao, W., Jiang, J. D., and Liu, J. (2005) Loss of epigenetic control of synuclein-gamma gene as a molecular indicator of metastasis in a wide range of human cancers. *Cancer Res* **65**, 7635-7643

70. Eftink, M. R., Helton, K. J., Beavers, A., and Ramsay, G. D. (1994) The unfolding of trp aporepressor as a function of pH: evidence for an unfolding intermediate. *Biochemistry* **33**, 10220-10228

71. Nguyen, H. H., Park, J., Kang, S., and Kim, M. (2015) Surface plasmon resonance: a versatile technique for biosensor applications. *Sensors (Basel)* **15**, 10481-10510

72. Lakowicz, J. R., Gryczynski, I. I., and Gryczynski, Z. (1999) High Throughput Screening with Multiphoton Excitation. *J Biomol Screen* **4**, 355-362

73. Bock, P. E., Panizzi, P., and Verhamme, I. M. (2007) Exosites in the substrate specificity of blood coagulation reactions. *J Thromb Haemost* **5 Suppl 1**, 81-94

74. Li, W., Adams, T. E., Nangalia, J., Esmon, C. T., and Huntington, J. A. (2008) Molecular basis of thrombin recognition by protein C inhibitor revealed by the 1.6-A structure of the heparin-bridged complex. *Proc Natl Acad Sci U S A* **105**, 4661-4666

75. Evans, S. A., Olson, S. T., and Shore, J. D. (1982) p-Aminobenzamidine as a fluorescent probe for the active site of serine proteases. *J Biol Chem* **257**, 3014-3017

76. Krem, M. M., and Di Cera, E. (2003) Dissecting substrate recognition by thrombin using the inactive mutant S195A. *Biophys Chem* **100**, 315-323

77. Pozzi, N., Chen, Z., Gohara, D. W., Niu, W., Heyduk, T., and Di Cera, E. (2013) Crystal structure of prothrombin reveals conformational flexibility and mechanism of activation. *J Biol Chem* **288**, 22734-22744

78. Rydel, T. J., Tulinsky, A., Bode, W., and Huber, R. (1991) Refined structure of the hirudin-thrombin complex. *J Mol Biol* **221**, 583-601

79. Pineda, A. O., Chen, Z. W., Marino, F., Mathews, F. S., Mosesson, M. W., and Di Cera, E. (2007) Crystal structure of thrombin in complex with fibrinogen gamma' peptide. *Biophys Chem* **125**, 556-559

80. Mann, K. G., Brummel-Ziedins, K., Orfeo, T., and Butenas, S. (2006) Models of blood coagulation. *Blood Cells Mol Dis* **36**, 108-117

81. Hofsteenge, J., Braun, P. J., and Stone, S. R. (1988) Enzymatic properties of proteolytic derivatives of human alpha-thrombin. *Biochemistry* **27**, 2144-2151

CHAPTER 5.1

Subtilisin from *Bacillus subtilis* cleaves Human Transthyretin (hTTR) and generates the amyloidogenic fragment hTTR(59-127)

INTRODUCTION

Human transthyretin (hTTR) is a 55-kDa homo-tetrameric protein, mainly produced in the liver and brain, and abundantly present in human plasma (0.2 mg/ml, 3.6 μM) (**1**). In its native tetrameric conformation, hTTR transports thyroid hormones in the blood and cerebrospinal fluid and contributes to retinol delivery through the binding to the retinol binding protein (**2**). Thyroid hormones are bound to a hydrophobic channel in hTTR, positioned at the centre of the tetramer in the intersubunit space. Each hTTR monomer consists of 127 amino acids and forms eight β-strands, named from A to H, which are arranged in a β-sandwich of two four-stranded β-sheets and one small α-helix, which is located between β-strands E and F (**3-5**). The monomers tightly interact with each other to form stable dimers, mainly stabilised by extensive hydrogen bonds networks between adjacent antiparallel strands H-H′ and F-F′ (**6**). The two dimers then interact weaklier to form the final tetrameric structure, which is stabilised mainly through hydrophobic interactions involving the A-B and G-H loops (**5**).

hTTR aggregation causes transthyretin amyloidosis (ATTR), which is associated to three different pathological conditions, traditionally referred to as: i) acquired senile systemic amyloidosis (SSA), ii) familial amyloid polyneuropathy (FAP), and iii) familial amyloid cardiomyopathy (FAC) (**7**). SSA involves wild-type hTTR and affects the heart and tendons, more often of elderly people (**8-10**). Cardiomyopathy is the main clinical manifestation of SSA, which is usually diagnosed by *post mortem* exams of patients. In contrast, FAP and FAC are hereditary disorders caused by single point mutations affecting the hTTR gene. Such systemic diseases involve both the peripheral nerves (FAP) and heart (FAC) resulting in polyneuropathy and cardiomyopathy, respectively. Val30Met is the most frequent genetic mutation responsible for the onset of FAP (**11**), whereas Val122Ile is the most common mutation leading to cardiomyopathic complications (**12**). It is widely accepted that hTTR aggregation occurs after dissociation of the tetramer into monomer subunits, which, upon partial unfolding, undergo self-association into amyloid aggregates (**13**). In this context, single point mutations leading to FAP and FAC have been found to destabilize the tetramer, making it more prone to dissociation and subsequent aggregation (**14**). Consistent with these results, hTTR mutants that stabilize the tetrameric structure are less prone to aggregate (**15**). More recent findings indicate that

aggregation and fibril formation in hTTR familial amyloidosis is dependent not only on the type of mutation, but also on the susceptibility of hTTR genetic variants to proteolysis (**16-18**). Indeed, fibrils that are formed *in vivo* contain fragments of hTTR spanning the protein C-terminal region from Ser46 to Glu127 (**19**). In particular, the constituents of hTTR amyloid deposits in cardiac and adipose tissues have been chemically characterized, thus setting the basis for their classification into two distinct categories (**20,21**): type-A fibrils, predominantly formed by hTTR fragments, and type-B fibrils, mainly formed by intact TTR (**21**). Intriguingly, the presence of fragments does not seem to be influenced by the nature nor the position of the amino acid substitution (**22**). Rather, it is correlated to the anatomical district where amyloid deposits are formed, i.e. heart, brain, or intestine (**23**). Although the protease(s) responsible for proteolysis-induced hTTR amyloidosis *in vivo* have not yet been identified, mounting evidences indicate that digestive (i.e. trypsin) (**23**) and fibrinolytic (i.e. plasmin) (**24**) proteases of the chymotrypsin family are able to cleave hTTR, under shear stress *in vitro* conditions, and generate amyloidogenic fragments, e.g. hTTR(49-127), which have been previously identified in hTTR amyloid deposits of patients (**25**).

Starting from these considerations, we decided to screen several different digestive, coagulative, fibrinolytic, leukocyte, and bacterial proteases with respect to their ability to cleave hTTR and generate amyloidogenic fragments. Here we show that subtilisin, a serine protease secreted from *Bacillus subtilis*, triggers hTTR amyloid deposition by efficiently cleaving purified hTTR at the Leu58-Thr59 bond, under static conditions (pH 7.4, 37°C), generating the C-terminal fragment hTTR(59-127) which is resistant to further proteolysis and forms amyloid fibrils. Notably, hTTR(59-127) has been already found in amyloid deposits of some ATTR patients (**26**). Overall, the subtilisin-hTTR cleavage system herein highlighted might be useful not only for investigating the biophysics of proteolysis-dependent amyloidosis of hTTR, but also for addressing novel pathogenic mechanisms and risk factors for ATTR. With respect to this point, *B. subtilis* is a Gram-positive bacterium abundantly present as a commensal in the gut microbiota of normal individuals (i.e. 10,000 spores/g of faeces) (**27**), while the permeability of the gut mucosa is remarkably increased in elderly people (**28**) and in patients with Inflammatory Bowel Diseases (IBDs) (**29**), allowing passage of even large molecules (MW < 70 kDa) (**30**) and proteases, i.e. trypsin, chymotrypsin, and papain (**31**). Furthermore, clinical studies demonstrate a positive relation between aging/IBDs and the incidence of acquired ATTR (**32**). Hence, it is possible that, under certain physio-pathological conditions, extracellular bacterial proteases may translocate across the intestinal mucosa to the bloodstream and trigger the generation of the amyloidogenic fragment hTTR(59-127).

EXPERIMENTALS

Reagents

Subtilisin Carlsberg (EC 3.4.21.62) from *B. subtilis*, thermolysin (EC 3.4.24.27) from *B. thermoproteolyticus rokko*, cathepsin G (EC 3.4.21.20), endoproteinase Glu-C (EC 3.4.21.19), trypsin (EC 3.4.21.4) and chymotrypsin (EC 3.4.21.1) were purchased from Sigma (Saint Louis, MO, USA); plasmin (EC 3.4.21.7), α-thrombin (αT) (EC-3.4.21.5), factor VIIa (EC 3.4.21.21), factor IXa (EC 3.4.21.22), factor Xa (EC 3.4.21.6), and factor XIa (EC 3.4.21.27) were purchased from Haematologic Technologies (Essex Junction, VT, USA); proteinase 3 (EC 3.4.21.76) and human neutrophil elastase (EC 3.4.21.37) were from Athens Research & Technology (Athens, GA, USA); neutral protease (EC 3.4.24.28) from *B. subtilis* was a generous gift from EniRicerche (San Donato, Milan, Italy). Diflunisal was purchased from (Sigma). Fluorescein isothiocyanate (FITC) and phenylmethylsulfonyl fluoride (PMSF) were from Sigma. All other salts, solvents and reagents were of analytical grade and purchased from Sigma or Merck.

Purification of human plasma hTTR

The purification of hTTR from human plasma was carried out following essentially the phenol precipitation method previously reported (**33,34**) with minor modifications. Plasma samples from blood donors and non-smokers healthy subjects were obtained from the Institutional Blood Bank of the University Hospital of Padua or the Institute of Experimental Medicine, Saint Petersburg, Russia. All subjects gave their informed consent to the present study. Briefly, pooled plasma (100 ml) was thawed at 4°C, added with 20% (w/v) NaCl, and diluted 1:1 (v/v) dropwise under gentle stirring with a 5.5% (w/v) phenol solution. After precipitation, the suspension was centrifuged at 17.000 x g for 25 min at 4°C. The supernatant containing hTTR was withdrawn and extensively dialyzed overnight at 4°C against 50 mM Tris-HCl buffer, pH 7.4, with a cellulose membrane (3-kDa cut-off) (Sartorius AG, Germany). The dialyzed solution was loaded onto a home-made (1 x 10 cm) Q-sepharose column, equilibrated with 10 mM Tris-HCl buffer, pH 7.4, and eluted with a linear gradient of the same buffer containing 1M NaCl at a flow-rate of 1 ml/min. Fractions were collected and analysed by reducing SDS-PAGE (4-12% acrylamide) to identify the presence of hTTR, migrating as a 13-kDa band. hTTR-containing fractions were pooled, dialyzed overnight at 4°C against 50 mM Tris-HCl buffer, pH 7.4, and fractionated by size-exclusion chromatography on a (1 x 30 cm) Superose12 column (GE-Healthcare, USA), eluted with 5 mM Tris-HCl buffer, pH 7.4, 0.15 M NaCl (TBS), at a flow-rate of 0.5 ml/min. The material eluted in correspondence of the major chromatographic peak was stored at -20° for subsequent analysis.

Reaction of hTTR with proteolytic enzymes

hTTR (1 mg/ml, 18 μM tetramer) in 5 mM Tris-HCl buffer, pH 7.4, 0.15 M NaCl (TBS), containing 5 mM CaCl$_2$ was incubated at 37°C in the presence of the selected protease, at an enzyme:substrate ratio of 1:20 (mol/mol of tetramer). After 24h-reaction, aliquots (10 μg) of each proteolysis mixture was quenched with H$_2$O/TFA-0.1% (v/v) and then analysed by reducing SDS-PAGE (4-15% acrylamide) followed by Coomassie staining. The chemical identity of the fragments generated during hTTR proteolysis with subtilisin was determined by LC-MS analysis by loading an acid quenched aliquot (35 μg) of the reaction mixture, after 10-h proteolysis, onto a microbore column eluted (50 μl/min) with linear aqueous acetonitrile-0.1% (v/v) formic acid gradient from 10% to 70% in 30 min. A Waters Xevo G2-S Q-TOF mass spectrometer, connected to a Waters Acquity H-Class UPLC system, was used to identify the proteolytic fragments.

Kinetics of hTTR cleavage by subtilisin

To measure the kinetics of hTTR degradation and hTTR(59-127) generation by subtilisin cleavage, purified hTTR (1 mg/ml) was incubated at 37°C with subtilisin (20:1 molar ratio) in TBS-CaCl$_2$. At time points, aliquots (20 μl) of the reaction mixture were taken, acid quenched with 0.1% (v/v) aqueous TFA (80 μl), frozen at -20°C and then analysed by reducing SDS-PAGE (4-20% acrylamide), followed by Coomassie staining and densitometric analysis, and RP-HPLC using a (4.6 x 300 mm) Zorbax 300SB-C18 column (Agilent Technologies), eluted with a linear acetonitrile-0.1% TFA gradient and monitoring the absorbance of the effluent at 226 nm. Quantification of intact hTTR and fragment hTTR(59-127) by integrating the corresponding chromatographic peaks and taking into account their different chain length and aromatic amino acids composition, yielding a molar absorptivity value for the fragment at 226 nm (ε_{226}) approximately 2/3 of intact hTTR. Both SDS-PAGE densitometric and RP-HPLC data were plotted vs. time and fitted with **equation 1,** describing a pseudo-first order reaction:

$$[S] = [S_0] \cdot e^{-kt}$$ **eq. 1**

where $[S_0]$ and $[S]$ are the hTTR concentrations at the beginning of the reaction and after time t, respectively, and k is the observed cumulative kinetic constant for hydrolysis, obtained as a fitting parameter.

Purification and characterization of hTTR(59-127)

After 10-h proteolysis with subtilisin, the reaction mixture (1 ml, 18 μM hTTR tetramer added with 0.9 μM subtilisin) was quenched with 4% (v/v) aqueous TFA (25 μl). hTTR(59-127) fragment was purified by RP-HPLC by loading 100-μl aliquots of the reaction mixture onto a (Grace-Vydac) semi-preparative (1 x 25 cm) C18 column, eluted (1.5 ml/min) with a linear acetonitrile-0.078% TFA gradient from 10 to 55% in 45 min, recording the absorbance at 226 nm. hTTR(59-127) fragment, eluting in correspondence of the major chromatographic peak at 36 min (peak volume: ~2.5 ml), was collected, immediately frozen at -20°C and lyophilised for about 6 h in a Savant SpeedVac concentrator (Thermo-Fischer Scientific). After lyophilisation, hTTR(59-127) was dissolved by gentle vortexing in 10 mM phosphate buffer, pH 7.4, and analysed with respect to its conformation, ThT binding, and fibril formation properties.

Analytical techniques

SDS-PAGE. The purity of hTTR preparation was established by reducing SDS-PAGE (4-12% acrylamide), followed by Coomassie staining and densitometric analysis of the electrophoretic bands with the Image-J software (www.imagej.nih.gov).

RP-HPLC and mass spectrometry (MS). The chemical modifications present in the structure of purified hTTR at Cys10 were characterised by RP-HPLC and high-resolution mass spectrometry. Typically, aliquots (5-10 μg) of purified hTTR were loaded onto an analytical (4.6 x 150 mm) C4 column (Grace-Vydac, MD, USA) eluted with a linear acetonitrile-0.078%TFA gradient from 20% to 55% in 30 min at a flow-rate of 0.8 ml/min. For LC-MS analyses, separations were carried out on a (1 x 50 mm) C4 or C18 microbore column (Grace-Vydac), connected to a Waters (Milford, MO, USA) Acquity H-Class UPLC system and to a Waters Xevo G2-S Q-TOF mass spectrometer. The column was eluted (50 μl/min) with 1:1 (v/v) water:acetonitrile-1% (v/v) formic acid. Mass analyses were carried out in the positive ion mode, with the capillary potential set at 1.5 kV and source temperature at 100 °C. Monoisotopic mass values were determined at a resolution > 35.000 and an accuracy < 5 ppm. Data were acquired with the Mass-Lynks 4.1 software and integration of mass peaks was performed with the BioPharmaLynks suite (Waters).

Analytical size-exclusion chromatography (SEC). Purified hTTR (10 μg) was loaded onto a (7.8 x 150 mm) Yarra-3 μm SEC-3000 column (Phenomenex, CA, USA), eluted (0.6 ml/min) with 20 mM Tris-HCl buffer, pH 6.8, 0.15 M NaCl. The apparent molecular weight (MW) of hTTR was determined using a calibration curve obtained with standard proteins, as earlier described (**35**).

Derivatisation of subtilisin with FITC and PMSF. Irreversible inhibition of subtilisin at the active site was achieved by incubating subtilisin (0.5 mM) with PMSF (2 mM) in 0.1 M Na₂CO₃ pH

9.0 for 2 hours at 25°C, to yield PMS-subtilisin. Fluoresceinated subtilisin was prepared following the procedure previously described, with minor modifications (**36**). Briefly, fluorescein isothiocyanate (FITC) (220 μl) in DMSO (20 mg/ml, 51 mM) was slowly added to subtilisin or PMS-subtilisin solution (600 μl, 73 μM) in 0.1 M Na_2CO_3 buffer, pH 9.0. The reaction was carried out for 3 hours in the dark at 25°C. The reaction mixture was desalted on a HiTrap G-25 fast-flow column (5 ml) (GE-Healthcare), eluted (1.0 ml/min) with 10 mM sodium phosphate buffer, pH 7.4, 0.15 M NaCl (PBS). Labelled subtilisin samples for Transwell assays were desalted on a Zeba-Spin column (0.5 ml) from Thermo-Fischer Scientific (Waltham, MA, USA) in 10 mM HEPES buffer, pH 7.4, 10 mM glucose. The incorporation of a single PMS- or FTC-moiety was established by mass spectrometry. The derivatisation site in subtilisin sequence was established by enzymatic peptide mass fingerprint analysis. Briefly, FTC-PMS-subtilisin was treated with trypsin from Promega (Madison, WI, USA) (1:20 trypsin:subtilisin molar ratio) for 4 h at 25°C. The proteolysis mixture was fractionated with a C18 (1 x 100 mm) microbore column (Grace-Vydac) connected to an Agilent Technologies (Santa Clara, CA, USA) 1290 UPLC system and equipped with a 1290-Infinity diode array UV-Vis detector. FTC-tryptic peptide was identified by recording the absorbance of the effluent at the λ_{max} (494 nm) of fluorescein and characterized by mass spectrometry.

Spectroscopic techniques

UV-Vis absorption spectroscopy. hTTR and hTTR(59-127) concentration was determined spectrophotometrically by measuring the absorption of protein solutions at 280 nm on a Jasco (Tokyo, Japan) V-630 double beam spectrophotometer, using an absorptivity ($\varepsilon_{0.1\%}$) value of 1.35 mg^{-1}·cm^2 for intact hTTR and 1.67 mg^{-1}·cm^2 for hTTR(59-127).

Circular dichroism (CD). Measurements were carried out on a Jasco J-1500 spectropolarimeter, equipped with a Peltier temperature control system, using the Spectra Manager software (Jasco). CD spectra were recorded in a 1-mm and 5-mm path length quartz cell in the far- or near-UV region, at a scan-speed of 10 nm/min, with a response time of 16 sec, and resulted from the average of four accumulations after baseline subtraction. CD signal was expressed as the mean residue ellipticity $[\theta] = \theta_{obs} \cdot MRW/(10 \cdot l \cdot c)$, where θ_{obs} is the observed signal in degrees, MRW is the protein mean residue weight, l is the cuvette path length in cm, and c is the protein concentration in g/ml. Estimation of the secondary structure content from far-UV CD spectra was carried out using the software program BestSel, available on-line at the website www.bestsel.elte.hu (**37**).

Fluorescence. Spectra were recorded on a Jasco FP-6500 spectropolarimeter, equipped with a Peltier temperature control system, at a scan speed of 200 nm/min, with excitation/emission slits of 3/3 nm. The final spectra were the average of four accumulations, after baseline subtraction. To

prevent photodegradation of Trp-residues, a 1-cm path length cuvette (2 ml internal volume) with two opaque walls, that can diffuse the incident light inside the sample, was used.

Dynamic light scattering (DLS). DLS measurements were performed on a Zetasizer Nano-S instrument (Malvern Instruments, UK) at 25°C in 5 mM Tris-HCl buffer, pH 7.4, 0.15M NaCl, at a fixed angle (173°) from the incident light, generated by a He–Ne 4 mW laser source at 633 nm. Disposable polystyrene cuvettes (1-cm path length, 100μl) (Hellma, Switzerland) were used for all measurements. Each measurement consisted of a single run (15s). The refractive index (n) and viscosity (η) of the protein solutions were taken as 1.450 and 0.887cP, respectively at 25°C. Scattering data were analyzed with the Nano-6.20 software and expressed as % mass or % intensity size distribution. The reliability of DLS measurements was estimated from the value of the correlation coefficient (> 0.5), extracted from the autocorrelation curve.

Fibril generation assays

Turbidimetry. Aggregation of intact hTTR and fragment hTTR(59-127) (0.1 mg/ml) at increasing time points was monitored by recording the Abs_{260}/Abs_{280} ratio in the UV-Vis spectra of the proteolysis mixture of hTTR with subtilisin in TBS buffer, pH 7.4, containing 5 mM $CaCl_2$ or by recording the turbidmetric signal, as the apparent increase in the absorbance at 400 nm. The effect of diflunisal on hTTR aggregation induced by proteolysis with subtilisin was investigated by incubating hTTR (0.2 mg/ml, 3.6 μM) with subtilisin (20:1 molar ratio) in the absence or in the presence of diflunisal (3.6 μM). Protein samples (800 μl) were incubated in 20 mM potassium phosphate, pH 7.6, 0.1 M KCl, 1 mM EDTA for 72 h at 37°C without stirring. Diflunisal was added from a 720 μM stock solution in DMSO (4 μL). After 72 h, the samples were gently vortexed to suspend the fibrils and the turbidity of the suspension was measured at 400 nm using a Jasco V-630 spectrophotometer. For comparison, aggregation of intact hTTR was induced after 72-h incubation at 37°C under acidic conditions (0.2 M potassium acetate buffer, pH 4.4) (**38**).

ThT fluorescence binding. hTTR amyloid fibril formation was assessed by Thioflavin T (ThT) fluorescence binding assay. To the reaction mixture of hTTR with subtilisin (400 μl) in TBS buffer, pH 7.4, 5 mM $CaCl_2$, were added 100 μl of a ThT stock solution (100 μM) in the same buffer, to a final concentration of 20 μM. After 1-h incubation at 25°C, samples were excited at 450 nm and the emission recorded in the 465-650 nm range, with excitation/emission slits of 3/10 nm.

CaCo-2 permeability assay

Permeability of the intestinal epithelium to subtilisin was estimated *in vitro* by challenging a monolayer of Caco-2 (human epithelial colorectal adenocarcinoma) cells with the fluorescein-labelled enzyme, both in its active (FTC-subtilisin) and inactivated (FTC-PMS-subtilisin) form.

Briefly, Caco-2 cells were seeded on three Transwell permeable inserts (1.0 cm^2 growth surface area, 0.4 μm pore size) in a 12-wells sterile plate, using DMEM medium added with 20% (v/v) fetal calf serum and 1% (w/v) penicillin and streptomycin. After 14 days, the formation of cellular monolayers was assessed by Transepithelial Electrical Resistance (TEER) measurements, and DMEM was replaced with Opti-MEM medium. After confluence of the cells, aliquots (0.2 μM, 400 μl) of catalytically active FTC-subtilisin or inactivated FTC-PMS-subtilisin were added to the apical chamber of the Transwell inserts. After 7-h incubation at 37°C, protein translocation across the Caco-2 cells epithelium was evaluated on a 50-μl aliquot withdrawn from the basolateral compartment, by exciting the samples at 488 nm and measuring the fluorescence intensity at 535 nm on a Victor X2 (Perkin-Elmer, CA, USA) 96-wells plate reader. Subtilisin translocation was quantified using a calibration curve obtained with known concentrations of labelled enzyme, allowing to relate fluorescence intensities with the concentration of labelled-subtilisin. Blank experiments were performed under identical experimental conditions, in the absence of subtilisin.

Computational methods

Accessible surface area (ASA) calculations were carried out on the X-ray structure of the recombinant tetrameric hTTR complexed to retinol-binding protein, RBP, (1rlb) (**39**) after removal of RBP coordinates. The software program POPS, available on-line at the website www.mathbio.crick.ac.uk (**40**), was used for ASA calculations, with a water molecule probe radius of 1.4 Å. The crystallographic B-factor plot was generated using the program What If, available on-line at the website www.swift.cmbi.umcn.nl (**41**). Images were generated using the program UCSF Chimera vs. 1.12 (**42**).

RESULTS AND DISCUSSION

Purification and characterization of human plasma TTR

hTTR was purified to homogeneity from human plasma (100 ml) in three steps, as previously described (**33**), with some modifications. Briefly, in the first step, a hTTR enriched extract was obtained by precipitating most of the plasma proteins with an aqueous 5.5% phenol solution, with a minimal loss of hTTR that remained in solution. After centrifugation, the supernatant was extensively dialysed to eliminate excess phenol. The extract was then fractionated by Ion-Exchange chromatography on a Q-Sepharose column (**Figure 1A**) and the collected fractions were analysed by reducing SDS-PAGE (**Figure 1B**). The Q-Sepharose elution profile is quite simple, showing: i) a minor peak (1), eluting at low ionic strength and containing protein components at 7 and 40 kDa that are unrelated to hTTR molecular weight (~14 kDa), ii) a shoulder at higher NaCl (peak-2), containing

higher molecular weight components (60-150 kDa), and a major peak, eluting at ~ 0.4 M NaCl, containing the hTTR at 14 kDa, a minor component at 150 kDa and a faint band at 34 kDa, corresponding to the hTTR dimer which is known to be still present even under the denaturing conditions of SDS-PAGE sample preparation (**5**). The hTTR-containing fractions from Q-Sepharose chromatography were then concentrated by ultra-filtration and loaded onto a SEC Superose-12 column (**Figure 1C**). Fractions were analysed by reducing SDS-PAGE. The chromatogram shows a minor peak (1), eluting after 7 min and containing the high-molecular weight components at ~150 kDa, and a major peak (2), eluting after 12 min and containing the highly homogenous band of hTTR migrating at 14 kDa. Notably, peak-2 also contains the weak band of hTTR dimer at 34 kDa (**Figure 1C, *Inset***). The purity of the final hTTR preparations was always > 98%, as estimated by densitometric analysis of the polyacrylamide gel bands after Coomassie staining, while the purification yields were never < 35%, considering an average hTTR plasma concentration of 0.2 mg/ml.

The homogeneity of purified hTTR was further checked by RP-HPLC using an analytical C4 column, eluted with an aqueous/TFA-acetonitrile gradient. The RP-HPLC profile in **Figure 1D** documents remarkable heterogeneity, in keeping with earlier results obtained on plasma purified hTTR (**43**). Fractions were collected and analyzed by high-resolution mass spectrometry (MS) (**Figure 1E**). As already reported in earlier work (**44**), Cys-10 in hTTR was found to undergo extensive chemical modification and that the unmodified form (mass peak **5:c** in **panel 1E**) accounts for only about **5%** of hTTR isoforms (**Figure 1F**). Notably, the molecular weight of the unmodified form almost perfectly matches the theoretical mass value deduced from the hTTR amino acid sequence, with a Δm of -0.2 a.m.u. The base peak in **Figure 1E**, i.e. mass peak 4:h, accounts for about **22%** of the abundance of hTTR isoforms and has been assigned to hTTR with Cys10 forming a disufide bridge with a free cysteine. All the chemical modifications identified in our hTTR preparations are reported in **Figure 1F**.
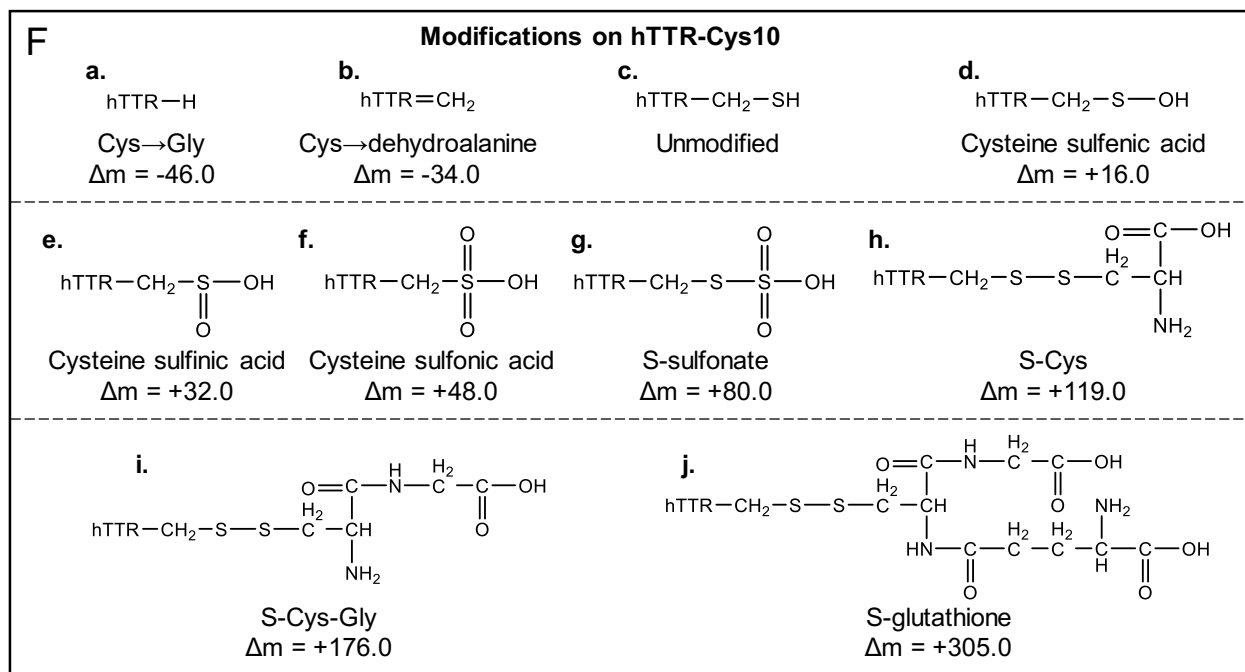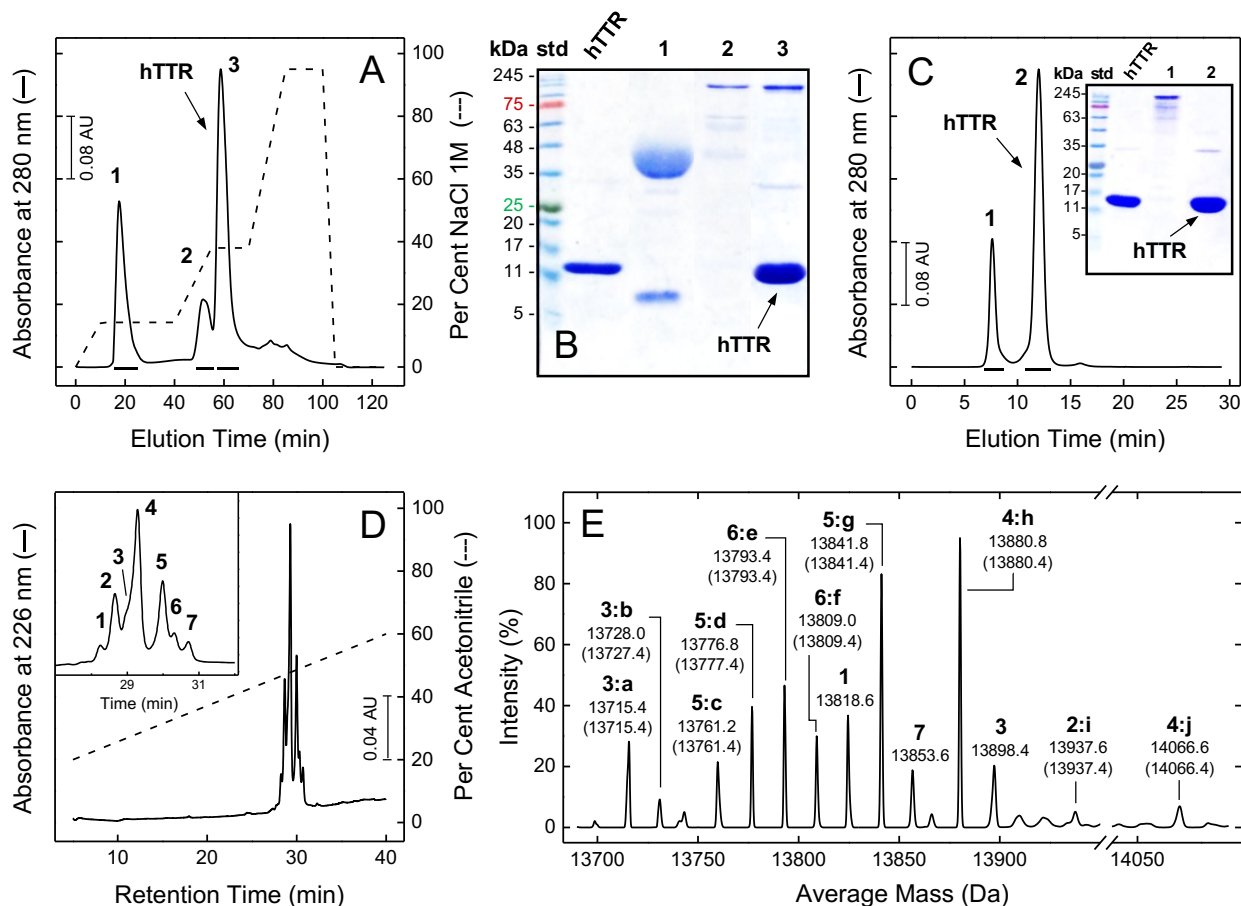
Figure 1. Purification and chemical characterization of human plasma hTTR. (**A**) Anion exchange chromatography. After phenol precipitation and centrifugation, the supernatant solution containing hTTR was loaded onto a Q-Sepharose column, equilibrated with 10 mM Tris-HCl, pH 7.4 and eluted with a gradient of NaCl (---) at a flow rate of 1.0 ml/min. (**B**) Reducing SDS-PAGE (4-12% acrylamide) analysis of the fractions 1, 2, and 3 (10-µl aliquots) eluted from the Q-Sepharose column in panel A; std: molecular weight protein standard; hTTR: commercial hTTR from human plasma. (**C**) Size exclusion chromatography. An aliquot of fraction 3 in panel A was loaded onto a Superose-12 column, eluted with 5 mM Tris·HCl buffer, pH 7.4, 0.15 M NaCl, containing 5 mM CaCl$_2$. ***Inset***, Reducing SDS-PAGE (4-12% acrylamide) analysis of the fractions (10-µl aliquots) eluted from the Superose-12 column in panel C. (**D**) RP-HPLC analysis of purified hTTR. An aliquot (20 µg) of fraction 2 in panel C was loaded onto an analytical C4 column, eluted with a linear acetonitrile-0.078%TFA gradient (---) at a flow-rate of 0.8 ml/min. ***Inset***, Close-up view of the RP-HPLC chromatogram. The numbers near the chromatographic peaks indicate the fractions that were collected and further analysed by mass spectrometry. (**E**) Deconvoluted mass spectrum of hTTR purified by SEC, as in panel C. An aliquot (1 µg) of fraction 2 was added with 1:1 water:acetonitrile solution (10 µl) containing 1% (v/v) formic acid and loaded onto a Xevo G2S Q-TOF mass spectrometer. The numbers and letters near the mass peaks indicate the elution order of each species in the RP-HPLC chromatogram in panel D (Inset) and the corresponding chemical modification reported in panel F, respectively. For instance, the notation **5:g** identifies the species eluting as peak **5** in panel D and containing the modification **g** at Cys10, i.e. the S-sulfonate derivative. Mass values are reported as average mass and the numbers in parenthesis refer to the theoretical values of each hTTR species. (**F**) Chemical modifications of hTTR at Cys10, as reported (**43**). Δm values refer to the mass differences existing between each modified hTTR species and the unmodified hTTR.

The oligomeric state and size of purified plasma hTTR was assessed by analytical SEC (**Figure 2A**) and Dynamic Light Scattering (DLS) (**Figure 2B**). hTTR eluted from a high-resolving Yarra SEC-3000 column as a single, sharp and symmetrical peak and, after proper calibration of the column with protein standards, a molecular weight of 57±3 kDa was estimated, thus confirming the tetrameric nature of hTTR. Likewise, DLS measurements allowed us to estimate a hydrodynamic radius (R$_h$) of 3.8 nm for hTTR, very close to that determined earlier (**45**). The molecular size distribution was expressed as %Mass and a single, mono-dispersed, hTTR species was found with an abundance of 99.9% a polydispersity index of 24.6%. However, when the size distribution was expressed as %Intensity, another component with a R$_h$ of 82 nm was found. Although this large component only accounts for about 0.1% of hTTR molecules in the sample, it scatters incident light much more intensely than smaller oligomers. DLS data indicate that purified plasma hTTR predominantly exists as a monodispersed tetramer. Nevertheless, very small amounts of large hTTR polymers are also present in solution.
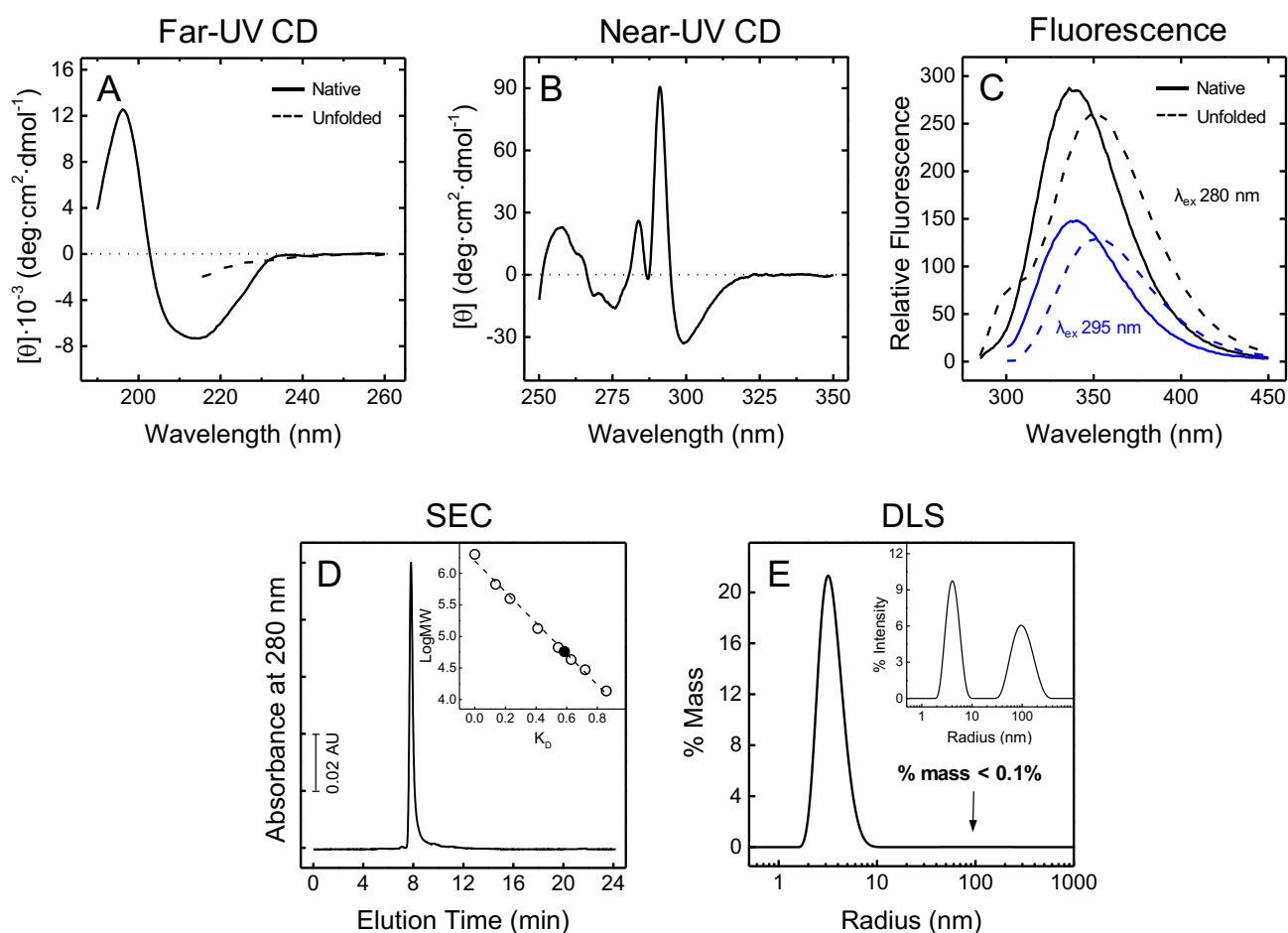
Figure 2. Conformational characterization and oligomerization state of purified hTTR. (**A**, **B**) Circular dichroism spectra of purified hTTR in the far- (**A**) (0.1 mg/ml) and near-UV (**B**) (1.5 mg/ml) region, under native and denaturing conditions. Fluorescence spectra of purified hTTR (25 μg/ml), under native and denaturing conditions, after excitation at 280 nm (black lines) and 295 nm (blue lines). All measurements were carried out at 25.0 ± 0.1°C, after baseline subtraction, under native (━, 10 mM sodium phosphate buffer, pH 7.4) and denaturing (---,10 mM sodium phosphate buffer, pH 7.4, 7 M Gnd-HCl) conditions. (**D**) SEC analysis of hTTR. An aliquot (10 μl) of a purified hTTR stock solution (1 mg/ml) was loaded onto a Yarra SEC-3000 column, eluted with 20 mM Tris-HCl buffer, pH 6.8, 0.15 M NaCl at a flow-rate of 0.6 ml/min. (***Inset***) The apparent molecular weight of hTTR (●) was obtained using a calibration curve with standard proteins (○): blue dextran (2.000 kDa), thyroglobulin (669 kDa), apoferritin (443 kDa), BSA dimer (134 kDa) and monomer (67 kDa), ovoalbumin (43 kDa), carbonic anhydrase (29 kDa), and RNase-A (13.7 kDa). A molecular weight of 57 ± 3 kDa was estimated for hTTR, consistent with the protein tetrameric structure. (**E**) DLS analysis of hTTR. Prior to analysis, hTTR samples (1 mg/ml, 50 μl) were equilibrated for 30 min at 25°C in 5 mM Tris·HCl buffer, pH 7.4, 0.15 mM NaCl. DLS data are expressed as % mass size distribution, with a R_h = 3.8 ± 1.0 nm and % PD = 24.6. (**Inset**) DLS spectrum of hTTR is reported as % intensity size distribution. An additional component is present, with a R_h = 82.1 ± 37.2 nm and % PD = 41.5.

The spectroscopic characterization of hTTR was carried out by far- and near-UV circular dichroism (CD) and fluorescence spectroscopy, after excitation at 280 and 295 nm, either under native and denaturing conditions. CD in the far-UV region provides key information on the secondary structure content of proteins (**46**). The far-UV CD spectrum of hTTR under native conditions resembles that of a protein containing a high β-sheet content, with a minimum centered at 214 nm and a maximum at 198 nm (**Figure 2C**). Analysis of the CD spectrum with the BestSel software (**37**) yielded a β-sheet content of 42%, 10% α-helix, and 48% irregular structure. These values are comparable to those deduced from the crystallographic structure of hTTR (1dvq), 49% β-sheet, 4% α-helix and 47% irregular structure (**47**). The CD spectrum of hTTR in the near-UV display unique features, with a minimum centered at 300 nm and a strong positive band at 291 nm (**Figure 2D**). The latter absorption can be assigned to the contribution of the two Trp-residues, namely Trp-41 and Trp-79 which are embedded into rigid and asymmetric environments in hTTR structure (**5**). The fluorescence spectrum of hTTR, recorded under native conditions, displays a λ_{max} at 337 nm, suggesting that the two Trp-residues are located in a region of medium polarity (**Figure 2E**). After protein denaturation with 7 M Gnd-HCl, the λ_{max} value becomes red-shifted to 351 nm and the contribution of Tyr-residues appear as a distinct shoulder at 303 nm, indicating that in the folded hTTR structure there is an efficient energy transfer between the five Tyr-residues and the two Trp-residues, which is lost in the denatured state.

Proteolysis of human plasma TTR

Starting from the seeding work of Bellotti and co-workers (**23**), here we decided to screen several different proteases for their ability to cleave human purified hTTR under static conditions, i.e. in the absence of shear stress, and generate amyloidogenic fragments. To this aim, natural hTTR was incubated with digestive (i.e., trypsin and chymotrypsin), coagulative (i.e. αT, FVIIa, FIXa, FXa, FXIa), fibrinolytic (i.e. plasmin), and neutrophil (i.e., elastase, cathepsin-G and proteinase-3) proteases, using an enzyme:substrate ratio of 1:20, in TBS-CaCl$_2$ pH 7.4 for 24 h at 37°C. The proteolytic mixtures were analysed by reducing SDS-PAGE. The same procedure was used to check the hTTR-cleaving properties of some bacterial proteases, including subtilisin and V8 protease from *S. aureus*, two serine proteases secreted from *Bacillus subtilis* and *Staphylococcus aureus*, respectively, and neutral protease (NP) and thermolysin (TLN), two zinc-dependent metalloproteases secreted from *B. subtilis* and *B. thermoproteolyticus*, respectively. The proteolytic enzymes we have tested in this work cover a wide range of substrate specificities, whereby trypsin and V8 protease display strict specificity for basic and acidic residues, respectively, at the primary specificity site (P1). Likewise, coagulative and fibrinolytic proteases display even narrower substrate specificity for basic

amino acids preceded by unique sequence patterns. Conversely, chymotrypsin, neutrophil proteases, and bacterial protease all have quite a broad specificity for apolar amino acids of different size (**48**).
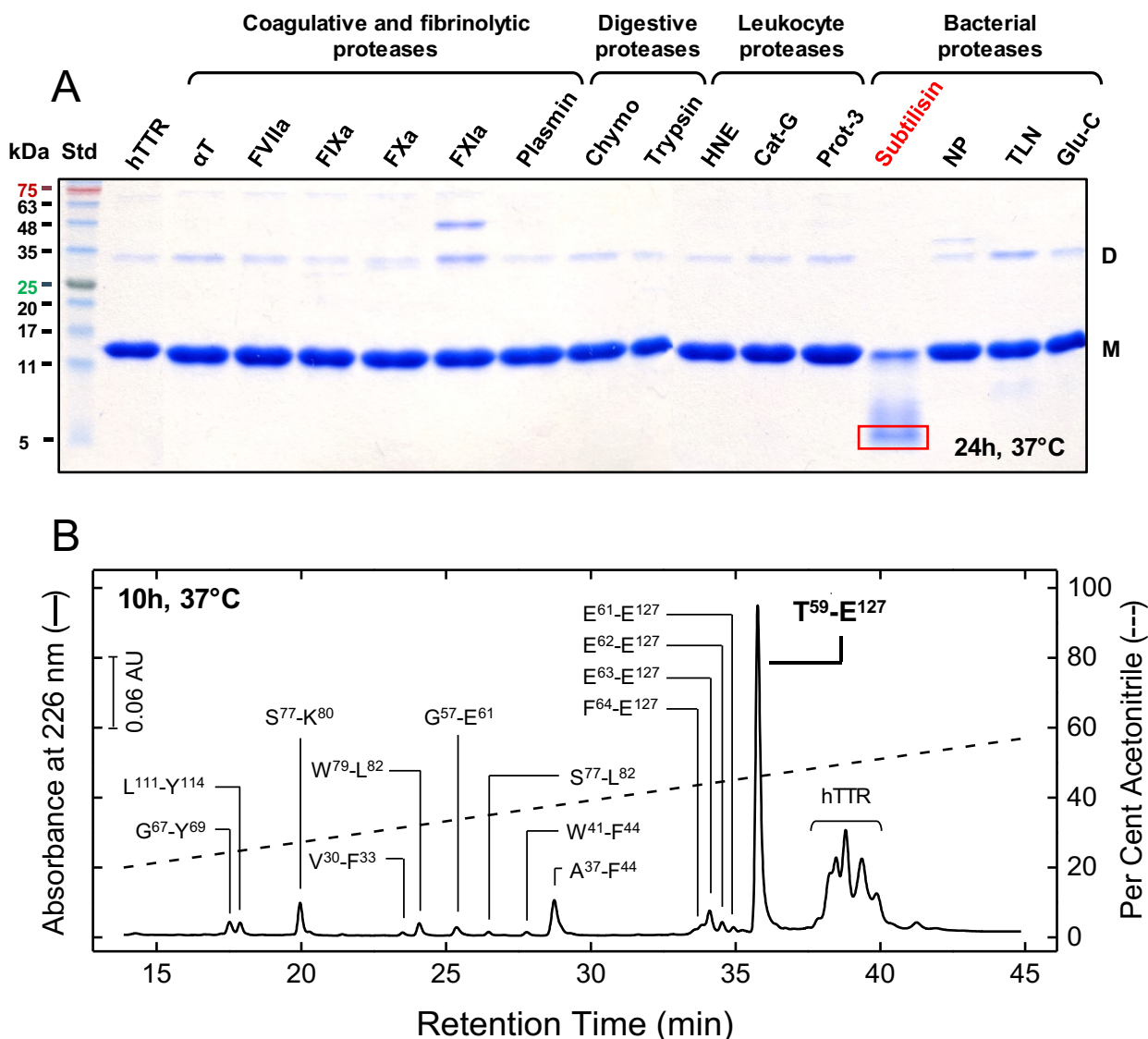
Figure 3. Proteolysis of hTTR by different proteases. (**A**) hTTR (1 mg/ml) was reacted at 37°C in TBS pH 7.4, containing 5 mM CaCl₂, with different proteases at an enzyme:hTTR ratio of 1:20 (mol/mol). After 24-h reaction, the proteolysis mixtures were analysed by reducing SDS-PAGE (4-15% acrylamide) and Coomassie stained. hTTR was resistant to all proteases tested, except to subtilisin. Gels bands corresponding to the monomeric (M) and dimeric form (D) of hTTR are indicated. Shallow bands at molecular weights higher than hTTR dimmers are due to the proteases added. (**B**) RP-HPLC analysis of the proteolysis reaction of hTTR with subtilisin. The reaction was conducted as in **panel A**. After 10-h reaction, the proteolysis mixture was acid quenched and fractionated on an analytical C18 column. Fractions were collected and analysed by high-resolution mass spectrometry, allowing to establish the chemical identity of the peptide material eluted in correspondence of the chromatographic peaks. Small fragments were identified in most cases. Of note, the fragment eluting with the major chromatographic peak was identified as Leu59-Glu127 peptide (7757.4 Da) and was found to be resistant to further proteolysis.

From the electrophoretic analyses reported in **Figure 3A**, among the 15 proteases tested, only subtilisin proved to cleave plasma hTTR under static conditions, generating a shorter fragment at ~7 kDa, whereas it seems that all other proteases failed to cleave hTTR. To better characterize the proteolytic products, hTTR-subtilisin proteolysis reaction was analysed by RP-HPLC combined with MS. The data reported in **Figure 3B** allowed us to conclude that, despite the broad substrate specificity of subtilisn, hTTR is attacked by far most efficiently at the single peptide bond Leu58-Thr59 (**Figure 5A**), generating the C-terminal fragment hTTR(59-127), which was quite resistant to further proteolysis up to 24 hours. Conversely, the complementary N-terminal fragment hTTR(1-58) could not be isolated, most likely because, once formed, it was suddenly degraded to smaller fragments eluting with the void volume of the RP-HPLC column.
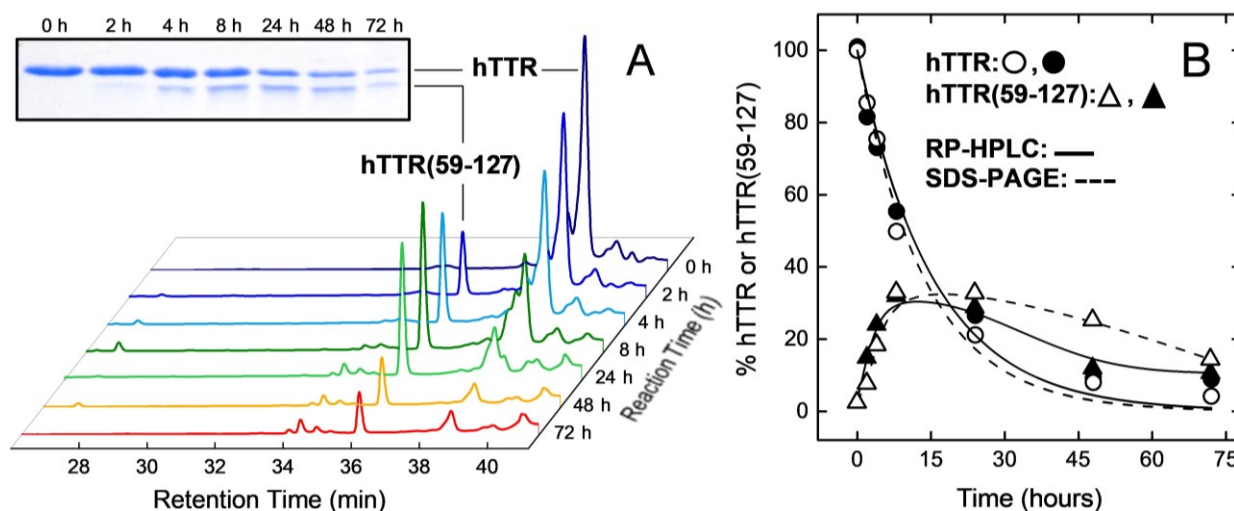
Figure 4. Time-course analysis of hTTR proteolysis by subtilisin. hTTR (1 mg/ml) was reacted in TBS, pH 7.4, containing 5 mM CaCl$_2$, with subtilisin (0.9 μM) at an enzyme/hTTR ratio of 1:20 (mol/mol) at 37°C. At increasing time points, the proteolysis mixtures were acid-quenched and aliquots (20 μg) analysed by RP-HPLC and SDS-PAGE. (**A**) RP-HPLC waterfall plot of hTTR proteolysis by subtilisin. Aliquots of the reaction mixture were loaded onto a C18 analytical column and eluted with a linear aqueous acetonitrile-0.1% TFA gradient from 10% to 45% in 30 minutes, at a flow rate of 0.8 ml/min. The absorbance of the effluent was recorded at 226 nm. (***Inset***) SDS-PAGE (4-20% acrylamide) analysis was carried by loading aliquots (5 μg) of the reaction mixture under reducing conditions, followed by Coomassie staining. (**B**) Time-course plot of hTTR degradation (●, ○) and hTTR(59-127) generation (▲, △) monitored by RP-HPLC (—) or SDS-PAGE (---). Data points were obtained by integration of the chromatographic peak areas or by densitometric analysis of the gel bands in **panel A**. The data relative to hTTR proteolysis were fitted with **eq. 1**, to yield an observed, cumulative kinetic constant, k, of hTTR hydrolysis of $k = 1.6 \pm 0.2 \times 10^{-5} \cdot s^{-1}$ for both chromatographic and electrophoretic data. The fitting curves relative to hTTR(59-127) generation are only intended to help the reader to follow the data points.
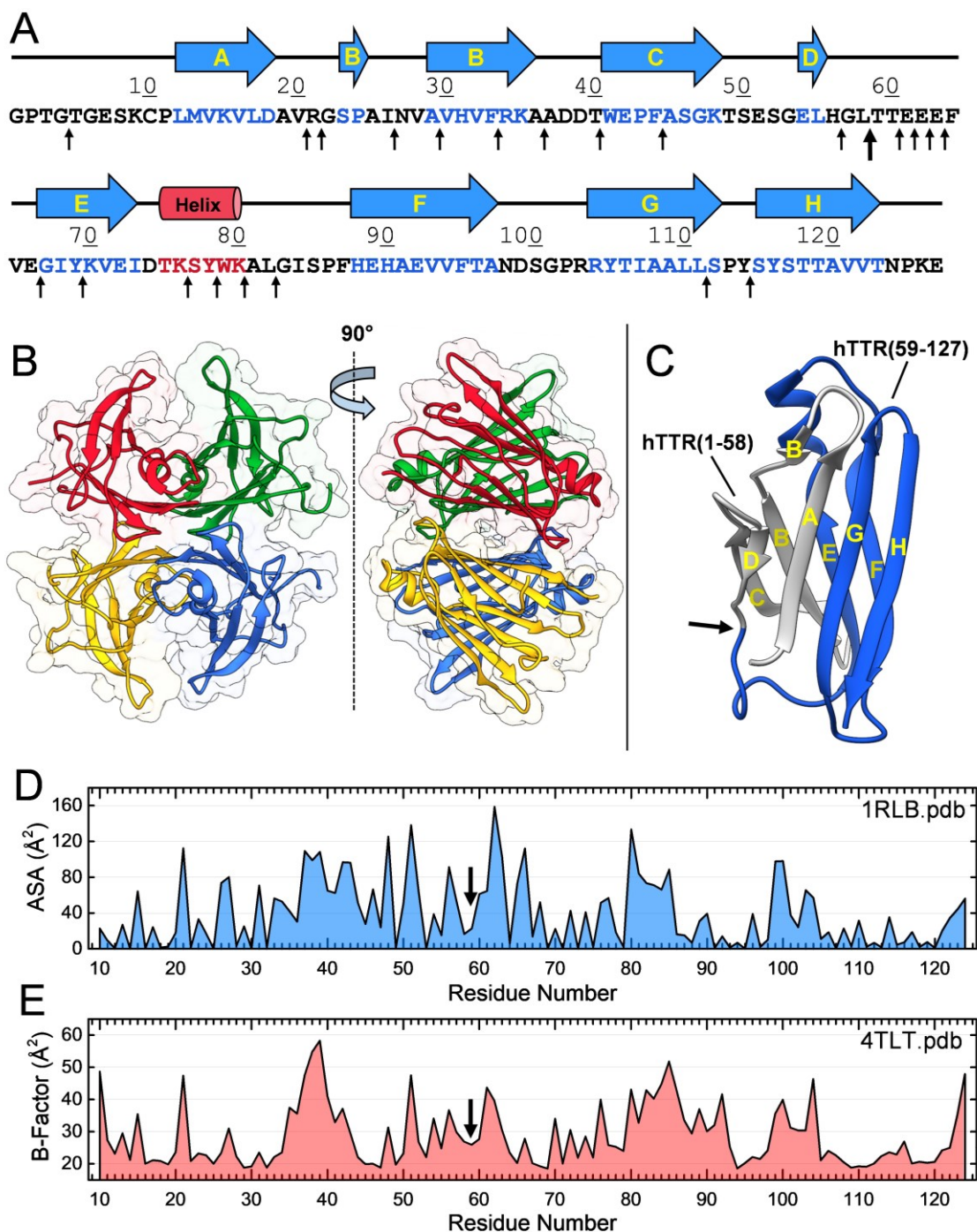
Figure 5. Schematic representation of the subtilisin cleavage site on hTTR. (**A**) Amino sequence and secondary structure of hTTR monomer. Vertical arrows indicate the cleavage sites, as reported in **Fig. 3B**. The scissile Leu58-Thr59 bond is identified with a thicker arrow. (**B**) Ribbon drawing of the threedimensional structure of tetrameric hTTR (1rlb), complexed to the retinol binding protein (RBP). The coordinates of RBP have been digitally removed. The arrows indicate the subtilisin cleavage site on each subunit. (**C**) Close-up view of hTTR monomer (4tlt). The arrow indicates the cleavage site Leu58-Thr59 for subtilisin (scissors). The resulting C-terminal fragment hTTR(59-127) (blue ribbon) is resistant to further proteolysis, whereas the N-termiinal region 1-58 (grey ribbon) is extensively degraded by subtilisin. (**D**) Accessible surface area and (**E**) *B*-factor flexibility plot of hTTR tetramer (4tlt). The vertical arrow indicates the peptide bond Leu58-Thr59.

The time-course kinetics of hTTR proteolysis by subtilisin was monitored by RP-HPLC and SDS-PAGE, by integrating the area under the chromatographic peaks or by densitometric analysis of the gel bands (**Figure 4**). The residual amount of intact hTTR was plotted as a function of the reaction time and the data were interpolated with **eq. 1** describing a pseudo-first order reaction, allowing to extract an observed kinetic constant of hTTR cleavage. Notably, degradation of intact hTTR was not quantitatively accounted for by the concomitant generation of hTTR(59-127), likely because this fragment started aggregating/precipitating in solution or on the stationary phase of the RP-column.

Considered the broad substrate specificity of subtilisin action, the almost selective cleavage of hTTR at the Leu58-Thr59 bond might be explained taking into account that proteolysis occurs at exposed and flexible loop regions, whereas potential cleavage sites that are not accessible or embedded into rigid secondary structure elements are much more resistant to proteolytic attack. In the case of hTTR, the scissile bond is located in a region of non-regular secondary structure, i.e. in loop segment connecting β-strands D and E (**Figure 5B, C**). However, the cleavage site on hTTR is not particularly accessible or conformationally flexible, as documented by the plots of accessible surface area (ASA) (**Figure 5D**) and crystallographic B-factor (**Figure 5E**) of hTTR, where the B-factor is a measure of the segmental mobility of a give site in the protein crystal structure.

Probing aggregation of hTTR during proteolysis with subtilisin by turbidimetric and DLS measurements

The aggregation kinetics of hTTR(59-127) fragment, generated during proteolysis of hTTR by subtilsin, was monitored using two different spectroscopic signals, i.e. turbidity and DLS (**Figure 6A,B**). The increase of the turbidimetric signal, expressed as the $A_{260\,nm}/A_{280\,nm}$ ratio, is representative of the formation of large aggregates, which are known to scatter the incident light more intensely at shorter wavelengths. In DLS analysis, the time-dependent fluctuations of scattered light from molecules of different size in solution is measured and from the rate of these fluctuations the translational diffusion coefficient (D) is determined. The hydrodynamic radius (R_H), defined as the radius of a hard sphere that diffuses at the same rate as that of the molecule considered, is then derived from the Stokes-Einstein equation, $R_H = kT/6\pi\eta D$, where k is the Boltzmann constant, T is the absolute temperature and η is the solution viscosity. From DLS analysis, it is also possible to calculate the percent polydispersity (%PD), a parameter describing the width of the particle size distribution of a protein in a given sample.

At fixed time points (0 – 72 h), aliquots (50 µl) of hTTR-subtilisin proteolysis mixture (1 mg/ml) were withdrawn and immediately stored at -20°C for turbidimetric and DLS measurements. The data in **Figure 6A,B** indicate the formation of large hTTR aggregates after 24-h reaction and

aggregation gradually increased at longer incubation times. The formation of aggregates was also documented by DLS measurements (**Figure 6C, Table 1**), showing that after 24-h incubation of hTTR alone, without subtilisin, the size of the tetrameric structure (R_h = 3.8 nm), measured immediately after sample preparation (peak A), was only slightly increased (R_h = 4.3 nm). Conversely, the size of the species at 82 nm (peak B), assigned to the presence of large aggregates in equilibrium with tetramer, increased up to 110 nm. Importantly, DLS analysis reveals that the size of the low-molecular weight species (A) is further increased to 5.1 nm, with a concomitant increase of %PD, while the species at 82 nm (B) disappears and a much larger component at 640 nm (peak C) is generated. These data provide clear-cut evidence that the formation of large aggregates is caused by proteolysis of hTTR by subtilisin.
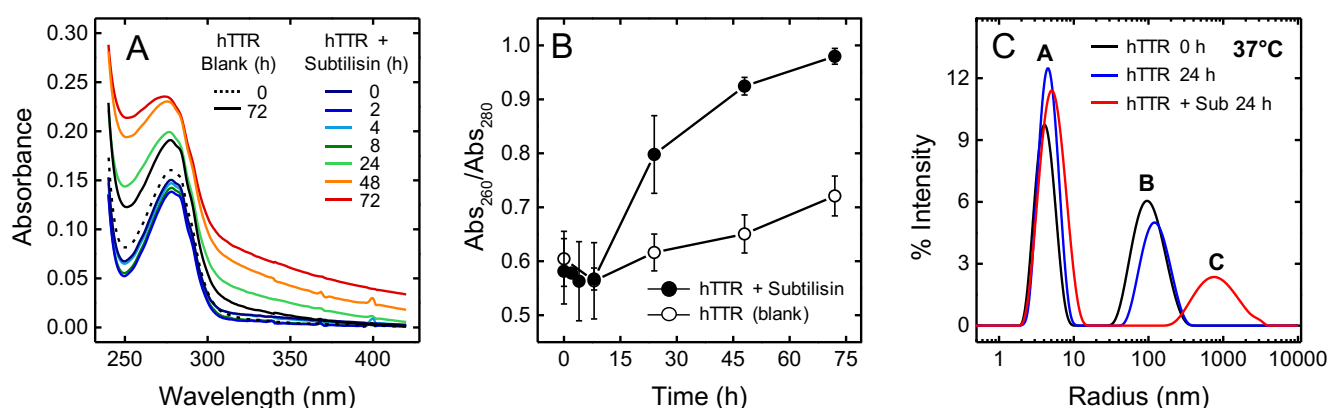
Figure 6. Time-course analysis of hTTR aggregation induced by subtilisin. hTTR (1 mg/ml) was treated at 37°C with subtilisin in TBS buffer, pH 7.4, containing 5 mM $CaCl_2$ at an enzyme:hTTR ratio of 1:20 (mol/mol). At time points, aliquots (50 µl) of the proteolysis reaction were withdrawn, diluted ten-fold with the same buffer and analysed by UV-Vis absorption spectroscopy (**A, B**) at 25°C and DLS at 37°C (**C**). (**A**) UV-Vis absorption spectra of the proteolysis reaction of hTTR with subtilisin at increasing reaction time. (**B**) Plot of the Abs_{260}/Abs_{280} ratio *vs.* time of a hTTR solution (0.1 mg/ml) in the presence (●) and absence (○) of subtilisin. The data points results from three different experiments, with error bars as the standard deviation. (**C**) DLS analysis of hTTR proteolysis by subtilisin after 24-h reaction (━). DLS traces of hTTR alone, after 0 (━) or 24-h (━) incubation are shown as controls. DLS data are reported as % intensity size distribution. For each trace, the values of R_h, %Intensity and %PD of the oligomeric/polymeric species A, B, and C were measured and reported in **Table 1**.

Table 1. DLS data of hTTR alone or in the presence of subtilisin

Peak	hTTR, 0 h			hTTR, 24 h			hTTR + Subtilisin, 24 h		
	R_h (nm) ± SD[a]	% Intensity	% PD	R_h (nm) ± SD	% Intensity	% PD	R_h (nm) ± SD	% Intensity	% PD
A	3.8 ± 1.0	53.3	24.6	4.3 ± 1.0	63.3	28.4	5.1 ± 2.0	75	35.7
B	82.1 ± 37.2	46.7	41.5	110.1 ± 62.0	36.7	48.2	-	-	-
C	-	-	-	-	-	-	640.7 ± 465.3	25	59.4

[a] SD: Standard Deviation

Probing hTTR amyloid fibril formation during proteolysis with subtilisin by Tioflavin T binding and Transmission electron microscopy

Whereas turbidimetric assays monitor the formation of protein aggregates, ThT assay is a specific method to detect amyloid fibrils (**49**) as ThT binds specifically to ordered amyloid fibrils, with a resulting strong increase of fluorescence quantum yield and a blue-shift of the λ_{max}. ThT is a small molecule that, only upon binding to fibrillar aggregates, gives strong fluorescence at 482 nm when excited at 450 nm. The enhancement of ThT fluorescence is caused by the immobilization of the C-C bond connecting the aniline and the benzothiazole rings upon binding to fibrillar structures containing a minimum of four consecutive β-strands (**50**). As observed with turbidimetric measurements, the data in **Figure 7A,B** indicate that after 24-h reaction of hTTR with subtilisin there is a strong increase (> 15-fold) of ThT emission intensity at 482 nm. The kinetics of ThT fluorescence exhibited a characteristic sigmoidal curve, which comprises an initial lag phase, followed by a rapid growth phase, and a final equilibrium phase. This trend is compatible with a nucleation-dependent polymerization model in which the lag phase corresponds to the nucleation step and the to the exponential part to fibril growth (**51**).

Finally, Transmission Electron Microscopy (TEM) was used to study hTTR fibril formation induced by subtilisin in TBS at pH 7.4 after 72-h reaction (**Figure 7C**). As a negative control, TEM micrographs of intact hTTR, taken under identical conditions, did not show the presence of any aggregate (**not shown**). As a positive control, TEM analysis of hTTR incubated for 72 h under mild acidic conditions (pH 4.4) was also carried out (**Figure 7D**). In both cases, a similar nodular morphology was observed, with irregular and wavy fibrils (50-100 nm long and 5-10 nm wide), resembling those already reported previously for hTTR under different experimental conditions (**13,52,53**).
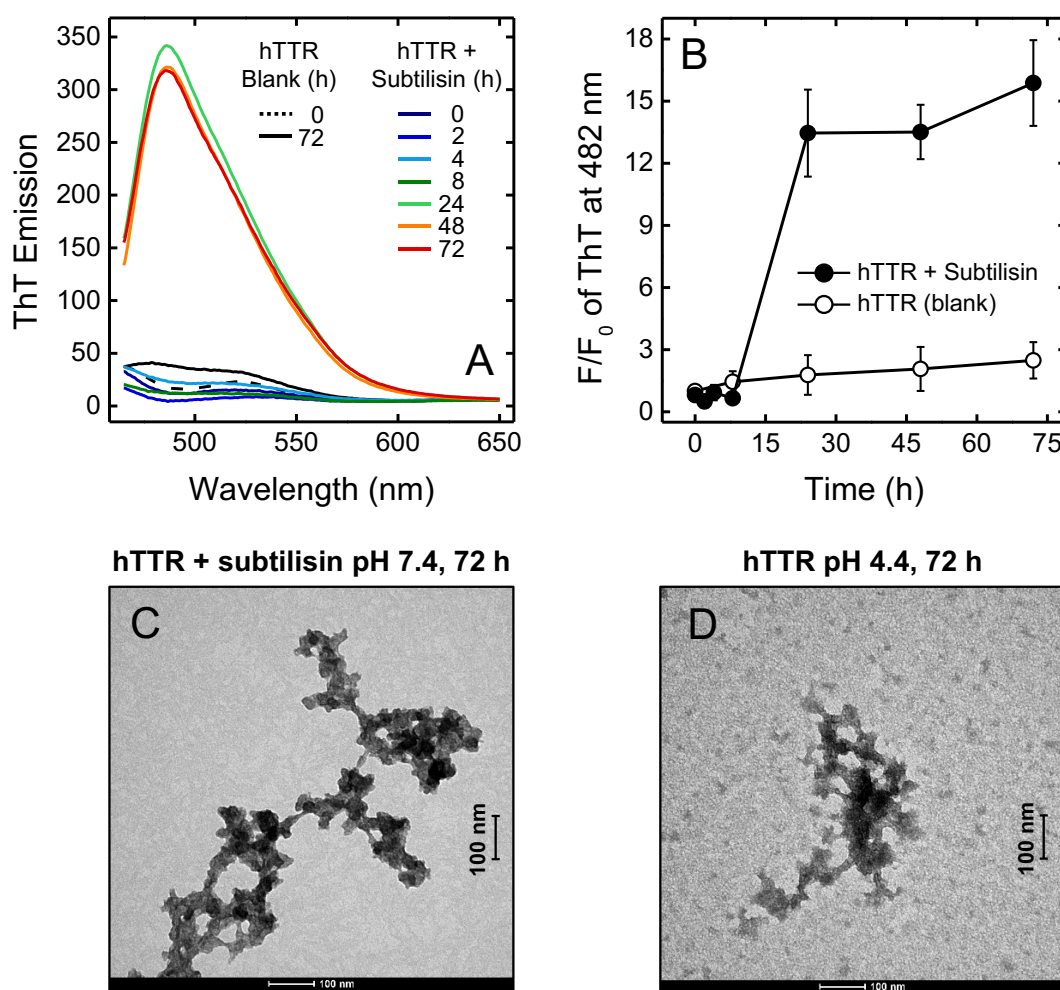
Figure 7. hTTR amyloid fibril formation during proteolysis with subtilisin. hTTR (**1 mg/ml**) was treated at 37 °C with subtilisin in TBS buffer, pH 7.4, 5 mM $CaCl_2$ at an enzyme:hTTR ratio of 1:20 (mol/mol). At time points, aliquots (50 µl) of the proteolysis reaction were withdrawn, diluted ten-fold with the same buffer, and analysed by ThT binding assay (**A, B**) and TEM (**C**). (**A**) Fluorescence emission spectra of ThT during proteolysis of hTTR (0.1 mg/ml) with subtilisin. At the indicated time points, aliquots of the proteolysis mixture were added with ThT (20 µM) and samples were excited at **450 nm** and 25 ± 0.1°C. (**B**) Time-course fluorescence intensity of ThT at 482 nm during subtilisin-induced proteolytis of hTTR (●). The data points results from the average of three different experiments, with error bars as the standard deviation. The time-course emission of ThT, in the presence of intact hTTR alone (without subtilisn), is reported as a control (O). The fluorescence signal is expressed as F/F_0, where F_0 is the emission intesity of ThT at time = 0 min. (**C**) Representative TEM micrograph of hTTR fibrils, generated after 72-h incubation of hTTR (**0.2 mg/ml**) with subtilisin at 37 °C. (**D**) For comparison, a representative micrograph of hTTR fibrils, generated after incubation of intact hTTR (**0.2 mg/ml**) under acidic conditions (0.2 M potassium acetate buffer, pH 4.4) for 72 h at 37 °C is also reported. The scale bar (100 nm) is indicated.

Production, purification, and amyloid formation properties of hTTR(59-127)

To investigate the putative amyloidogenic properties of hTTR(59-127), the fragment was purified to homogeneity by RP-HPLC, using a semi-preparative C18 column eluted with an aqueous/TFA-acetonitrile gradient (**Figure 8A**). The material eluted with the major chromatographic peak was collected, immediately frozen at -20°C for 2 h, and lyophilised in a SpeedVac concentrator at room temperature. Aliquots of the lyophilised sample were dissolved in 1:1 water:acetonitrile containing 1% formic acid, pH 2.0, or in SDS-PAGE reducing sample loading buffer for further analysis. The acidic sample was analysed by high-resolution MS, yielding an accurate mass of 7757.4 kDa, as reported above. When analysed by SDS-PAGE, hTTR(59-127) migrated as a single band at 10 kDa. TTR(59-127) fragment was then subjected to a spectroscopic characterization. Far-UV CD spectrum in native conditions (**Figure 8B**) displays a higher negative ellipticity compared to the full length hTTR, with a minimum centered at 205 nm and a broad shoulder at 218 nm. The overall shape changes significantly and does not match with any canonical secondary structure (α, β or mixed α/ β). The fitting curve obtained using BestSel software yielded a β-sheet content of 35%, 12% α-helix, and 53% irregular structure, whereas the secondary structure calculated staring from the crystallographic coordinates of the full-length hTTR (1dvq) were: 9% helix, 50% β-sheet, 41% irregular structure. The discrepancy suggests that the purified hTTR(59-127) fragment assumes a different conformational state with respect to the original one (when it is embedded into the intact protein). This conformational rearrangement could be explained by i) intrinsic propensity of the fragment to fold into different conformations, ii) assembly of multiple units of hTTR(59-127) into oligomers. The fluorescence spectrum of the fragment recorded under native conditions (**Figure 8C**) displays a λ_{max} at 341 nm, indicating that the unique Trp-79 is located in a medium-high polar region. After protein denaturation, the λ_{max} value becomes red-shifted (351 nm) with a distinct shoulder at 303 nm. The latter data was very similar to that obtained with the full-length protein, suggesting that the energy transfer phenomenon is attributable mainly to the Trp-79.
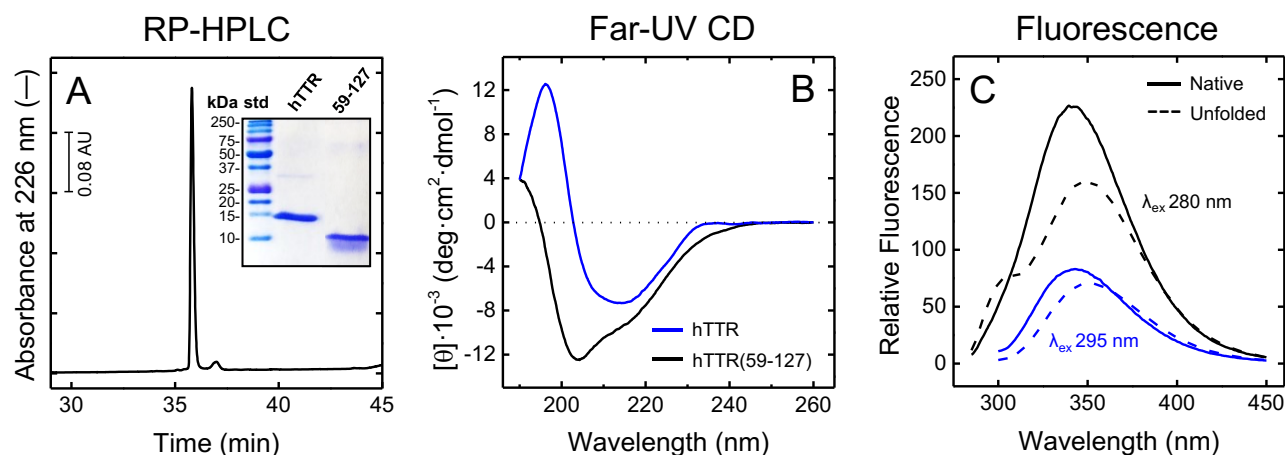
Figure 8. Characterization of purified hTTR(59-127) fragment. (**A**) RP-HPLC purity check of hTTR(59-127). After lyophilisation, an aliquot of purified fragment was dissolved in 10 mM phosphate buffer, pH 7.4 and immediately injected onto an analytical C18 column, eluted (0.8 ml/min) with an acetonitrile-0.1%TFA gradient from 10 to 45% in 30 min. (***Inset***) SDS-PAGE (4-20% acrylamide) analysis of purified hTTR(59-127) (5 μg) under reducing conditions and Coomassie staining. For comparison, purified intact hTTR was also analysed. (**B**) Far-UV circular dichroism spectra of full-length hTTR and hTTR(59-127) fragment. CD spectra and were recorded at a protein concentration of 0.1 mg/ml in 10 mM phosphate buffer, pH 7.4, at 25 °C. (**C**) Fluorescence spectra of hTTR(59-127) under native, 10 mM phosphate buffer, pH 7.4, (continuous lines) and denaturing, 10 mM phosphate buffer, pH 7.4, 7 M Gnd-HCl, (dashed lines) conditions. Samples (1.6 μM) were excited at 25 °C at 280 nm (black lines) and 295 nm (blue lines). All spectra were recorded immediately after dissolving the protein lyophilisate with phosphate buffer, as indicated.

After the spectroscopic characterization, we evaluated the propensity of the purified hTTR(59-127) fragment to aggregate and form fibrils. Intriguingly, immediately after resuspension, hTTR(59-127) revealed the presence of aggregates/fibrils, as documented by DLS, ThT binding assay, and TEM analysis (**Figure 9A, B, C**). With respect to the fragment within the proteolysis mixture, the fibril-forming ability of the purified hTTR(59-127) was remarkably higher and more ordered fibrils with a typical morphology (length: 200±50 nm; thickness: 20±50 nm) were detected. These data suggest that, during hTTR-subtilisin fibril formation, other factors may participate (such as full-length hTTR or Nt-Peptides) or at least interfere with the mechanism of fibril assembly.
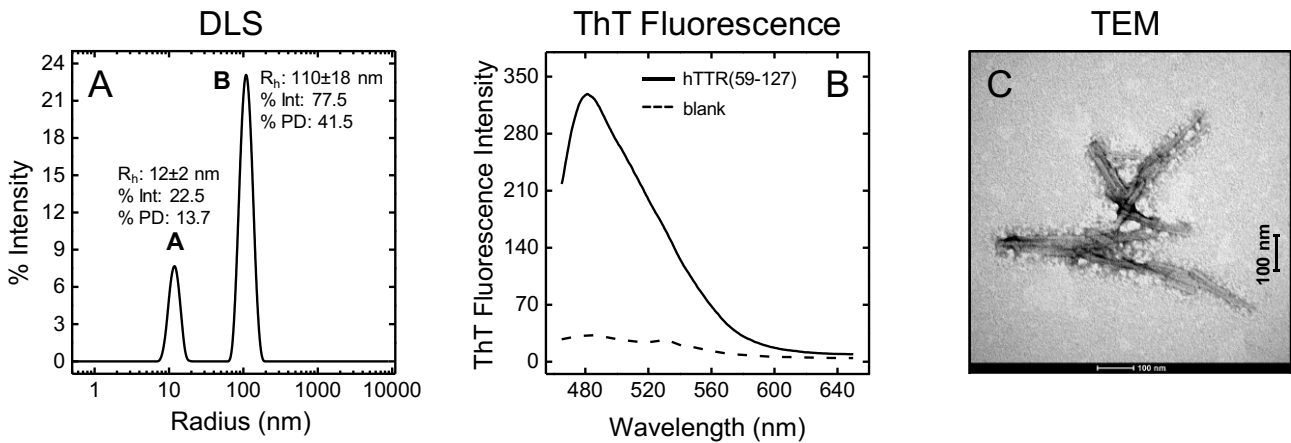
Figure 9. Analysis of hTTR(59-127) amyloid fibril formation. After lyophilisation, purified hTTR(59-127) was dissolved (0.23 mg/ml) in TBS, pH 7.4, 5 mM CaCl$_2$ at 25 °C and amyloid fibril formation was immediately tested by DLS, ThT binding assay (**B**), and TEM (**C**). (**A**) DLS analysis of hTTR(59-127) (0.23 mg/ml) was carried out at 25°C. DLS data are expressed as % intensity size distribution. For the polymeric species A and B, the values of R$_h$, %Intensity and %PD are reported. (**B**) ThT fluorescence emission in the presence (—) or absence (---) of hTTR(59-127). Measurements were carried out by incubating ThT (20 µM) with hTTR(59-127) (50 µg/ml) for 1 hour at 25°C and exciting ThT at 450 nm. (**C**) TEM micrograph of hTTR(59-127) at 0.6 mg/ml. The average length and diameter of hTTR(59-127) fibrils was estimated as 200 ± 50 nm and 20 ± 5 nm, respectively. The scale bar (100 nm) is indicated.

Translocation of FTC-subtilisin across CaCo-2 simulated intestinal epithelium

Once established that subtilisin is able to generate the amyloidogenic hTTR(59-127) fragment, we attempted to estimate its translocation through the gut-vascular barrier (GVB) from the gut lumen, where subtilisin is secreted by the commensal *B. subtilis*, to the bloodstream, where hTTR circulates. The intestinal epithelium, macroscopically shaped in *villi* and crypts, is composed of a single layer of polarized enterocytes connected by tight junctions, adherens junctions and desmosomes, thus ensuring the integrity of the physical barrier. Paneth cells, producing antimicrobial peptides and goblet cells, secreting mucin, complete the epithelium, which is covered by a thick protective mucus layer on the top, hosting the gut microbiota (**54,55**).

For our purposes, the GVB was simulated *in vitro* using Caco-2 cells, an immortalized human colon adenocarcinoma cellular line that differentiates into polarized enterocytes connected by tight junctions, with a well-defined brush border on the apical surface. When cultured on semipermeable supports (Transwell) fitting multi-wells culture plates, Caco-2 cells reach confluence (typically after 21 days), thus defining an apical and a basolateral chamber. Although Caco-2 monolayers present an overall lower complexity degree with respect to a natural epithelium (e.g. lacking of mucus, cytochrome P450 enzymes and secreted antimicrobial peptides, presence of unstirred buffer layer), yet the presence of tight junctions and of active transport proteins make them an excellent *in vitro* model to study intestinal absorption and permeability (**56**).

To estimate subtilisin ability to cross the GVB and to unravel its mechanism of translocation, Caco-2 monolayers were challenged with samples (0.2 μM) of either active or covalently inhibited protein. After 7 hours of incubation, about 10% of active (32 nM) and inactivated (18 nM) subtilisin were recovered from the basolateral slot (**Figure 10**). These comparable values indicate that subtilisin translocation is only partially mediated by the disruption of tight junctions and self-enhanced paracellular transport, while it mainly occurs through a passive route (**31**).
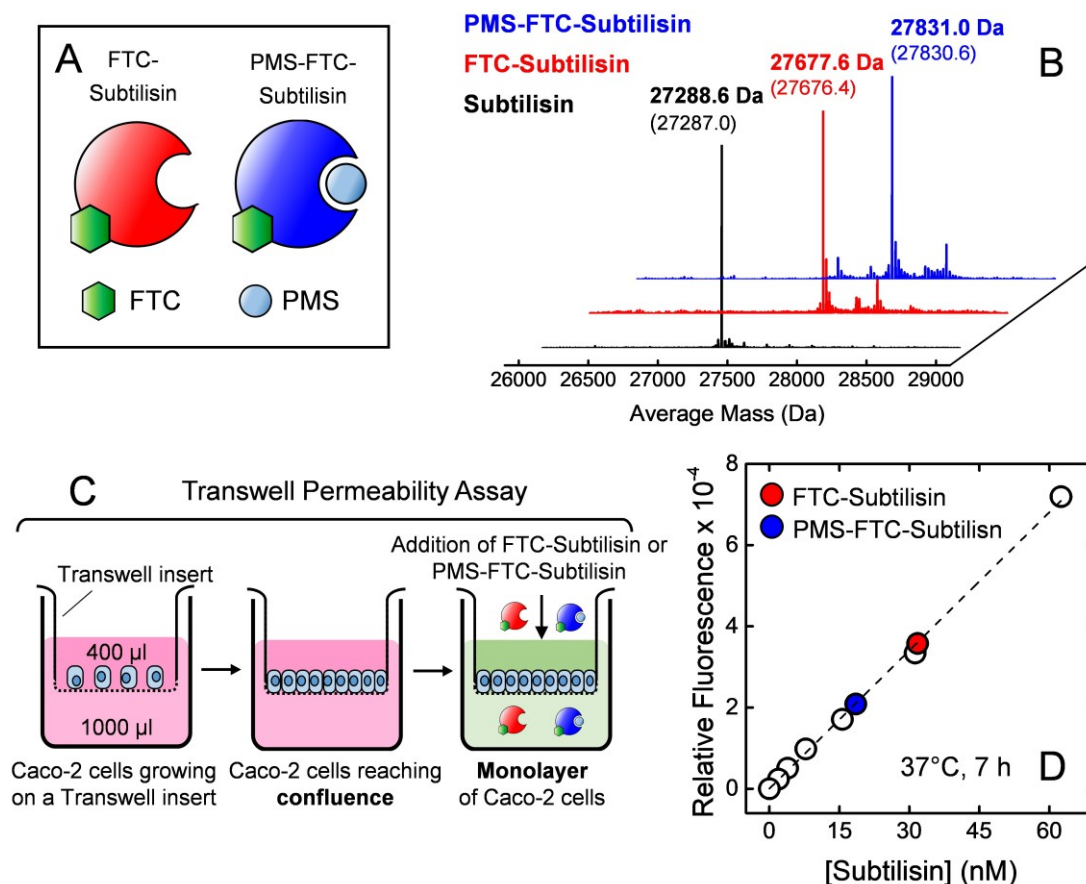
Figure 10. Caco-2 cells permeability assay of fluoresceinated subtilisin. (**A, B**) Derivatisation of subtilisin with fluorescein isothiocyanate (FITC) and phenylmethylsulfonyl fluoride (PMSF). The fluorescein thiocarbamoyl-derivative of subtilisin (FTC-Subtilisin) was prepared by reacting the enzyme (73 μM) with FITC (13 mM) for 3 h. Irreversible active-site inhibition of FTC-subtilisin was achieved by incubating FTC-subtilisin (0.5 μM) with PMSF (2 μM) for 2 h, to yield FTC-PMS-subtilisin. Both reactions were conducted at 25° in 0.1 M Na_2CO_3, pH 9.0. After extensive desalting to eliminate excess reagents, the purity and chemical identity of labelled subtilisin preparations was checked by RP-HPLC and mass spectrometry. The numbers in parenthesis in **panel B** refer to the theoretical average mass values of subtilisin derivatised with a single FTC- and a single PMS-moiety. (**C**) Schematic representation of Caco-2 cells permeability assay. Monolayers of Caco-2 cells on the Transwell permeable inserts (1.0 cm^2 growth surface area; 0.4 μm pore size) were prepared as detailed in the **Methods**. Subtilisin translocation was assessed by adding catalytically active FTC-subtilisin or inactive FTC-PMS-subtilisin (0.2 μM, 400 μl), in 10 mM HEPES, pH 7.4, 10 mM glucose, on the apical chamber and measuring the intensity of fluorescein emission in the basolateral chamber after 7-h incubation at 37°C. Blank experiments were carried out in the absence of subtilisin. (**D**) Quantification of subtilisin translocation. The concentration of translocated labelled subtilisins was determined using a calibration curve obtained with known concentrations of labelled enzyme (O). Samples were excited at 488 nm and the fluorescence intensity of labelled subtilisin was measured at 535 nm, after baseline subtraction. From the linear interpolation (---) of fluorescence data, an estimate of translocated FTC-subtilisin (●) and FTC-PMS-subtilisin (●) of 32 nM and 18 nM, respectively, was obtained.

Fibril formation of hTTR at physiological concentration and effect of diflunisal

Finally, in order to study the amyloidogenicity of subtilisin in a more physiological contest, we prepared an experiment in which hTTR is incubated at 0.2 mg/ml, which corresponds to its concentration in plasma. In parallel, we also probed the effect of diflunisal on the aggregation induced by subtilisin. (**57**). It was proposed that, upon binding to the thyroxine binding site, diflunisal kinetically stabilizes the hTTR tetrameric structure, preventing the dissociation and thus the release of the hTTR monomer, which is necessary to expose the buried aggregation-driving portion required for amyloidogenesis (**13,58**). For comparison purposes, the formation of aggregates was induced by lowering the pH to 4.4. In fact, it is known that the acidic environment promotes the disruption of the hTTR tetrameric form and the subsequent fibrillation. The aggregation was monitored by simple turbidity measurement at 400 nm after 72 h incubation at 37°C.

Our experimental data clearly demonstrate that subtilisin triggers fibril formation even at physiological hTTR concentration (**Figure 11**). The presence of fibrillar structures was also confirmed by ThT binding assay (data not shown). The amount of fibril formation, expressed as percentage was ~35% with respect to the acid catalysed sample, fixed as 100%. Surprisingly, the presence of diflunisal in the proteolysis mixture lowered the aggregation process to 8.5%, indicating that, beyond the cleavage operated by subtilisin, it is necessary that hTTR dissociates before starting aggregation. A close inspection of the crystallographic structure of hTTR bound to diflunisal (3D2T.pdb) revealed that the thyroxin pocket, in which diflunisal is located, is too far away from the cleavage site forming the hTTR(59-127) fragment. This simple observation excludes the possibility that diflunisal could interfere with the proteolysis. Kinetic measurements of hTTR proteolysis conducted in the presence of diflunisal confirmed that fragmentation occurs at the same rate. Thus, we propose that diflunisal, even if proteolysis occurs, somehow held together the two newly-generated fragments and prevent the exposure of the cryptic strands required for aggregation. This hypothesis is supported by the fact that diflunisal binds to hTTR at the dimer-dimer interface of the C-terminal level, more precisely through amino acids that belong to the strand G (A108, L110) and H (T119, V121) (**38**).
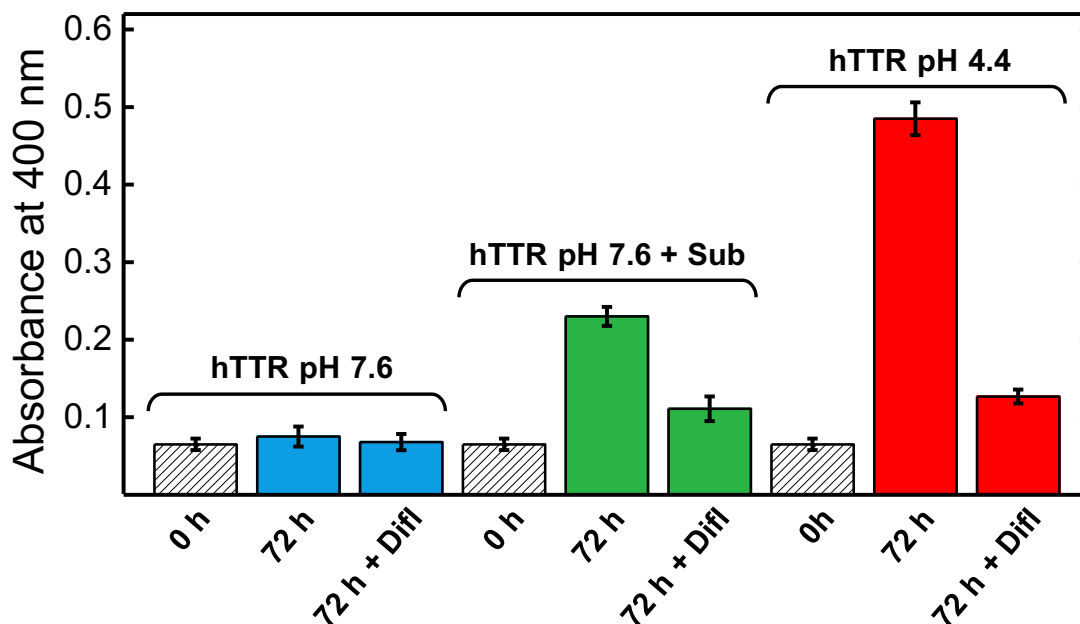
Figure 11. Effect of diflunisal on hTTR fibril formation induced by proteolysis with subtilisin. hTTR (**0.2 mg/ml, 3.6 μM**) was dissolved in 20 mM potassium phosphate buffer, pH 7.6, 0.1 M KCl, 1 mM EDTA and incubated at 37°C with subtilisin (0.18 μM) in the presence or in the absence absence of diflunisal (3.6 μM). After 72 h, fibril formation was determined by measuring the turbidimetric signal of the reaction mixture at 400 nm. For comparison, fibril formation obtained by incubating intact hTTR (**0.2 mg/ml**) for 72 h at 37 °C under acidic conditions (0.2 M potassium acetate buffer, pH 4.4) is also reported. Histograms are the average of three different experiments, with error bars as the standard deviation.

CONCLUSIONS

In this work, we show for the first time that, under naïve conditions (pH 7.4, 37°C), subtilisin cleaves hTTR at the peptide bond Leu58-Thr59, generating the fragment hTTR(59-127) which was resistant to further cleavage and formed amyloid-like fibrils in the proteolysis reaction mixture, as documented by turbidimetric analysis and ThT binding assay. Notably, a time-dependent increase of the turbidimetry, expressed as the A260nm/A280nm absorbance ratio, was observed along with a 15-fold increase of ThT. The amyloidogenicity was also confirmed under physiological hTTR concentration, and diflunisal was found to be effective in preventing aggregation. For the subtilisin-catalysed aggregates TEM analysis revealed a morphology quite similar to that obtained with full-length hTTR under acidic condition. hTTR(59-127) was purified to homogeneity by RP-HPLC and chemically characterized by SDS-PAGE and high-resolution mass spectrometry (7757.2±0.2 kDa). Purified hTTR(59-127) was dissolved in Tris-buffered saline, pH 7.4, and protein aggregates were detected by both turbidimetry or ThT binding assay. Analysis of hTTR(59-127) deposits by TEM revealed the presence of amyloid-like fibrils (length: 200±50 nm; thickness: 20±5 nm) much more ordered compared to those obtained from the hTTR-subtilisin mixture.
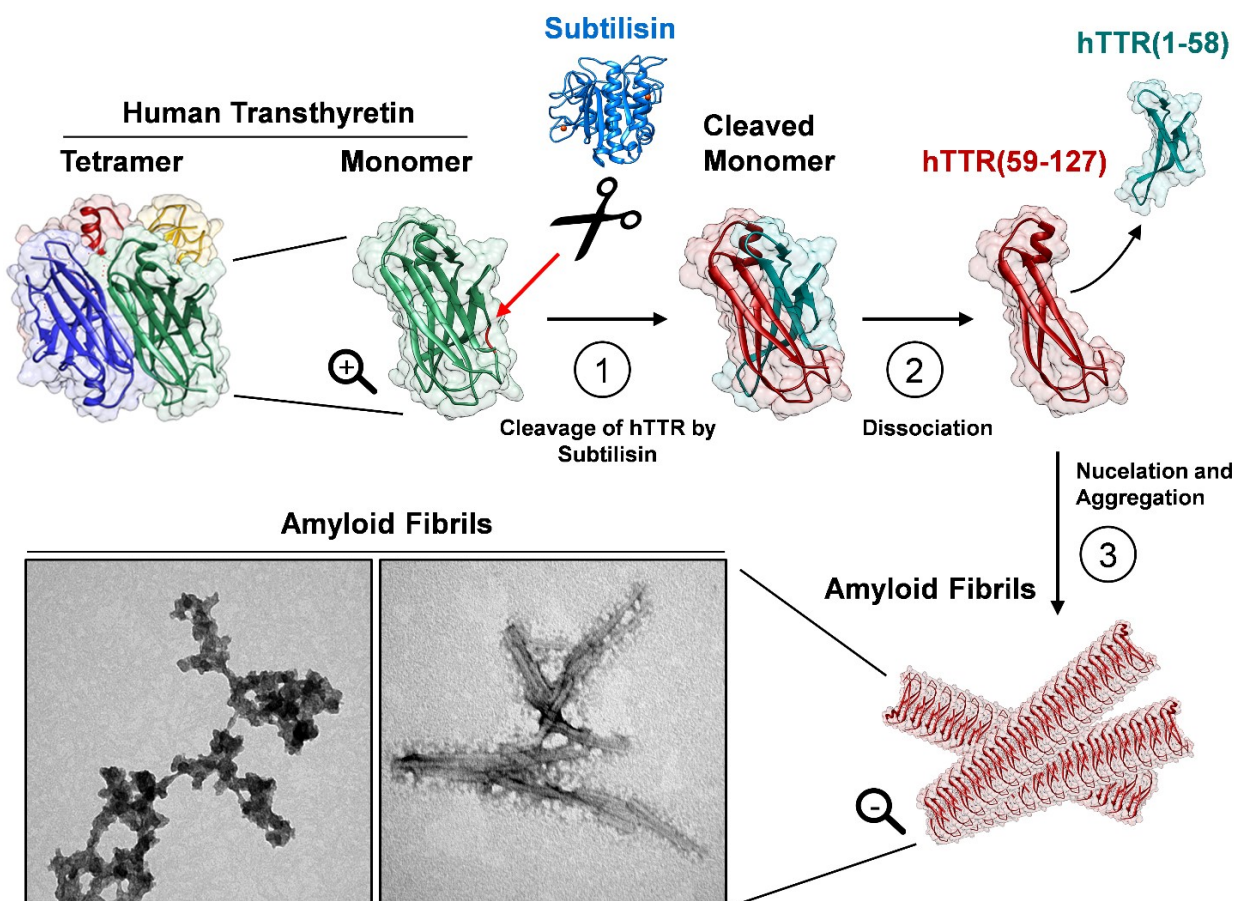
Figure 12. Amyloidogenesis of hTTR triggered by subtilisin. Schematic overview of the possible sequential events leading to hTTR amyloid fibril formation induced by proteolytic cleavage. 1) Subtilisin cleaves hTTR at peptide bond L58-T59, generating the amyloidogenic fragment hTTR(59-127). 2) The proteolytic cleavage facilitates the dissociation of the fragment from the tetrameric structure which in turn causes the exposure to the solvent of the F and G strands, aggregation-driving segments in hTTR. 3) Aggregation of hTTR(59-127). Newly-generated hTTR fragments as well as the full-length hTTR monomer could participate or interfere with the aggregation process.

The data reported here suggested that subtilisin induces hTTR aggregation by a multi-step mechanism (**Figure 12**). At first, subtilisin cleaves hTTR at the peptide bond L58-T59 generating the amyloidogenic C-terminal fragment T59-E127. This step is crucial, because it facilitates the dissociation of the tetrameric structure with the consequent exposure of the hTTR hydrophobic core. In this context, designing a specific subtilisin inhibitor could be a good strategy to prevent aggregation. Then, dissociation of the hTTR(59-127) fragment occurs, which was found to be the rate-limiting step. The latter data provided another avenue for intervention. In fact, even if cleaved, diflunisal, which bound at the dimer-dimer interface of the tetramer, was found to reduce the fragment hTTR(59-127) dissociation and to prevent amyloid nucleation and formation.

These findings might have relevant implications in hTTR-based amyloidogenic complications, often associated to Inflammatory Bowel Diseases (IBD) (**59**). In fact, subtilisin is a

serine protease, not belonging to the trypsin family, secreted from *B. subtilis* which is an abundant commensal in the gut microbiota. In IBD, the permeability of the intestinal mucosa is much increased (**30**), allowing the translocation of subtilisin to the bloodstream where the protease might cleave hTTR to hTTR(59-127), facilitating dissociation and fibril formation.

REFERENCES

1.   Stabilini, R., Vergani, C., Agostoni, A., and Agostoni, R. P. (1968) Influence of age and sex on prealbumin levels. *Clin Chim Acta* **20**, 358-359

2.   Chung, C. M., Connors, L. H., Benson, M. D., and Walsh, M. T. (2001) Biophysical analysis of normal transthyretin: implications for fibril formation in senile systemic amyloidosis. *Amyloid* **8**, 75-83

3.   Foss, T. R., Wiseman, R. L., and Kelly, J. W. (2005) The pathway by which the tetrameric protein transthyretin dissociates. *Biochemistry* **44**, 15525-15533

4.   Blake, C. C., Swan, I. D., Rerat, C., Berthou, J., Laurent, A., and Rerat, B. (1971) An x-ray study of the subunit structure of prealbumin. *J Mol Biol* **61**, 217-224

5.   Hamilton, J. A., and Benson, M. D. (2001) Transthyretin: a review from a structural perspective. *Cell Mol Life Sci* **58**, 1491-1521

6.   Azevedo, E. P., Ledo, J. H., Barbosa, G., Sobrinho, M., Diniz, L., Fonseca, A. C., Gomes, F., Romao, L., Lima, F. R., Palhano, F. L., Ferreira, S. T., and Foguel, D. (2013) Activated microglia mediate synapse loss and short-term memory deficits in a mouse model of transthyretin-related oculoleptomeningeal amyloidosis. *Cell Death Dis* **4**, e789

7.   Faria, T. Q., Almeida, Z. L., Cruz, P. F., Jesus, C. S., Castanheira, P., and Brito, R. M. (2015) A look into amyloid formation by transthyretin: aggregation pathway and a novel kinetic model. *Phys Chem Chem Phys* **17**, 7255-7263

8.   Pinney, J. H., Whelan, C. J., Petrie, A., Dungu, J., Banypersad, S. M., Sattianayagam, P., Wechalekar, A., Gibbs, S. D., Venner, C. P., Wassef, N., McCarthy, C. A., Gilbertson, J. A., Rowczenio, D., Hawkins, P. N., Gillmore, J. D., and Lachmann, H. J. (2013) Senile systemic amyloidosis: clinical features at presentation and outcome. *J Am Heart Assoc* **2**, e000098

9.   Alhamadsheh, M. M., Connelly, S., Cho, A., Reixach, N., Powers, E. T., Pan, D. W., Wilson, I. A., Kelly, J. W., and Graef, I. A. (2011) Potent kinetic stabilizers that prevent transthyretin-mediated cardiomyocyte proteotoxicity. *Sci Transl Med* **3**, 97ra81

10. Westermark, P., Sletten, K., Johansson, B., and Cornwell, G. G., 3rd. (1990) Fibril in senile systemic amyloidosis is derived from normal transthyretin. *Proc Natl Acad Sci U S A* **87**, 2843-2845

11. Sipe, J. D. (1994) Amyloidosis. *Crit Rev Clin Lab Sci* **31**, 325-354

12. Jiang, X., Buxbaum, J. N., and Kelly, J. W. (2001) The V122I cardiomyopathy variant of transthyretin increases the velocity of rate-limiting tetramer dissociation, resulting in accelerated amyloidosis. *Proc Natl Acad Sci U S A* **98**, 14943-14948

13. Saelices, L., Johnson, L. M., Liang, W. Y., Sawaya, M. R., Cascio, D., Ruchala, P., Whitelegge, J., Jiang, L., Riek, R., and Eisenberg, D. S. (2015) Uncovering the Mechanism of Aggregation of Human Transthyretin. *J Biol Chem* **290**, 28932-28943

14. Hurshman Babbes, A. R., Powers, E. T., and Kelly, J. W. (2008) Quantification of the thermodynamically linked quaternary and tertiary structural stabilities of transthyretin and its disease-associated variants: the relationship between stability and amyloidosis. *Biochemistry* **47**, 6969-6984

15. Hammarstrom, P., Jiang, X., Hurshman, A. R., Powers, E. T., and Kelly, J. W. (2002) Sequence-dependent denaturation energetics: A major determinant in amyloid disease diversity. *Proc Natl Acad Sci U S A* **99 Suppl 4**, 16427-16432

16. Mizuguchi, M., Hayashi, A., Takeuchi, M., Dobashi, M., Mori, Y., Shinoda, H., Aizawa, T., Demura, M., and Kawano, K. (2008) Unfolding and aggregation of transthyretin by the truncation of 50 N-terminal amino acids. *Proteins* **72**, 261-269

17. Liz, M. A., Mar, F. M., Franquinho, F., and Sousa, M. M. (2010) Aboard transthyretin: From transport to cleavage. *IUBMB Life* **62**, 429-435

18. Saad, M., Lu, C., Koya, C., and Basak, A. (2016) Proteolytic truncation of human transthyretin linked to amyloidosis is mediated by a trypsin like enzyme: In vitro demonstration using model peptides. *Biochemical Compounds* **4**, 5

19. Kingsbury, J. S., Theberge, R., Karbassi, J. A., Lim, A., Costello, C. E., and Connors, L. H. (2007) Detailed structural analysis of amyloidogenic wild-type transthyretin using a novel purification strategy and mass spectrometry. *Anal Chem* **79**, 1990-1998

20. Ihse, E., Rapezzi, C., Merlini, G., Benson, M. D., Ando, Y., Suhr, O. B., Ikeda, S., Lavatelli, F., Obici, L., Quarta, C. C., Leone, O., Jono, H., Ueda, M., Lorenzini, M., Liepnieks, J., Ohshima, T., Tasaki, M., Yamashita, T., and Westermark, P. (2013) Amyloid fibrils containing fragmented ATTR may be the standard fibril composition in ATTR amyloidosis. *Amyloid* **20**, 142-150

21. Bergstrom, J., Gustavsson, A., Hellman, U., Sletten, K., Murphy, C. L., Weiss, D. T., Solomon, A., Olofsson, B. O., and Westermark, P. (2005) Amyloid deposits in transthyretin-derived amyloidosis: cleaved transthyretin is associated with distinct amyloid morphology. *J Pathol* **206**, 224-232

22. Ihse, E., Stangou, A. J., Heaton, N. D., O'Grady, J., Ybo, A., Hellman, U., Edvinsson, A., and Westermark, P. (2009) Proportion between wild-type and mutant protein in truncated compared to full-length ATTR: an analysis on transplanted transthyretin T60A amyloidosis patients. *Biochem Biophys Res Commun* **379**, 846-850

23. Mangione, P. P., Porcari, R., Gillmore, J. D., Pucci, P., Monti, M., Porcari, M., Giorgetti, S., Marchese, L., Raimondi, S., Serpell, L. C., Chen, W., Relini, A., Marcoux, J., Clatworthy, I. R., Taylor, G. W., Tennent, G. A., Robinson, C. V., Hawkins, P. N., Stoppini, M., Wood, S. P., Pepys, M. B., and Bellotti, V. (2014) Proteolytic cleavage of Ser52Pro variant transthyretin triggers its amyloid fibrillogenesis. *Proc Natl Acad Sci U S A* **111**, 1539-1544

24. Mangione, P. P., Verona, G., Corazza, A., Marcoux, J., Canetti, D., Giorgetti, S., Raimondi, S., Stoppini, M., Esposito, M., Relini, A., Canale, C., Valli, M., Marchese, L., Faravelli, G., Obici, L., Hawkins, P. N., Taylor, G. W., Gillmore, J. D., Pepys, M. B., and Bellotti, V. (2018) Plasminogen activation triggers transthyretin amyloidogenesis in vitro. *J Biol Chem* **293**, 14192-14199

25. Thylen, C., Wahlqvist, J., Haettner, E., Sandgren, O., Holmgren, G., and Lundgren, E. (1993) Modifications of transthyretin in amyloid fibrils: analysis of amyloid from homozygous and heterozygous individuals with the Met30 mutation. *Embo j* **12**, 743-748

26. Hermansen, L. F., Bergman, T., Jornvall, H., Husby, G., Ranlov, I., and Sletten, K. (1995) Purification and characterization of amyloid-related transthyretin associated with familial amyloidotic cardiomyopathy. *Eur J Biochem* **227**, 772-779

27. Tam, N. K., Uyen, N. Q., Hong, H. A., Duc le, H., Hoa, T. T., Serra, C. R., Henriques, A. O., and Cutting, S. M. (2006) The intestinal life cycle of Bacillus subtilis and close relatives. *J Bacteriol* **188**, 2692-2700

28. Thevaranjan, N., Puchta, A., Schulz, C., Naidoo, A., Szamosi, J. C., Verschoor, C. P., Loukov, D., Schenck, L. P., Jury, J., Foley, K. P., Schertzer, J. D., Larche, M. J., Davidson, D. J., Verdu, E. F., Surette, M. G., and Bowdish, D. M. E. (2018) Age-Associated Microbial Dysbiosis Promotes Intestinal Permeability, Systemic Inflammation, and Macrophage Dysfunction. *Cell Host Microbe* **23**, 570

29. Michielan, A., and D'Inca, R. (2015) Intestinal Permeability in Inflammatory Bowel Disease: Pathogenesis, Clinical Evaluation, and Therapy of Leaky Gut. *Mediators Inflamm* **2015**, 628157

30. Spadoni, I., Zagato, E., Bertocchi, A., Paolinelli, R., Hot, E., Di Sabatino, A., Caprioli, F., Bottiglieri, L., Oldani, A., Viale, G., Penna, G., Dejana, E., and Rescigno, M. (2015) A gut-vascular barrier controls the systemic dissemination of bacteria. *Science* **350**, 830-834

31. Lorkowski, G. (2012) Gastrointestinal absorption and biological activities of serine and cysteine proteases of animal and plant origin: review on absorption of serine and cysteine proteases. *Int J Physiol Pathophysiol Pharmacol* **4**, 10-27

32. Petre, S., Shah, I. A., and Gilani, N. (2008) Review article: gastrointestinal amyloidosis - clinical features, diagnosis and therapy. *Aliment Pharmacol Ther* **27**, 1006-1016

33. Bashor, M. M., Hewett, J., Lackey, A., Driskell, W. J., and Neese, J. W. (1987) Purification of prealbumin from human serum. *Prep Biochem* **17**, 209-227

34. Colon, W., and Kelly, J. W. (1992) Partial denaturation of transthyretin is sufficient for amyloid fibril formation in vitro. *Biochemistry* **31**, 8654-8660

35. Sokolov, A. V., Acquasaliente, L., Kostevich, V. A., Frasson, R., Zakharova, E. T., Pontarollo, G., Vasilyev, V. B., and De Filippis, V. (2015) Thrombin inhibits the anti-myeloperoxidase and ferroxidase functions of ceruloplasmin: relevance in rheumatoid arthritis. *Free Radic Biol Med* **86**, 279-294

36.   Acquasaliente, L., Peterle, D., Tescari, S., Pozzi, N., Pengo, V., and De Filippis, V. (2016) Molecular mapping of alpha-thrombin (alphaT)/beta2-glycoprotein I (beta2GpI) interaction reveals how beta2GpI affects alphaT functions. *Biochem J* **473**, 4629-4650

37.   Micsonai, A., Wien, F., Bulyaki, E., Kun, J., Moussong, E., Lee, Y. H., Goto, Y., Refregiers, M., and Kardos, J. (2018) BeStSel: a web server for accurate protein secondary structure prediction and fold recognition from the circular dichroism spectra. *Nucleic Acids Res* **46**, W315-w322

38.   Adamski-Werner, S. L., Palaninathan, S. K., Sacchettini, J. C., and Kelly, J. W. (2004) Diflunisal analogues stabilize the native state of transthyretin. Potent inhibition of amyloidogenesis. *J Med Chem* **47**, 355-374

39.   Monaco, H. L., Rizzi, M., and Coda, A. (1995) Structure of a complex of two plasma proteins: transthyretin and retinol-binding protein. *Science* **268**, 1039-1041

40.   Cavallo, L., Kleinjung, J., and Fraternali, F. (2003) POPS: A fast algorithm for solvent accessible surface areas at atomic and residue level. *Nucleic Acids Res* **31**, 3364-3366

41.   Vriend, G. (1990) WHAT IF: a molecular modeling and drug design program. *J Mol Graph* **8**, 52-56, 29

42.   Pettersen, E. F., Goddard, T. D., Huang, C. C., Couch, G. S., Greenblatt, D. M., Meng, E. C., and Ferrin, T. E. (2004) UCSF Chimera--a visualization system for exploratory research and analysis. *J Comput Chem* **25**, 1605-1612

43.   Poulsen, K., Bahl, J. M., Tanassi, J. T., Simonsen, A. H., and Heegaard, N. H. (2012) Characterization and stability of transthyretin isoforms in cerebrospinal fluid examined by immunoprecipitation and high-resolution mass spectrometry of intact protein. *Methods* **56**, 284-292

44.   Theberge, R., Connors, L., Skinner, M., Skare, J., and Costello, C. E. (1999) Characterization of transthyretin mutants from serum using immunoprecipitation, HPLC/electrospray ionization and matrix-assisted laser desorption/ionization mass spectrometry. *Anal Chem* **71**, 452-459

45.   Ferreira, N., Saraiva, M. J., and Almeida, M. R. (2011) Natural polyphenols inhibit different steps of the process of transthyretin (TTR) amyloid fibril formation. *FEBS Lett* **585**, 2424-2430

46.   Kelly, S. M., Jess, T. J., and Price, N. C. (2005) How to study proteins by circular dichroism. *Biochim Biophys Acta* **1751**, 119-139

47.   Klabunde, T., Petrassi, H. M., Oza, V. B., Raman, P., Kelly, J. W., and Sacchettini, J. C. (2000) Rational design of potent human transthyretin amyloid disease inhibitors. *Nat Struct Biol* **7**, 312-321

48.   Jiang, P., and Mellors, A. (2004) Handbook of proteolytic enzymes. London: Elsevier

49.   Naiki, H., Higuchi, K., Hosokawa, M., and Takeda, T. (1989) Fluorometric determination of amyloid fibrils in vitro using the fluorescent dye, thioflavin T1. *Anal Biochem* **177**, 244-249

50.   Srivastava, A., Singh, P. K., Kumbhakar, M., Mukherjee, T., Chattopadyay, S., Pal, H., and Nath, S. (2010) Identifying the bond responsible for the fluorescence modulation in an amyloid fibril sensor. *Chemistry* **16**, 9257-9263

51.   Uversky, V. N. (2007) Neuropathology, biochemistry, and biophysics of alpha-synuclein aggregation. *J Neurochem* **103**, 17-37

52.   Sartiani, L., Bucciantini, M., Spinelli, V., Leri, M., Natalello, A., Nosi, D., Maria Doglia, S., Relini, A., Penco, A., Giorgetti, S., Gerace, E., Mannaioni, G., Bellotti, V., Rigacci, S., Cerbai, E., and Stefani, M. (2016) Biochemical and Electrophysiological Modification of Amyloid Transthyretin on Cardiomyocytes. *Biophys J* **111**, 2024-2038

53.   Gustavsson, A., Engstrom, U., and Westermark, P. (1991) Normal transthyretin and synthetic transthyretin fragments form amyloid-like fibrils in vitro. *Biochem Biophys Res Commun* **175**, 1159-1164

54.   Hiippala, K., Jouhten, H., Ronkainen, A., Hartikainen, A., Kainulainen, V., Jalanka, J., and Satokari, R. (2018) The Potential of Gut Commensals in Reinforcing Intestinal Barrier Function and Alleviating Inflammation. *Nutrients* **10**

55.   Yu, L. C., Wang, J. T., Wei, S. C., and Ni, Y. H. (2012) Host-microbial interactions and regulation of intestinal epithelial barrier function: From physiology to pathology. *World J Gastrointest Pathophysiol* **3**, 27-43

56.   van Breemen, R. B., and Li, Y. (2005) Caco-2 cell permeability assays to measure drug absorption. *Expert Opin Drug Metab Toxicol* **1**, 175-185

57.   Castano, A., Helmke, S., Alvarez, J., Delisle, S., and Maurer, M. S. (2012) Diflunisal for ATTR cardiac amyloidosis. *Congest Heart Fail* **18**, 315-319

58.   Sekijima, Y. (2014) Recent progress in the understanding and treatment of transthyretin amyloidosis. *J Clin Pharm Ther* **39**, 225-233

59.   Serra, I., Oller, B., Manosa, M., Naves, J. E., Zabana, Y., Cabre, E., and Domenech, E. (2010) Systemic amyloidosis in inflammatory bowel disease: retrospective study on its prevalence, clinical presentation, and outcome. *J Crohns Colitis* **4**, 269-274

APPENDIX

Appendix A

Abbreviations and Symbols

Å, Angstrom

aa, Amino acid

AD, Alzheimer's disease

Amp, Ampicillin

a.m.u., Atomic mass units

aPC, Active protein C

αSyn, Human α-synuclein

αT, Human α-thrombin

ATIII, Antithrombin

AU, Aggregation units

AUC, Area under the curve

BSA, Bovine serum albumin

β2GpI, β2-Glicoprotein I

β_TT, β-thrombin obtained by tryptic digestion

Cat-G, Cathepsin G

CD, Circular dichroism

ChCl, Choline chloride

Chymo., Chymotrypsin

Da, Dalton

DIC, Disseminated intravascular coagulation

DLS, Dynamic light scattering

DMSO, Dimethylsulfoxide

DTT, Dithiothreitol

EDTA, Ethylenediaminetetraacetic acid

ESI, Electrospray ionization

EtOH, Ethanol

F1·2, Prothrombin fragments 1 and 2

FI-FXIII, Coagulation factors

FIa-FXIIIa, Activated coagulation factors

Fmoc, Fluorenylmethoxycarbonyl

FpA/B, Fibrinopeptide A or B

Gla, γ-carboxyglutammic acid

Glu-C, Endoproteinase Glu-C

Gnd-HCl, Guanidine hydrochloride

HBS, 20mM HEPES pH 7.4, 0.15M NaCl, 0.1% PEG-8000 (w/v)

HBS-CaCl$_2$, HBS added with 5mM CaCl$_2$

HBS-EP, 10mM HEPES pH 7.4, 0.15M NaCl, 50μM EDTA, 0.005% tween-20

HEPES, 4-(2-hydroxyethyl)-1-piperazine ethanesulfonic acid

HM2, Hirudin variant 2 from *Hirudinaria manillensis*

HNE, Human Neutrophil Elastase

hTTR, human Transthyretin

hTTR(59-127), human Transthyretin fragment 59-127

HV1, Hirudin variant 1 from *Hirudo medicinalis*

IMAC, Immobilized metal ions affinity chromatography

IPTG, Isopropyl-β-D-1-thiogalactopyranoside

K1-2, Kringle domain-1 or -2

LB, Lurea Bertani broth

LBs, Lewy Bodies

LC-MS, Liquid chromatography coupled to mass spectrometry

Lnk, Linker in prothrombin sequence

mIIa, Meizothrombin

MS, High-resolution mass spectrometry

MW, Molecular Weight

m/z, Mass to charge ratio

NF-κB, Nuclear factor kappa-light-chain-enhancer of activated B cells

NP, Neutral Protease

NP-40, Nonyl-phenoxypolyetoxylethanol

NTA, Nitrilotriacetic acid

OD, Optical density

PARs, Protease activated receptors

PBS, 10mM TRIS-HCl, 0.15M NaCl

PC, Protein C

PD, Parkinson's disease

PEG, PolyEthylene Glycol

pNA, para-nitroanilide

PPACK, inhibitor of αT, D-phenylalanyl-L-prolyl-L-arginine chloromethyl ketone

Pre2, Prethrombin-2

ProT, Human prothrombin

Prot-3, Proteinase 3

SDS, Sodium Dodecyl Sulfate

SDS-PAGE, SDS-PolyAcrylamide Gel Electrophoresis

σPre2, Subtilisin-activated Pre2 or ProT

RP-HPLC, Reverse-phase high-pressure liquid chromatography

rT, Recombinant αT from *E. coli*

RU, Response Units

S2238, D-Phe-Pip-Arg-pNA

SPR, Surface plasmon resonance

TBS, 10mM TRIS-HCl, pH 8.0

TCA, Trichloroacetic acid

TEM, Transmission Electron Microscopy

TFA, Trifluoroacetic acid

TFPI, Tissue factor pathway inhibitor

ThT, Thioflavin-T

TLN, Thermolysin

TM, Thrombomodulin

TOF, Time-of-flight

TRAP, Tartrate resistant acid phosphatase

TRIS, tris(hydroxymethyl)aminomethane

UL-vWF, Ultra large von Willebrand Factor multimers

UV-Vis, Ultraviolet visible spectrophotometry

vWF, von Willebrand Factor

v/v, Volume/volume

w/v, Weight/volume

Appendix B

Amino Acids

Ala	A	Alanine
Arg	R	Arginine
Asp	D	Aspartic acid
Asn	N	Asparagine
Cys	C	Cysteine
Gly	G	Glycine
Gln	Q	Glutamine
Glu	E	Glutamic acid
His	H	Histidine
Ile	I	Isoleucine
Lys	K	Lysine
Leu	L	Leucine
Met	M	Methionine
Phe	F	Phenylalanine
Pro	P	Proline
Ser	S	Serine
Thr	T	Threonine
Tyr	Y	Tyrosine
Trp	W	Tryptophan
Val	V	Valine

Appendix C

Thrombin Numbering Scheme

Chym	T1h	F1g	G1f	S1e	G1d	E1c	A1b	D1a	C1	G2	L3	R4
Ch-A	1	2	3	4	5	6	7	8	9	10	11	12
Ch-B	-	-	-	-	-	-	-	-	-	-	-	-
ProT	285	286	287	288	289	290	291	292	293	294	295	296

Chym	P5	L6	F7	E8	K9	K10	S11	L12	E13	D14	K14a	T14b
Ch-A	13	14	15	16	17	18	19	20	21	22	23	24
Ch-B	-	-	-	-	-	-	-	-	-	-	-	-
ProT	297	298	299	300	301	302	303	304	305	306	307	308

Chym	E14c	R14d	E14e	L14f	L14g	E14h	S14i	Y14j	I14k	D14l	G14m	R15
Ch-A	25	26	27	28	29	30	31	32	33	34	35	36
Ch-B	-	-	-	-	-	-	-	-	-	-	-	-
ProT	309	310	311	312	313	314	315	316	317	318	319	320

Chym	I16	V17	E18	G19	S20	D21	A22	E23	I24	G25	M26	S27
Ch-A	37	38	39	40	41	42	43	44	45	46	47	48
Ch-B	1	2	3	4	5	6	7	8	9	10	11	12
ProT	321	322	323	324	325	326	327	328	329	330	331	332

Chym	P28	W29	Q30	V31	M32	L33	F34	R35	K36	S36a	P37	Q38
Ch-A	49	50	51	52	53	54	55	56	57	58	59	60
Ch-B	13	14	15	16	17	18	19	20	21	22	23	24
ProT	333	334	335	336	337	338	339	340	341	342	343	344

Chym	E39	L40	L41	C42	G43	A44	S45	L46	I47	S48	D49	R50
Ch-A	61	62	63	64	65	66	67	68	69	70	71	72
Ch-B	25	26	27	28	29	30	31	32	33	34	35	36
ProT	345	346	347	348	349	350	351	352	353	354	355	356

Chym	W51	V52	L53	T54	A55	A56	H57	C58	L59	L60	Y60a	P60b
Ch-A	73	74	75	76	77	78	79	80	81	82	83	84
Ch-B	37	38	39	40	41	42	43	44	45	46	47	48
ProT	357	358	359	360	361	362	363	364	365	366	367	368

Chym	P60c	W60d	D60e	K60f	N60g	F60h	T60i	E61	N62	D63	L64	L65
Ch-A	85	86	87	88	89	90	91	92	93	94	95	96
Ch-B	49	50	51	52	53	54	55	56	57	58	59	60
ProT	369	370	371	372	373	374	375	376	377	378	379	380

Chym	V66	R67	I68	G69	K70	H71	S72	R73	T74	R75	Y76	E77
Ch-A	97	98	99	100	101	102	103	104	105	106	107	108
Ch-B	61	62	63	64	65	66	67	68	69	70	71	72
ProT	381	382	383	384	385	386	387	388	389	390	391	392

Chym	R77a	N78	I79	E80	K81	I82	S83	M84	L85	E86	K87	I88
Ch-A	109	110	111	112	113	114	115	116	117	118	119	120
Ch-B	73	74	75	76	77	78	79	80	81	82	83	84
ProT	393	394	395	396	397	398	399	400	401	402	403	404

Chym	Y89	I90	H91	P92	R93	Y94	N95	W96	R97	E97a	N98	L99
Ch-A	121	122	123	124	125	126	127	128	129	130	131	132
Ch-B	85	86	87	88	89	90	91	92	93	94	95	96
ProT	405	406	407	408	409	410	411	412	413	414	415	416

Chym	D100	R101	D102	I103	A104	L105	M106	K107	L108	K109	K110	P111
Ch-A	133	134	135	136	137	138	139	140	141	142	143	144
Ch-B	97	98	99	100	101	102	103	104	105	106	107	108
ProT	417	418	419	420	421	422	423	424	425	426	427	428

Chym	V112	A113	F114	S115	D116	Y117	I118	H119	P120	V121	C122	L123
Ch-A	145	146	147	148	149	150	151	152	153	154	155	156
Ch-B	109	110	111	112	113	114	115	116	117	118	119	120
ProT	429	430	431	432	433	434	435	436	437	438	439	440

Chym	P124	D125	R126	E127	T128	A129	A129a	S129b	L129c	L130	Q131	A132
Ch-A	157	158	159	160	161	162	163	164	165	166	167	168
Ch-B	121	122	123	124	125	126	127	128	129	130	131	132
ProT	441	442	443	444	445	446	447	448	449	450	451	452

Chym	G133	Y134	K135	G136	R137	V138	T139	G140	W141	G142	N143	L144
Ch-A	169	170	171	172	173	174	175	176	177	178	179	180
Ch-B	133	134	135	136	137	138	139	140	141	142	143	144
ProT	453	454	455	456	457	458	459	460	461	462	463	464

Chym	K145	E146	T147	W148	T149	A149a	N149b	V149c	G149d	K149e	G150	Q151
Ch-A	181	182	183	184	185	186	187	188	189	190	191	192
Ch-B	145	146	147	148	149	150	151	152	153	154	155	156
ProT	465	466	467	468	469	470	471	472	473	474	475	476

Chym	P152	S153	V154	L155	Q156	V157	V158	N159	L160	P161	I162	V163
Ch-A	193	194	195	196	197	198	199	200	201	202	203	204
Ch-B	157	158	159	160	161	162	163	164	165	166	167	168
ProT	477	478	479	480	481	482	483	484	485	486	487	488

Chym	E164	R165	P166	V167	C168	K169	D170	S171	T172	R173	I174	R175
Ch-A	205	206	207	208	209	210	211	212	213	214	215	216
Ch-B	169	170	171	172	173	174	175	176	177	178	179	180
ProT	489	490	491	492	493	494	495	496	497	498	499	500

Chym	I176	T177	D178	N179	M180	F181	C182	A183	G184	Y184a	K185	P186
Ch-A	217	218	219	220	221	222	223	224	225	226	227	228
Ch-B	181	182	183	184	185	186	187	188	189	190	191	192
ProT	501	502	503	504	505	506	507	508	509	510	511	512

Chym	D186a	E186b	G186c	K186d	R187	G188	D189	A190	C191	E192	G193	D194
Ch-A	229	230	231	232	233	234	235	236	237	238	239	240
Ch-B	193	194	195	196	197	198	199	200	201	202	203	204
ProT	513	514	515	516	517	518	519	520	521	522	523	524

Chym	S195	G196	G197	P198	F199	V200	M201	K202	S203	P204	F204a	N204b
Ch-A	241	242	243	244	245	246	247	248	249	250	251	252
Ch-B	205	206	207	208	209	210	211	212	213	214	215	216
ProT	525	526	527	528	529	530	531	532	533	534	535	536

Chym	N205	R206	W207	Y208	Q209	M210	G211	I212	V213	S214	W215	G216
Ch-A	253	254	255	256	257	258	259	260	261	262	263	264
Ch-B	217	218	219	220	221	222	223	224	225	226	227	228
ProT	537	538	539	540	541	542	543	544	545	546	547	548

Chym	E217	G219	C220	D221	R221a	D222	G223	K224	Y225	G226	F227	Y228
Ch-A	265	266	267	268	269	270	271	272	273	274	275	276
Ch-B	229	230	231	232	233	234	235	236	237	238	239	240
ProT	549	550	551	552	553	554	555	556	557	558	559	560

Chym	T229	H230	V231	F232	R233	L234	K235	K236	W237	I238	Q239	K240
Ch-A	277	278	279	280	281	282	283	284	285	286	287	288
Ch-B	241	242	243	244	245	246	247	248	249	250	251	252
ProT	561	562	563	564	565	566	567	568	569	570	571	572

Chym	V241	I242	D243	Q244	F245	G246	E247
Ch-A	289	290	291	292	293	294	295
Ch-B	253	254	255	256	257	258	259
ProT	573	574	575	576	577	578	579

In the **first row** the chymotrypsinogen numeration of thrombin is indicated; in the **second row** the numeration in which the first residue of the A-chain is designated as 1 is indicated.; in the **third row** the numeration in which the first residue of the B-chain is designated as 1 is indicated; finally, the **last row** show the numeration of prothrombin.